# Modeling and Design Considerations for a Micro-Hydraulic Piezoelectric Power Generator



by

Onnik Yaglioglu

B.S. Mechanical Engineering
Bogazici University, 1999

Submitted to the Department of Mechanical Engineering and the
Department of Electrical Engineering and Computer Science
in Partial Fulfillment of the Requirements for the Degrees of

Master of Science in Mechanical Engineering

and

Master of Science in Electrical Engineering and Computer Science

at the
MASSACHUSETTS INSTITUTE OF TECHNOLOGY
February 2002



Signature of Author .....
Department of Mechanical Engineering
January 15, 2002

Certified by .....
Nesbitt W. Hagood, IV
Associate Professor of Aeronautics and Astronautics
Thesis Supervisor

Certified by .....
Alexander H. Slocum
Professor of Mechanical Engineering, MacVicar Faculty Fellow
Departmental Reader

Accepted by .....
Ain A. Sonin
Chairman, Department Committee on Graduate Students
Department of Mechanical Engineering

Accepted by .....
Arthur C. Smith
Chairman, Committee on Graduate Students
Department of Electrical Engineering and Computer Science

# Modeling and Design Considerations for a Micro-Hydraulic Piezoelectric Power Generator

by

Onnik Yaglioglu

Submitted to the Department of Mechanical Engineering and the
Department of Electrical Engineering and Computer Science
on January 15, 2002, in partial fulfillment of the
requirements for the degrees of
Master of Science in Mechanical Engineering
and
Master of Science in Electrical Engineering and Computer Science

## Abstract

Piezoelectric Micro-Hydraulic Transducers are compact high power density transducers, which can function bi-directionally as actuators/micropumps and/or power generators. They are designed to generate 0.5-1W power at frequencies of ~10-20kHz, resulting in high power densities approaching 500W/kg. These devices are comprised of a main chamber, two actively controlled valves, a low-pressure reservoir and a high-pressure reservoir. This thesis reports on modeling and design considerations for Micro-Hydraulic Piezoelectric Power Generators. Since these devices are complex fluid and structural systems, comprehensive simulation tools are needed for effective design. Operation of each subcomponent of the device is highly coupled and every design decision should be made with remaining components in mind. A system level simulation tool has been developed using Matlab/Simulink, by integrating models for different energy domains, namely fluids, structures, piezoelectrics and circuitry. The simulation architecture allows for integration of the elastic equations of structural members into the dynamic simulations as well as monitoring of important parameters such as chamber pressure, flowrate, and various structural component deflections and stresses. Using the simulation, the operation of the system is analyzed and important design considerations are evaluated. Fluidic oscillations within the system are analyzed and an optimization procedure for the membrane structure within the main chamber is presented. Parameter studies are performed for different piezoelectric materials, system compliances, and circuit topologies. Tradeoffs between operation conditions and their effect on the performance are discussed. A design procedure is developed. Results indicate that system efficiency is highly dependent on compliances within the device structure, the type of piezoelectric material used and rectifier circuit topology.

Thesis Supervisor: Nesbitt W. Hagood, IV
Title: Associate Professor of Aeronautics and Astrtonautics

Departmental Reader: Alexander H. Slocum
Title: Professor of Mechancial Engineering, MacVicar Faculty Fellow

# Acknowledgements

Special thanks goes to my family and my girlfriend. Without their support, this thesis could not have been completed. I would like to thank to my family for their continuous support and care. And, many thanks to my girlfriend for her patience and support.

Many thanks to Hagop Hachickian and Hachickian family for their continuous support and help since the very first day I came to Boston.

I would like to thank my colleagues in the MHT group. Yu Hsuan Su, thanks very much for your help and valuable insights you provided me. David Roberts, thanks for your guidance and valuable discussions. And Jorge Carretero, thanks for your support throughout the completion of this thesis.

I also would like to thank to Harry Callahan for his help in circuit modeling. Boston is missing you and your guitar sound! Next time you come, we are definitely going to jam!

Finally, I would like to thank to Boston. It is such a great city to have fun and relax. I don't know what I would do without the R&B and Jazz clubs. And, Cantab Lounge is always going to be my favorite place.

This thesis is dedicated to my family.

This research work was sponsored by DARPA under Grant #DAAG55-98-1-0361 and by ONR under Grant #N00014-97-1-0880.

# Nomenclature

| | |
|---|---|
| $P_{HPR}$ | high pressure reservoir pressure |
| $P_{LPR}$ | low pressure reservoir pressure |
| $P_{ch}$ | main chamber pressure |
| $\Delta P_{ch}$ | main chamber pressure band |
| $P_{int-in}$ | inlet valve intermediate pressure |
| $P_{int-out}$ | outlet valve intermediate pressure |
| $Q_{in}$ | inlet valve flow rate |
| $Q_{out}$ | outlet valve flow rate |
| $vo_{in}$ | inlet valve opening |
| $vo_{out}$ | outlet valve opening |
| $C_s$ | structural compliance of main chamber |
| $C_{eff}$ | effective compliance of the main chamber |
| $V_o$ | initial fluid volume of the main chamber |
| $\beta_f$ | bulk modulus of working fluid |
| $E$ | Young modulus of Silicon |
| $\nu$ | Poissons ratio of silicon |
| $\rho$ | density of working fluid |
| $D_{ch}$ | chamber diameter |
| $D_{pis}$ | piston diameter |
| $R_{vc}$ | valve cap radius |
| $w_t$ | tether width |
| $H_{ch}$ | chamber height |

| | |
|---|---|
| $D_p$ | piezoelectric element diameter |
| $L_p$ | piezoelectric element length |
| $t_{top}$ | top support structure thickness |
| $t_{bot}$ | bottom support structure thickness |
| $t_{pis}$ | piston thickness |
| $t_{tetop}$ | top tether thickness |
| $t_{tebot}$ | bottom tether thickness |
| $x_{pis}$ | piston deflection |
| $x_{te}$ | tether deflection |
| $x_b$ | bottom support structure deflection |
| $\Delta V_{tp}$ | volume swept by top support structure |
| $\Delta V_{pis}$ | volume swept by deflection of piston |
| $\Delta V_{pb}$ | volume swept by bending of piston |
| $\Delta V_{te}$ | volume swept by tether bending |
| $F_{te}$ | force between piston and tethers |
| $F_p$ | force on piezoelectric element |
| $d_{33}$ | piezoelectric constant |
| $s_{33}^D$ | open circuit compliance of piezoelectric element |
| $s_{33}^E$ | closed circuit compliance of piezoelectric element |
| $k_{33}$ | coupling coefficient of piezoelectric element |
| $k_{eff}$ | effective coupling factor |
| $V_p$ | voltage on piezoelectric element |
| $I_p$ | current through piezoelectric element |
| $V_b$ | battery voltage |
| $I_b$ | current through battery |
| $Q_p$ | charge on piezoelectric element |
| $\sigma_d$ | depolarization stress of piezoelectric element |
| $f$ | operation frequency |
| $\eta$ | system efficiency |
| $W$ | generated power |

# Contents

# List of Figures

# List of Tables

# Chapter 1

# Introduction

This chapter presents the configuration, operation and motivation of microhydraulic-piezoelectric power generators. Preliminary design considerations are discussed. The objective, scope and organization of the thesis are presented.

## 1.1 Microhydraulic Piezoelectric Transducers

Transducers are devices that convert physical energy from one form to another. Actuators and power generators are examples of transducer devices. The performance and usefulness of a transducer for most applications are highly dependent on two important characteristics: compactness and power density, that is, power output of the transducer per its unit volume. Conventional transducers, generally, not only tend to be heavy and bulky, but are also limited in terms of power transduction capabilities because of their low bandwidths. For instance, conventional hydraulic systems possess high single-stroke work, but their power densities are greatly reduced by their large mass. Recent advances in active materials technology have led to the development of many compact solid-state transducers. However, the power output from these solid-state transducers is fairly limited for most macro applications. Although the single-stroke work output of solid-state materials such as piezoelectric materials is relatively small, such materials possess very high bandwidths, and as such, are capable of high power output. However, since most applications do not require high frequency actuation, the high bandwidth potential of piezoelectric materials is not fully utilized. Since a transducer's power

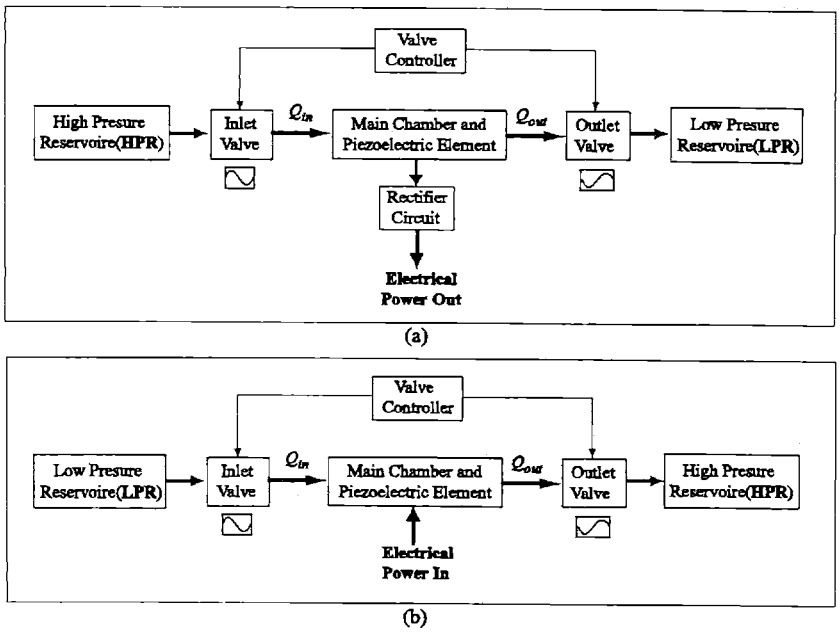


Figure 1-1: (a) Configuration of power generator (b) Configuration of actuator/ micopump. The actuator/micropump configuration can also be operated with check valves instead of active valves, which are necessary for power generator configuration.

output is the product of its single stroke energy and its bandwidth, it is feasible to create high performance transducers by combining high single-stroke force of a hydraulic system and high frequency displacements of a piezoelectric element in a synergistic manner[1]. This concept can be further exploited to create high performance transducers with very high power densities by miniaturizing the transducer systems. The state-of-the-art micromachining (or MEMS) technology has the potential to allow for the implementation of this concept at the micro scale.

Research and development of microfluidic devices has received a significant amount of interest in the past years. The feasibility of micromachining many of the key building blocks (flow channels, pumps, active/passive valves) of a micro-fluidic system including the integration of solid-state materials such as piezoelectric materials to actuate valves has already been demonstrated, and researchers are now striving to create complete microfluidic systems. However, the microfluidic devices developed thus far mostly feature small flow conductance, limited stroke, and low power density, and are mostly geared towards small flow/force applications such as microdosing of fluids. An extensive literature review on microfluidic devices can be found in

[2].

A unique feature of piezoelectric microhydraulic transducers is their ability to operate as both an actuator and a power generator, by merely reversing the direction of their operation. As actuators, these transducers transform electrical energy input into mechanical/hydraulic energy output, and as power generators, the transducers transform mechanical/hydraulic energy input into electrical energy that can be stored in a battery or a capacitor. These high performance transducers can significantly enhance the scope of micromachined transducers technology by enabling many novel applications. When utilized as actuators, they are capable of extending the usefulness of active material based structural actuation beyond small strain applications [1]. These actuators can also be useful in miniature robotics. As power generators, the transducers can extract electrical energy from wasted mechanical energy sources such as vibrations of operating machinery, heel strike of human gait, wind, sound and function as disposable batteries for numerous small electronic devices in both civilian and military applications. A literature survey about piezoelectric power generation will be presented in Chapter 2. Detailed information and comparisons of various transducers can be found in [2] where a feasibility analysis of Micro Hydraulic Transducers has been performed.

## 1.2 Configuration and Operation

The concept of piezoelectric micro-hydraulic transducer (MHT) is schematically illustrated in Figure 1-1 for actuator and power generator configurations. The transducers are comprised of the following generic components: the main chamber which houses a piezoelectrically driven tethered piston, two actively controlled valves, a low-pressure fluid reservoir (LPR), and a high-pressure fluid reservoir (HPR). The power generator configuration requires rectification circuitry to rectify and store the voltage generated by the piezoelectric element. The two active valves, one operating between the HPR and the main chamber and the other one operating between the main chamber and the LPR regulate the fluid flow into and out of the main chamber. The piezoelectric element within the pump chamber serves as the main energy transducing element. A detailed drawing of the device is shown in Figure 1-2.

When operating as an actuator/pump, the electrical signal applied to the piezoelectric

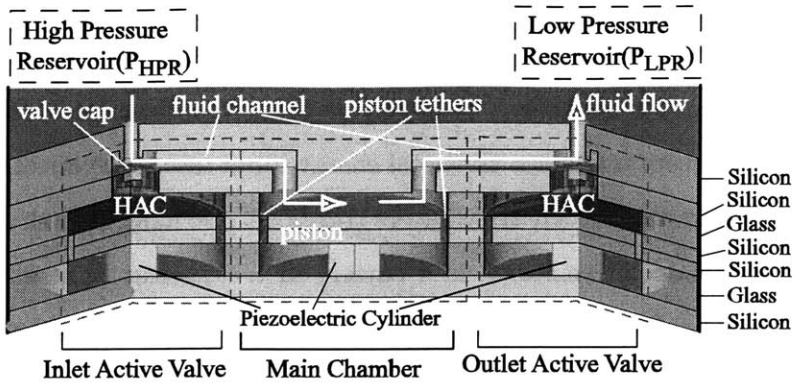


Figure 1-2: Device layout for power generator configuration. Top and bottom packaging pyrex layers not shown.

element results in pressure fluctuations inside the main chamber. When operating as a power generator, pressure fluctuations within the main chamber are converted to an electrical signal, which is rectified and stored in a battery or capacitor. In the actuator configuration, the voltage applied to the piezoelectric element induces a strain in the element resulting in a net volume change in the pump chamber. A controller synchronized with the pump signal cycles the active valves out of phase with each other in a specified duty cycle, transforming the volume oscillations of the chamber into a net fluid flow from the low pressure reservoir to the high pressure reservoir.

In the power generator configuration, the transducer operates in a manner that is reverse of the actuator. The controller toggles the valves with a phasing that allows fluid flow from the high pressure reservoir to the low pressure reservoir, thus transforming the static fluid pressure into high frequency pulses on the piezoelectric element via the piston. Valve actuation at high frequency creates a near sinusoidal cyclic stress on the piezoelectric element, thereby generating electrical charge across the element. Coupled circuitry rectifies this electrical energy and stores it in a battery or capacitor. It should be noted that, for the actuator/micropump configuration, check valves can also be used, instead of active valves, which is demonstrated in [3]. However, for the power generator configuration, active valves are necessary in order to convert the static pressure differential into pressure fluctuations on the piston. Generic operation duty cycle of the power generator configuration is shown in Figure 1-3.

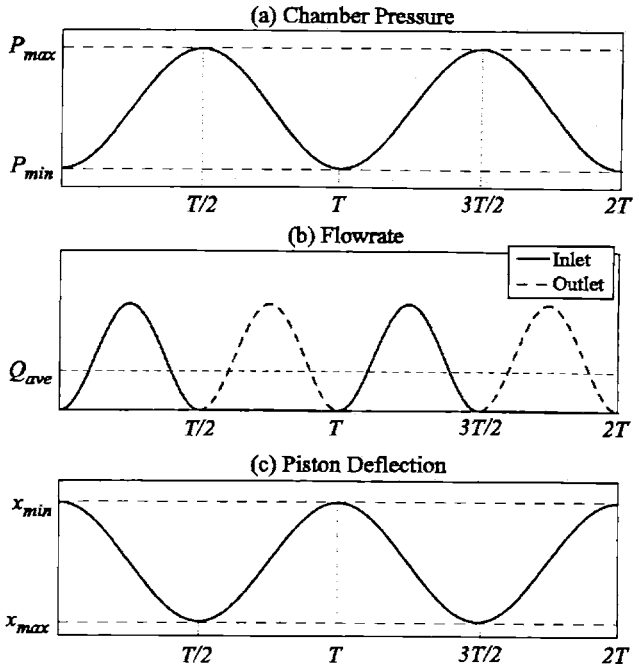


Figure 1-3: Generic operation duty cycle of the power generator.

Active valves are comprised of a similar chamber/piston structure, called hydraulic amplification chamber (HAC), which incorporates a fluid enclosed in the volume between the piston and the valve diaphragm, which effectively serves to amplify the small displacements of the piezoelectric material into significantly larger displacements of the valve cap and effectively transmits the high force actuation capability of the piezoelectric material. As the piston in the active valve is displaced by the piezoelectric element, the pressure of the compressed fluid acts to deform the smaller area valve membrane located at the top of the chamber. Deflection of the rigid cap at the center of the valve membrane blocks fluid flow through the corresponding fluid orifice. The utilization of the hydraulic amplification chamber also leads to minimization of the actuator material, and thus helps in achieving high power densities. The ability to micromachine the device provides the scope to further miniaturize the system to micro scales, leading to higher valve frequencies and therefore enhanced device power densities.

As shown in Figure 1-2, in each chamber, namely inlet HAC, main chamber (energy harvesting chamber) and outlet HAC, a piezoelectric element is sandwiched between the device

structure and a moveable piston plate. The piston plate is sufficiently thick for rigidity and is tethered to the chamber wall through thin flexible diaphragms that extend radially from the outer edges of the cylinder. The structure effectively constitutes a piston that can move vertically up and down when a net force is applied to it.

The prototype MHT device consists of a 9-layer stack of pyrex and silicon micromachined layers, as shown in Figure 1-2 and Figure 1-4. Sealing of the piston in the main chamber is provided by annular tethers which are created through Deep Reactive Ion Etching (DRIE) of a SOI wafer. The tether thickness ($\tilde{}10\mu$m) is defined by the SOI device layer, and the buried oxide acts as an etch stop. All glass layers are patterned by conventional diamond core drilling. Piezoelectric cylinders are core drilled from piezoelectric substrate plates, onto which a Ti-Pt-AuSn-Au multilayer film is sputter-deposited for eutectic bonding. The device assembly is accomplished through anodic bonding of the glass layers to the silicon layers at $300^0$C, a process which also enables the AuSn eutectic alloy to melt. Upon cooling, the alloy solidifies, bonding the piezoelectric cylinders to the silicon layers. Detailed information about the fabrication techniques developed for piezoelectric micro-hydraulic transducers can be found in[3], [6], and [7].

## 1.3 Preliminary Design Considerations

The proposed MHT devices derive their enhanced performance from several inherent design features. For efficient device operation, the compliances within the system, which result from the deformations of the structural members like piston, tether and support structures, and compression of the working fluid within the chambers should be minimum. This implies that the chambers should have small volumes and the structural members should be as thick as possible. This introduces trade-offs between fabrication limitations and design requirements. The type of piezoelectric element also affects system efficiency since the coupling coefficient of the element determines the electromechanical energy conversion work-cycle. For the power generator configuration the rectifier circuit topology is another factor affecting system efficiency, since it determines the electromechanical energy conversion work-cycle along with the piezoelectric material.

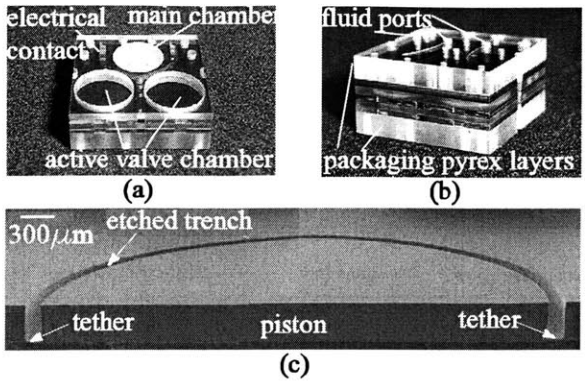


Figure 1-4: (a) 5-layer device for subcomponent testing (b) Complete 9-layer device (c) SEM of micromachined tethered piston structure [7].

Design of the piston tether structure is very crucial for system operation. The tethers should be flexible enough to allow sufficient motion of the piston, yet stiff enough to avoid introduction of excessive compliance into the system. Similar design consideration is also valid for the valve membrane. Achieving high power density critically depends on valves having high bandwidth (frequencies in the tens of kilohertz), sufficient actuation force to overcome large pressures (~1-2 MPa) and large stroke (~20-30$\mu m$). The valve membranes should be designed such that they are flexible enough to allow for large valve stroke and stiff enough to operate against high pressures and have high natural frequencies. Large stroke actuation of the valve cap generally results in nonlinear membrane behavior.

Possible fluidic and structural oscillations within the system should be considered. For example the fluid channels and the main chamber constitute a resonating system similar to a Helmholtz resonator. Similarly, piezoelectric element and piston dynamics, which affect the bandwidth of the device, should also be considered.

Important design limitations are maximum allowable stress in the membranes and the depolarization stress of the piezoelectric material. The stress in the tether structures shouldn't exceed 1GPa [7]. Piezoelectric materials also differ in their depolarization stress, which determines the energy density of the material. If during the operation, the stress on the piezoelectric element exceeds the depolarization stress, the element looses its functionality.

The choice of working fluid is also important since different fluids have different bulk moduli,

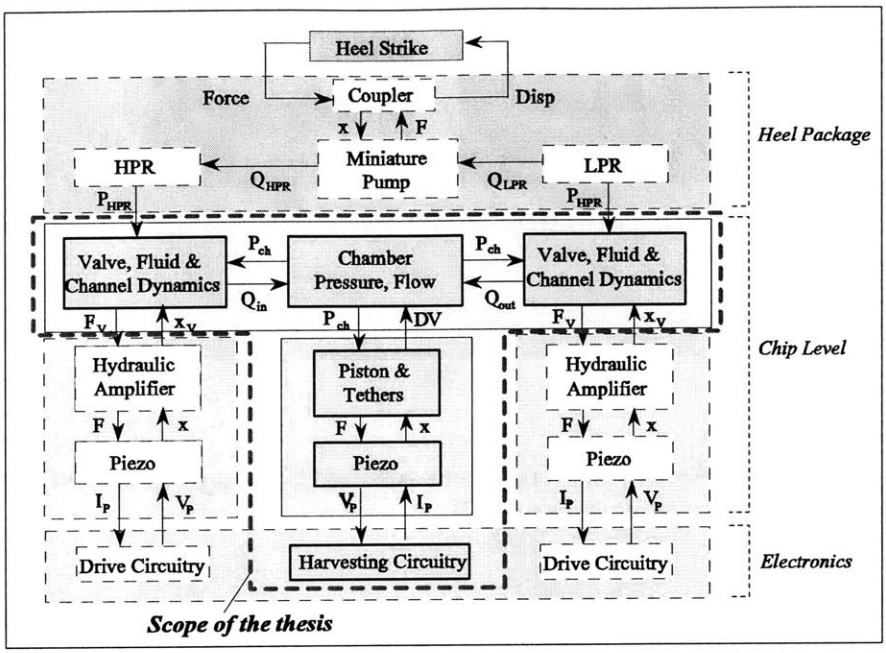


Figure 1-5: Overall system architecture for the heel strike power generation configuration.

densities and viscosities.

## 1.4 Objective, Scope and Organization of the Thesis

Since these devices are complex, comprehensive simulation tools are needed for effective design. Operation of each subcomponent of the device is highly coupled and every design decision should be made with remaining components in mind. The simulation tool should allow for the monitoring of important parameters such as chamber pressure, flowrate, and various structural component deflections and stresses. A system level simulation tool is needed which should be developed by integration of different energy domains, namely fluids, structures, piezoelectric material and circuitry. The challenges in modeling and simulation are: microscale fluid flow, incorporation of membrane behavior into dynamic simulation, prediction of structural compliances and incorporation of the elastic equations of the structural members into simulation.

The MHT group at MIT Active Material and Structures Laboratory(AMSL) has obtained good experimental correlation for subcomponent models from tests on piezoelectrically driven

piston/tether structure, hydraulic amplification chamber structure and valve membrane [6], flow tests through macro disc valves [4], and micropumps [3].

This thesis focuses on the modeling and design of piezoelectric microhydraulic transducers used as power generators. The system architecture for a possible application, namely heel strike power generation configuration is shown in Figure 1-5. The scope of the thesis is shown with the dashed line in the system architecture. The heel package design will not be discussed. Also design of the active valve structure will not discussed, which is detailed in [5]. Orifice models developed in [4] are used for fluid flow through the valves.

The objectives of this thesis are:

- To develop a comprehensive system level model and simulation tool to analyze the main chamber and the associated fluid channels and valves,

- To gain insight into system operation and understand the factors affecting the system performance,

- Develop a design procedure, which should be complemented by the design of the active valves.

The organization of the thesis is as follows: Chapter 2 presents an analysis of piezoelectric power generation based on linear electromechanical energy conversion. Effect of circuitry and piezoelectric material on energy density and effective coupling factor is discussed. Chapter 3 presents a simple model of the energy harvesting chamber, simulations with the coupled circuitry and preliminary design considerations. The interaction of the main chamber and the circuitry is discussed. The circuits presented in Chapter 2 and different piezoelectric materials are compared in terms of flowrate and frequency requirements for a given pressure differential and power, and in terms of system efficiency. Chapter 4 presents the detailed modelling of the energy harvesting chamber and investigates the contribution of different structural components on the effective compliance of the chamber. It also presents the simulation architecture used for integrating elastic equations into system level simulation. Chapter 5 discusses further design considerations for choosing chamber geometry with regard to operation conditions like maximum pressure, operation frequency and flowrate. Parameter studies are performed and a design procedure is developed. Chapter 6 summarizes important results and conclusions presented in previous chapters and presents recommendations for future work.

# Chapter 2

# Piezoelectric Power Generation and Circuitry

This chapter presents an analysis of piezoelectric power generation based on linear electromechanical energy conversion. Effect of circuitry and piezoelectric material on electromechanical energy conversion and energy density is discussed.

## 2.1 Introduction

Piezoelectric materials are mostly used as sensors and actuators. Since they are capable of electromechanical energy conversion and some have high coupling coefficients, which is an indication of the efficiency of the electromechanical energy conversion, they can be also used as power generators from ambient vibration or impact energy, and as structural vibration dampers. The idea and the governing principles are the same for power generation and structural vibration damping, using piezoelectric elements and passive circuit elements. Damping of structural vibrations with passive electrical circuit elements is discussed in [15] and [14]. This method eliminates the need for viscoelastic materials or mechanical vibration absorbers attached to the structure, or complex amplifiers which are required by the piezoelectric materials for active structural control systems [15]. The coupling between mechanical and electrical domains provided by the piezoelectric effect allows the damping mechanism to be implemented as electrical circuit elements rather than physical masses, springs and dampers. Most of the discussions

which are valid for the structural damping applications with piezoelectric elements are valid for the power generation from ambient vibration or impact energy with piezoelectric elements. In both cases, the purpose is to transfer as much energy from the mechanical to the electrical domain. The transferred energy to the electrical domain can be either dissipated or stored. If a piezoelectric element is shunted with a resistor or with a resistor and inductor network, the converted electrical energy is basically dissipated. However, if the piezoelectric element is connected to a rectifier circuit, a diode bridge for example, with a capacitor or battery, the converted electrical energy can be stored.

## 2.2 Previous Work

Structural damping with piezoelectric elements shunted with a resistor and a resistor-inductor network is analyzed in [15]. In the resistive shunting the electromechanical energy conversion efficiency depends on the operation frequency, and the optimum frequency depends on the resistance value. In other words, optimum efficiency is obtained when the impedance of the piezoelectric element is equal to the impedance of the resistance. Shunting with a resistor and inductor introduces an electrical resonance, which can be optimally tuned to structural resonances for maximum vibration damping.

Linear shunting components such as resistive elements or resistive-inductive-capacitive circuits produce behavior analogous to that of viscoelastic damping materials and tuned proof-mass dampers. Nonlinear piezoelectric shunting for structural damping using a piezoelectric element attached to a diode bridge and a DC voltage is presented in [14]. The rectified DC shunt performs less well in terms of energy conversion efficiency compared with the resistive shunt at optimum frequency. However, unlike the resistive shunt, the rectified DC shunt is independent of frequency and the transferred energy can be recovered depending on the implementation of the DC voltage source.

Power generation characteristics of piezoelectric elements in response to impact loads are investigated in [9], [10] and [11]. In the first two, a ball is dropped from a certain height onto a piezoelectric plate vibrator. In the first one, the piezoelectric vibrator is shunted with a resistor and the efficiency of transformation from mechanical to electrical energy in terms of initial

height and shunted resistance value is investigated. The efficiency is defined as the ratio of the electrical energy dissipated in the resistor to the initial impact energy. The input mechanical impact energy effects the efficiency due to nonlinearity in the vibrator and as expected there is an optimum resistance value. They conclude that efficiency increases with decreasing input impact energy, increasing mechanical quality factor $Q_m$, increasing electromechanical coupling coefficient $k_{33}^2$ and decreasing dielectric loss $\tan\delta$. They obtain a maximum efficiency of 52%.

The same authors of [9] investigate the power generation characteristics of the same system attached to a diode bridge and capacitor instead of a resistor in [10]. In this case the transformation efficiency is defined as the ratio of the impact energy to the energy stored in the capacitor. As the capacitance of the capacitor increases, the electric charge increases because the duration of the oscillation becomes longer and the output voltage decreases. They conclude that there exists an optimum capacitance value in terms of transformation efficiency. They obtain a maximum efficiency of 35%. It should be noted that, if a force were imposed on a piezoelectric element, the voltage on the capacitor would always increase until half of the open circuit voltage which corresponds to the maximum stress on the piezoelectric element, regardless of the capacitance of the capacitor. The value of the capacitance would change the duration in which the maximum voltage is reached and the stored energy in the capacitor would be proportional to its capacitance, since the maximum voltage is constant for a given maximum stress. In the paper discussed above, the force on the piezoelectric element is not imposed, it is determined depending on the impedances of the vibrator and the capacitor. In this case, the impedance matching principle cannot be applied since the system is nonlinear because of the diode bridge. No power density figures are reported in [9] and [10].

Piezoelectric power generation from thermal energy is presented in [20]. This paper discusses an energy conversion system in which thermal energy is converted to high frequency, high voltage electric a.c energy. The conversion system is composed of a thermal-acoustic natural heat engine and a piezoelectric transduction system to convert the acoustic energy to electric energy.

Another system to convert acoustic energy to electric energy is presented in [35]. The device is designed to convert waste acoustic energy, e.g. in automobile or airplane jet engines to electrical energy in a predetermined frequency range. The system consists of a piezoelectric bending element, means for mounting the piezoelectric bending element in an acoustic energy

path and a tuning means mounted on to the piezoelectric bending element to set the resonant frequency of oscillation of the piezoelectric bending element within the predetermined frequency range.

The idea of piezoelectric power generation from the ocean waves is patented in [27]-[32] by Ocean Power Technologies, Inc. The motivation in these studies is to utilize the enormous amount of mechanical energy present in the oceans. [27] relates to the generation of electrical power from waves on the surface of bodies of water, and particularly to the conversion of the mechanical energy of such waves to electrical energy by means of piezoelectric materials. The system consists of piezoelectric elements in the form of one or a laminate of sheets, each sheet having an electrode on opposite surfaces thereof, a support means for maintaining the structure in a preselected position within and below the surface of the water. In certain embodiments, the elements are designed to enter into mechanical resonance in response to the passage of waves thereover, increasing the mechanical coupling efficiency between the waves and the elements. Similar approaches are presented in [28] and [30]. In [28], a float on a body of water is mechanically coupled to a piezoelectric material member for causing alternate straining and de-straining of the member in response to the up and down movement of the member in response to passing waves, thereby causing the member to generate electric energy. The output impedance of the float is matched to the input impedance of the member for increasing the energy transfer from the float to the member. In [30], the system comprises a weighted member supported from a piezoelectric element for applying a preselected strain to the element. In one embodiment, the element is supported by a float floating on the surface of the water. In another embodiment, the element is supported above the surface of the water and the weighted member, of negative buoyancy, is immersed in the water. Means are provided for tuning the natural frequency of the system to cause it to enter into mechanical resonance in response to passing waves. Similar approaches are presented in [29], [31] and [32].

Some circuitry considerations for piezoelectric power generation are presented in [33] and [26]. [33] presents a DC bias scheme for improved efficiency for applications including electrostrictive materials, which have very weak piezoelectric characteristics. However, if a DC bias is applied, the piezoelectric characteristics can be significantly increased. [26] presents an alternative rectifier circuit, which includes an inductor, a SCR(silicon controlled rectifier) and

a voltage detection circuit in the conduction path between the piezoelectric element and the storage element, a capacitor for example. The object is to optimize the transfer of the energy produced by a piezoelectric transducer to a load. Another circuit designed for a wide variety of applications is presented in [36].

Piezoelectric power generation for electronic wristwatch applications is presented in [23]-[25]. [23] presents an electronic wristwatch having a piezoelectric generator in it. The generator converts energy from mechanical to electrical energy to drive the electronic wristwatch. The oscillation of a weight produces mechanical energy as it oscillates. A wheel train transmits the mechanical energy to the generator by applying a torque to the generator. The generated voltage is rectified with a diode bridge. Similar systems are presented in [24] and [25].

Piezoelectric power generation from wind energy is presented in [21] and [22]. The system presented in [22] consists of a piezoelectric transducer mounted on a resilient blade which in turn is mounted on an independently flexible support member. Fluid flow against the blade causes bending stresses in the piezoelectric polymer which produces electric power.

Other piezoelectric power generation systems are presented in [34], [39], [38] and [37]. [34] presents a piezoelectric fluidic-electric generator which consists of a piezoelectric bending element, means for driving the piezoelectric bending element to oscillate with the energy of the fluid stream, and electrodes connected to the piezoelectric element to conduct current generated by the oscillatory motion of the piezoelectric element. [39] presents a system which consists of a piezoelectric array which is mounted on one or more tires of a motor vehicle. As the vehicle drives on the road, the tire is flexed during each revolution to distort the piezoelectric elements and generate electricity.

Piezoelectric materials are also used in power electronics applications such as transformers. Piezoelectric transformers are composite resonators made of two bonded piezoelectric parts. The vibration of one part, excited by an input electric voltage, induces an output voltage across the other part [40]. In other words, a piezoelectric transformer works by using the direct and converse piezoelectric effects to acoustically transform power from one voltage and current level to another [44]. Detailed information about the operational characteristics of piezoelectric transformers can be found in [41] and [42].

Piezoelectric transformers have low-electric noise because they transmit power by mechan-

ical vibration. They can also operate efficiently at high frequencies, whereas conventional electromagnetic transformers are not efficient at high frequencies because of core loss and copper loss. Other advantages over the electromagnetic transformers can be stated as high voltage isolation between primary and secondary, high frequency operation leading to reduction in the filter capacitors and low weight and size [43]. Since piezoelectric transformers have much higher power densities than electromagnetic transducers, they are very promising as power electronic components for miniature and lightweight electrical equipment.

Fundamental limits on energy transfer of piezoelectric transformers are discussed in [44]. The discussion details similar considerations to those of the piezoelectric power generation concept. One has to consider the work cycle of electromechanical energy conversion and associated circuitry. Also the maximum electric field, the maximum surface charge density, the maximum stress and the maximum strain of the piezoelectric element are important criteria to consider when determining the limitations of power transfer in a piezoelectric transformer, as well as in a piezoelectric power generation system.

## 2.3 Theoretical Background

The linear electromechanical energy conversion process with piezoelectric ceramics is by far the easiest to handle, since the piezoelectric, dielectric and elastic constants can be applied directly [8]. In linear analysis, the coefficients mentioned above are assumed to be constant during the operation. The nonlinearity at high fields and hysteresis effects are ignored, i.e. the losses due to nonlinear effects are not considered. It is also assumed that the operation frequency is well below the lowest resonant frequency of the piezoelectric element, i.e. the operation can be considered as quasi-static. The linear constitutive relationships for a general piezoelectric element are:

$$\begin{bmatrix} D \\ S \end{bmatrix} = \begin{bmatrix} \varepsilon^T & d \\ d_t & s^E \end{bmatrix} \begin{bmatrix} E \\ T \end{bmatrix} \tag{2.1}$$

where $D$ is a vector of electric displacements or charge density(charge/area), $S$ is the vector of material engineering strains, $E$ is the vector of electrical field in the material(volts/meter),

$T$ is the vector of material stresses (force/area), $\varepsilon$ is the matrix of dielectric constants, $d$ is the matrix of piezoelectric constants and $s$ is the matrix of compliance coefficients of the piezoelectric element. The superscripts $()^T$ and $()^E$ signify that the coefficients are measured at constant stress and constant electric field respectively and the subscript $()_t$ denotes the matrix transpose. In this chapter, a specific case will be considered where the piezoelectric element is subjected to compression parallel to the polarization of the element. It is assumed that the lateral dimensions are small compared to the axial dimension, so that only the axial stress $T_3$ needs to be considered ($T_1 = T_2 \approx 0$). Or, it can be assumed that, the element is free to expand in lateral directions so that $T_3$ is the only nonzero stress component. Under these conditions, equation 2.1 reduces to

$$\begin{bmatrix} D_3 \\ S_3 \end{bmatrix} = \begin{bmatrix} \varepsilon_{33}^T & d_{33} \\ d_{33} & s_{33}^E \end{bmatrix} \begin{bmatrix} E_3 \\ T_3 \end{bmatrix} \tag{2.2}$$

where the first and second subscripts of the piezoelectric, dielectric and elastic constants denote the orientation of the electric field and the stress respectively.

Quasi-static coupling factors, or coefficients, are very common and useful definitions for piezoelectric energy conversion. The coupling coefficients are dimensionless and thus they provide a useful comparison between different piezoelectric materials independent of the specific values of permittivity or compliance. The definition of the coupling coefficient described above is given in [18]. Figure 2-1 illustrates graphically the meaning of the coupling coefficient $k_{33}$. The cycle shown is as follows: first, the piezoelectric element is compressed under short circuit condition, then the compressive stress is removed under open circuit condition, and then the cycle is completed under constant stress condition by applying an ideal electric load. As work is done on the electric load, the strain returns to its initial state. For the idealized case illustrated in Figure 2-1(a), the coupling coefficient is defined as:

$$(k_{33})^2 = \frac{W_1}{W_1 + W_2} = \frac{s_{33}^E - s_{33}^D}{s_{33}^E} = \frac{d_{33}^2}{s_{33}^E \varepsilon_{33}^T} \tag{2.3}$$

where $W_1$ is the work done on the electric load and $W_2$ is the part of the energy unavailable to the electric load or the reversible stored elastic energy(strain energy).

Similarly, the coupling coefficient for energy conversion from electrical energy to mechanical

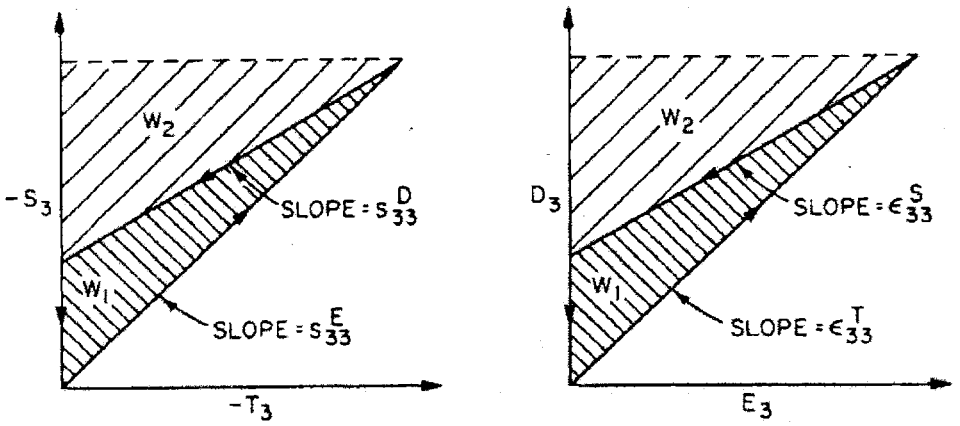


Figure 2-1: Graphic illustration of electromechanical energy conversion and definition of the piezoelectric coupling factor $k_{33}$ given in [18] (a) Conversion of energy from a mechanical source to electrical work (b) Conversion of energy from an electrical source to mechanical work.

energy can be derived using the idealized cycle illustrated in Figure 2-1(b). First, the element is mechanically free when the electric source is connected. Then the element is blocked mechanically parallel to polarization before the electric source is disconnected. Then with $E_3 = 0$ the mechanical block is removed and in its place a finite mechanical load is provided. For this idealized cycle of work illustrated in Figure 2-1(b), the coupling coefficient is defined as:

$$(k_{33})^2 = \frac{W_1}{W_1 + W_2} = \frac{e_{33}^T - e_{33}^{S_3=0}}{\varepsilon_{33}^T} = \frac{d_{33}^2}{s_{33}^E \varepsilon_{33}^T} \tag{2.4}$$

where $W_1$ is the work done on the mechanical load and $W_2$ is the part of the energy unavailable to the mechanical load.

The idealized work cycles illustrated in Figure 2-1 correspond to the standard definition of the piezoelectric coupling coefficient. Berlincourt proposes alternative work cycles of reversible electromechanical energy conversion in [8]. These cycles are shown in Figure 2-2. The first one, which is illustrated in Figure 2-2(a) corresponds to a case where the element is compressed with the electric load not connected, i.e. under open circuit conditions, then the electric load is connected with stress maintained, then the mechanical stress is reduced to zero with the electric load again disconnected and finally the electric load is connected and the element

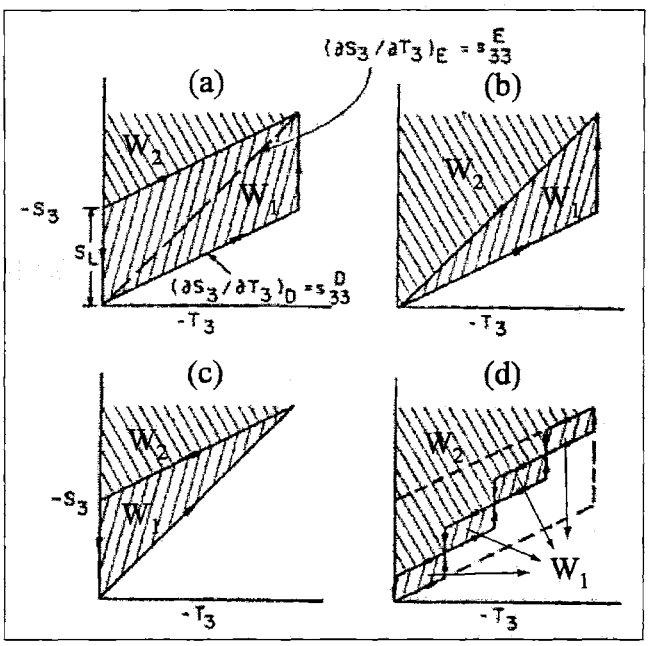


Figure 2-2: Alternative idealized work cycles given in [8].

returns to its initial state under constant stress. In the cycle illustrated in Figure 2-2(b), the element is compressed under open circuit condition, then the electric load is connected with stress maintained and finally the electric load is connected and the stress is reduced under closed circuit condition and the element returns to its initial state. The cycle in Figure 2-2(c) is identical to the cycle used for deriving the coupling coefficient in Figure 2-1. The cycle in Figure 2-2(d) corresponds to a case where the energy conversion occurs at several intermediate levels.

Berlincourt [8] defines an *effective coupling factor*, which is equal to

$$k_{eff}^2 = \frac{W_1}{W_1 + W_2} \tag{2.5}$$

He applies this definition to each of the different work cycles described above. Then he expresses the effective coupling factors for each of the different cycles in terms of the standard coupling coefficient given in Equation 2.3 as follows:

$$k_{eff(a)} = k_{33}\sqrt{2/(1+k_{33}^2)} \tag{2.6}$$

$$k_{eff(b)} = k_{33}\sqrt{1+k_{33}^2} \tag{2.7}$$

$$k_{eff(c)} = k_{33} \tag{2.8}$$

$$k_{eff(d)} = k_{33}\sqrt{2/(n+k_{33}^2)} \tag{2.9}$$

where $k_{33}$ is the standard coupling coefficient and $n$ is the number of intermediate levels in Figure 2-2(d). From equation 2.6 it is apparent that the coupling coefficient corresponding to the first case in Figure 2-2 is greater than the standard coupling coefficient defined previously.

It is important to note that, the cycles described so far are idealized or hypothetical cycles. The energy conversion process occurs with the mechanical and electrical energy sources connected and disconnected at will. However, no explanation has been given in terms of how these cycles can be achieved or approximated in a real application. In other words, the mechanical and electrical infrastructures which would allow these cycles to occur are not discussed. In this chapter, conversion from mechanical to electrical energy is considered, with emphasize on the circuitry used which basically determines the work-cycle. In other words, the rectifying circuitry is the electrical infrastructure in the power generation process. In the following sections two different circuit topologies will be analyzed in detail in terms of the effective coupling factor and energy density.

## 2.4 Circuitry Considerations

Although in the literature different mechanisms for piezoelectric power generation has been presented and some studies performed for piezoelectric material characterization for power generation, no detailed analysis has been presented in terms of effective coupling factor, energy density and piezoelectric material comparison with regard to circuitry. This section analyzes two different circuits for rectifying and storing the electrical energy generated by the piezoelectric element. These circuits constitute examples of nonlinear shunting of piezoelectric elements. The first one is a regular full bridge rectifier with a battery attached to it. The second circuitry is the same circuit proposed in [26] for piezoelectric power generation, which consists of a full bridge

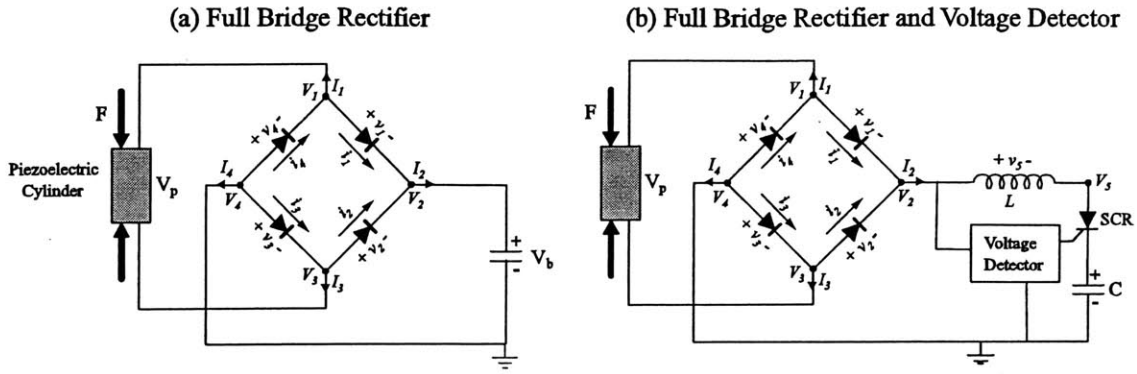


Figure 2-3: Alternative circuits to rectify and store the electrical energy generated by the piezoelectric element.

rectifier, an inductor, a silicon controlled rectifier (SCR), a voltage detector and a capacitor to store the electrical energy. The circuits are shown in Figure 2-3.

### 2.4.1 Modeling

This section presents the modeling of the piezoelectric element and the circuitry. The models are same for the two circuits under consideration except some small differences.

#### Piezoelectric Element

Linear piezoelectric constitutive relationships are assumed. The form of the constitutive equations used here is as follows:

$$\begin{bmatrix} S \\ E \end{bmatrix} = \begin{bmatrix} s_{33}^{D} & \frac{d_{33}}{\varepsilon_{33}^{T}} \\ \frac{d_{33}}{\varepsilon_{33}^{T}} & -\frac{1}{\varepsilon_{33}^{T}} \end{bmatrix} \begin{bmatrix} T \\ D \end{bmatrix} \tag{2.10}$$

where $D$ is the charge field, $S$ is the strain, $E$ is the electric field, and $T$ is the stress. For a cross-sectional area of $A_p$ and length of $L_p$, the expressions for the deflection of the piezoelectric element and the voltage across it become:

$$x_p = \frac{L_p}{A_p}(s_{33}^{D} F_p + \frac{d_{33}}{\varepsilon_{33}^{T}} Q_p) \tag{2.11}$$

$$V_p = \frac{L_p}{A_p}(\frac{d_{33}}{\varepsilon_{33}^T}F_p - \frac{1}{\varepsilon_{33}^T}Q_p) \tag{2.12}$$

where $x_p$ is the deflection, $Q_p$ is the charge, $F_p$ is the force applied on the piezoelectric cylinder, and $V_p$ is the voltage across the piezoelectric cylinder. And the current through the piezoelectric element is given by:

$$I_p = \frac{dQ_p}{dt} \tag{2.13}$$

**Diode Bridge**

The model of the diode bridge rectifier is based on [52]. The governing equations can be derived using Kirchoffs laws and diode equations. The notation in Figure 2-3 is used. Applying Kirchoffs Current Law*(KCL)* in the junctions 1,2,3,and 4, we get:

$$\begin{aligned} I_1 &= i_4 - i_1 \\ I_2 &= i_1 + i_2 \\ I_3 &= i_3 - i_2 \\ I_4 &= -i_3 - i_4 \end{aligned} \tag{2.14}$$

The voltages across the diodes are given by:

$$\begin{aligned} v_1 &= V_1 - V_2 \\ v_2 &= V_3 - V_2 \\ v_3 &= V_4 - V_3 \\ v_4 &= V_4 - V_1 \end{aligned} \tag{2.15}$$

Applying Kirchoffs Voltage Law *(KVL)* around the loops corresponding to the cases where $V_p > 0$ and $V_p < 0$ we get:

$$
\begin{aligned}
-V_p + v_1 + V_b + v_3 &= 0 \quad \text{for} \quad V_p > 0 \\
V_p + v_2 + V_b + v_4 &= 0 \quad \text{for} \quad V_p < 0
\end{aligned}
\tag{2.16}
$$

For the case where $V_p > 0$, the currents flowing through diodes #1 and #3 are the same, and for the case where $V_p < 0$, the currents flowing through diodes #2 and #4 are the same. Since all the diodes have the same constitutive relationship, we can write:

$$
\begin{aligned}
V_1 - V_2 &= V_4 - V_3 \quad \text{for} \quad V_p > 0 \\
V_4 - V_1 &= V_3 - V_2 \quad \text{for} \quad V_p > 0
\end{aligned}
\tag{2.17}
$$

Recognizing that $V_p = V_1 - V_3$ ,$V_2 = V_b$, $V_4 = 0$(ground) and using equation 2.17 we can write:

$$
\begin{aligned}
V_1 &= \frac{V_b + V_p}{2} \\
V_3 &= \frac{V_b - V_p}{2}
\end{aligned}
\tag{2.18}
$$

The $voltage - current$ relationships (constitutive law) of the diodes are:

$$
\begin{aligned}
i_n &= I_o[\exp \frac{qv_n}{\eta kT} - 1] \,, \qquad v_n \geq 0 \\
i_n &= 0 \qquad\qquad\qquad\qquad\quad v_n < 0
\end{aligned}
\tag{2.19}
$$

where the subscript $()_n$ denotes the diode number, $q = 1.60 \times 10^{-19}(C)$ is the electron charge, $k = 1.38 \times 10^{-23}(J/K)$ is the Boltzman constant and $T$ is the temperature($T = 300K$). $I_o$ and $\eta$ are diode properties. For CS57-04 diode (Collmer Semiconductor, Inc.), whose values will be used throughout the thesis, they are measured to be: $I_o = 10^{-6}$ and $\eta = 17.25$ [19].

### Diode Bridge and Voltage Detection Circuit

For the diode bridge with the voltage detection circuit, the model is similar. The equations 2.14, 2.15, and 2.19 are valid. However because of the implementation of the voltage detection circuit and SCR, the simulation architecture is different [53], which is shown in Appendix A. The voltage detection circuit is not modeled. Only its function is implemented in Simulink. The Kirchoffs Voltage Law can be written for this case using the notation in Figure 2-3 as:

$$\begin{aligned} -V_p + v_1 + v_5 + V_{SCR} + V_c + v_3 &= 0 \quad \text{for} \quad V_p > 0 \\ V_p + v_2 + v_5 + V_{SCR} + V_c + v_4 &= 0 \quad \text{for} \quad V_p < 0 \end{aligned} \tag{2.20}$$

The voltage across the inductor is given by:

$$v_5 = L\frac{d(I_2)}{dt} \tag{2.21}$$

And we can also write

$$V_c = \frac{1}{C}\int I_2 \tag{2.22}$$

## 2.4.2 Simulation and Analysis

Simulations are performed using Matlab/Simulink. The Simulink blocks and additional details are given in the Appendix A. The Simulink architecture is shown in Figure 2-4. The piezoelectric element block includes the constitutive relationships and the circuit block includes the equations corresponding to the circuitry. The piezoelectric element is excited with an imposed force on it. The geometry and operation conditions chosen for the simulation are shown in Table 2.1.

The imposed force is sinusoidal with an offset, namely it fluctuates between zero and the force corresponding to the maximum applicable stress, which is the depolarization stress of the piezoelectric element. In the case of PZN-4.5%PT, the depolarization stress is measured to be around $10MPa$ [19]. For the chosen piezoelectric cylinder diameter, the maximum force is $31.4N$. Detailed comparison of different piezoelectric materials will be presented in section 2.6.

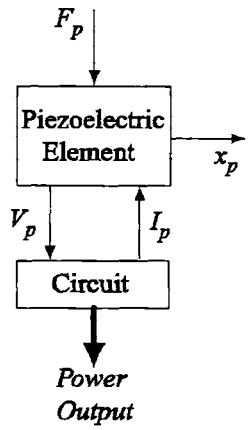


Figure 2-4: Simulation architecture used to simulate the piezoelectric element connected to the full bridge rectifier. The force is imposed on the piezoelectric element.

| | |
|---|---|
| Length of the piezoelectric element, $L_p$ | $1mm$ |
| Diameter of the piezoelectric element, $D_p$ | $2mm$ |
| Operation frequency, $f$ | $20kHz$ |
| Maximum force, $F_p$ | $31.4N$ |
| Optimum battery voltage, $V_b$ | $90V$ |
| Piezoelectric material | $PZN - 4.5\%PT$ |

Table 2.1: Geometry and operation conditions used in simulation

### Full Bridge Rectifier

**Simulation** Simulation time histories are shown in Figure 2-5. The operation at steady state can be summarized as follows: During the compression of the piezoelectric element the voltage on it increases. If it reaches the battery voltage, current starts to flow through the battery and in fact the piezoelectric element voltage is a little bit higher than the battery voltage during this interval which causes the current to flow. The amount which the piezoelectric element voltage exceeds the battery voltage during this interval depends on the diode properties and other resistances in the system. When the force on the piezoelectric element begins decreasing, the voltage decreases too and when it becomes less than the battery voltage current stops flowing through the battery. As the force on the piezoelectric element keeps decreasing, the voltage on the piezoelectric elements keep decreasing until it reaches the negative value of the battery voltage. At this point, current begins to flow through the battery, now, however, from a different branch of the diode bridge, namely through different diodes. Again during this interval the voltage on the piezoelectric element exceeds the battery voltage a little bit (in this case it is lower than the negative value of the battery voltage). When the force begins increasing, the voltage begins increasing too and again no current flows through the battery. Throughout the operation, the voltage on the piezoelectric element fluctuates between the negative and positive values of the battery voltage.

In order to get insight into the energy conversion mechanism and to derive the governing equations in the next section, it is worthwhile to look at the force vs. deflection and voltage vs. charge plots of the piezoelectric element. These are plotted in Figure 2-6. The most important observation is that there are two major regimes during the operation: Operation under open circuit conditions, where the compliance of the piezoelectric element is small, i.e the piezoelectric element is hard; and operation under closed circuit conditions, where the compliance of the piezoelectric element is large, i.e the piezoelectric element is soft. The compliances in these regimes are $s_{33}^D$ and $s_{33}^E$ for open circuit and closed circuit conditions respectively. The shaded region in Figure 2-6 corresponds to the stored electrical energy in one cycle. The generated power is then simply this energy times the operation frequency.

The battery voltage has an important effect on the performance. The simulation results presented in Figure 2-5 and Figure 2-6 correspond to the optimum battery voltage ($90V$). The

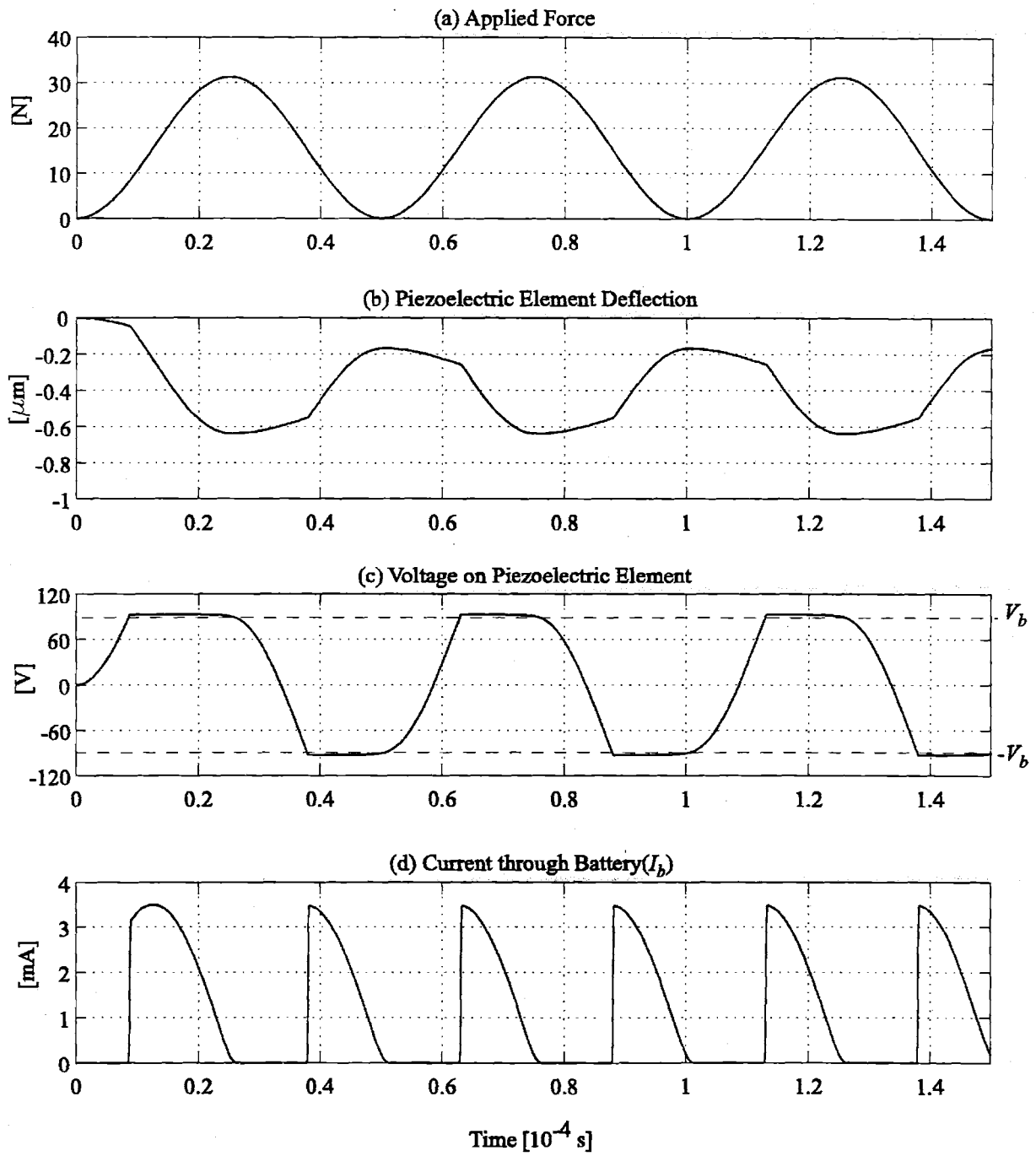


Figure 2-5: Time histories from the simulation of the piezoelectric element connected to the full bridge rectifier for the case of imposed force. The generated power is $I_b V_b$.

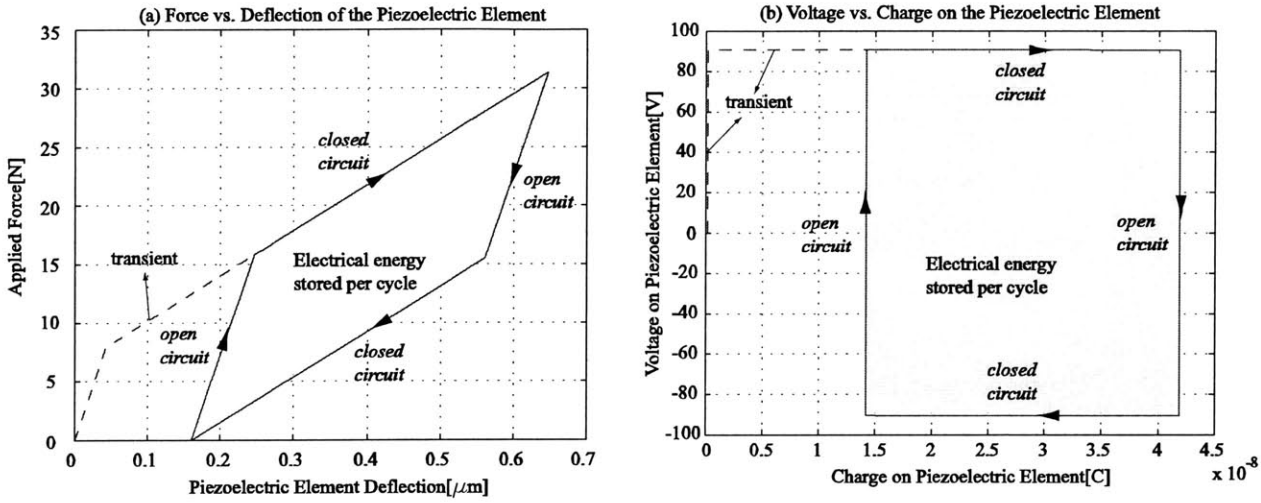


Figure 2-6: Force vs. deflection and voltage vs. charge plots of the piezoelectric element compressed under the applied force for the case of full bridge rectifier.

force vs. deflection of the piezoelectric element for different values of battery voltage is shown in Figure 2-7. It is found that, the maximum power is obtained with an optimum battery voltage of:

$$V_{b(opt)} = \frac{V_{oc}}{4} = \frac{1}{4}\frac{\sigma(s_{33}^E - s_{33}^D)L_p}{d_{33}} \tag{2.23}$$

where $V_{oc}$ is the open circuit voltage of the piezoelectric element, $s_{33}^E$ and $s_{33}^D$ are the closed circuit and open circuit compliances of the piezoelectric element respectively, $d_{33}$ is the piezoelectric coefficient, $\sigma$ is the maximum stress on the piezoelectric element, and $L_p$ is the length of the piezoelectric element. Open circuit voltage at a given stress is the voltage generated by the piezoelectric element when compressed under open circuit conditions. In fact the optimum battery is the voltage which optimizes the shape of the force vs. displacement curve for maximum enclosed area.

It should be noted that the above analysis is done for a case where the force on the piezoelectric element is varying between zero and a maximum value which corresponds to the depolarization stress of the piezoelectric element. In order to analyze the case where the force is biased, the system is simulated for nonzero positive or negative minimum forces. It has been discovered

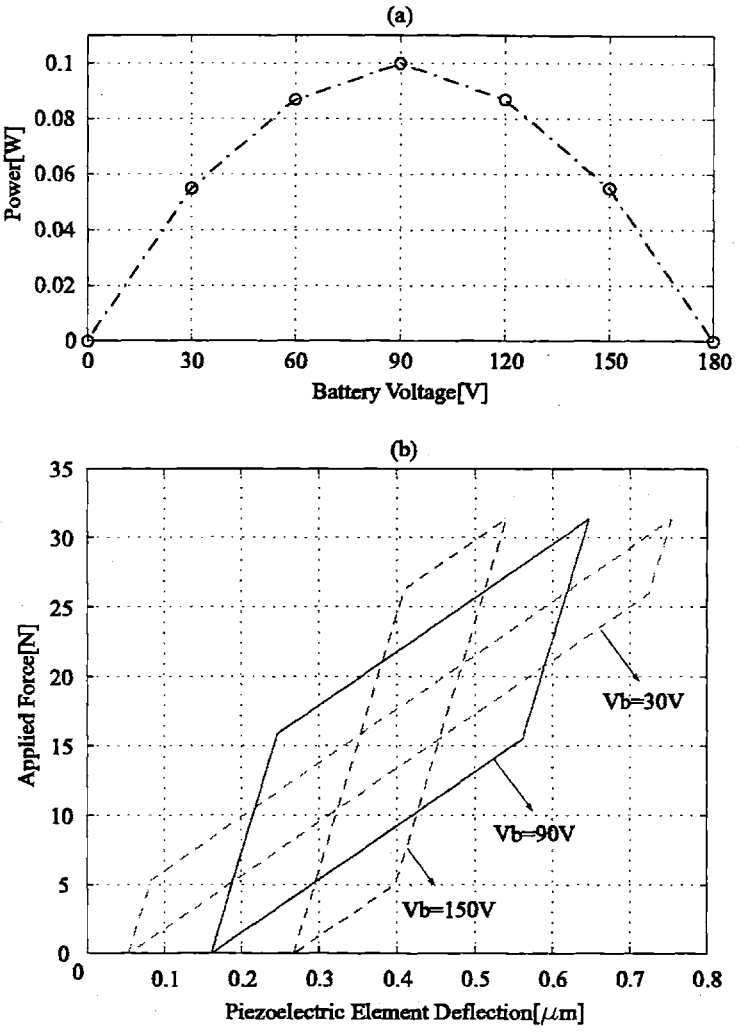


Figure 2-7: Effect of battery voltage on power.

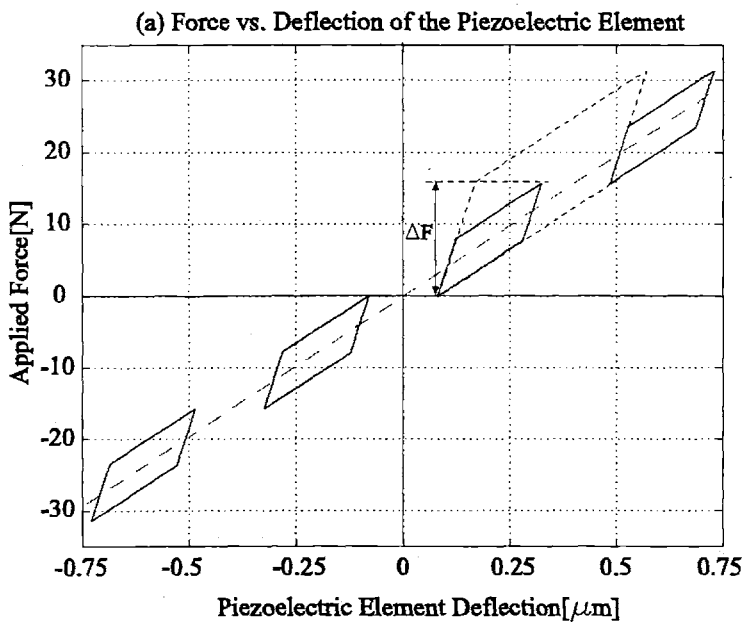


Figure 2-8: Effect of bias force on the workcycle.

that the optimum battery voltage depends only on the stress band on the piezoelectric element, namely on the difference of the maximum and minimum stresses on the piezoelectric element. Figure 2-8 shows the workcycles for different applied forces which have the same peak to peak values but different bias values. For each case the optimum battery voltage is the same since the stress band resulting from each case is the same. Equation 2.23 can be rewritten as:

$$V_{b(opt)} = \frac{1}{4}\frac{\Delta\sigma(s_{33}^{E} - s_{33}^{D})L_p}{d_{33}} \tag{2.24}$$

where $\Delta\sigma$ is the stress band on the piezoelectric element.

**Analysis** In order to investigate the work cycle of the piezoelectric element, we can analyze the stress vs. strain and electric field vs.charge density plots of the piezoelectric element in detail. Important features of the work cycle is shown in Figure 2-9 which corresponds to the optimum battery voltage case. It is important to not that, the dashed line, which corresponds to the case in which the piezoelectric element would be compressed in closed circuit conditions, passes through the middle of the stress vs. strain curve. We also know the slopes of the curve

in the two different regimes, namely open circuit and closed circuit regimes. Using simple geometry, we can derive the coordinates of the corner points. From the voltage vs. charge plot in Figure 2-6 we see that the voltage of the piezoelectric element fluctuates between the positive and negative values of the battery voltage. Using constitutive relationships to calculate the corresponding charge on the piezoelectric element at different states, we can get the electric field vs. the charge density plot. These are shown in Figure 2-9.

The electrical energy stored (per piezoelectric element volume) in the battery in one cycle for the case of optimum battery voltage, which is equal to the enclosed area by the stress vs. strain or electric field vs charge density curve can obtained using simple geometry from Figure 2-9 as:

$$E = \frac{1}{4}(s_{33}^{E} - s_{33}^{D})\sigma^2 \tag{2.25}$$

where $s_{33}^{E}$ and $s_{33}^{D}$ are the closed circuit and open circuit compliances of the piezoelectric element respectively and $\sigma$ is the maximum stress on the piezoelectric element.

Then, the generated power by the piezoelectric element can be expressed as:

$$W = \frac{1}{4}(s_{33}^{E} - s_{33}^{D})\sigma^2 V_p f \tag{2.26}$$

where $V_p$ is the volume of the piezoelectric element and $f$ is the operation frequency. From the above equation it can be seen that the power depends heavily on the stress on the piezoelectric element. The most important limitation on piezoelectric power generation is the depolarization stress. For stresses larger than this, piezoelectric element coefficients degrade and performance decreases drastically. Each piezoelectric element has a different depolarization stress, which constitute an important factor when determining their feasibility as power generators. Detailed comparison of different piezoelectric elements will be presented in Section 2.6.

Effective coupling factor for an electromechanical energy conversion mechanism, in this case a system which converts mechanical energy into electrical energy is defined as the ratio of the mechanical work done on the system to the electrical energy stored in one cycle. This definition is the same as the one used to derive the coupling coefficient. This is illustrated in Figure 2-10. From the above definition we can write:

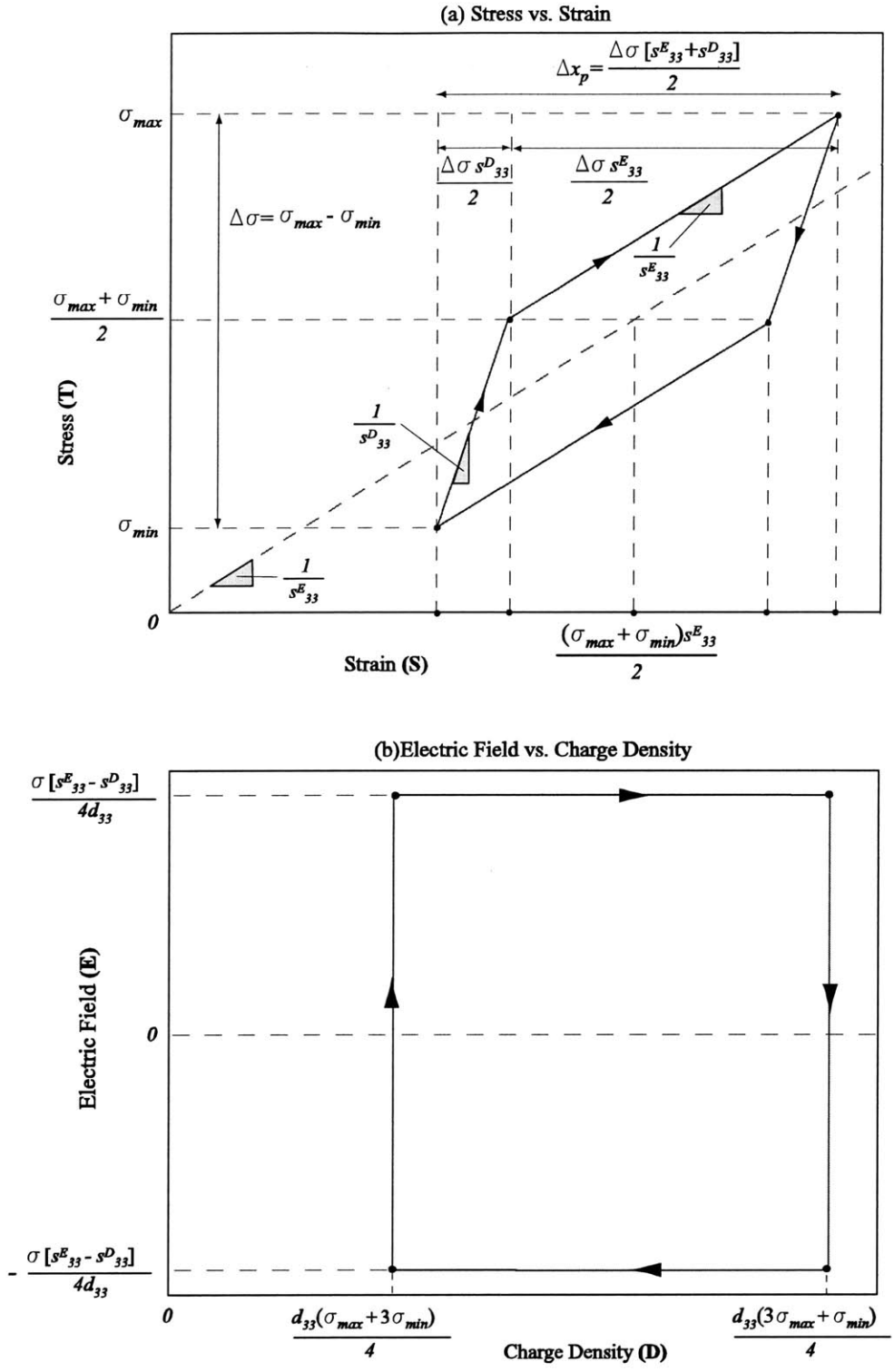


Figure 2-9: General presentation of the work cycle of the piezoelectric element in terms of stress, strain, electric field and charge density for the case of regular diode bridge.

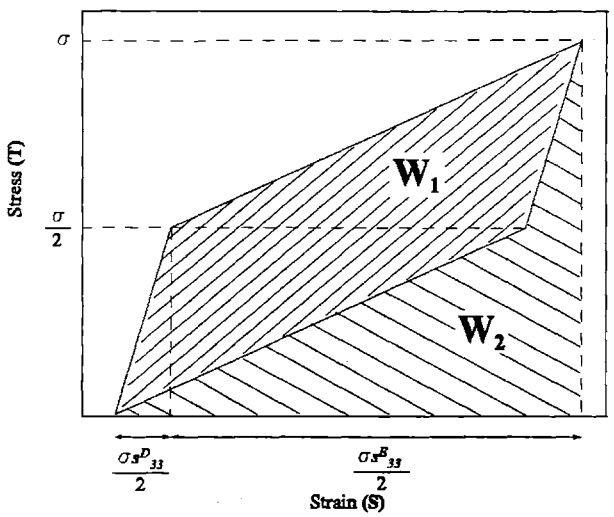


Figure 2-10: Illustration of the effective coupling factor for the case of regular diode bridge.

$$k_{eff}^2 = \frac{W_1}{W_1 + W_2} \tag{2.27}$$

Again using geometry, the effective coupling factor can be derived in terms of the piezoelectric material compliances as:

$$k_{eff}^2 = \frac{2(s_{33}^E - s_{33}^D)}{3s_{33}^E + s_{33}^D} \tag{2.28}$$

The definition of the coupling coefficient of a piezoelectric element was given in section 2.3. Using equations 2.3 and 2.28, the effective coupling factor for the full bridge rectifier case can be expressed in terms of the coupling coefficient as:

$$k_{eff}^2 = \frac{2k_{33}^2}{k_{33}^2 + 2} \tag{2.29}$$

### Full Bridge Rectifier and Voltage Detection Circuit

The operation of this circuit is as follows: The voltage detector circuit detects the voltage right after the diode bridge ($V_2$). Initially, the SCR is in "off" state. If $V_2$ reaches its maximum and begins decreasing, the voltage detector sends a current signal to SCR which turns it on. If the detected voltage reaches zero, the voltage detector sends another signal to SCR which turns it

off.

**Simulation** The simulation architecture is the same as in Figure 2-4. The implementation of the switching of the SCR and additional details of the Simulink model are presented in Appendix A. Again, the force is imposed on the piezoelectric element. The geometry, operation frequency and the piezoelectric material are the same as in the previous section. The time histories resulting from the simulation are shown in Figure 2-11.

Again, in order to get insight into the energy conversion mechanism and to derive the governing equations, it is worthwhile to look at the force vs. deflection and voltage vs. charge plots for the piezoelectric element. These are plotted in Figure 2-12. We can see that there are two basic operation regimes. The first one is operation under open circuit conditions, where the compliance of the piezoelectric element is low, i.e the piezoelectric element is hard. The second operation regime is defined with the *almost flat* lines in Figure 2-12. This regime corresponds to the time intervals, where the switch (SCR) is on. In this regime, the piezoelectric material behaves as a very soft material.

Since the SCR is initially closed, the piezoelectric element is first compressed under open circuit conditions, until the applied force reaches its maximum and begins to decrease (period 1-2). In this period, the voltage on the piezoelectric element reaches the open circuit voltage corresponding to the maximum stress applied on the element. Once the force begins to decrease, the detected voltage, which is the rectified piezoelectric element voltage, begins to decrease too, which causes the switch to turn on. After the switch turns on, the voltage decreases very fast and the piezoelectric element is compressed with a very small effective stiffness. The switch turns again off once the voltage reaches zero. During the period when the switch is on (2-3), the piezoelectric element is squeezed until the point, as if it was being squeezed under the same stress and closed circuit conditions. We can verify this by looking to the voltage vs. charge plot. In state 3, the voltage on the piezoelectric element is zero and the force on it is almost the maximum force. Of course, this rapid compression occurs in finite time and during this time interval, the force decreases a little bit, which results in the *almost flat* region in force vs. deflection plot. The shorter the "on" state, the flatter will be the line. It can be concluded that, the performance of the system with this cycle depends highly on the time history of the

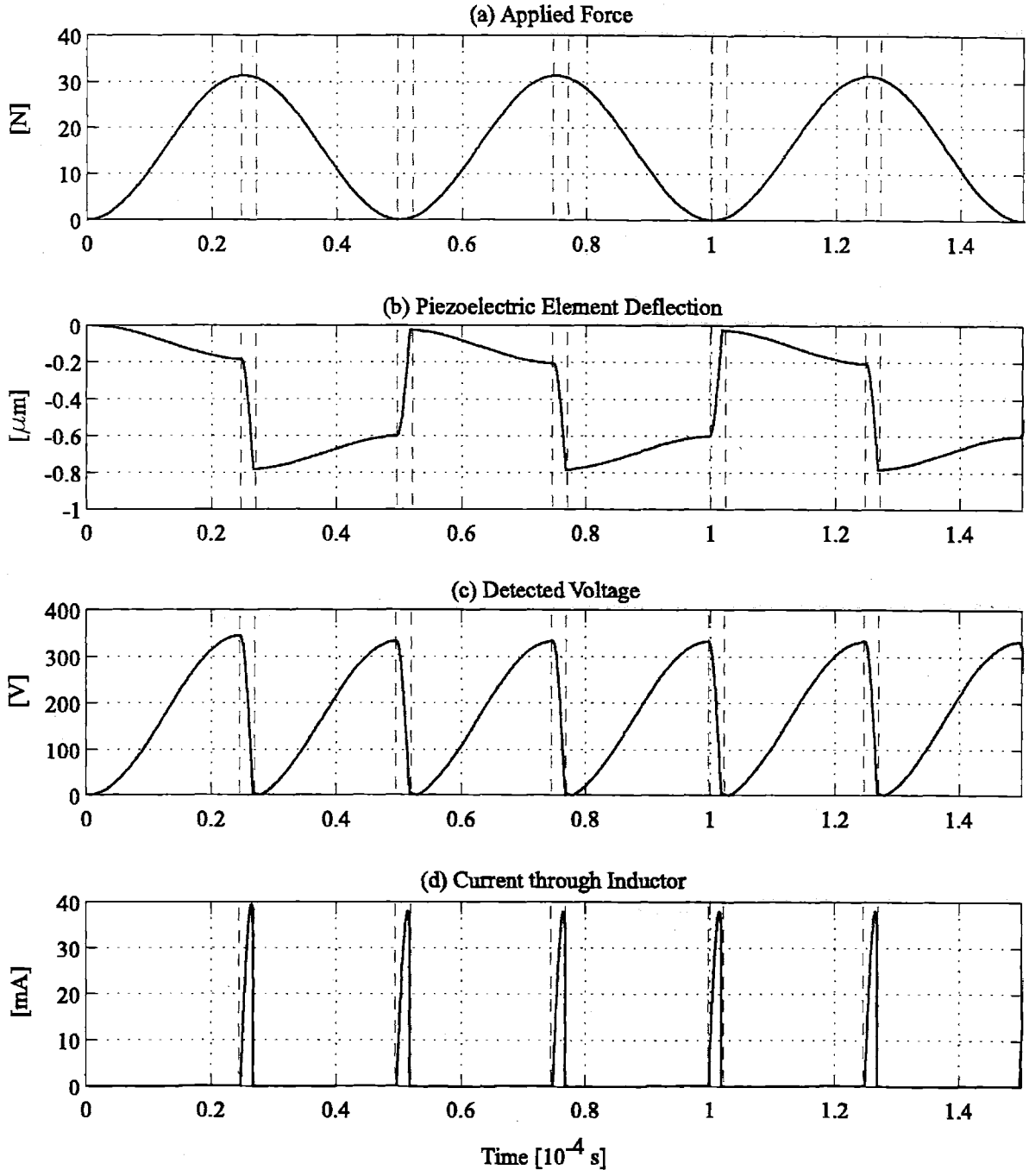


Figure 2-11: Time histories from the simulation of the piezoelectric element connected to the full bridge rectifier and voltage detector circuit. The time intervals between the dashed lines present the intevals where the switch(SCR) is in its "on" state.

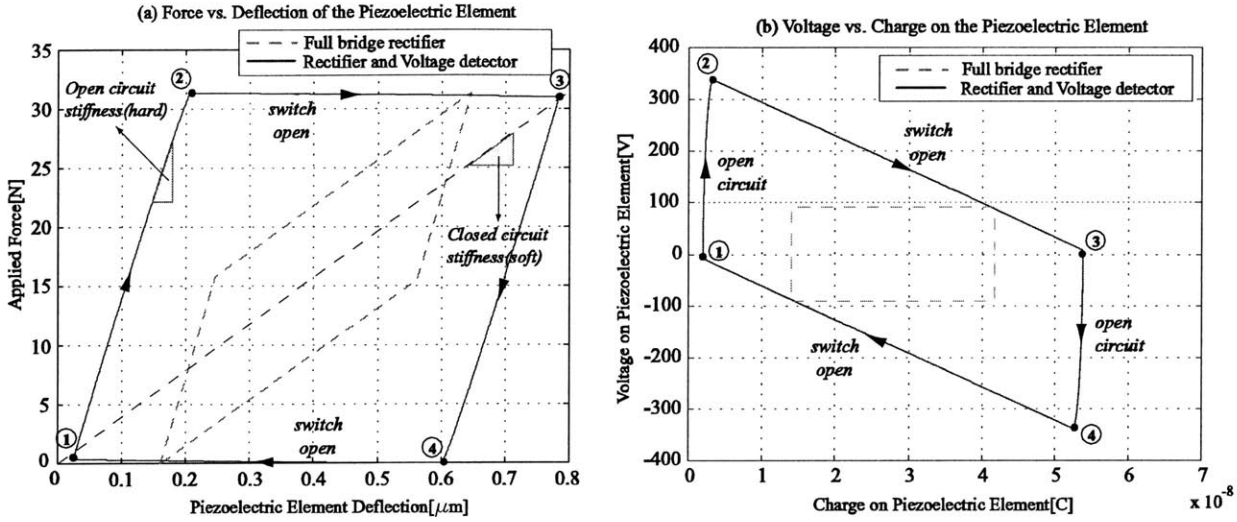


Figure 2-12: Force vs. deflection and voltage vs. charge plots of the piezoelctric element compressed under the applied force for the case of full bridge rectifier and voltage detector circuit.

applied force.

**Analysis** After the observations done in the previous section, we can derive the equations which determine the maximum strain and charge of the piezoelectric element, the energy stored per cycle and the effective coupling factor. To keep the analysis more general, we again analyze the work cycles in terms of stress vs. strain and electric field vs. charge density plots. Important features of the idealized work cycles are shown in Figure 2-13. As mentioned earlier, there is a finite time associated with the transition between states 2-3 and 4-1, where the force does not remain at its maximum value. This time interval depends highly on the value of the inductor used. In the simulation, an inductor of *20mH* is used. It should be also mentioned that, the capacitor has to be large enough to avoid saturation. The simulation results are very close to the idealized cycles, which can be seen comparing Figure 2-12 and Figure 2-13. It should be also mentioned that, the difference between these figures should be counted partly on a simulation artifact. The switch operation and open circuit and closed circuit conditions are simulated using very large and very small resistances respectively. It can be concluded that, the idealized curves in Figure 2-13 are very good approximations to the actual work cycles.

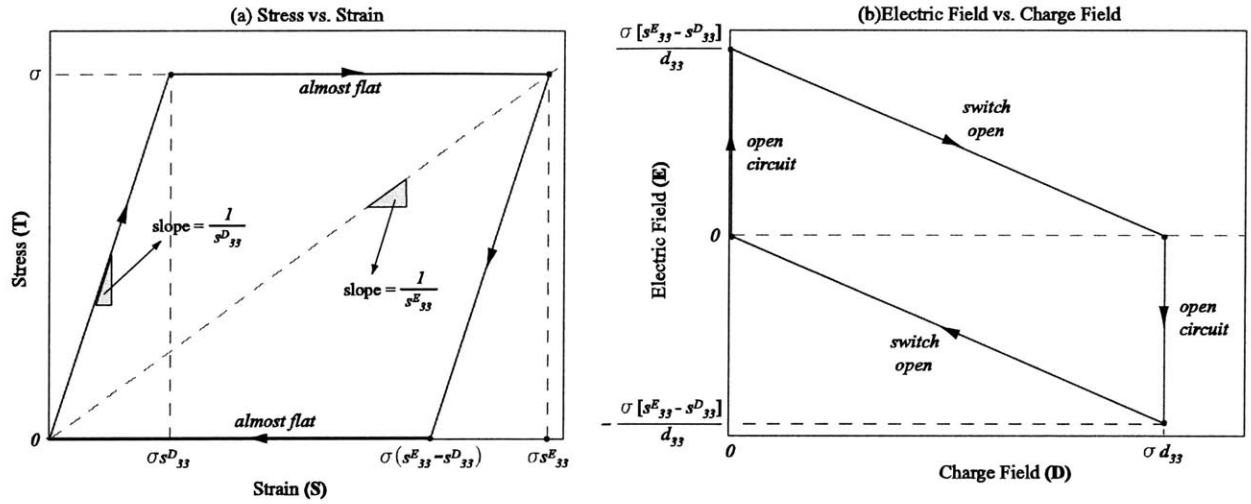


Figure 2-13: General presentation of the work cycle of the piezoelectric element in terms of stress, strain, electric field and charge density for the case of the full bridge rectifier and voltage detector circuit.

The derivation of the coordinates of the points in Figure 2-13 is straightforward. The strain values can be found by using the slopes of the stress vs. strain curve. The maximum charge can be calculated using the constitutive relationships for the condition of zero electric field and maximum stress. The electrical energy stored in the capacitor in one cycle, which is equal to the enclosed area by the stress vs.strain and electric field vs.charge density curve can be obtained easily as:

$$E = (s_{33}^E - s_{33}^D)\sigma^2 \tag{2.30}$$

where $s_{33}^E$ and $s_{33}^D$ are the closed circuit and open circuit compliances of the piezoelectric element respectively and $\sigma$ is the maximum stress on the piezoelectric element.

Then, the generated power by the piezoelectric element can be expressed as:

$$W = (s_{33}^E - s_{33}^D)\sigma^2 V_p f \tag{2.31}$$

where $V_p$ is the volume of the piezoelectric element and $f$ is the operation frequency. From the above equation it can be seen that the power depends heavily on the stress on the piezo-

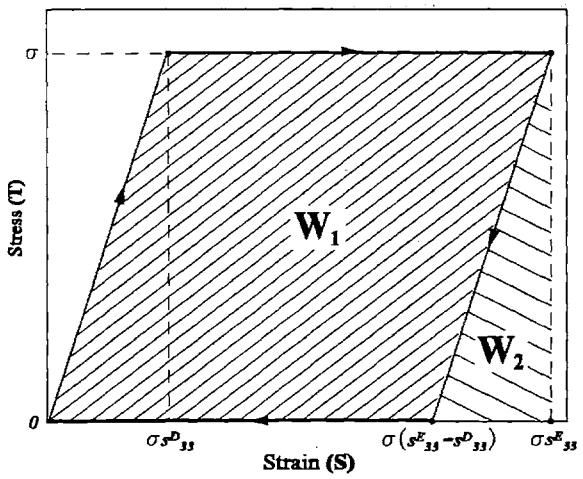


Figure 2-14: Illustration of the effective coupling factor for the full bridge rectifier and voltage detection circuit.

electric element. The power generated with this circuitry is four times bigger than the power generated using the full bridge rectifier under the same conditions, namely same applied force and frequency.

Using the definition in equation 2.27 and from Figure 2-14, the effective coupling factor can be obtained as:

$$k_{eff}^2 = \frac{W_1}{W_1 + W_2} = \frac{2(s_{33}^E - s_{33}^D)}{2s_{33}^E - s_{33}^D} \tag{2.32}$$

Using equations 2.3 and 2.32, we can express the effective coupling factor of the coupling coefficient as:

$$k_{eff}^2 = \frac{2k_{33}^2}{k_{33}^2 + 1} \tag{2.33}$$

It is very interesting to note that the diode bridge and the voltage detection circuit proposed by Smalser in [26] result in the hypothetical electromechanical energy conversion work-cycle proposed by Berlincourt [8]. This cycle is shown in Figure 2-2(a). The expression in equation 2.6 is identical to equation 2.33.

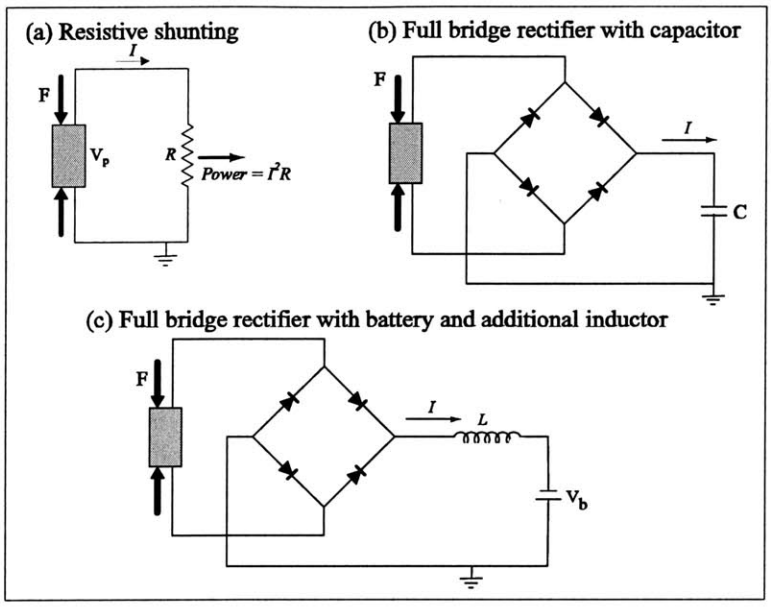


Figure 2-15: Other alternative circuits for piezoelectric power generation.

## 2.5 Other Circuits

This section discusses some other alternative circuits for piezoelectric power generation, shown in Figure 2-15. The geometry, operation frequency and the piezoelectric material used for the simulations are the same as in the previous section.

A much simpler circuit than the ones presented in previous sections is that involving just a resistor. Resistive shunting of piezoelectric elements for structural damping is discussed in [15]. The resistive shunting exhibits frequency dependent behavior and the converted electrical energy is dissipated, not stored. Figure 2-16 shows the force vs. deflection and voltage vs. charge plots from the simulation of the piezoelectric element shunted by a resistor. It can be seen that, for relatively small resistance values, the piezoelectric element behaves close to the closed circuit condition, whereas for large resistance values, it behaves close to the open circuit condition. It should be noted that the simulations presented in Figure 2-16 are performed at a certain frequency. If one were to keep the resistance constant and change the frequency, similar behavior would be observed. Namely, at very large frequencies the behavior would be close to open circuit behavior, whereas at very low frequencies, the behavior would be close to closed

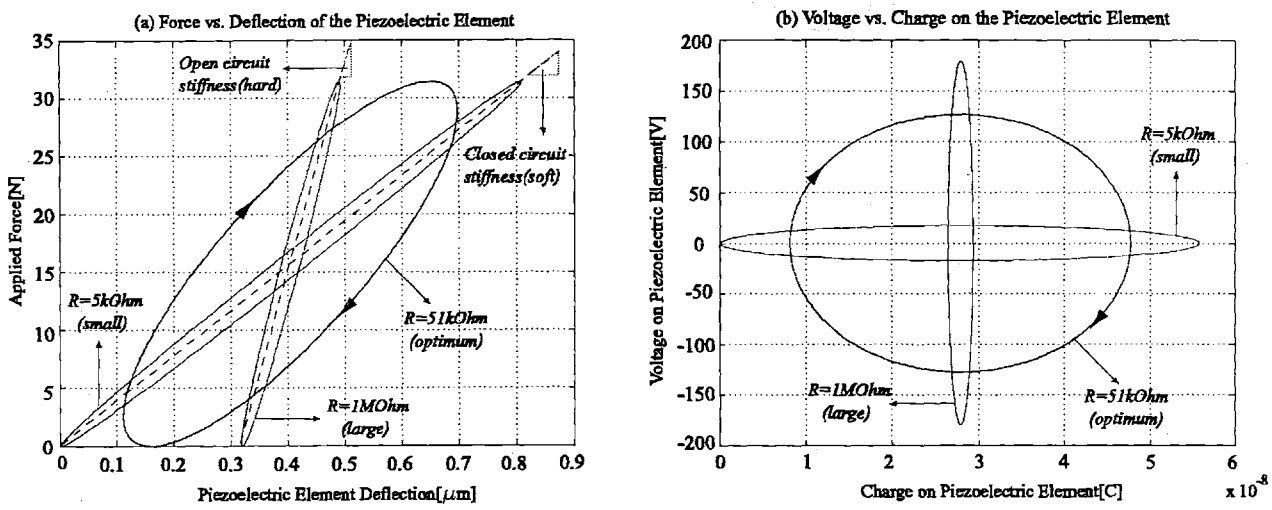


Figure 2-16: Simulation results of the piezoelectric element shunted by a resistor for different resistance values.

circuit behavior. Indeed, the maximum electromechanical energy conversion occurs when the impedance of the load, which is the resistor, is matched to the impedance of the piezoelectric element. In other words, for a given piezoelectric element and geometry, at any given resistance value there exists an optimum frequency, or at any given frequency there exists an optimum resistance value. The optimum resistance value is given as:

$$R_{opt} = \frac{1}{2\pi f C^T} \tag{2.34}$$

where $f$ is the operation frequency and $C^T$ is the capacitance of the piezoelectric element under constant stress, which can be expressed as:

$$C^T = \frac{e_{33}^T A_p}{L_p} \tag{2.35}$$

where $e_{33}^T$ is the dielectric constant and $A_p$ and $L_p$ are the cross-sectional area and the length of the piezoelectric element respectively.

Figure 2-17 compares the resistive shunting (for optimum resistance value) with the circuits presented in previous sections. Resistive shunting performs better compared to the full bridge rectifier in terms of electromechanical energy conversion. However, as mentioned earlier, the

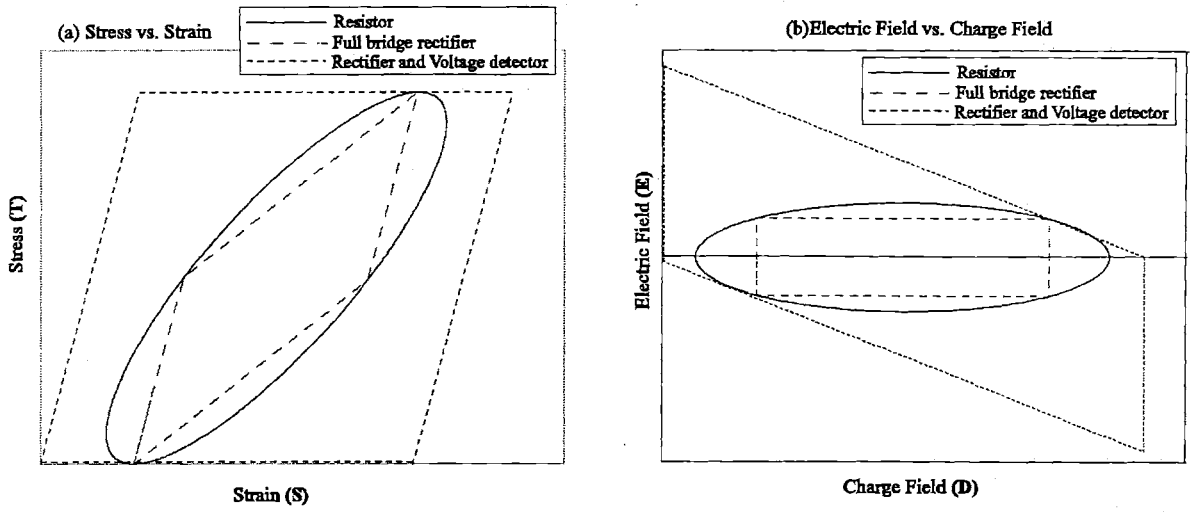


Figure 2-17: Comparison of resistive shunting(at optimum resistance) with full bridge rectifier and full bridge rectifier with voltage detector.

performance depends heavily on operation frequency and the electrical energy is not stored, which make resistive shunting not a suitable option for power generation.

An alternative circuit can be full bridge rectifier and a capacitor connected to it, instead of a battery or a DC voltage source as presented in section 2.4.2. This is actually the same circuit configuration as presented in [10]. The simulation results are shown in Figure 2-18. As can be seen from the plots, the behavior heavily depends on the value of the capacitor. Obviously, energy cannot be transferred to the capacitor after the voltage of the capacitor nearly reaches half of the open circuit voltage of the piezoelectric element, which corresponds to the maximum stress. As expected, the higher the capacitance, the larger is the stored energy, since the final voltage is the same regardless of the capacitance value. This statement contradicts with the conclusion made in [10] because in this simulation the force is imposed on the piezoelectric element. In [10], no force is imposed on the piezoelectric element. The dynamics of the system (falling ball, vibration of the plate etc.) is determined by the circuitry, i.e. the capacitor and there exists an optimum capacitance value for maximum energy transfer.

Another alternative would be to add an inductor to the full bridge rectifier in series with the battery. The simulation results corresponding to the optimum inductor value are shown in Figure 2-19. It can be seen that both the stored energy per cycle and the effective coupling

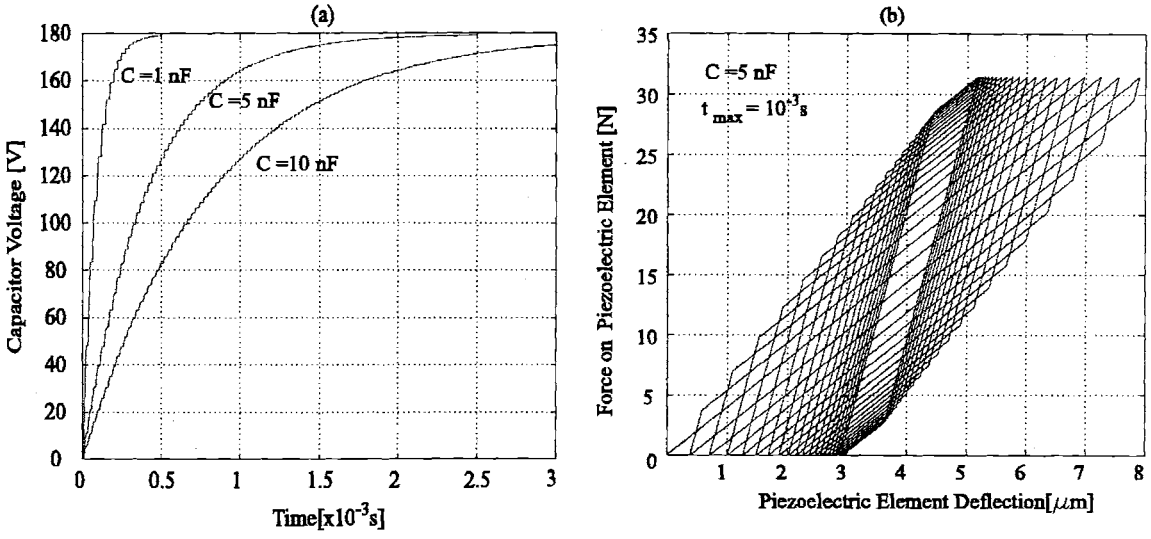


Figure 2-18: Simulation results of the full bridge rectifier connected to a capacitor.

factor increases with the addition of the inductor. However, in order to get this behavior, the value of the inductor should be tuned to the optimum value at a given frequency and for this particular example the required inductance is about 100mH, which is physically very large and not practical.

We can generally conclude that, the circuits discussed in the previous section are better suited for piezoelectric power generation since they can store the electrical energy and the behavior is not frequency dependent.

## 2.6 Piezoelectric Material Comparison

Section 2.4 presented an analysis of two different circuits and expressions derived for the effective coupling factor and generated power. This section presents a comparison of different piezoelectric materials in terms of energy density and effective coupling factor for different shunting conditions, i.e. with different circuits connected, using the expressions derived in Section 2.4. The important expressions for energy density and effective coupling factor are summarized in Table 2.2. The effective coupling factors for the two circuits presented in Table 2.2 are plotted as a function of the coupling coefficient in Figure 2-20. It can be seen that the effective coupling

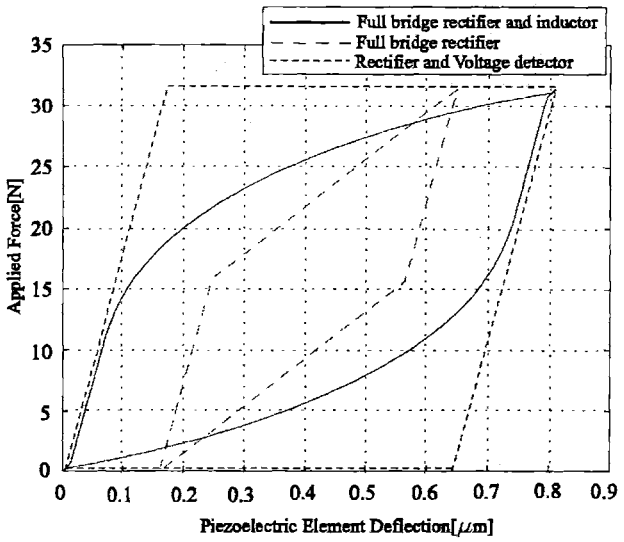


Figure 2-19: Force vs. deflection plot from the simulation of the full bridge rectifier with additional inductor.

| | Rectifier | Rectifier+Voltage Detector |
|---|---|---|
| Energy Density | $ED = \frac{1}{4}(s_{33}^E - s_{33}^D)\sigma_d^2$ | $ED = (s_{33}^E - s_{33}^D)\sigma_d^2$ |
| Effective coupling factor | $k_{eff}^2 = \frac{2k_{33}^2}{k_{33}^2 + 2}$ | $k_{eff}^2 = \frac{2k_{33}^2}{k_{33}^2 + 1}$ |

Table 2.2: Comparison of circuitry in terms of energy density and effective coupling factor

factor for the case of the diode bridge is always smaller than the coupling coefficient whereas the effective coupling factor for the case of the diode bridge with voltage detector is always larger than the coupling coefficient. This can be also presented with the following inequality:

$$\sqrt{\frac{2k_{33}^2}{k_{33}^2 + 2}} < k_{33} < \sqrt{\frac{2k_{33}^2}{k_{33}^2 + 1}} \tag{2.36}$$

which is valid since $k_{33} < 1$.

The energy density of a piezoelectric material, i.e. the maximum energy which can be extracted from a piezoelectric element in one cycle is mostly limited by the depolarization stress of the piezoelectric element, which means that if a stress higher than the depolarization stress

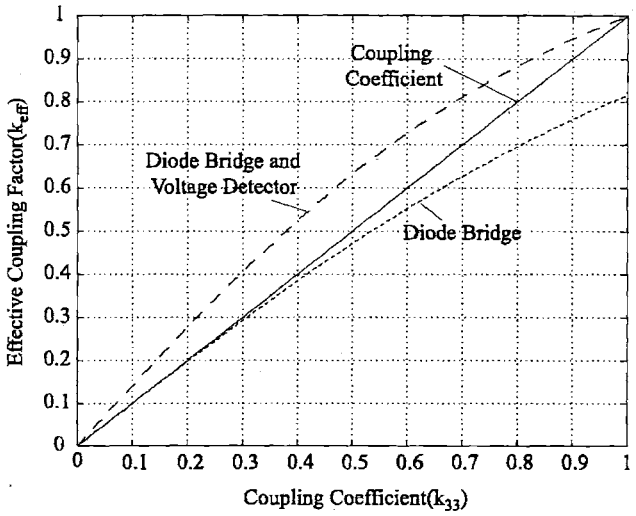


Figure 2-20: Effective coupling factors of the diode bridge and the diode bridge with voltage detector as a function of the couping coefficient.

is applied, the material begins to dipole and the piezoelectric, dielectric and elastic coefficients begin to degrade. Behavior of different PZT ceramics and PZN-PT single crystal piezoelectric elements under high stress are investigated in [46] and [19] respectively. The assumption for the maximum stress limit, i.e. the assumed values for the depolarization stress are based on the above mentioned references. Other studies about piezoelectric elements under high fields are presented in [45]-[49]. Elastic and piezoelectric properties of different piezoelectric materials along with depolarization stress values are compiled in Table 3.3.

Different piezoelectric materials are compared in terms of their energy densities and effective coupling factors for different circuitry in Figure 2-10. It is interesting to note that, although the single crystal piezoelectric material(PZN-PT) has very high effective coupling factor, it has a very low energy density compared to PZT-8 or PZT-4S because of its small depolarization stress. We can generally say that, the effective coupling factor is a function of the coupling coefficient and the circuitry, whereas the energy density is a function of coupling coefficient, circuitry and the depolarization stress. As mentioned earlier, for a piezoelectric element, the energy density obtained with the diode bridge and voltage detector circuit is four times larger than the energy density obtained with just the diode bridge.

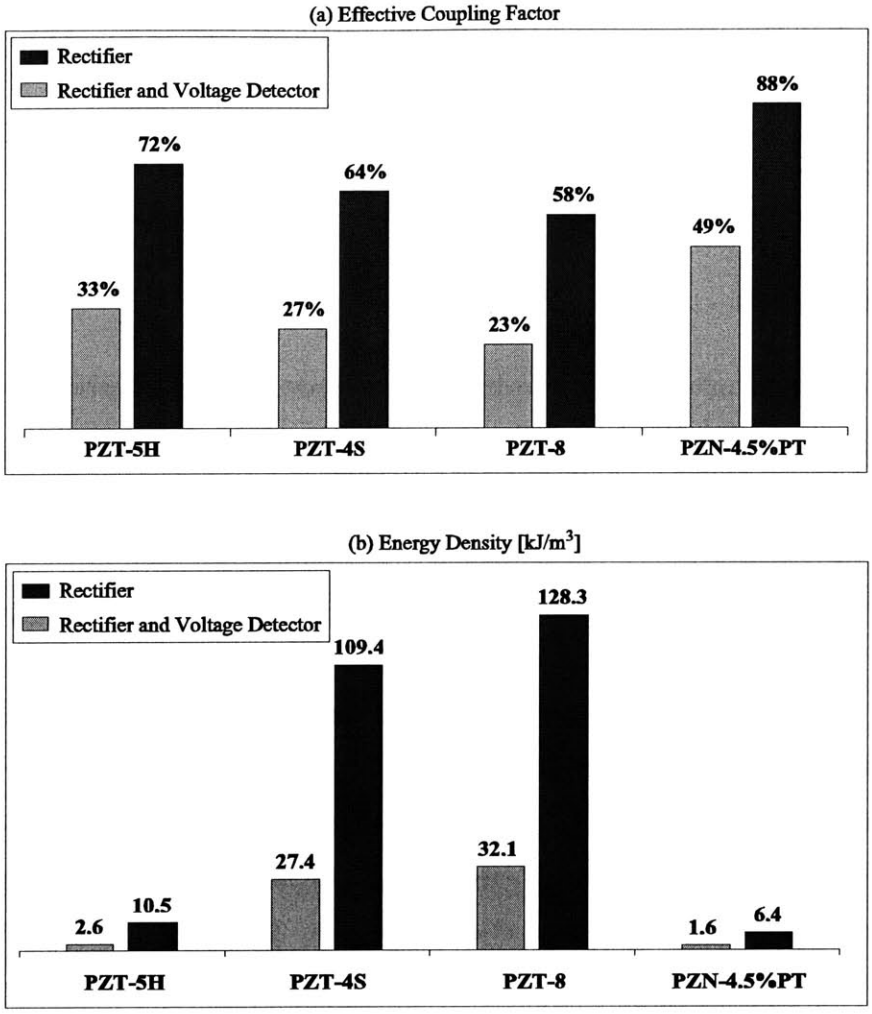


Figure 2-21: Piezoelectric Material Comparison: (a) Effective coupling factor (b) Energy density.

| | PZT-4S | PZT-5H | PZT-8 | PZN-4.5%PT |
|---|---|---|---|---|
| $s_{33}^{E}[10^{-12}m^2/N]$ | 15.5 | 20.7 | 13.9 | 81 |
| $s_{33}^{D}[10^{-12}m^2/N]$ | 7.9 | 9.01 | 8.2 | 17 |
| $k_{33}$ | 0.7 | 0.75 | 0.64 | 0.89 |
| $d_{33}[10^{-12}m/V]$ | 350 | 593 | 250 | 1780 |
| *Depolarization Stress*$[MPa]$ | 120 | 30 | 150 | 10 |

Table 2.3: Properties of different piezoelectric materials

## 2.7 Conclusion

This chapter presented an analysis of two different circuitries for piezoelectric power generation. Analytical expressions are derived for the generated power and effective coupling factor for a given piezoelectric material and circuitry. Different piezoelectric materials are compared in terms of their power generation characteristics. Among the materials analyzed, PZT-8 has the highest energy density. Despite its large coupling coefficient, the single crystal material PZN-PT has very low energy density, which is a consequence of its low depolarization stress. However, the coupling coefficient becomes an important criteria if the piezoelectric element is considered along with its surrounding system, for example the infrastructure which provides the force on the element, which is the energy harvesting chamber in the microhydraulic power generation device. It should be remembered that in the analysis presented in this chapter a prescribed force is imposed on the piezoelectric element. This issue will be addressed in the next chapter.

# Chapter 3

# Energy Harvesting Chamber and Preliminary Design Considerations

This chapter presents a simple model of the energy harvesting chamber, simulations with the coupled circuitry and preliminary design considerations. The interaction of the energy harvesting chamber and the circuitry is discussed. The two circuits presented in Chapter 2 and different piezoelectric materials are compared in terms of the flowrate and frequency requirements for a given pressure differential and power, and in terms of system efficiency.

## 3.1 Configuration and Operation of the Energy Harvesting Chamber

The Energy Harvesting Chamber consists of a fluid chamber, a piston and a piezoelectric cylinder. The configuration of the energy harvesting chamber and its basic components are shown in Figure 3-1.

The piston converts the pressure in the chamber to a force on the piezoelectric cylinder. The inlet and outlet valves operate $180^0$ out of phase at high frequency and convert the static pressure differential ($P_{HPR} - P_{LPR}$) into pressure fluctuations in the chamber. This results in cyclic compression of the piezoelectric cylinder, which is coupled to the circuitry. The generic operation and typical duty cycles are shown in Figure 3-2.

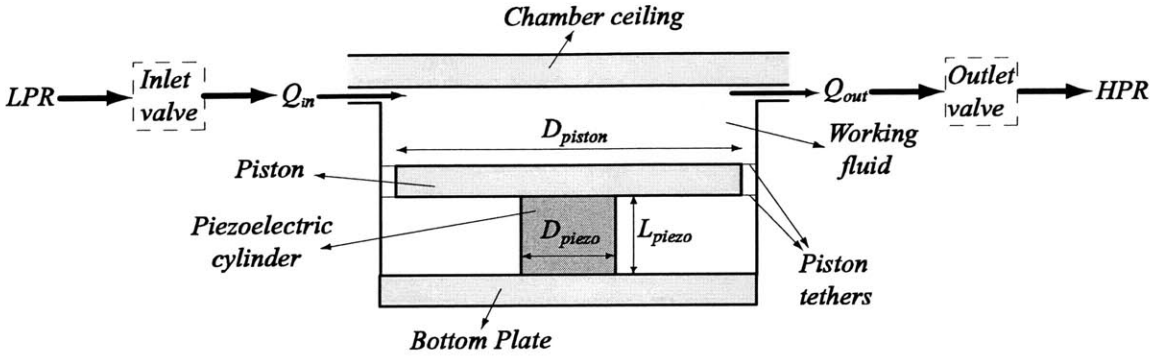


Figure 3-1: Energy harvesting chamber configuration.

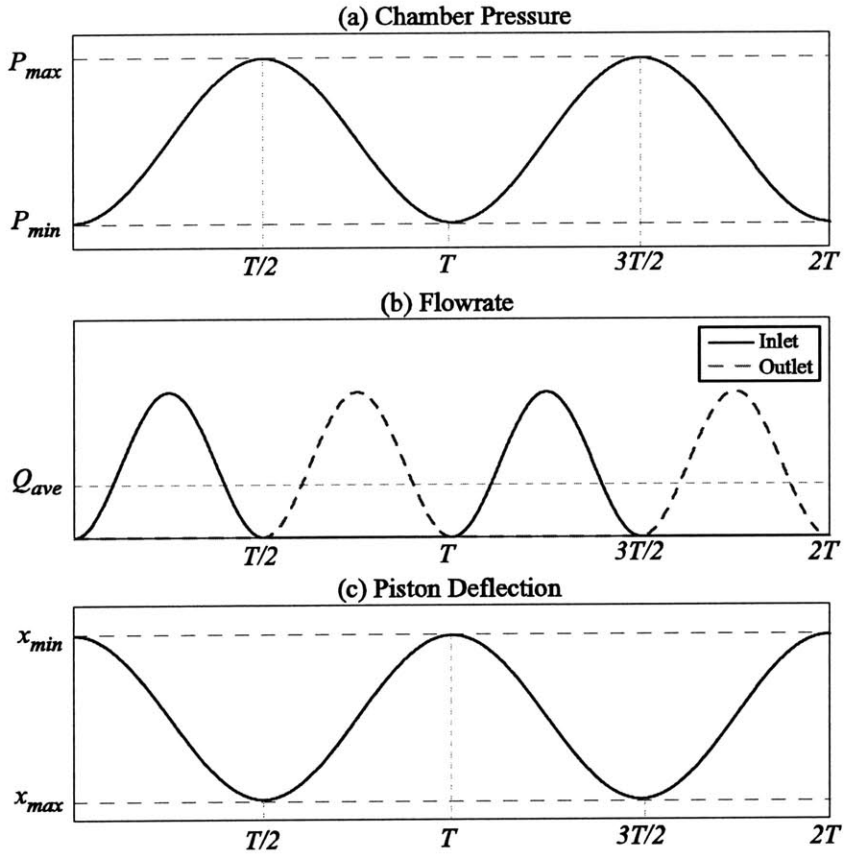


Figure 3-2: Duty cycles of generic operation of the energy harvesting chamber. The valve openings have the same duty cycle as the flowrates and are not shown here.

In the chamber, the hydraulic energy is converted into mechanical energy, which is converted into electrical energy in the piezoelectric element and then the electrical energy is stored in the coupled circuitry. There is a strong coupling between the hydraulic/mechanical system and the circuitry, in other words, the electrical circuit affects the behavior of the system dramatically, an issue which should be analyzed in detail.

## 3.2 Modeling

In order to understand the interaction between the hydraulic, mechanical and electrical system, a simple model of the energy harvesting chamber will be used to simulate a representative system. The basic assumptions are:

- The effect of piston tethers on the motion of the piston is neglected perfect sealing between the piston and the chamber walls is assumed

- An effective compliance, $C_{eff}$, is assigned for the chamber, which includes the combined effect of the bending of the piston, chamber ceiling (top plate), bottom plate and piston tethers as well as fluid compression inside the chamber. $C_{eff}$ will be defined in section 3.2.2.

- Piston dynamics is neglected.

The detailed structural modeling and analysis of the compliance contributions of the structural members in the chamber will be presented in Chapter 4.

### 3.2.1 Piezoelectric Cylinder

The piezoelectric material is modeled using the same constitutive relationship given in Chapter 2, namely:

$$\begin{bmatrix} S \\ E \end{bmatrix} = \begin{bmatrix} s_{33}^{D} & \frac{d_{33}}{\varepsilon_{33}^{T}} \\ \frac{d_{33}}{\varepsilon_{33}^{T}} & -\frac{1}{\varepsilon_{33}^{T}} \end{bmatrix} \begin{bmatrix} T \\ D \end{bmatrix} \tag{3.1}$$

where $D$ is the charge field, $S$ is the displacement field (strain), $E$ is the electric field, and $T$ is the stress. For a cross-sectional area of $A_p$ and length of $L_p$, the expressions for the deflection

of the piezoelectric element and the voltage across it become:

$$x_p = \frac{L_p}{A_p}(s_{33}^D F_p + \frac{d_{33}}{\varepsilon_{33}^T} Q_p) \tag{3.2}$$

$$V_p = \frac{L_p}{A_p}(\frac{d_{33}}{\varepsilon_{33}^T} F_p - \frac{1}{\varepsilon_{33}^T} Q_p) \tag{3.3}$$

where $x_p$ is the deflection, $Q_p$ is the charge, $F_p$ is the force applied on the piezoelectric cylinder, and $V_p$ is the voltage across the piezoelectric cylinder. And the current through the piezoelectric element is given by:

$$I_p = \frac{dQ_p}{dt} \tag{3.4}$$

### 3.2.2 Chamber Continuity

The chamber converts the hydraulic energy into mechanical energy via the piston, which applies a force on the piezoelectric cylinder. In order to derive the expression for the chamber pressure, continuity equation inside the chamber should be considered. Consider an initial fluid volume inside the chamber. The time rate of the pressure change in the chamber is given by:

$$\frac{dP_{ch}}{dt} = \frac{\beta_f}{V_o}\frac{dV}{dt} \tag{3.5}$$

where $\beta_f$ is the bulk modulus of the fluid, $V_o$ is the initial volume of the fluid inside the chamber and $\frac{dV}{dt}$ is the volume change of the fluid. Sources of the volume change are:

- Net flowrate into the chamber

- Piston Movement

- Additional volume created inside the chamber by the deformation of the structural members due to chamber pressure

Then, the time rate of the total volume change in the chamber can be expressed as:

$$\frac{dV}{dt} = Q_{in} - Q_{out} - \frac{dx_p}{dt}A_{pis} - \frac{dV_s}{dt} \tag{3.6}$$

where $x_p$ is the displacement of the piston, which is equal to the deflection of the piezoelectric cylinder, $A_{pis}$ is the cross-sectional area of the piston, and $V_s$ is the total volume displaced by

the deformation of the structural members inside the chamber. The source of this additional volume might be the deformation of the top and bottom plate of the chamber, deformation of the piston tethers and deformation of the piston itself. The individual sources of the structural compliance of the chamber will be analyzed in detail in Chapter 4.

Combining equations 3.5 and 3.6, we get:

$$\frac{dP_{ch}}{dt} = \frac{\beta_f}{V_o}\left(Q_{in} - Q_{out} - \frac{dx_p}{dt}A_{pis} - \frac{dV_s}{dt}\right) \tag{3.7}$$

We can define the overall structural compliance as:

$$C_s = \frac{dV_s}{dP_{ch}} \tag{3.8}$$

From equations 3.7 and 3.8, we get the expression for the chamber pressure as:

$$\frac{dP_{ch}}{dt} = \left(\frac{V_o}{\beta_f} + C_s\right)^{-1}\left(Q_{in} - Q_{out} - \frac{dx_p}{dt}A_{pis}\right) \tag{3.9}$$

For simplicity, we can define an effective compliance for the chamber, which represents all the compliance sources as:

$$C_{eff} = \left(\frac{V_o}{\beta_f} + C_s\right) \tag{3.10}$$

where the first and the second terms correspond to the fluidic compliance and structural compliance respectively, which act like parallel capacitors in electrical circuit analogy.

We can rewrite 3.9 as follows:

$$\frac{dP_{ch}}{dt} = \frac{1}{C_{eff}}\left(Q_{in} - Q_{out} - \frac{dx_p}{dt}A_{pis}\right) \tag{3.11}$$

It is important to note that, in the above analysis the initial fluid volume inside the chamber, $V_o$, is assumed to be much larger than the volume displaced by the piston and the volume displaced due to the deformation of the structural members inside the chamber. If the deflection of the piston becomes comparable to the chamber height, the volume displaced by the piston becomes comparable with the initial volume of the chamber, and that effect should be taken into consideration, which will result in nonlinear behavior, i.e nonlinear compliance.

The generic duty cycle of the operation is shown in Figure 3-2. The average flowrate can be calculated using the following relationship:

$$Q_{ave} = \frac{\int_0^{T/2} Q_{in} dt}{T} = \frac{\int_{T/2}^{T} Q_{out} dt}{T} \tag{3.12}$$

It is also important to note that:

$$\int_{T/2}^{T} Q_{in} dt = \int_0^{T/2} Q_{out} dt = 0 \tag{3.13}$$

Integrating equation 3.11 from $t = 0$ to $t = \frac{T}{2}$, using equation 3.12 and arranging terms, we get the expression for the average flowrate as:

$$Q_{ave} = A_{pis}(x_{\max} - x_{\min})f + C_{eff}(P_{\max} - P_{\min})f \tag{3.14}$$

where $A_{pis}$ is the cross-sectional area of the piston and $f$ is the operation frequency. The same expression can be obtained by integrating equation 3.11 from $t = \frac{T}{2}$ to $t = T$. The first term in equation 3.14 corresponds to the flowrate required to move the piston and squeeze the piezoelectric element. The second term corresponds to the flowrate required due to the compliances in the chamber.

### 3.2.3 Fluid Model

The schematic of the device with pressures at different locations within the system is shown in Figure 3-3 where $P_{int-in}$ is the intermediate pressure at the exit of the inlet channel, and $P_{int-out}$ is the intermediate pressure at the entrance to the outlet valve. Inlet and outlet channels have the same geometry. Details of the Simulink architecture is given in the Appendix A.

#### Valve Orifice Flow Relations

Work by previous researches has shown that for small openings, poppet valves, such as the valve cap in the active valves within the MHT systems, behave as long orifices in which the effects of flow separation and subsequent re-attachement dominate the valve flow dynamics[5].

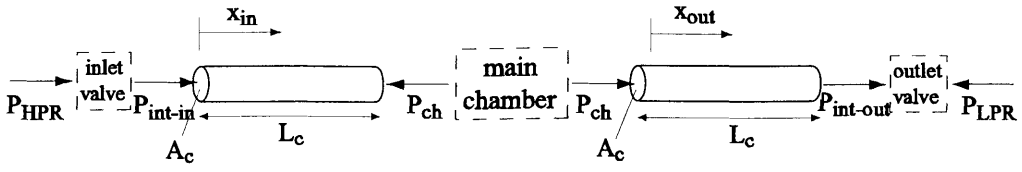


Figure 3-3: Device schematics showing pressures at different locations.

Qualitatively, the valve flow can be approximated by a simplified order-of-magnitude valve model. The valve orifice may be characterized as a flow contraction followed by a flow expansion as shown in Figure 3-4(a) and (b). An integral analysis gives a relationship for the combined effect of the flow expansion and contraction. The loss coefficient $\zeta_{orifice}$ is defined as the total pressure drop $\Delta P = P_{HPR} - P_{int}$ (for the inlet valve) over the dynamic pressure based on the orifice local mean velocity ($\bar{u} = \frac{Q}{A_o}$)

$$\zeta_{orifice} = \frac{\Delta P}{\frac{1}{2}\rho \bar{u}^2} = \left[\frac{1}{2}\left(1 - \frac{A_o}{A_1}\right)^{\frac{3}{4}} + \left(1 - \frac{A_o}{A_2}\right)^2\right] \tag{3.15}$$

where the upstream, throat and downstream flow areas can be approximated as:

$$A_2 = 2\pi R_{vc} H_c \tag{3.16}$$

$$A_o = 2\pi R_{vc} x_{vc} \tag{3.17}$$

$$A_1 = \pi R_{vc}^2 \tag{3.18}$$

respectively, where $H_c$ is the height of the radial flow channel above the valve membrane, $x_{vc}$ is the valve cap distance from the valve stop structure and $R_{vc}$ is the radius of the valve cap.

This approximation, however, is independent of the Reynolds number and therefore holds only for Re$\geq 10,000$, where the flow is in fully turbulent regime. In the MHT power generator, Reynolds numbers are expected to fluctuate between approximately 10 and 20,000 as the valves

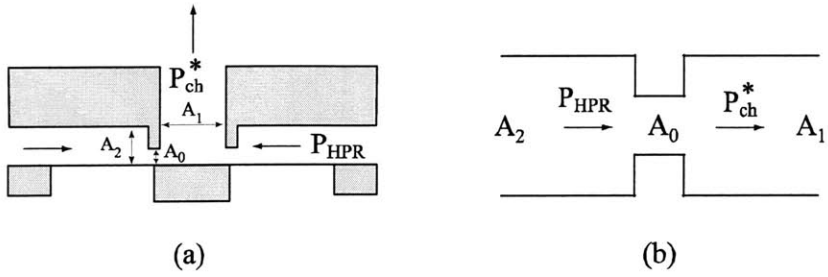


Figure 3-4: Valve orifice representation:(a) Valve cap geometry and fluid flow areas, (b) Representation of flow through the valve as a flow contraction followed by a flow expansion.

open and close. For this reason, correction factors obtained from experimental results need to be employed to obtain better estimates of the loss coefficients for these low turbulence and laminar flow regimes[4]. A loss coefficient for each of the contraction and expansion geometries, $\zeta_{contraction}$ and $\zeta_{expansion}$, respectively, is used to approximate the total loss coefficient through the valve, as detailed in the following relation:

$$\zeta^*_{orifice} = \zeta_{contraction}(\mathrm{Re}, \frac{A_o}{A_2}) + \zeta_{expansion}(\mathrm{Re}, \frac{A_o}{A_1}) \tag{3.19}$$

where Reynolds number is defined as:

$$\mathrm{Re} = \frac{1}{\pi} \frac{Q}{R_{vc}\nu} \tag{3.20}$$

Figure 3-5(a) plots $\zeta_{contraction}$ as a function of Reynolds number and contraction area ratio $\frac{A_o}{A_2}$, and Figure 3-5(b) plots $\zeta_{expansion}$ as a function of Reynolds number and the expansion area ratio $\frac{A_o}{A_1}$. As a result, the pressure-flow relation for the full valve orifice geometry can be written as:

$$\Delta P = \frac{1}{2}\rho\zeta^*_{orifice}\left(\frac{Q^2}{A_o^2}\right) \tag{3.21}$$

All subsequent fluid models discussed in this thesis incorporate these higher-order correction factors to obtain an accurate estimation of the flow behavior. These flow models are based on steady flow phenomenon and do not capture frequency dependent losses. For a specific value of valve cap opening at a given time during the cycle, a relationship therefore exists for the

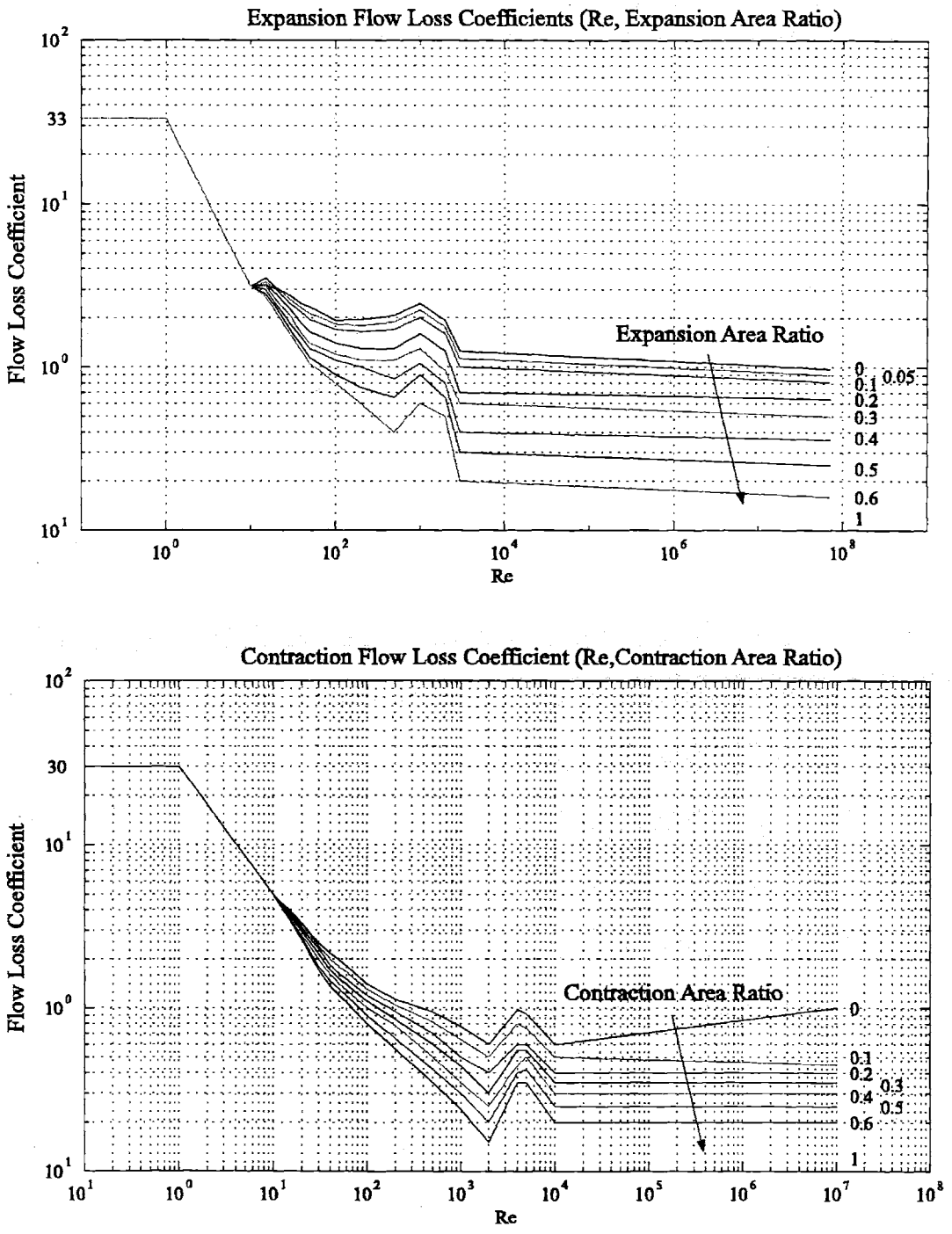


Figure 3-5: Look-Up tables used for flow loss contraction and expansion coefficients. The loss coefficients are obtained from [51].

instantaneous fluid flow through the valve as a function of the pressure drop across the valve.

Equation 3.21 can be rewritten for inlet and outlet valves using the notation in Figure 3-3 as:

$$P_{HPR} - P_{int-in}(t) = R_{in}(Q_{in}, vo_{in})Q_{in}^2 \tag{3.22}$$

$$P_{int-out}(t) - P_{LPR} = R_{out}(Q_{out}, vo_{out})Q_{out}^2 \tag{3.23}$$

where $R_{in}$ and $R_{out}$ represent the flow resistances of the inlet and outlet valves, respectively, which are functions of the flowrate and the corresponding valve opening at a given instant of time.

### Flow in the Channels

Due to the high Reynolds numbers, the flow in the channels is expected to be inertia dominated. Furthermore, the compliance in the fluid channels is usually negligible due to the fact that the channels are surrounded by rigid walls and their volume is much smaller than that of the chamber. Under this assumptions the flow inside the channels is modeled as one dimensional inviscid and incompressible flow. The pressure-flowrate relationship in this case is given as:

$$\Delta P = I\frac{dQ}{dt} = \left(\frac{\rho L_c}{A_c}\right)\frac{dQ}{dt} \tag{3.24}$$

where $I$ is defined as the fluid inductance inside the channel, $\rho$ is the fluid density and $L_c$ and $A_c$ are the length and cross-sectional area of the fluid channel respectively. For the case of inlet valve and outlet valve fluid channels, the pressure-flow relations can be written as:

$$P_{int-in}(t) - P_{ch}(t) = \left(\frac{\rho L_c}{A_c}\right)\frac{dQ_{in}}{dt} \tag{3.25}$$

$$P_{ch}(t) - P_{int-out}(t) = \left(\frac{\rho L_c}{A_c}\right)\frac{dQ_{out}}{dt} \tag{3.26}$$

For a long channel with small cross-sectional area, one can expect fluid inertial effects to

play a significant role as the pressure difference builds up to accelerate the fluid slug into the chamber. Conversely, for short channels with large cross-sectional areas, the inertial effects are negligible and the pressure $P_{int-in}$ and $P_{ch}$ or $P_{ch}$ and $P_{int-out}$ will not differ much. It is important to consider inertial effects when designing hydraulic systems containing small channels.

#### Governing Equations

Combining equations 3.22, 3.23, 3.25, and 3.26 we can obtain the governing equations for the fluid flow in the system, which are integrated into the system level simulation, as:

$$P_{HPR} - P_{ch}(t) = R_{in}(Q_{in}, vo_{in})Q_{in}^2 + \left(\frac{\rho L_c}{A_c}\right)\frac{dQ_{in}}{dt} \tag{3.27}$$

$$P_{ch}(t) - P_{LPR} = R_{out}(Q_{out}, vo_{out})Q_{out}^2 + \left(\frac{\rho L_c}{A_c}\right)\frac{dQ_{out}}{dt} \tag{3.28}$$

Although not explicitly seen, the intermediate pressures can be easily calculated and monitored in the system level simulation, which are important in terms of stresses in the valve membranes and power consumption in the active valves since they are assumed to act on the valve cap, where the reservoir pressures are assumed to act on the membranes[6].

### 3.2.4 Circuitry

The same circuit models presented in Chapter 2 will be used.

## 3.3 Working Fluid

Fluid properties which are important in terms of system performance are listed in Table 3.3 for alternative working fluids. The density of a working fluid effects the dynamic behavior of the system because of the fluid inductance in the fluid channels. A low density fluid is desirable since it would increase the bandwidth of the system. The viscosity of a working fluid effects the energy dissipated in the valves. A more viscous fluid would provide the same amount of flowrate with larger valves or valve openings, causing an increase in power consumption in the

| | Density$[kg/m^3]$ | Viscosity$[Pa/s]$ | Bulk Modulus$[GPa]$ |
|---|---|---|---|
| Water | 1000 | 1.0e-3 | 2.24 |
| Mercury | 13,570 | 1.5e-3 | 25.0 |
| Silicone Oil | 760 | 4.9e-4 | 2.0(degassed) |

Table 3.1: Comparison of different working fluids

| | |
|---|---|
| *Length of the piezoelectric cylinder* | $1mm$ |
| *Diameter of the piezoelectric cylinder* | $2mm$ |
| *Diameter of the piston* | $4.5mm$ |
| *Effective chamber compliance* $(C_{eff})$ | $2 \times 10^{-18}[m^3/Pa]$ |
| $P_{HPR}$ | $2MPa$ |
| $P_{LPR}$ | $0MPa$ |
| *Operation Frequency* | $10kHz$ |
| *Fluid channel length* | $1mm$ |
| *Fluid channel cross-section* | $50\mu m$ x 100 $\mu m$ |
| *Piezoelectric Material* | *PZN-4.5%PT* |

Table 3.2: The geometry and operation conditions used in the simulation

valves. The bulk modulus effects the system compliance. Silicone oil is chosen as the working fluid because of its low density, low viscosity and a bulk modulus comparable to that of water.

## 3.4 Simulation and Analysis

The equations presented in the previous section will be simulated using Simulink. The coupled equations used to simulate the system are 3.2, 3.3, 3.4, 3.11, 3.27, 3.28 and equations for the circuitry, which were given in Chapter 2.

The simulation architecture is shown in Figure 3-6. For the analysis in this chapter, a representative system will be analyzed, for which the geometry and operation conditions are presented in Table 3.2.

In the following analysis, the valve openings are imposed and reservoir pressures are assumed to be constant. The valve size and opening are adjusted such that the pressure in the energy harvesting chamber attains the high pressure reservoir pressure ($P_{HPR}$) and low pressure reservoir pressure ($P_{LPR}$) as its maximum and minimum pressures respectively. In other words, the pressure inside the chamber fluctuates between $P_{HPR}$ and $P_{LPR}$. The valves operate $180^0$ out of phase.

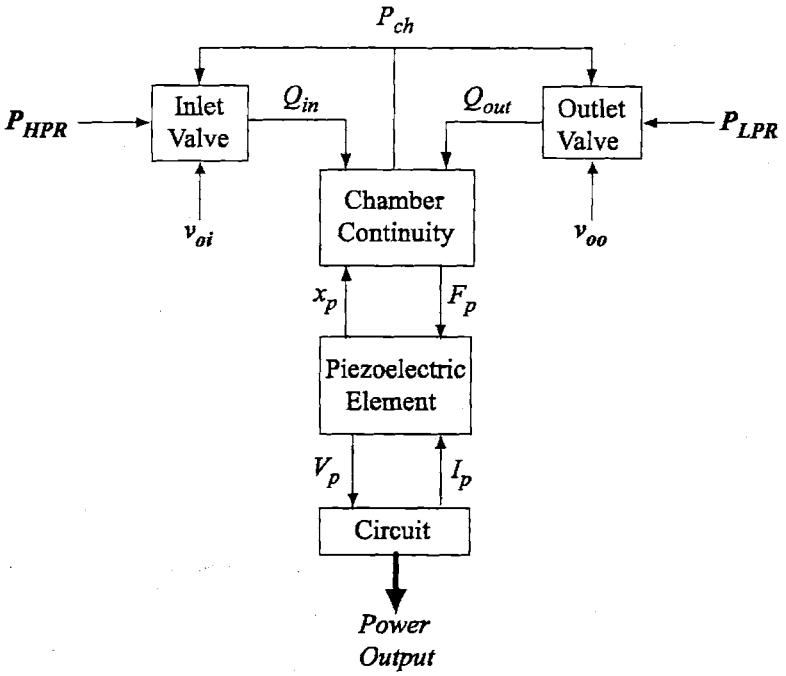


Figure 3-6: Simulation architecture used in Simulink.

### 3.4.1 Energy Harvesting Chamber and Full Bridge Rectifier

This section presents the simulation and analysis of the energy harvesting chamber attached to the full bridge rectifier using the model presented in the previous section. The time histories of the chamber pressure, flowrate and piston deflection, which is equal to the deflection of the piezoelectric element, are shown in Figure 3-7.

In order to understand the interaction between the hydraulic/mechanical system and the circuitry, and its implications on flowrate and frequency for a given power requirement, it is worthwhile to investigate the plot of force on the piezoelectric element vs displacement of the piezoelectric element. This is shown in Figure 3-8. It is interesting to note that the curve in Figure 3-8 has the exact same shape of the force vs. displacement curve presented in Chapter 2 for the case of the imposed force on a piezoelectric cylinder attached to a diode bridge. From this we can conclude that the force vs. displacement curve of a piezoelectric element attached to the full bridge rectifier does not depend on the time history of the applied force. So, the equations derived in Chapter 2 for the full bridge rectifier will be used here to derive

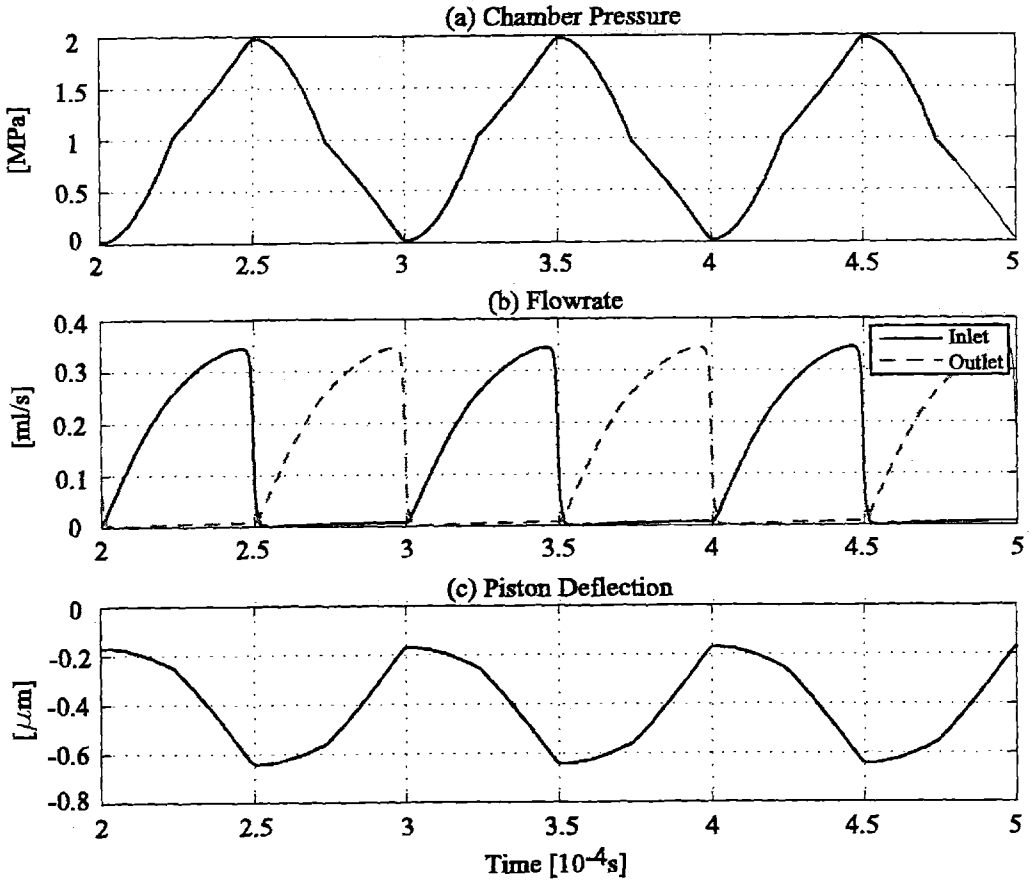


Figure 3-7: Simulation of the energy harvesting chamber attached to the full bridge rectifier circuit.

the governing equations for required frequency, flowrate and system efficiency.

For a given operation frequency and power requirement, the required cross-sectional area of the piezoelectric element can be obtained from equation 2.25 as:

$$A_p = \frac{4W}{(s_{33}^E - s_{33}^D)\sigma^2 L_p f} \tag{3.29}$$

where $W$ is the generated power, $L_p$ is the length of the piezoelectric cylinder and $f$ is the operation frequency. Since the maximum pressure in the chamber is $P_{HPR}$, the cross-sectional area of the piston should be equal to:

$$A_{pis} = \frac{\sigma_d A_p}{P_{HPR}} \tag{3.30}$$

where $\sigma_d$ is the depolarization stress of the piezoelectric element. From the results derived in Chapter 2, the total deflection of the piston/piezoelectric cylinder is given by:

$$\Delta x_p = \frac{1}{2}\sigma_d L_p (s_{33}^E + s_{33}^D) \tag{3.31}$$

Using equations 5.31, 3.29, 3.30, and 3.31, the required flowrate for a given power requirement and maximum chamber pressure can be derived as follows:

$$Q = \frac{2(s_{33}^E + s_{33}^D)W}{(s_{33}^E - s_{33}^D)P_{HPR}} + C_{eff} P_{HPR} f \tag{3.32}$$

The first term in equation 3.32 corresponds to the flowrate which is required just to move the piston. The second term corresponds to the additional flowrate required due to the chamber compliance. If we consider the ideal case, where the chamber is not compliant, i.e $C_{eff} = 0$, the minimum required flowrate is given by

$$Q_{\min} = \frac{2(s_{33}^E + s_{33}^D)W}{(s_{33}^E - s_{33}^D)P_{HPR}} \tag{3.33}$$

In order to evaluate the performance of the energy harvesting chamber, we can define the efficiency of the chamber as follows:

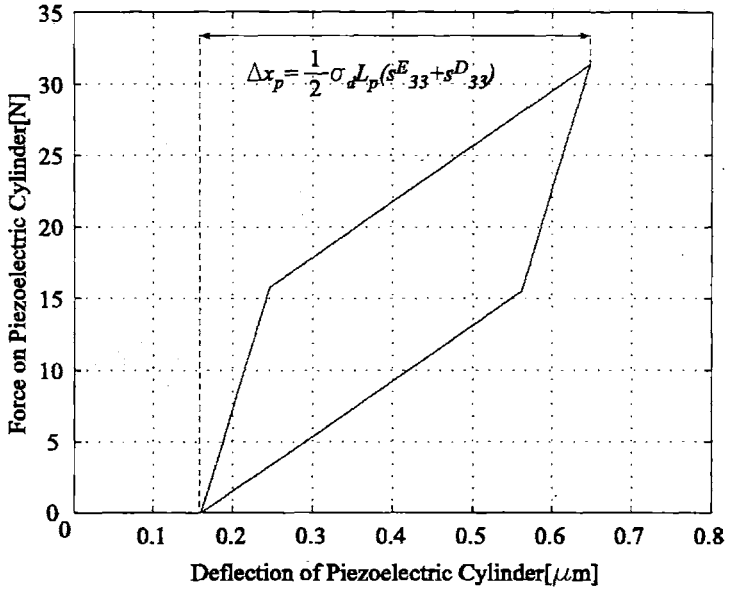


Figure 3-8: Force vs. displacement curve of the piezoelectric element from the simulation of the harvesting chamber attached to the full bridge rectifier.

$$\eta_{ch} = \frac{\text{Electrical } \textit{Power Out}}{\textit{Hydraulic Power In}} = \frac{W}{QP_{HPR}} \tag{3.34}$$

In the extreme case, where the effective chamber compliance is zero, the efficiency has its maximum value, which can be obtained from equations 3.32 and 3.34 as:

$$\eta_{ch\,\max} = \frac{(s^E_{33} - s^D_{33})}{2(s^E_{33} + s^D_{33})} = \frac{k^2_{33}}{4 - 2k^2_{33}} \tag{3.35}$$

It is interesting to note that the maximum efficiency of the chamber depends only on the coupling coefficient of the piezoelectric material. This suggests that, regardless of the geometry and operation conditions, the above expression puts an upper bound on the system efficiency, which is only a function of the piezoelectric element chosen. It is important to note that the above definition of the efficiency corresponds only to the energy harvesting chamber. If the overall system is considered, the electrical power consumption in the active valves should be taken into consideration.

### 3.4.2 Energy Harvesting Chamber and Full Bridge Rectifier with Voltage Detector Circuit

This section presents the simulation and analysis of the Energy Harvesting Chamber attached to the full bridge rectifier and voltage detector circuit. The geometry and the operation conditions are the same as in the previous section. The time histories of the chamber pressure, flowrate and piston deflection are shown in Figure 3-9.

It is interesting to note that there are sudden pressure drops inside the chamber and the time histories of the chamber pressure and the piston deflection are quite different from the time histories presented in the previous section. The most important observation is that during the periods when the switch is on, the pressure decreases/increases suddenly because the fluid cannot fill/evacuate the chamber immediately due to the fluid inertia of the fluid in the channels. In order to understand the interaction between the hydraulic/mechanical system and the circuit, and its implications on flowrate and frequency requirements for a given power, we can investigate the force vs.displacement plot of the piezoelectric element which is shown in Figure 3-10.

In Figure 3-10, the force vs. displacement curve of the piezoelectric element for this case is compared to the chamber attached to full bridge rectifier and to the case where the force is imposed on the piezoelectric element attached to the regular diode bridge and voltage detector. It is interesting to note that the new curve is much different than the imposed force case. In the latter case, which was discussed in Chapter 2, during the interval when the switch is on, the force is almost constant, and the portion of the curve corresponding to that period is almost flat. However, for the chamber, during the interval when the switch is on, the piezo becomes very soft, and the piston moves up or down very rapidly, which causes sudden pressure drops/rises inside the chamber, as can be seen in Figure 3-9. In order to analyze the behavior of the system, we can divide the time history into four periods, as shown in Figure 3-11.

In the periods 1-2 and 3-4 the piezoelectric element is open circuited, and the deflections at the states 1 and 3 correspond to the deflection as if the material was short circuited and the same force as in 1 and 3 was applied. In other words, $F_1, F_3, x_1$, and $x_3$ should satisfy the following equations.

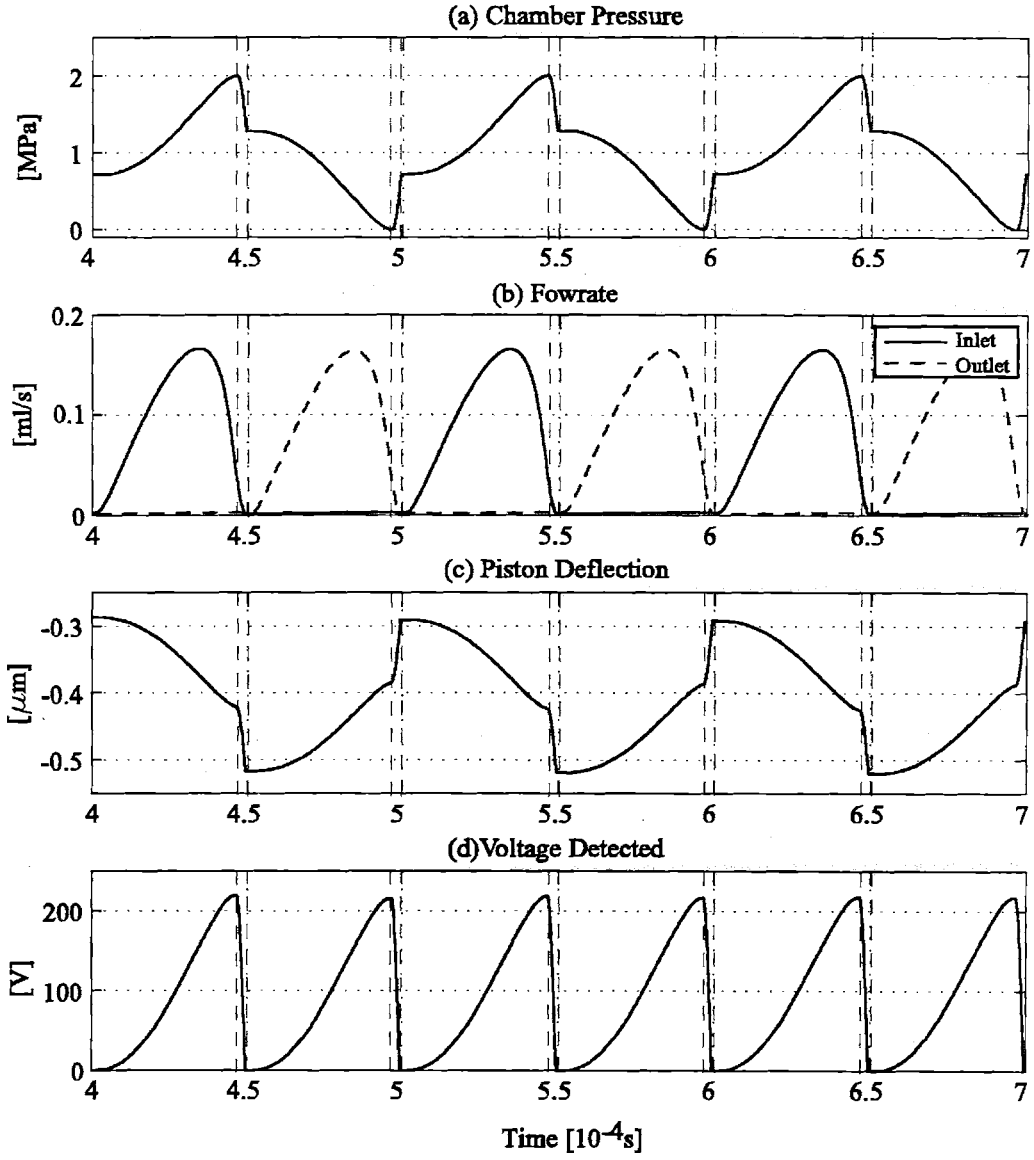


Figure 3-9: Simulation of the energy harvesting chamber attached to the full bridge rectifier and voltage detector circuit. The time intervals between the dashed lines present the intervals where the switch(SCR) is in its "on" state.

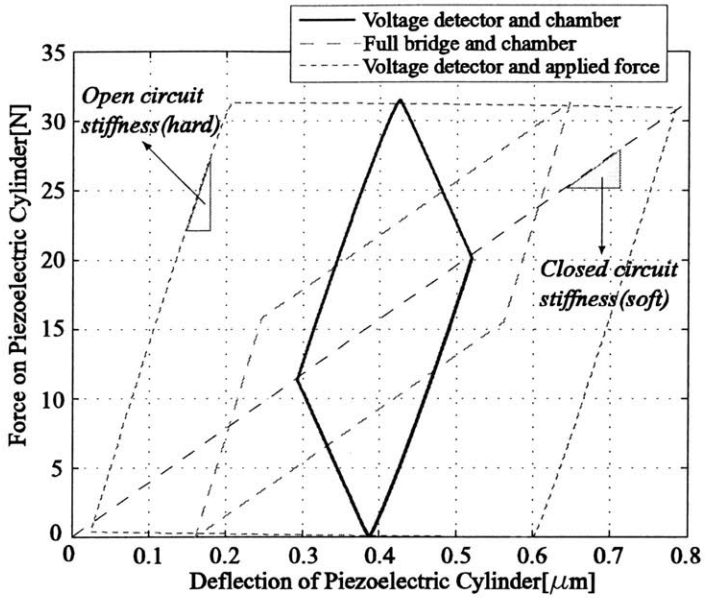


Figure 3-10: Force vs. displacement curve of the piezoelectric element from the simulation of the energy harvesting chamber attached to the full bridge rectifier and voltage detector circuit.

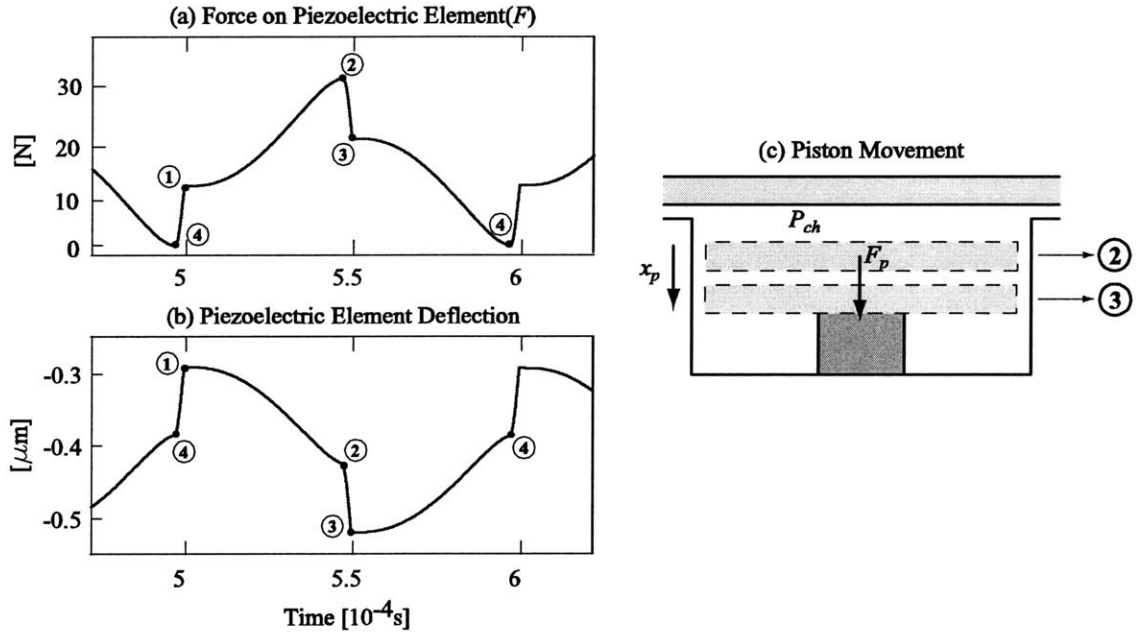


Figure 3-11: Time histories of the force and deflection of the piezolelectric element.

$$x_1 = F_1 \frac{s_{33}^E L_p}{A_p} \tag{3.36}$$

$$x_3 = F_3 \frac{s_{33}^E L_p}{A_p} \tag{3.37}$$

Since in the periods 1-2 and 3-4 the piezoelectric element is open circuited, the slope of the force vs deflection curve in these periods is simply the open circuit stiffness of the piezoelectric element and the following equations should be satisfied.

$$F_2 - F_1 = \frac{A_p}{s_{33}^D L_p}(x_2 - x_1) \tag{3.38}$$

$$F_3 - F_4 = \frac{A_p}{s_{33}^D L_p}(x_3 - x_4) \tag{3.39}$$

In order to understand the behavior in the periods 2-3 and 4-1, let us consider the period 2-3. At state 2, the pressure is maximum and at state 3, the voltage on the piezoelectric element is zero. In the period 2-3, there is almost no flowrate, which suggests that the pressure change in the chamber in this period, which is the sudden pressure drop, is only because of the volume change due to piston movement. In other words, the pressures at states 2 and 3 should satisfy the following equation.

$$P_2 - P_3 = (x_3 - x_2)\frac{A_{pis}}{C_{eff}} \tag{3.40}$$

where

$$P = \frac{F}{A_{pis}} \tag{3.41}$$

From equations 3.40 and 3.41, we can write:

$$F_2 - F_3 = (x_3 - x_2)\frac{(A_{pis})^2}{C_{eff}} \tag{3.42}$$

Similarly for the period 4-1, we can write:

$$F_1 - F_4 = (x_4 - x_1)\frac{(A_{pis})^2}{C_{eff}} \tag{3.43}$$

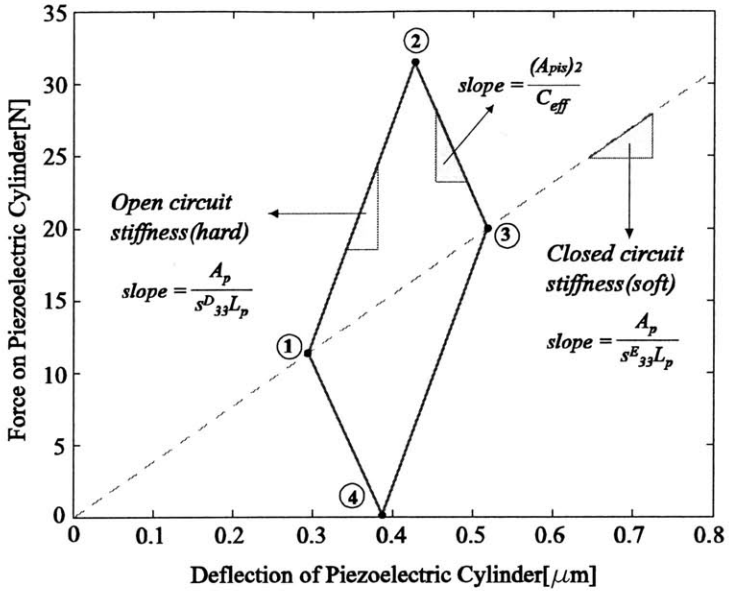


Figure 3-12: Force vs. displacement curve of the piezoelectric element and slopes at different periods of operations.

We also know that:

$$F_2 = \sigma_d A_p \qquad \text{and} \qquad F_4 = 0 \tag{3.44}$$

where $\sigma_d$ is the depolarization stress of the piezoelectric element.

By solving equations 3.36, 3.37, 3.38, 3.39, 3.42, 3.43, and 3.44 we can determine the coordinates of the force vs. deflection curve of the piezoelectric element and we can also calculate the electrical energy stored per cycle, which is the area enclosed by the force vs. deflection curve, the effective coupling factor and system efficiency in terms of chamber geometry, piezoelectric cylinder geometry, chamber compliance and maximum pressure inside the chamber. The force vs. displacement curve of the piezoelectric element and the slopes of the curve at different periods are shown in Figure 3-12. It is interesting to note that in this case, the force vs. deflection curve depends on the chamber compliance, whereas in the case of the energy harvesting chamber attached to the full bridge rectifier, the slopes were determined only by the piezoelectric material geometry and properties.

The coordinates of the force vs displacement curve are as follows:

$$(x_1, F_1) = \left( \frac{\sigma_d A_{pis}^2 L_p^2 s_{33}^E (s_{33}^E - s_{33}^D)}{C_{eff} A_p + A_{pis}^2 L_p (2s_{33}^E - s_{33}^D)}, \frac{\sigma_d A_{pis}^2 L_p A_p (s_{33}^E - s_{33}^D)}{C_{eff} A_p + A_{pis}^2 L_p (2s_{33}^E - s_{33}^D)} \right) \tag{3.45}$$

$$(x_2, F_2) = \left( \frac{\sigma_d L_p^2 (s_{33}^E)^2 A_{pis}^2 + \sigma_d C_{eff} L_p A_p s_{33}^D}{C_{eff} A_p + A_{pis}^2 L_p (2s_{33}^E - s_{33}^D)}, \sigma_d A_p \right) \tag{3.46}$$

$$(x_3, F_3) = \left( \frac{\sigma_d L_p^2 (s_{33}^E)^2 A_{pis}^2 + \sigma_d C_{eff} L_p A_p s_{33}^E}{C_{eff} A_p + A_{pis}^2 L_p (2s_{33}^E - s_{33}^D)}, \frac{\sigma_d A_p L_p A_{pis}^2 s_{33}^E + \sigma_d C_{eff} A_p^2}{C_{eff} A_p + A_{pis}^2 L_p (2s_{33}^E - s_{33}^D)} \right) \tag{3.47}$$

$$(x_4, F_4) = \left( \frac{(\sigma_d s_{33}^E A_{pis}^2 L_p^2 + \sigma_d C_{eff} L_p A_p)(s_{33}^E - s_{33}^D)}{C_{eff} A_p + A_{pis}^2 L_p (2s_{33}^E - s_{33}^D)}, 0 \right) \tag{3.48}$$

Using the coordinates of the points given in the above equations, electrical energy stored per cycle can be calculated as:

$$E = \frac{\sigma_d^2 L_p A_p (s_{33}^E - s_{33}^D)(A_p C_{eff} + s_{33}^E A_{pis}^2 L_p)(A_p C_{eff} + s_{33}^D A_{pis}^2 L_p)}{[A_{pis}^2 L_p (2s_{33}^E - s_{33}^D) + C_{eff} A_p]^2} \tag{3.49}$$

From equation 5.31 we can write the expression for the flowrate as:

$$Q_{ave} = A_{pis}(x_3 - x_1) f + C_{eff} P_{HPR} f \tag{3.50}$$

For a given power requirement $W$, we can determine the required frequency using:

$$f = \frac{W}{E} \tag{3.51}$$

The required flowrate for a given power requirement can be derived from equations 3.45, 3.47, 3.49, 3.50, and 3.51 as:

$$\begin{aligned} Q_{ave} \quad = \quad & \frac{W[s_{33}^E C_{eff} P_{HPR}^2 + \sigma_d^2 L_p A_p s_{33}^E (2s_{33}^E - s_{33}^D)]}{P_{HPR}(C_{eff} P_{HPR}^2 + \sigma_d^2 L_p A_p s_{33}^E)(s_{33}^E - s_{33}^D)} + \\ & \frac{W P_{HPR} C_{eff} [C_{eff} P_{HPR}^2 + \sigma_d^2 L_p A_p (2s_{33}^E - s_{33}^D)]^2}{\sigma_d^2 A_p L_p (s_{33}^E - s_{33}^D)(C_{eff} P_{HPR}^2 + \sigma_d^2 L_p A_p s_{33}^E)(C_{eff} P_{HPR}^2 + \sigma_d^2 L_p A_p s_{33}^D)} \end{aligned} \tag{3.52}$$

In the extreme case where the effective chamber compliance is zero, namely $C_{eff} = 0$, the

expression for the required flowrate simply reduces to

$$Q_{\min} = \frac{(2s_{33}^E - s_{33}^D)W}{(s_{33}^E - s_{33}^D)P_{HPR}} \tag{3.53}$$

From the above expression we can get the maximum system efficiency using the definition given in equation 3.34 as

$$\eta_{ch\,\max} = \frac{(s_{33}^E - s_{33}^D)}{(2s_{33}^E - s_{33}^D)} = \frac{k_{33}^2}{1 + k_{33}^2} \tag{3.54}$$

where, as in the previous section, the maximum efficiency depends only on the coupling coefficient of the piezoelectric material.

Figure 3-13 shows the force vs. deflection curve of the piezoelectric element for different values of chamber compliance. It is interesting to note that, as the chamber compliance increases, the curve approaches the curve for the case where the force is imposed. One might think that having large compliance would have a positive effect on system performance, since the area inside the curve, which is the electrical energy stored per cycle, increases with increasing compliance. For a given power requirement lower frequencies and lower flowrates would be required. However, as the compliance increases, the required flowrate increases dramatically due to the second term in equation 3.50. This effect overwhelms the effect of decreased flowrate due to lower frequency requirement and the maximum system efficiency occurs again for the case where the chamber compliance is zero. The two extreme cases, namely $C_{eff} = 0$ and $C_{eff} = \infty$ are shown in Figure 3-13 (b).

The effective coupling factor from mechanical to electrical energy was defined in Chapter 2 and the expressions were derived for different circuits for the imposed force case. For the case of the energy harvesting chamber attached to the full bridge rectifier, the effective coupling factor is the same as the one for the imposed force case since for the full bridge rectifier, the force vs. displacement curve doesn't depend on the time history of the force on the piezoelectric element. However, it was found that, the force vs. displacement curve for full bridge rectifier and voltage detector depends on the time history of the force on the piezoelectric element, and in this case the curve depends on the chamber compliance. The effective coupling factor was defined in Chapter 2. From Figure 3-13 we can write:

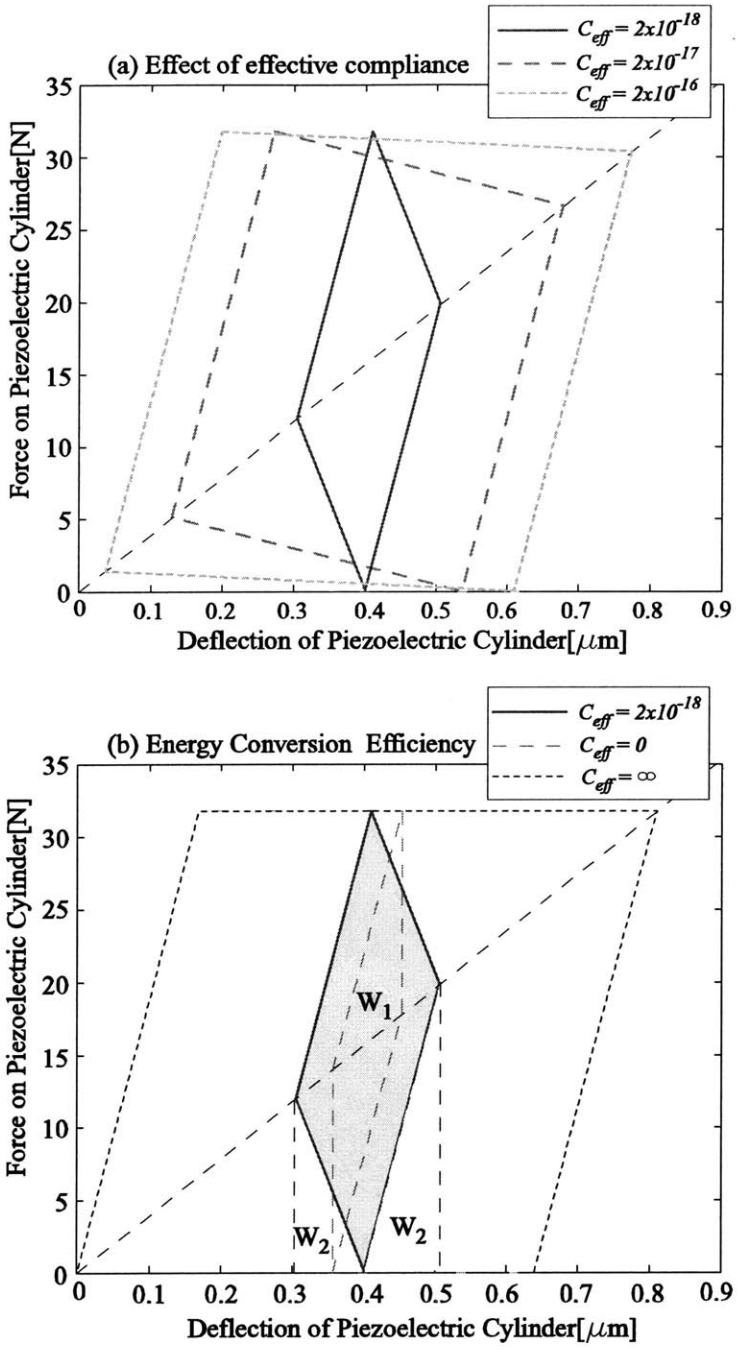


Figure 3-13: The effect of effective chamber compliance on force vs. deflection curve and effective coupling factor.

$$k_{eff}^2 = \frac{W_1}{W_1 + W_2} \tag{3.55}$$

The effective coupling factor can be calculated using the coordinates of the force vs. deflection curve. For the case where the effective chamber compliance is infinity, the effective coupling factor is:

$$C_{eff} = \infty \rightarrow k_{eff}^2 = \frac{2(s_{33}^E - s_{33}^D)}{2s_{33}^E - s_{33}^D} \tag{3.56}$$

for which case the electrical energy stored per cycle is:

$$E_{(C_{eff}=\infty)} = (s_{33}^E - s_{33}^D)\sigma_d^2 A_p L_p \tag{3.57}$$

which is the same amount of energy stored for the case of imposed force on piezoelectric element with the same circuitry.

For the case where the effective chamber compliance is zero, the effective coupling factor becomes:

$$C_{eff} = 0 \rightarrow k_{eff}^2 = \frac{2(s_{33}^E - s_{33}^D)}{3s_{33}^E - 2s_{33}^D} \tag{3.58}$$

for which case the electrical energy stored per cycle is:

$$E_{(C_{eff}=0)} = \frac{\sigma_d^2 A_p L_p (s_{33}^E - s_{33}^D) s_{33}^E s_{33}^D}{(2s_{33}^E - s_{33}^D)^2} \tag{3.59}$$

## 3.5 Discussion

This section presents a comparison of circuitry and piezoelectric materials in terms of their effect on important performance metrics such as flowrate, frequency and efficiency using the results obtained in previous sections of this chapter. Let us consider the system analyzed in Section 3.4, for which the geometric parameters were given in Table 3.2. Now, however, the effective chamber compliance will be varied and its effect on system performance will be investigated. This could be accomplished, for example, by changing the thicknesses of the structural members or by changing the chamber height. For a power requirement of $0.5W$, the required frequency

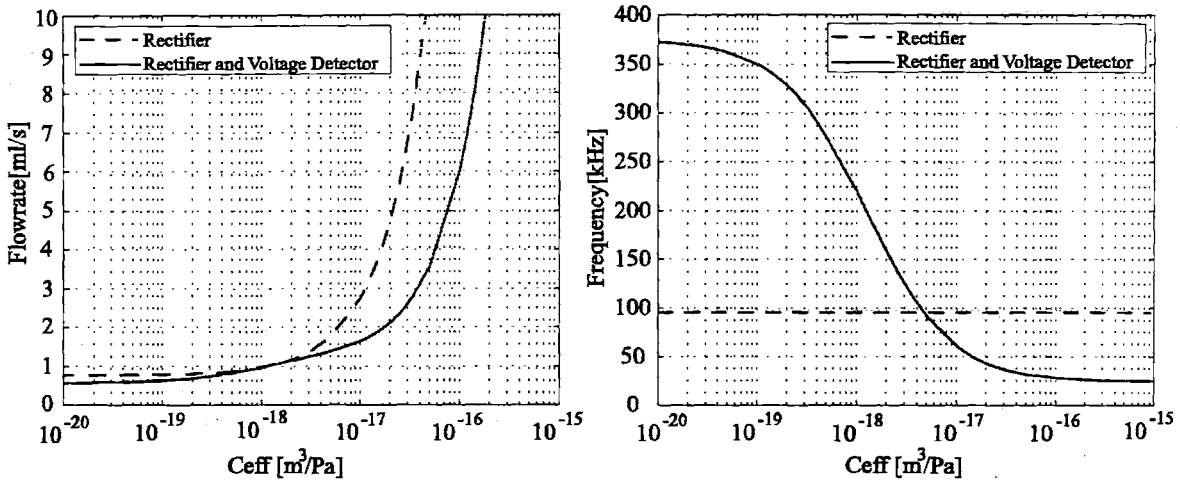


Figure 3-14: Flowrate and frequency requirement for 0.5 W power requirement.

and flowrate is plotted as a function of effective chamber compliance in Figure 3-14. It can be noted from Figure 3-14 that the frequency requirement for the full bridge rectifier case does not depend on effective chamber compliance since the force vs. displacement graph is the same for any chamber compliance and the energy stored per cycle depends only on the maximum stress on the piezoelectric element and piezoelectric material properties. However, since the force vs. displacement curve for the rectifier with voltage detector case depends heavily on the effective chamber compliance, the electrical energy stored per cycle depends on the compliance. So, for a given power requirement, the required frequency depends on the effective compliance as well. In terms of flowrate requirement, it can be easily seen that, as the system gets more compliant, the required flowrate increases dramatically. It should be pointed out that, for a microfluidic device, even flowrates on the order of $1ml/s$ can be considered very high, and special high performance microvalves are needed. It is obvious that, prediction of the effective chamber compliance will constitute a crucial part of the modelling and design process. This will be addressed in Chapter 4.

The system efficiency, which was defined in equation 3.34 is plotted as a function of the effective chamber compliance in Figure 3-15. It can be noted that, as the effective chamber compliance gets smaller and smaller, in other words, as the chamber gets less and less compliant, the efficiency values approach their maximum values which were given in equations 3.35 and

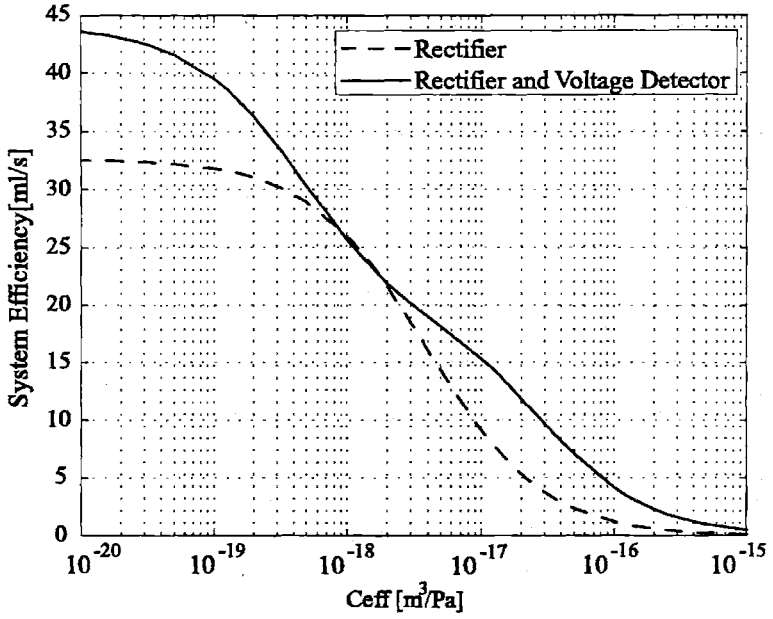


Figure 3-15: System efficiency as a function of the effective chamber compliance.

3.54 for the rectifier and rectifier and voltage detector circuit cases respectively. As mentioned earlier, these maximum efficiency values depend only on the piezoelectric material used.

Using the relations derived in previous sections, we can also compare different piezoelectric materials in terms of flowrate and frequency requirements and system efficiency. Again, let's consider the same system for the $0.5W$ power requirement. Figure 3-16 shows the required flowrates for different piezoelectric materials and different circuitry as a function of effective chamber compliance. It should be noted that for each piezoelectric material, the piezo diameter, $D_p$, is adjusted such that at the maximum chamber pressure, the stress on the piezoelectric element is equal to its depolarization stress, $\sigma_d$. The required flowrates for the rectifier circuit with voltage detector are significantly less than the case with just the rectifier. It can be also observed that PZN-PT requires the least flowrate and PZT-8 requires the most flowrate at low compliance values.

The required frequencies for different piezoelectric materials are shown in Figure 3-17. As mentioned earlier the required operation frequency in the case of rectifier circuit is constant, regardless of the effective chamber compliance. Since the force vs. displacement curve in the

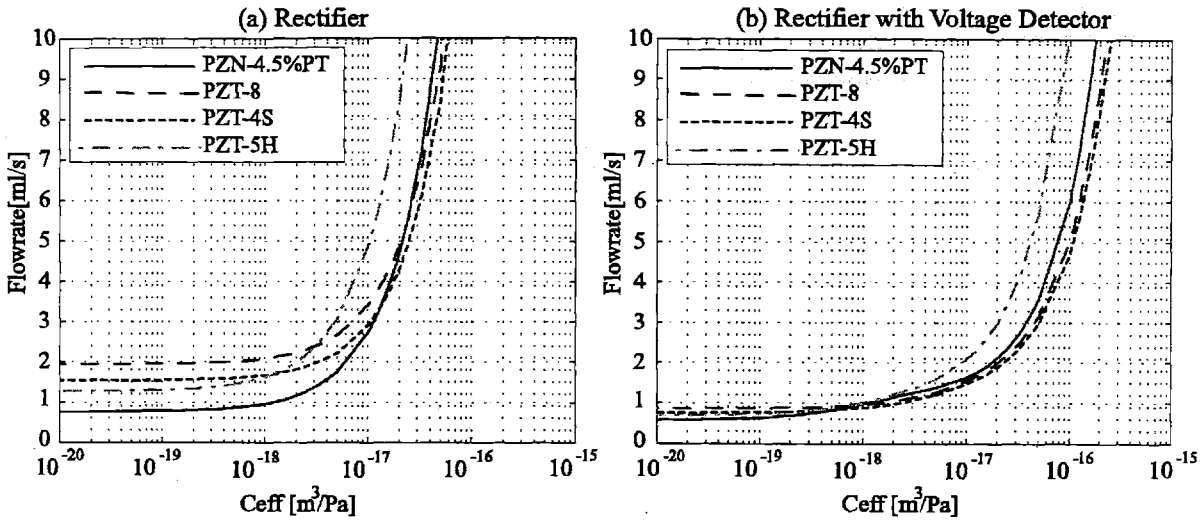


Figure 3-16: Required flowrates for 0.5 power generation. Comparison of different piezoelectric elements and different circuitry.

case of the rectifier and voltage detection circuit depends heavily on the effective chamber compliance, the required frequency for a certain power requirement depends on the effective chamber compliance. Since the materials PZT-8 and PZT-4S have very high depolarization stresses compared to PZT-5H and PZN-PT, the electrical energy stored per cycle for PZT-8 and PZT-4S is much larger, which means reduced frequency requirements for the same power requirement. For example, although PZN-PT has the highest coupling coefficient($k_{33} = 0.89$) among the piezoelectric materials discussed here, it requires higher operation frequencies due to its low depolarization stress.

Figure 3-18 shows the system efficiency for different piezoelectric materials and circuitry. It can be seen that, the chamber with the rectifier circuit and voltage detector is more efficient than the case with the rectifier. As the effective compliance gets smaller and smaller, the system efficiencies approach their maximum value, which are given by equations 3.35 and 3.54 for rectifier and rectifier with voltage detector cases respectively. As expected, PZN-PT is the most efficient material due to its high coupling coefficient($k_{33} = 0.89$) and PZT-8 is the least efficient material due to its low coupling coefficient($k_{33} = 0.64$). Although PZT-8 is the least efficient one, it might be a better suited material since the system with PZN-PT has very high

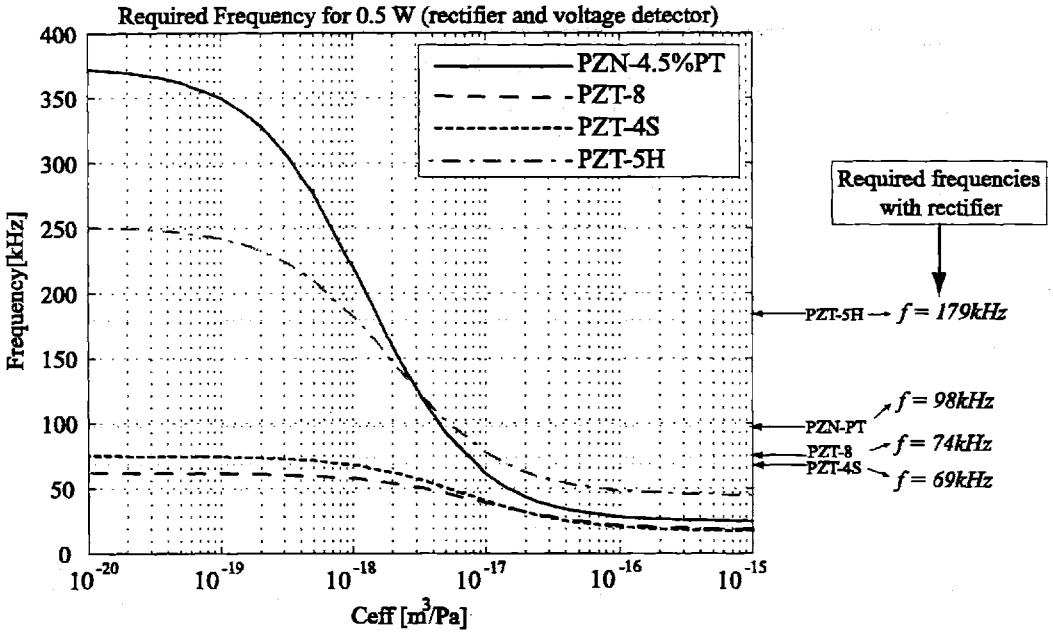


Figure 3-17: Required frequencies for the 0.5W power requirement. Comparison of different piezoelectric materials and circuitry. Note that the required frequency in the case of regular rectifier is independent of the chamber compliance.

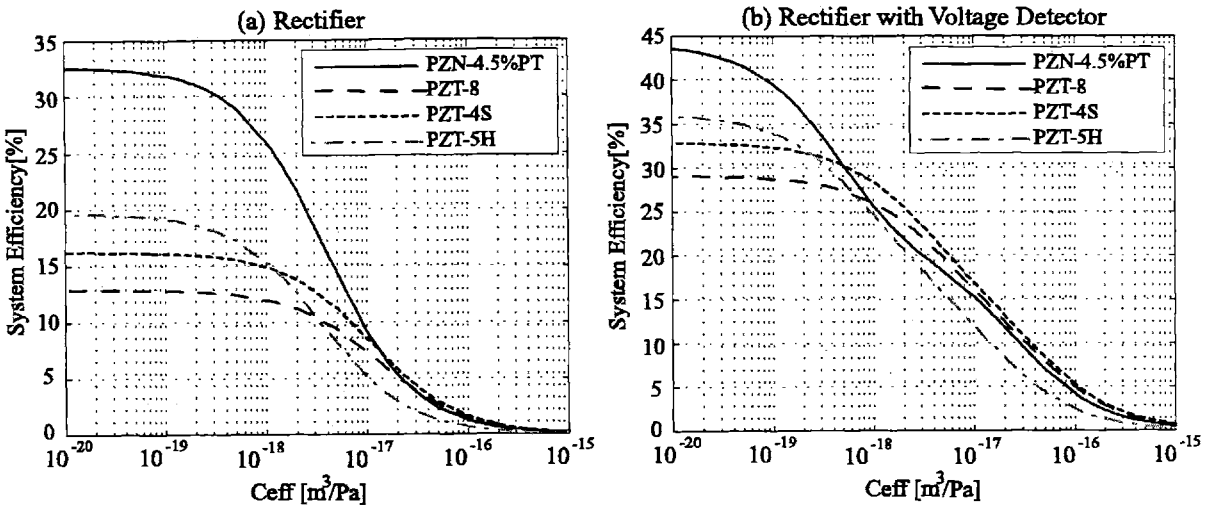


Figure 3-18: Comparison of different piezoelectric materials and circuitry in terms of system efficiency.

frequency requirements. The material selection process should address the design trade-offs and should take the remaining components of the system, for example the active valves, into consideration. One might choose to use PZN-PT which requires very high frequencies, but this frequency can exceed the bandwidth of the active valves. This issue will be addressed in Chapter 5.

One should remember that the analysis of the chamber attached to the rectifier and the voltage detector presented in this chapter assumed that the impedances(inductances) of the fluid channels are large enough such that there are sudden pressure drops inside the chamber and the governing equations are derived assuming that in the time interval where the SCR is in its "on" state, there is no net flowrate into the chamber.

## 3.6 Summary and Conclusion

This chapter presented a simple analysis of the energy harvesting chamber and a case study using a simulation for a predetermined chamber geometry and operating conditions. The interaction between the chamber and the circuitry has been investigated. Some of the important performance metrics derived in the previous sections are summarized in Table 3.3.

| | Rectifier | Rectifier+Voltage Detector |
|---|---|---|
| Effective Coupling Factor | $k_{eff}^2 = \frac{2k_{33}^2}{k_{33}^2+2}$ | $k_{eff(C_{eff}=0)}^2 = \frac{2k_{33}^2}{2k_{33}^2+1}$ |
| Minimum Required Flowrate | $Q_{\min} = \frac{(4-2k_{33}^2)W}{k_{33}^2 P_{HPR}}$ | $Q_{\min} = \frac{(1+k_{33}^2)W}{k_{33}^2 P_{HPR}}$ |
| Maximum System Efficiency | $\eta = \frac{k_{33}^2}{4-2k_{33}^2}$ | $\eta = \frac{k_{33}^2}{1+k_{33}^2}$ |

Table 3.3: Summary and comparison of circuitry in terms of performance indices

The first row summarizes the expressions obtained for the effective coupling factor for the two circuits analyzed in this chapter. The second expression in the first row represents the effective coupling factor for the rectifier with voltage detection circuit for the case where $C_{eff} = 0$, which corresponds to the most efficient operation condition for the energy harvesting chamber. However, maximum effective coupling factor for this circuit occurs when $C_{eff} = \infty$, which is the same as the effective coupling factor of the same circuit for the applied force case, which was presented in Chapter 2. The effective coupling factor for the full bridge rectifier case is the same regardless of the effective compliance of the energy harvesting chamber. The second row presents the minimum required flowrate for a given power requirement and maximum pressure in the chamber. The third row represent the maximum system efficiency. The second and third rows correspond to the case where $C_{eff} = 0$. As mentioned earlier, the maximum system efficiency of the energy harvesting chamber depends only on the piezoelectric material chosen, namely the coupling coefficient($k_{33}$). The expressions are plotted as a function of the coupling coefficient in Figure 3-19. A comparison of different piezoelectric materials is also made on the same plot.

The expressions for the maximum system efficiency in Table 3.3 put an upper limit on the system efficiency. It is interesting to note that, at $k_{33} = 1$ the two curves reach the same point, which is 50% efficiency. This means that, even with a perfect piezoelectric material($k_{33} = 1$) and zero effective compliance, which are not possible, the system efficiency cannot exceed 50%.

The most important conclusion of this chapter is that the performance of the energy harvesting chamber depends on

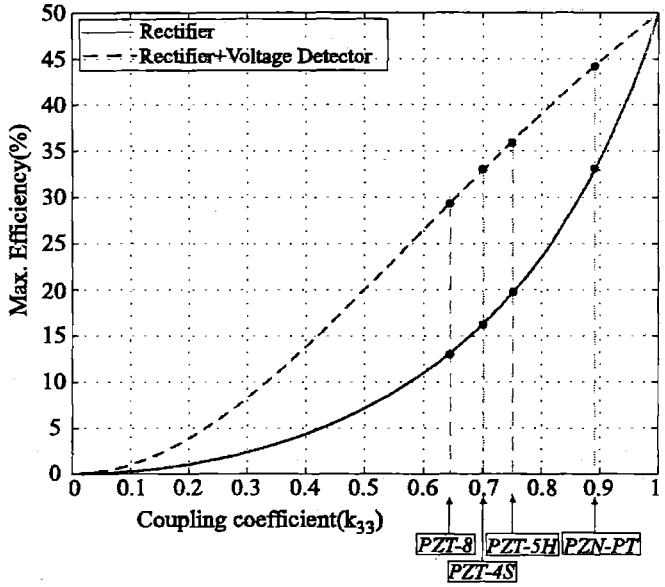


Figure 3-19: Maximum system efficiency(which corresponds to the case where the effective compliance of the chamber is zero)as a function of the coupling coefficient.

- Rectification circuit topology
- Piezoelectric material $(k_{33}, \sigma_d)$
- Chamber compliance$(C_{eff})$

Again it should be emphasized that the efficiency definition in this chapter corresponds only to the energy harvesting chamber. The electrical power consumption in the active valves is not considered.

# Chapter 4

# Detailed Model of the Energy Harvesting Chamber

This chapter presents the detailed modelling of the energy harvesting chamber. In Chapter 3, an effective chamber compliance ($C_{eff}$) based on a typical MHT device was assumed to be used in the simulation and the effect of compliance on system performance was analyzed. This chapter investigates the contribution of different structural components on the effective compliance of the chamber. It also presents the simulation architecture used for integrating elastic equations into the system level simulation.

## 4.1 Analysis of a Simplified Chamber Structure

Consider a simple circular chamber structure consisting of a fluid chamber and rigid walls, except the top portion of the chamber, as shown in Figure 4-1. The compliant portion can be modeled as a clamped circular plate which deforms under the action of uniform pressure underneath. For small deflections, the deformation of the top plate can be assumed to be linear and can be analyzed using linear plate theory [50].

For a uniform pressure distribution $P$ and a radius of $a$, the deflection of the top plate as a function of the radial distance is given as:

$$w(r) = \frac{P}{64D}\left(a^2 - r^2\right)^2 \tag{4.1}$$

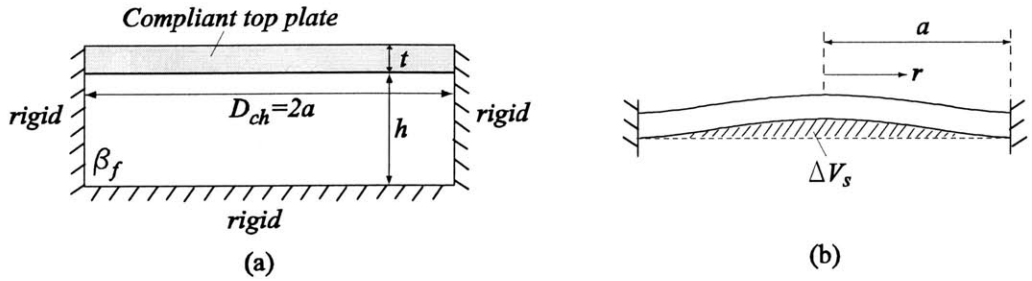


Figure 4-1: (a) Simplified chamber structure consisting of a fluid chamber with a compliant wall (b) Deformation of the top plate and swept volume.

where $D$ is the flexural rigidity of the plate given by:

$$D = \frac{Et^3}{12(1-\nu^2)} \tag{4.2}$$

where $E$ and $\upsilon$ is the Young Modulus and Poisson ratio of the material respectively, and $t$ is the thickness of the plate. The additional volume created in the chamber due to the deformation of the plate can be calculated by integrating equation 4.1 over the plate:

$$\Delta V_s = \int_0^a w(r) 2\pi r dr = \frac{P\pi a^6(1-\nu^2)}{16Et^3} \tag{4.3}$$

The structural compliance was defined in Chapter 3 as:

$$C_s = \frac{\Delta V_s}{\Delta P} \tag{4.4}$$

which represents the volume change of the chamber due to structural deformations in response to a change in chamber pressure. In this simple example, the top plate is the only compliant structural member. Using equations 4.4 and 4.3, the structural compliance can be calculated as:

$$C_s = \frac{\pi a^6(1-\nu^2)}{16Et^3} \tag{4.5}$$

The effective chamber compliance can be obtained as:

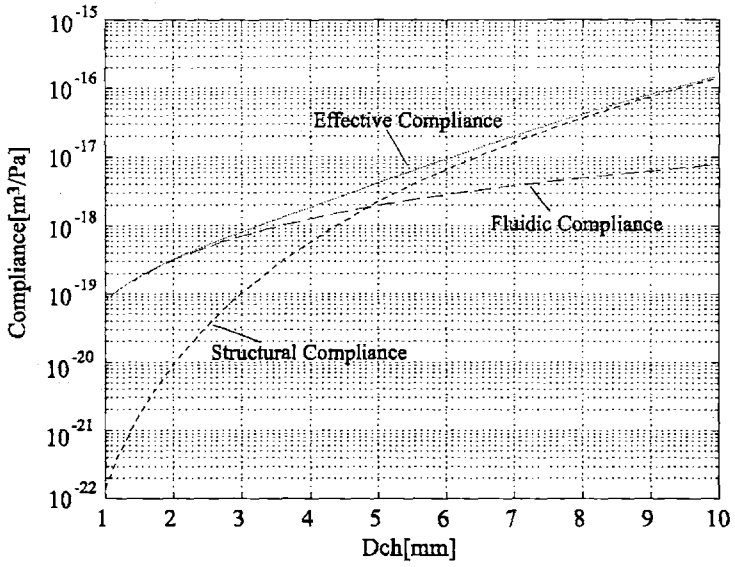


Figure 4-2: Comparison of fluidic and structural compliances for a generic chamber structure at different chamber diameters for fixed chamber height and top plate thickness.

$$C_{eff} = \left(\frac{V_o}{\beta_f} + C_s\right) = \left(\frac{\pi a^2 h}{\beta_f} + \frac{\pi a^6 (1-\nu^2)}{16Et^3}\right) \tag{4.6}$$

where $V_o$ is the initial fluid volume inside the chamber, $\beta_f$ is the bulk modulus of the fluid and $h$ is the height of the chamber.

Consider a chamber with top plate thickness of $500\mu m$ and chamber height of $200\mu m$. Figure 4-2 shows a comparison of fluidic and structural compliances for different chamber diameters. It can be seen that, for small chamber diameters, the compliance of the chamber is dominated by the fluidic compliance, whereas at large chamber diameters the structural compliance dominates. However, it should be noted that, if all the geometric parameters are scaled the same amount, the ratio of the fluidic and structural compliances will remain the same. This issue will be discussed further in Chapter 5.

## 4.2 Detailed Analysis of Structural Components

A simplified chamber structure consisting of a compliant top plate and a fluidic chamber has been analyzed in the previous section. This section will present detailed analysis of individual structural compliances of the energy harvesting chamber which will include the deformation of the top and bottom support structures, deformation of the piston and bending of the tethers. Figure 4-3 shows geometric parameters of the structural components, corresponding deformations and the free body diagrams which will be used in the formulations of the governing equations.

These deformations inside the energy harvesting chamber can be adequately represented by the linear plate theory [50]. Each component will be modeled as a plate with applied loading and boundary conditions to determine the deflections and swept volumes. In general, a symmetrically loaded circular plate will experience deflections due to bending as well as shearing. If the plate thickness is small compared to the plate outer radius, the deflection due to bending will be significantly larger than that due to shearing. Since the radii of the structural components analyzed are larger than the corresponding thicknesses, deformations only due to bending will be considered.

### 4.2.1 Top Support Structure

The top support structure is modeled as a clamped circular plate which deforms under the action of a uniform pressure distribution underneath. The governing differential equation for the symmetrical bending of a circular plate is given as:

$$\frac{d}{dr}\left[\frac{1}{r}\frac{d}{dr}\left(r\frac{dw(r)}{dr}\right)\right] = \frac{Q(r)}{D} \tag{4.7}$$

where $D$ is the flexural rigidity given in equation 4.2, $w(r)$ is the deflection of the plate, and $Q(r)$ is the shear force per unit length. For a uniformly loaded circular plate the shear force per unit length is given as:

$$Q(r) = \frac{P_{ch}r}{2} \tag{4.8}$$

where $P$ is the pressure. The boundary conditions are:

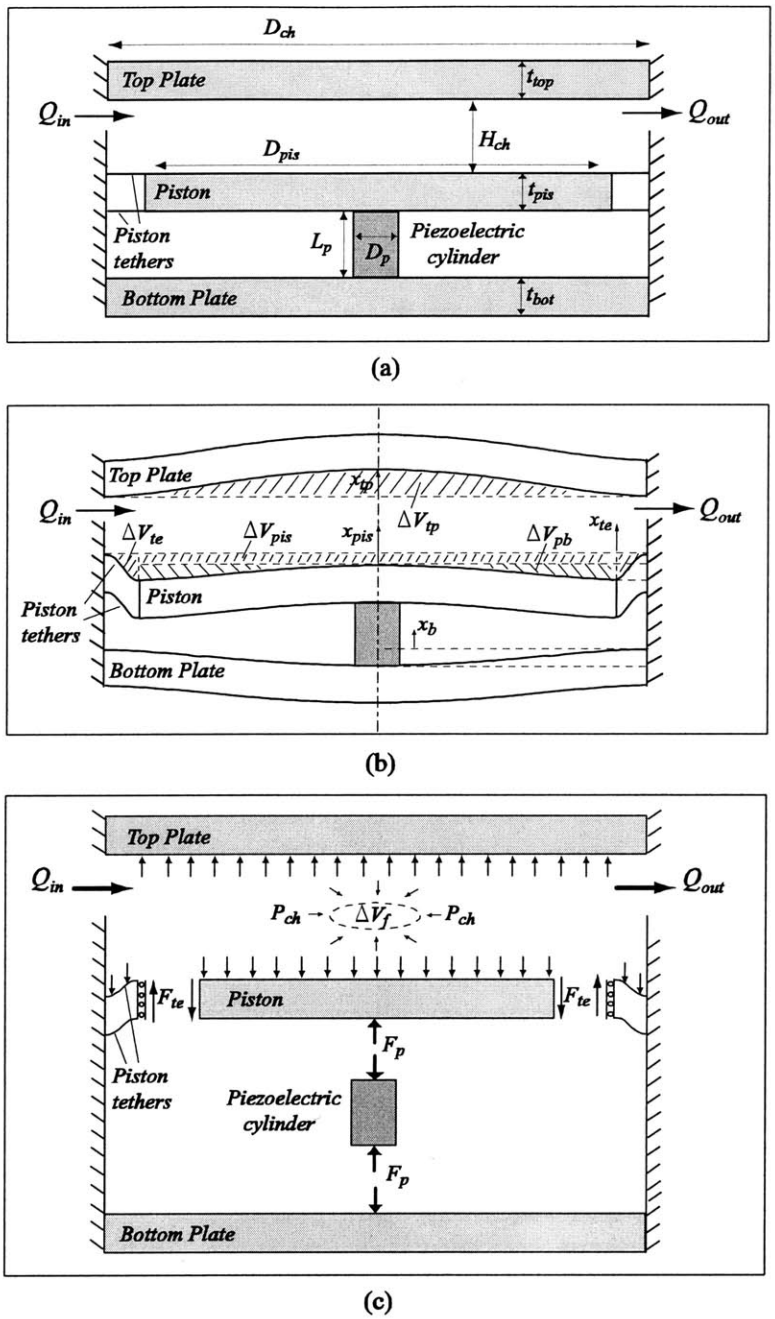


Figure 4-3: (a) Schematic illustrating the dimensional parameters of the chamber, (b) deformation of structural components and sign conventions, (c) free body diagrams and sign conventions. Deflections are exaggerated.

$$w(r=a)=0 \tag{4.9}$$

$$\frac{dw}{dr}(r=a)=0 \tag{4.10}$$

$$\frac{dw}{dr}(r=0)=0 \tag{4.11}$$

By integrating the governing differential equation and applying the boundary conditions, the deflection of the plate $w(r)$ can be determined as:

$$w(r)=\frac{P_{ch}}{64D}\left(a^2-r^2\right)^2 \tag{4.12}$$

The deflection of the midpoint of the top support structure can be obtained by calculating the deflection of the top plate at $r=0$ :

$$x_{tp}=\frac{3P_{ch}a^4(1-v^2)}{16Et^3}=k_{dtp}P_{ch} \tag{4.13}$$

where $k_{dtp}$ depends only on the chamber diameter and the top plate thickness.

The corresponding swept volume can be calculated by integrating equation 4.12 over the plate as:

$$\Delta V_{tp}=\int_0^a w(r)2\pi r dr=\frac{P_{ch}\pi a^6(1-\nu^2)}{16Et^3}=k_{tp}P_{ch} \tag{4.14}$$

where $k_{tp}$ depends only on the chamber diameter and the top plate thickness.

Equations 4.12 and 4.14 are the same equations used in the previous section.

### 4.2.2 Bottom Support Structure

A rigid bottom structure beneath the piezoelectric element would ensure that all of the deflection of the piston goes into the compression of the piezoelectric element. In reality, this structure is not rigid and as a result this bottom structure deformation results in less compression of the piezoelectric element at a given chamber pressure.

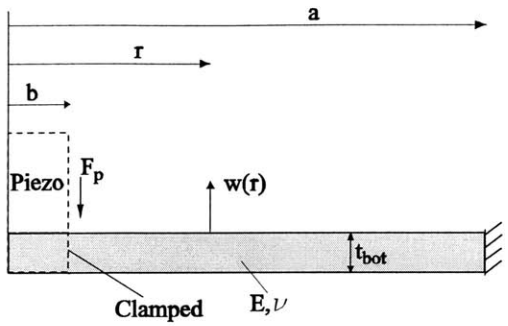


Figure 4-4: Model of the bottom support structure: circular plate with a circular hole at its center with guided boundary condition at inner radius b and clamped boundary condition at outer radius a.

The bottom support structure is modeled as a circular plate with a circular hole at the center which is clamped at its outer radius ($r = a$) and guided at its inner radius ($r = b$), shown in Figure 4-4. In this case the shear force per unit length is given as:

$$Q(r) = \frac{-F_p}{2\pi r} \tag{4.15}$$

where $F_p$ is the force acting on the bottom support structure through the guided support in the inner radius ($r = b$). The boundary conditions are:

$$w(r = a) = 0 \tag{4.16}$$

$$\frac{dw}{dr}(r = a) = 0 \tag{4.17}$$

$$\frac{dw}{dr}(r = b) = 0 \tag{4.18}$$

The deflection of the bottom plate, $x_b$, can be calculated by integrating equation 4.7 and applying the boundary conditions to obtain:

$$x_b = k_b F_p \tag{4.19}$$

where $k_b$ is the stiffness of the bottom plate which depends on the thickness of the bottom plate, $t_{bot}$, inner radius ($b = D_p/2$), and outer radius ($a = D_{ch}/2$).

### 4.2.3 Piston

The piston is modeled as a circular plate with a circular hole at the center which is simply supported at its outer radius ($r = a$) assuming that the tethers exert insignificant bending moments on the piston at its outer radius, and guided at its inner radius ($r = b$), shown in Figure 4-5. In this case the shear force per unit length is given as:

$$Q(r) = \frac{F_p}{2\pi r} - \frac{P_{ch} r}{2} \tag{4.20}$$

where $F_p$ is the force acting on the piston through the guided support in the inner radius ($r = b$).

The boundary conditions are:

$$w(r = a) = 0 \tag{4.21}$$

$$M_r(r = a) = -D\left(\frac{d^2 w(r = a)}{dr^2} + \frac{\nu}{r}\frac{dw(r = a)}{dr}\right) = 0 \tag{4.22}$$

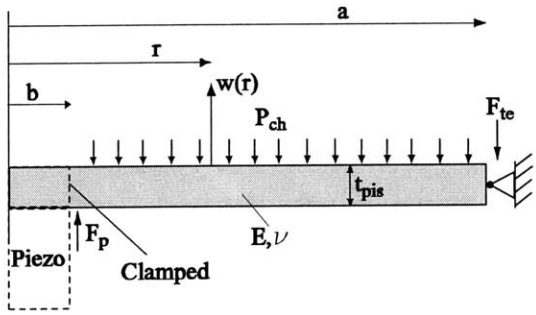


Figure 4-5: Model of the piston: circular plate with a circular hole at its center with guided boundary condition at inner radius b and clamped boundary condition at outer radius a.

$$\frac{dw}{dr}(r=b)=0 \tag{4.23}$$

where $M_r$ denotes the bending moment per unit length along circumferential sections of the plate. The deflection of the piston and the corresponding swept volume can be calculated by integrating equation 4.7 and applying the boundary conditions to obtain:

$$x_{pb} = x_{pis} - x_{te} = k_{p1}F_p + k_{p2}P_{ch} \tag{4.24}$$

$$\Delta V_{pb} = k_{p3}F_p + k_{p4}P_{ch} \tag{4.25}$$

where $k_{p1}, k_{p2}, k_{p3}$,and $k_{p4}$ depend on the thickness of the piston, $t_{pis}$, inner radius ($b = D_p/2$), and outer radius ($a = D_{pis}/2$). The dynamics of the piston can be represented using the free body diagram in Figure 4-3 as:

$$M_{pis}\frac{d^2x_{pis}}{dt^2} = -A_{pis}P_{ch} + F_p - F_{te} = F_{net} \tag{4.26}$$

### 4.2.4 Piston Tethers

In this section, tethers corresponding to a double layer piston structure will be analyzed which consist of a top and bottom tether structure. In order to allow for flexibility in design, the top and bottom tethers are defined to have different thicknesses ($t_{tetop}, t_{tobot}$). The top tether is modeled as a circular plate with a circular hole at the center which is clamped at its outer radius and guided at its inner radius, shown in Figure 4-6. It experiences a concentrated force, $F_{tetop}$, at its inner radius and a uniform pressure loading, $P_{ch}$. The shear force per unit length is given as:

$$Q(r) = \frac{F_{tetop}}{2\pi r} - \frac{P_{ch}(r^2 - b^2)}{2r} \tag{4.27}$$

The boundary conditions are:

$$w(r=a)=0 \tag{4.28}$$

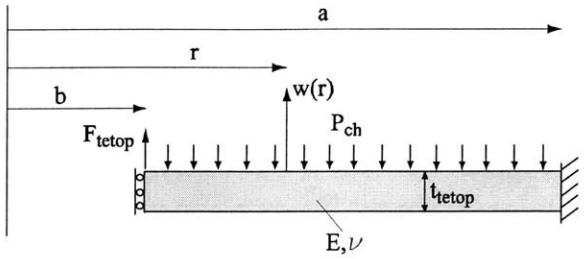


Figure 4-6: Model of the top tether: circular plate with a circular hole at its center with guided boundary condition at inner radius b and clamped boundary condition at outer radius a.

$$\frac{dw}{dr}(r = a) = 0 \tag{4.29}$$

$$\frac{dw}{dr}(r = b) = 0 \tag{4.30}$$

The deflection of the top tether and the corresponding swept volume can be calculated by integrating equation 4.7 and applying the boundary conditions to obtain:

$$x_{te} = k_{tt1}F_{tetop} + k_{tt2}P_{ch} \tag{4.31}$$

$$\Delta V_{te} = k_{tt3}F_{tetop} + k_{tt4}P_{ch} \tag{4.32}$$

where $k_{tt1}, k_{tt2}, k_{tt3}$,and, $k_{tt4}$ depend on the thickness of the top tether, $t_{tetop}$, inner radius ($b = D_{pis}/2$), and outer radius ($a = D_{ch}/2$).

Since the tethers are much thinner than the support structures and the piston, it is important to consider the stress in the tethers and make sure that they don't exceed the critical value of $1GPa$ [7]. For a circular plate subject to symmetrical bending, the two stress components can be calculated as:

$$\sigma_r = -\frac{6M_r}{h^2} \tag{4.33}$$

$$\sigma_t = -\frac{6M_t}{h^2} \tag{4.34}$$

where $M_r$ and $M_t$ are the bending moment per unit length along the circumferential sections of the plate and along the diametral section of the plate respectively, and $h$ is the thickness of the plate. The bending moments are obtained as:

$$M_r = -D\left(\frac{d^2w}{dr^2} + \frac{\nu}{r}\frac{dw}{dr}\right) \tag{4.35}$$

$$M_t = -D\left(\frac{1}{r}\frac{dw}{dr} + \nu\frac{d^2w}{dr^2}\right) \tag{4.36}$$

where $D$ is the flexural rigidity of the plate. Using the equations 4.33, 4.34, 4.35, 4.36, the stress components can be calculated after the governing plate equation 4.7 is integrated using appropriate boundary conditions and the deflection of the plate, $w$, is determined. As will be seen later in the next chapter, $\sigma_r$ is generally bigger than $\sigma_t$ and the maximum stress occurs at $a = D_{ch}/2$. Then we can write the maximum stress in the top tether as:

$$\sigma_{\max} = \sigma_{tt} = -\frac{6M_r(r = D_{ch}/2)}{t_{tetop}^2} \tag{4.37}$$

which can be alternatively expressed as:

$$\sigma_{tt} = s_{tt1}F_{tetop} + s_{tt2}P_{ch} \tag{4.38}$$

where $s_{tt1}$ and $s_{tt2}$ depend on the thickness of the top tether, $t_{tetop}$, inner radius ($b = D_{pis}/2$), and outer radius ($a = D_{ch}/2$).

The bottom tether is modeled in the same way as the top tether, except it experiences only a concentrated force, $F_{tebot}$, at its inner radius and no pressure loading. The shear force per unit length is:

$$Q(r) = \frac{F_{tebot}}{2\pi r} \tag{4.39}$$

The boundary conditions are the same as the boundary conditions for the top tether. The

deflection of the bottom tether, which is equal to the deflection of the top tether can be obtained by integrating equation 4.7 and applying the boundary conditions to obtain:

$$x_{te} = k_{tb} F_{tebot} \tag{4.40}$$

where $k_{tb}$ depends on the thickness of the bottom tether, $t_{tebot}$, inner radius ($b = D_{pis}/2$), and outer radius ($a = D_{ch}/2$).

Similarly, the stress in the bottom tether can be calculated as:

$$\sigma_{tb} = s_{tb} F_{tebot} \tag{4.41}$$

where $s_{tb}$ depends again on the thickness of the bottom tether, $t_{tebot}$, inner radius ($b = D_{pis}/2$), and outer radius ($a = D_{ch}/2$)

We can also write:

$$F_{te} = F_{tetop} + F_{tebot} \tag{4.42}$$

which represents the force balance at the connection point of the tethers with the piston.

Detailed derivations of the elastic equations of the structural components are detailed in Appendix C.

## 4.3 Simulation Architecture

This section will present the simulation architecture used for integrating the elastic equations into the system level simulation.

### Chamber Continuity

The continuity equation was derived in the previous chapter. In this section a more detailed equation will be derived considering the volume displaced in the chamber due to deformations of individual structural members. In the previous chapter, all the volume displaced by deformations was analyzed as a bulk value, namely $\Delta V_s$, and was used to define the structural compliance, $C_s$. Rewriting equation 3.5, we have:

$$\frac{dP_{ch}}{dt} = \frac{\beta_f}{V_o}\frac{dV}{dt} \tag{4.43}$$

where $\beta_f$ is the bulk modulus of the fluid, $V_o$ is the initial volume of the fluid inside the chamber and $\frac{dV}{dt}$ is the rate of the volume change of the fluid. Sources of the volume change are net flowrate into the chamber, piston movement and additional volume created inside the chamber due to structural deformations. Considering these effects and integrating equation 4.43, we can write:

$$P_{ch} = \frac{\beta_f}{V_o}\left(\int_0^t (Q_{in} - Q_{out})dt + \Delta V_{pis} + \Delta V_{pb} + \Delta V_{te} - \Delta V_{tp}\right) \tag{4.44}$$

where $\Delta V_{pis}, \Delta V_{pb}, \Delta V_{te}, \Delta V_{tp}$ represent the swept volume due to the motion of the piston, deformation of the piston, deformation of the top tether and deformation of the top support structure respectively. The swept volume due to the motion of the piston is simply equal to:

$$\Delta V_{pis} = x_{pis} A_{pis} \tag{4.45}$$

where $A_{pis}$ is the area of the piston. By arranging equation 4.44 we can obtain:

$$P_{ch} = \left(\frac{V_o}{\beta_f} + C_{tp}\right)^{-1}\left(\int_0^t (Q_{in} - Q_{out})dt + x_{pis}A_{pis} + \Delta V_{pb} + \Delta V_{te}\right) \tag{4.46}$$

where $C_{tp}$ represents the structural compliance corresponding to the deformation of the top support structure, which is given by equation 4.5.

### Piezoelectric Cylinder

For a cross-sectional area of $A_p$ and length $L_p$, the net deflection of the piezoelectric element and the voltage across it can be expressed using linear constitutive relationships as:

$$x_b - x_{pis} = \frac{L_p}{A_p}(s_{33}^D F_p + \frac{d_{33}}{\varepsilon_{33}^T} Q_p) \tag{4.47}$$

$$V_p = \frac{L_p}{A_p}(\frac{d_{33}}{\varepsilon_{33}^T} F_p - \frac{1}{\varepsilon_{33}^T} Q_p) \tag{4.48}$$

where $Q_p$ is the charge on the piezoelectric element.

Equations 4.13, 4.14, 4.19, 4.24, 4.25, 4.26, 4.31, 4.32, 4.38, 4.40, 4.41, 4.42, 4.44, 4.47, and 4.48 (15eqns) can be solved for the 15 unknowns, namely $V_p$, $x_{tp}$, $\Delta V_{tp}$, $\Delta V_{te}$, $\Delta V_{pb}$, $x_b$, $x_{te}$, $F_{te}$, $F_{te-top}$, $F_{te-bot}$, $\sigma_{tt}$, $\sigma_{tb}$, $F_p$, $P_{ch}$, and $F_{net}$ in terms of $Q_p, x_{pis}$, and $Q_{net}$ where

$$Q_{net} = \int_0^t (Q_{in} - Q_{out})dt \tag{4.49}$$

which represents the net fluid volume change inside the chamber due to the fluid flow into and out of the chamber [52]. The elastic equations along with the chamber continuity equation and piezoelectric element constitutive relationships are solved in Maple and the coefficients ($A_{11}$, $A_{12}$ ...) of the $15x3$ matrix required by the simulation architecture, shown in Figure 4-7, is calculated. The coefficients are then processed in a Matlab code to generate the $15x3$ matrix, which is fed to Simulink. The details are presented in Appendix B and Appendix C. The Simulink blocks of the system model are presented in Appendix A.

The matrix equation solved in Simulink is as follows:

$$\begin{bmatrix} V_p \\ x_{tp} \\ \Delta V_{tp} \\ \Delta V_{te} \\ \Delta V_{pb} \\ x_b \\ x_{te} \\ F_{te} \\ F_{te-top} \\ F_{te-bot} \\ \sigma_{tt} \\ \sigma_{tb} \\ F_p \\ P_{ch} \\ F_{net} \end{bmatrix} = \begin{bmatrix} A_{11} & A_{12} & A_{13} \\ A_{21} & A_{22} & A_{23} \\ A_{31} & A_{32} & A_{33} \\ A_{41} & A_{42} & A_{43} \\ A_{51} & A_{52} & A_{53} \\ A_{61} & A_{62} & A_{63} \\ A_{71} & A_{72} & A_{73} \\ A_{81} & A_{82} & A_{83} \\ A_{91} & A_{92} & A_{93} \\ A_{101} & A_{102} & A_{103} \\ A_{111} & A_{112} & A_{113} \\ A_{121} & A_{122} & A_{123} \\ A_{131} & A_{132} & A_{133} \\ A_{141} & A_{142} & A_{143} \\ A_{151} & A_{152} & A_{153} \end{bmatrix} \begin{bmatrix} Q_p \\ x_{pis} \\ Q_{net} \end{bmatrix} \tag{4.50}$$

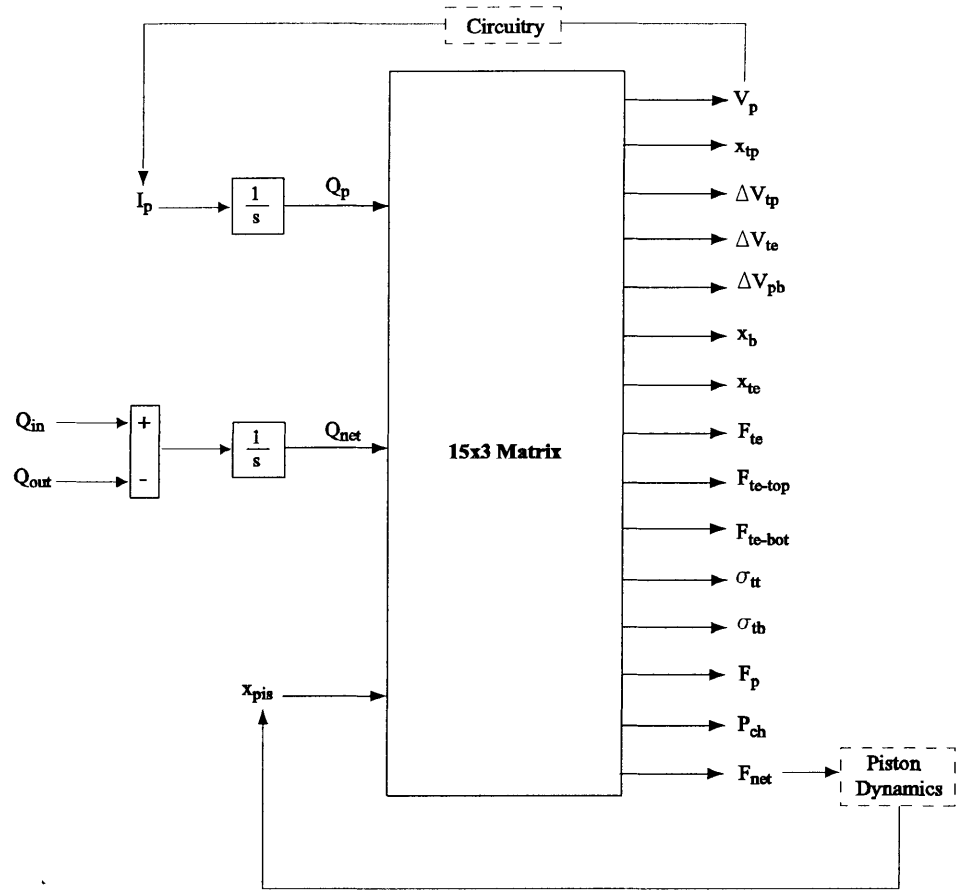


Figure 4-7: Simulation architecture used to integrate the elastic equations into system level simulation.

where the matrix coefficients are calculated using Maple.

The simulation architecture allows for integration of the elastic equations into the dynamic simulations as well as for monitoring important parameters like deflections and swept volumes of the individual structural components and stresses in the tethers.

## 4.4 Conclusion

This chapter presented detailed analysis of the energy harvesting chamber in terms of the deformations of individual structural components. The deformations are analyzed using linear plate theory. It is assumed that the deflections due to bending are significantly larger than those due to shearing. A simulation architecture is presented to be included in the overall system level simulation, which allows for inclusion of the elastic equations into the dynamic simulation and allows for monitoring important parameters.

# Chapter 5

# Further Design Considerations and Design Procedure

This chapter presents further design considerations in addition to those issues discussed in Chapter 3. These are fluidic oscillations within the system, chamber filling and evacuation, tether structure optimization and the effect of operation conditions and geometry on system performance. At the end of the chapter, a design procedure along with two design examples and simulation results will be presented. The system is analyzed only for the case where the chamber is attached to the regular bridge.

## 5.1 Further Design Considerations

### 5.1.1 Fluidic Oscillations

Inertial effects should be considered when designing hydraulic systems containing small channels. In fact, in the MHT devices, the fluid channels and the main chamber constitute a resonating system similar to a Helmholtz resonator, shown in Figure 5-1, which comprises a fluid channel and a chamber with an effective compliance $C$. The natural frequency of the Helmholtz resonator can be calculated by considering the free-body diagram of the fluid slug within the channel. The equation of motion of the fluid slug can be written as:

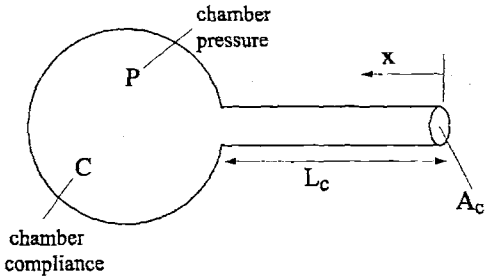


Figure 5-1: Helmholtz Resonator.

$$\rho A_c L_c \frac{d^2x}{dt^2} + PA_c = 0 \tag{5.1}$$

where $P$ is the pressure inside the chamber which builds up as a result of the additional fluid flow into the chamber, which can be expressed as:

$$P = \frac{A_c x}{C} \tag{5.2}$$

Combining equations 5.1 and 5.2 we can obtain the governing equation for the Helmholtz resonator as:

$$\ddot{x} + \left(\frac{A_c}{\rho C L_c}\right) x = 0 \tag{5.3}$$

The natural frequency of the resonator can be easily obtained from equation 5.3:

$$\omega_n = \sqrt{\frac{A_c}{\rho C L_c}} \tag{5.4}$$

We can conclude that the natural frequency of the oscillations similar to Helmholtz resonator within the system depends on the channel geometry($\frac{L_c}{A_c}$ ratio), the compliance of the chamber and the density of the working fluid. The chamber compliance here refers to the overall chamber, including the compression of the piezoelectric element. In Chapter 3, an effective chamber compliance, $C_{eff}$, was defined which took only the structural deformations and fluid compression into account, but not the compression of the piezoelectric element. In the context of this discussion, it is convenient to define an overall chamber compliance, $C$, which includes

the structural deformations, fluid compression, and the deformation of the piezoelectric element. The overall chamber compliance in this case can be defined as:

$$C = \frac{\Delta V_f}{\Delta P_{ch}} = \frac{\int (Q_{in} - Q_{out}) dt}{\Delta P_{ch}} \tag{5.5}$$

where $\Delta V_f$ is the fluid volume change in the chamber due to the fluid flow. In fact, this compliance is not a constant value in the actual power generator since the stiffness of the piezoelectric element changes constantly (the stiffness flips between open-circuit and close-circuit stiffnesses of the piezoelectric element) during the operation, as discussed in Chapter 2 and Chapter 3. In the following two subsections, the fluidic oscillations will be analyzed for two cases. In the first case, a constant overall chamber compliance will be assumed for simplicity and in order to get insight, and in the second case the actual system, i.e. the chamber attached to the rectifier circuit will be analyzed in terms of fluidic oscillations.

### Analysis with Constant Overall Chamber Compliance

Consider a chamber with constant overall chamber compliance, $C = 10^{-17}[m^3/Pa]$, as defined in equation 5.5. Figure 5-2 shows the simulation of the system for different chamber geometries, i.e. for different $L_c/A_c$ ratios. In the simulation, the operation conditions, valve size and openings are adjusted such that the chamber pressure fluctuates between $P_{HPR}$ and $P_{LPR}$ for the case where the inertial effects in the channels are negligible. These conditions are: $P_{HPR} = 2MPa$, $P_{LPR} = 0$, $f = 10kHz$, $R_{vc} = 200\mu m$, $vo_{in} = vo_{out} = 20\mu m$, and the working fluid is silicon-oil.

It can be see that there exists an optimum $L_c/A_c$ value for which the difference between the maximum and minimum pressures, i.e. the pressure band, $\Delta P_{ch}$, is maximum. This value is approximately $25000(1/m)$. The pressure band is not very sensitive to $L_c/A_c$ around the optimum value, i.e. $L_c/A_c = 24000$ or $L_c/A_c = 26000$ results pretty much in the same pressure band. In fact, the optimum value of the $L_c/A_c$ can be approximated using equation 5.4. Figure 5-3 shows the inlet flowrate time histories from the simulation. It can be seen that, the fluid inductance in the channel causes the flow to lag, i.e. the flowrate reaches its maximum at a later time compared to the case where the fluid inductance is negligible.

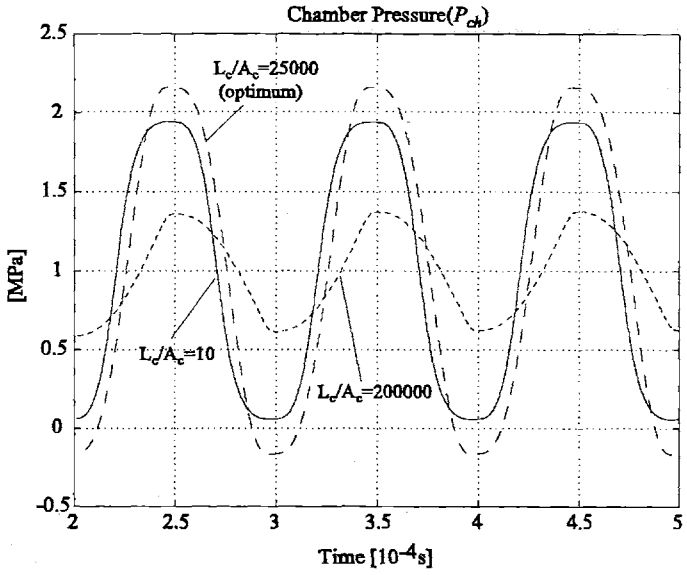


Figure 5-2: Simulation of the chamber with constant overall compliance for different channel geometries.

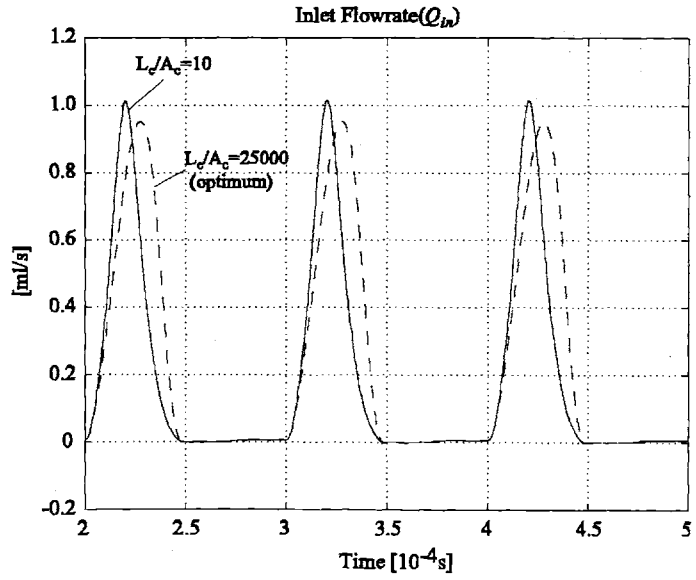


Figure 5-3: Comparison of flowrate time histories for different L/A ratios.

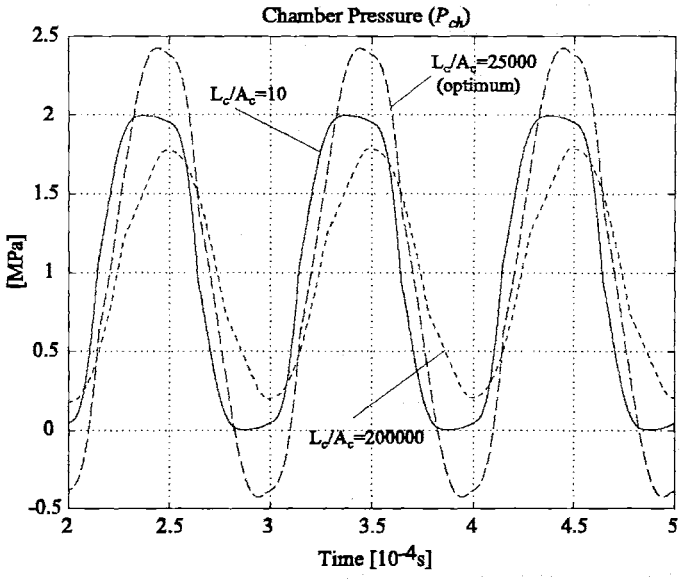


Figure 5-4: Simulation of the chamber attached to circuitry for different channel geometries.

### Analysis of the chamber attached to circuitry

Consider the chamber geometry, effective compliance and operation conditions presented in Table 3.2 of Chapter 3. Figure 5-4 shows the simulation of the same geometry for different $L_c/A_c$ ratios. Again, the valve size and opening is adjusted such that the chamber pressure fluctuates between $P_{HPR}$ and $P_{LPR}$ for the case where the inertial effects in the channels are negligible. These conditions are: $P_{HPR} = 2MPa$, $P_{LPR} = 0$, $f = 10kHz$, $R_{vc} = 200\mu m$, $vo_{in} = vo_{out} = 20\mu m$, the working fluid is silicon-oil, and the battery voltage, $V_b$, is $90V$, which is optimized for a pressure band of $2MPa$. Similar to the case where a constant overall chamber compliance was assumed, there exists an optimum $L_c/A_c$ value for which the difference between the maximum and minimum pressures, i.e. the pressure band, $\Delta P_{ch}$, is maximum.

Figure 5-5 shows the effect of $L_c/A_c$ ratio on pressure band and generated power. Throughout the simulations the battery voltage was not changed. In fact, in a design, the battery voltage should be determined according to the expected pressure band, which determines the stress band on the piezoelectric element. For example, for the optimum $L_c/A_c$ ratio, the pressure band is $2.435MPa$, which suggests a battery voltage of approximately $125V$. If the simulation is repeated with this value, the pressure band is now $2.472MPa$, which is slightly different than

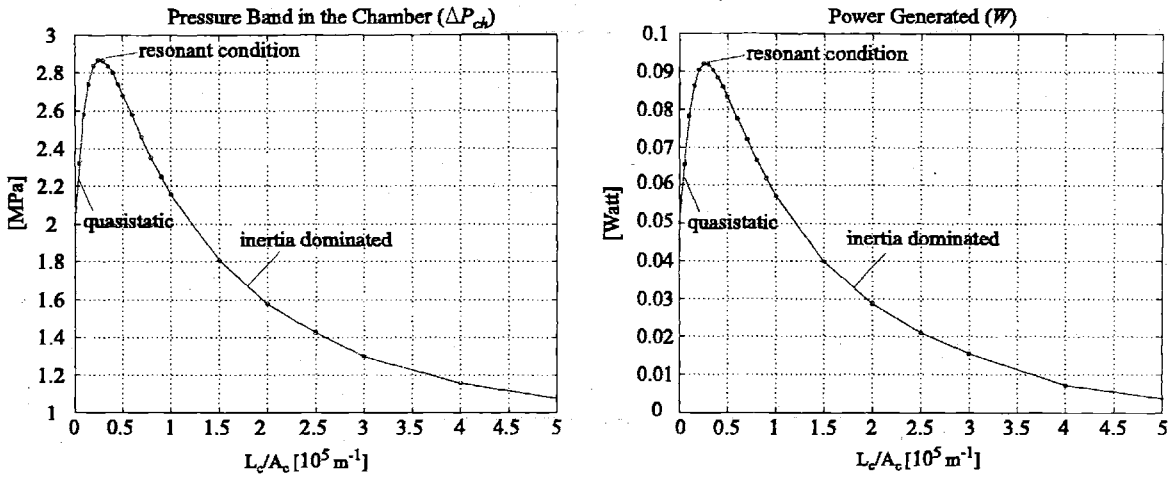


Figure 5-5: Effect of L/A ratio on pressure band and generated power.

the previous value, and the generated power is $0.1068W$. The slight change in the pressure band suggests that the change in the battery voltage caused a small change in the overall chamber compliance, because it basically determines the voltage level where the piezoelectric element will change its stiffness, and therefore effects the time intervals in which the piezoelectric element posses the different stiffnesses. The expression for the optimum battery voltage was given in Chapter 2 as:

$$V_b = \frac{1}{4}\frac{\Delta\sigma(s_{33}^E - s_{33}^D)L_p}{d_{33}} \tag{5.6}$$

which can be written in terms of the pressure band in the chamber as:

$$V_b = \frac{1}{4}\frac{\Delta P_{ch} A_{pis}}{A_p}\frac{(s_{33}^E - s_{33}^D)L_p}{d_{33}} \tag{5.7}$$

where $A_{pis}$ and $A_p$ are the piston area and the cross-sectional area of the piezoelectric cylinder respectively, and $\Delta\sigma$ is the stress band on the piezoelectric element. It should be noted that, when writing equation 5.7 the effect of tethers and piston dynamics is neglected. In other words, static force balance between the piston and piezoelectric element is assumed and the force applied by the tethers on the piston is neglected. This issue will be addressed later.

We can conclude that, for a given overall chamber compliance there exists an optimum $L_c/A_c$ ratio at a certain operation frequency, or similarly, there exists an optimum operation

frequency for a certain overall compliance and $L_c/A_c$ ratio. The fluidic oscillations should be considered in any design procedure and the channels should be designed accordingly. This will be addressed later in the discussion of the design procedure.

The overall chamber compliance was defined as the compliance of the chamber including the compliances due to structural deformations and fluidic compliance, which is represented by the effective compliance, $C_{eff}$, and the compliance due to the deflection of the piezoelectric element. The compliance due to the deflection of the piezoelectric element can be calculated considering the volume displaced by the piston due to the deflection of the element as a response to the pressure change in the chamber:

$$C_p = \frac{\Delta V_{pis}}{\Delta P_{ch}} = \frac{\Delta x_p A_{pis}}{\Delta P_{ch}} = \frac{\left(\frac{\Delta P_{ch} A_{pis}}{k_p}\right) A_{pis}}{\Delta P_{ch}} = \frac{A_{pis}^2}{k_p} \tag{5.8}$$

where $k_p$ is the stiffness of the piezoelectric element, which can be expressed as:

$$k_p = \frac{A_p}{s_{33} L_p} \tag{5.9}$$

where $A_p$ and $L_p$ are the cross-sectional area and the length of the piezoelectric element respectively, and $s_{33}$ is the compliance coefficient of the element. As mentioned earlier, the stiffness of the piezoelectric element changes constantly during the operation between the open circuit and closed circuit stiffnesses, which should be calculated using $s_{33}^D$ and $s_{33}^E$ respectively. Therefore the system is highly nonlinear and it is impossible to express the resonant frequency, or the optimum $L_c/A_c$ ratio analytically. However we can get a first order estimation of the resonant frequency using one of the stiffnesses above. For example using the open circuit compliance coefficient, $s_{33}^D$, and from equations 5.4, 5.8, and 5.9 we obtain:

$$f_n = \frac{1}{2\pi}\sqrt{\frac{A_c}{L_c \rho \left(C_{eff} + C_p\right)}} = \frac{1}{2\pi}\sqrt{\frac{A_c}{L_c \rho \left(\frac{V_o}{\beta_f} + C_s + \frac{s_{33}^D L_p A_{pis}^2}{A_p}\right)}} \tag{5.10}$$

where $C_{eff}$ is the effective chamber compliance.

It is very important to note that in the simulations presented in this and the previous

sections (Figures 5-2 and 5-4), the pressure in the chamber overshot the reservoir pressures ($P_{HPR}$ and $P_{LPR}$) in the resonance conditions, which resulted in negative pressures, which should be avoided because of cavitation. In the design procedure, the operation conditions should be adjusted such that there won't be any cavitation. For example the system can be biased, i.e. the reservoir pressures can be increased keeping the difference the same. Or, the valve openings can be adjusted accordingly. The motivation for operating at resonance condition is that the same pressure band can be achieved with smaller valve cap sizes or valve openings compared to the case of negligible or very large fluid inductance in the channels, resulting in reduced power consumption in the active valves.

### 5.1.2 Chamber filling and evacuation

In order to attain the desired pressure bands inside the chamber, it is important to design the valve sizes, openings and the operation frequency accordingly. Consider the chamber attached to the circuitry discussed in the previous section. Figure 5-6 shows the effect of valve opening on pressure band in the chamber. A valve opening of $20\mu m$ provides perfect filling and subsequent evacuation of the chamber in the required time interval and the chamber pressure fluctuates between the reservoir pressures. A small valve opening of $5\mu m$ results in poor(slow) filling and evacuation, resulting in a reduced pressure band. A large valve opening of $50\mu m$ provides very fast filling and evacuation, which causes the chamber pressure to retain its maximum and minimum values for long time intervals. The latter results in the same power generated, however it also results in more power consumption in the active valves due to the higher stroke. A similar result would be obtained by keeping the valve opening the same, but increasing the valve cap size. Again more power would be consumed in the active valves.

Figure 5-7 shows the effect of operation frequency on the pressure band in the chamber. It can be seen that, for a fixed valve opening, different operation frequencies result in system behaviors similar to the ones in Figure 5-6. At high frequency, there is not enough time for the valve to fill and evacuate the chamber in the required time interval. Similarly, at low frequency, there is more than enough time for the valves to fill and evacuate, which results in similar behavior to the case of large valve opening. This implies that, the valve opening can be reduced for reduced power consumption in the active valve and yet the same power can be

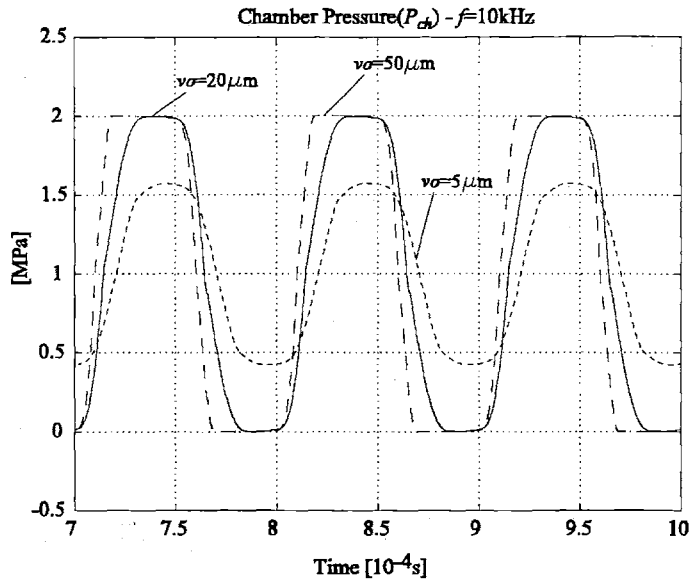


Figure 5-6: Effect of valve opening on the pressure band in the chamber.

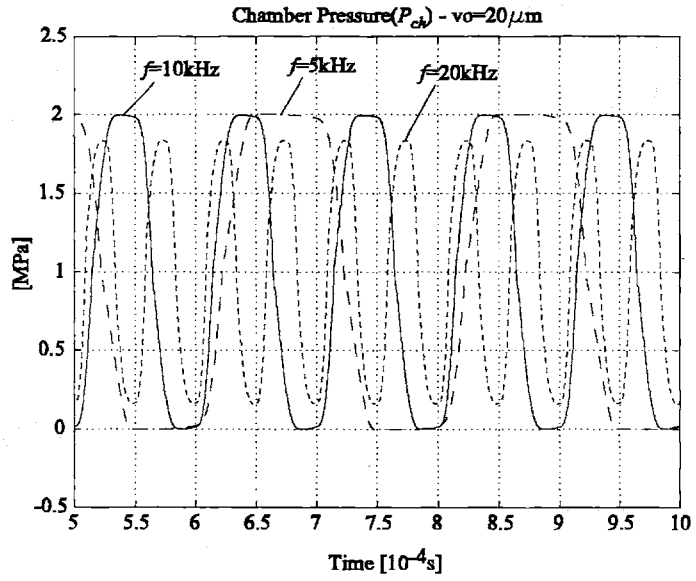


Figure 5-7: Effect of operation frequency on the pressure band in the chamber.

generated as long as the pressure band in the chamber is kept at the desired level.

In the two cases analyzed above, the valve cap size could be analyzed instead of valve opening, which would lead to the same conclusions. The combination of the valve size and the valve opening define the overall valve resistance. We can conclude that, for a designed operation frequency and pressure band, it is important to design the valve size and opening such that they will provide just enough filling and evacuation of the chamber in the required time interval, which is defined by the operation frequency, so that the chamber pressure fluctuates between the reservoir pressures in the most economical way. As will be addressed later, the pressure band is a very important design parameter, since the power generated is proportional to the square of the stress band on the piezoelectric element. Additional design considerations concerning the design of the valve size and opening is not within the scope of this thesis. The design optimization of the active valves is detailed in [5].

### 5.1.3 Tether Structure Optimization

Design of the piston tether structure is very crucial for system operation. The tethers should be flexible enough to allow sufficient motion of the piston, yet stiff enough to avoid introduction of excessive compliance into the system. The tethers have to be designed to allow maximum piezoelectric element compression for a given net fluid volume into the chamber, which occurs basically at every cycle during system operation. To analyze the tether structure, consider a simple hypothetical chamber which consists of a fluid chamber with rigid walls, a single layer piston attached to the wall with a single tether providing sealing, and a piezoelectric element. Figure 5-8 illustrates the hypothetical chamber and different tether designs. Figure 5-8(b) illustrates a good tether design where the tethers allow large piezoelectric element compression. Figure 5-8(c) illustrates a poor design where the tether is either too thin or the tether width, $t_w$, is very large ($t_w = [D_{ch} - D_{pis}]/2$). This results in low pressure in the chamber and small compression of the piezoelectric element since the compliance introduced by the tether is very large. In other words, pressure doesn't built up inside the chamber because of the excessive bending of the tether. Figure 5-8(d) illustrates another poor design where the tether is either too thick or the tether width, $t_w$, is very small. In this case the pressure in the chamber is high but the compression of the piezoelectric element is still very small since the very stiff tethers

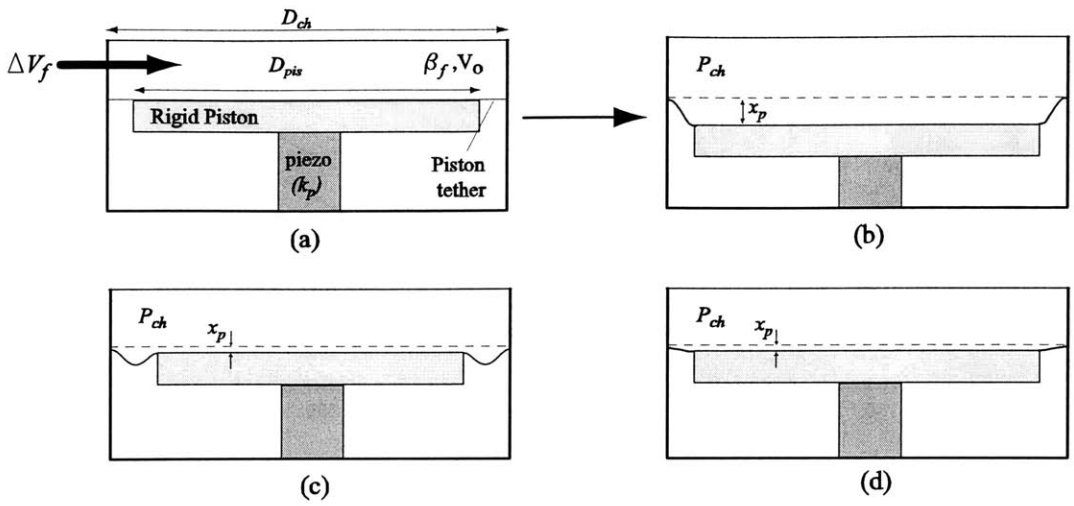


Figure 5-8: (a) Schematic illustrating the hypotethical chamber (b) good tether design providing large piezoelectric element compression (c) poor tether design, either too thin or large width, resulting in low chamber pressure and small piezoelectric element compression (d) poor tether design, either very thick or small width, resulting in large pressures but small piezoelectric element compression.

do not allow the piston to move although they introduce very small additional compliance into the system. This suggests that for a design where the chamber diameter(or piston diameter) is determined, the tether structure has to be optimized in conjunction with fabrication limitations, such as thickness of the tether, which is determined by the SOI wafer, or the maximum tether width which can be etched.

Consider a chamber of the following geometric parameters: $D_{ch} = 5mm$, $D_p = 1mm, L_p = 1mm$, and $H_{ch} = 200\mu m$. An additional fluid volume, $\Delta V_f = 10^{-11}m^3$, is introduced into the chamber. Figure 5-9 shows piston deflection/piezoelectric element deflection, pressure in the chamber and the compliance of the chamber for different tether thicknesses and widths. The tether width is varied by keeping the chamber diameter the same and changing the piston diameter. Since the tether width is very small compared to chamber or piston diameter, it doesn't matter which parameter is kept constant, i.e. the the piston diameter could be kept constant and the chamber diameter could be varied alternatively. Thus we can generalize this study for a nominal chamber diameter of $5mm$. It can be seen that for a tether thickness, there exists a range of values for tether widths where maximum deflection of the piston occurs. It

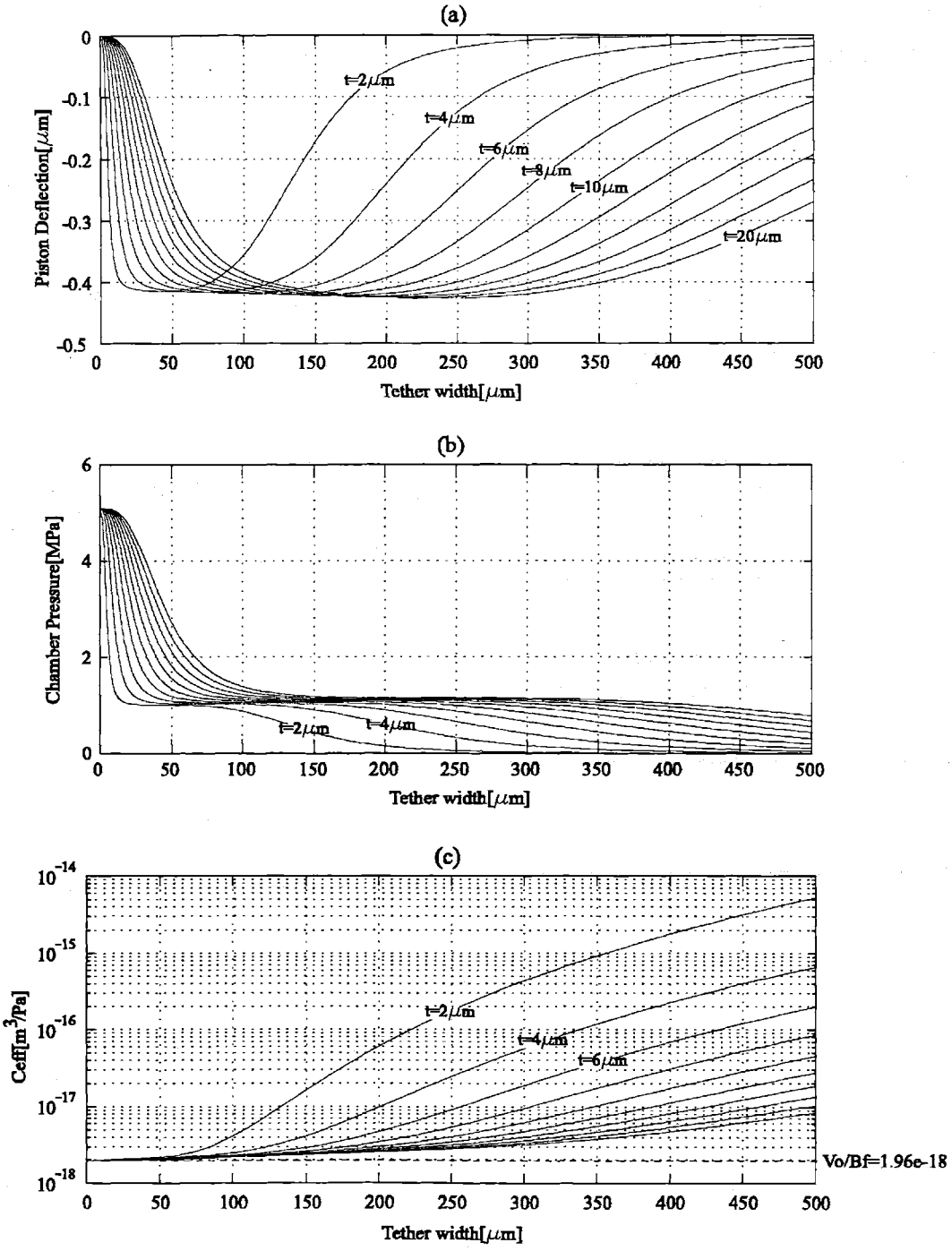


Figure 5-9: (a) Piston deflection for different tether thicknesses and widths,(b) corresponding pressures in the chamber (c) compliance of the chamber. The dashed line corresponds to the hypotethical case where piston diameter is equal to chamber diameter and there is perfect sealing.

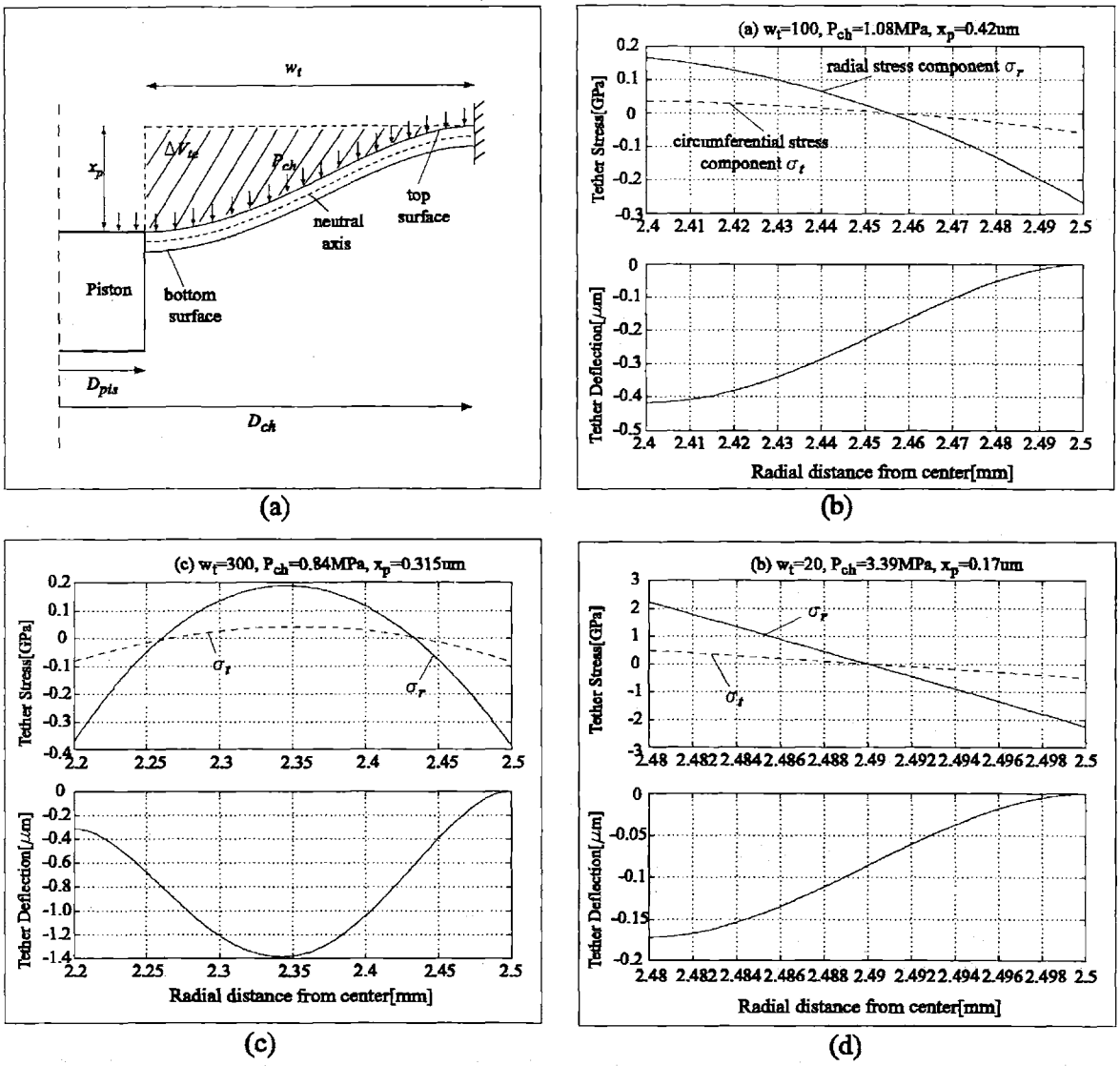


Figure 5-10: (a) Schetch illustrating tether deflection. (b),(c),and (d) show the stress components on the bottom surface and deflected shape of the tether for 3 different cases.(b) good tether design, (c) poor tether design where the tether is too compliant, and (d) poor tether design where the tether is too stiff.

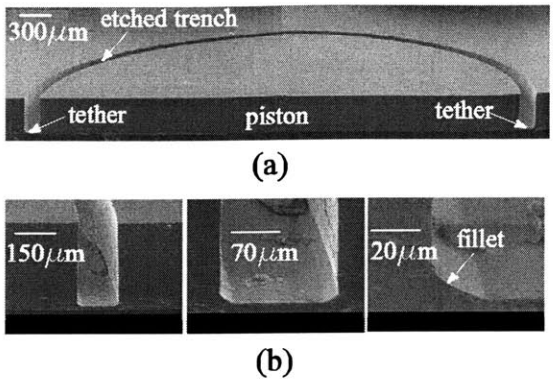


Figure 5-11: (a) SEM picture of micromachined piston structure [7](b)detailed view of the tether and the fillet.

can be also seen that for those values, the additional compliance introduced by the tethers is negligible.

Figure 5-10 illustrates the stresses and deflected shapes of the tether with a thickness of $10\mu m$ for three different cases. Figure 5-10(b) illustrates a good design where the tether width is optimized. Figure 5-10(c) illustrates a poor design where the tether width is very large and therefore the pressure in the chamber and piston deflection are small. Figure 5-10(d) illustrates another poor design where the tether width is small and therefore the tether is very stiff, which results in small piston deflection even though the pressure built up in the chamber is high. It can be also seen that the stresses in this case are very large compared to the previous two cases.

It should be noted that linear plate theory is used for this analysis which means that the neutral axis coincides with the central axis of the tether. In general, in a well-designed tether structure, the bottom surface of the tether experiences compressive stress near the chamber wall and tensile stress near the piston, which is the case in Figure 5-10(b), and the maximum stress occurs at the point where the tether is attached to the wall. The top surface experiences stresses with opposite signs.

It is also very important to consider the effect of the fillet on the stress and to note that the stresses calculated from the linear plate theory should be corrected using the proper stress concentration factor. However the stresses calculated using linear theory give a reasonable estimate and provide first order prediction about stresses during the design procedure. A

detailed study of the fillet radius and stress concentration factors can be found in [7]. A fabricated piston structure and the fillets are shown in Figure 5-11.

### 5.1.4 Operation Conditions and Trade-offs

In most of the analysis performed so far the basic parameters of the chamber, such as chamber diameter, and operation conditions such as reservoir pressures and operation frequency were fixed. This section will discuss how to choose chamber geometry and operation conditions for a given power requirement and will discuss trade-offs between operation conditions. The general design guidelines can be summarized as follows:

- The operation frequency should be kept as small as possible due to the bandwidth limitations imposed by the active valve structure,

- The flowrate should be kept as small as possible to minimize valve size and reduce power consumption in the valves,

- The maximum pressure in the chamber should be kept as small as possible in order to avoid high stresses in the tethers and active valve membranes.

For the analysis of this section, a relatively simple chamber structure will be assumed, namely the effect of the tethers, the deformation of the piston, and the deformation of the bottom plate will be ignored. This means that the effective compliance will be comprised of the fluidic compliance and structural compliance only due to the deflection of the top support structure. These assumptions are done for simplification of the analysis without loss of generality.

Fixed geometric parameters in this analysis are: chamber height, $H_{ch} = 200\mu$, length of piezoelectric element, $L_p = 1mm$, and top support structure thickness, $t_{top} = 1mm$. For each design point considered, piston area and cross-sectional area of the piezoelectric element satisfy the following relationship.

$$A_{pis} = \frac{\sigma_d A_p}{P_{HPR}} \tag{5.11}$$

which represents the static force balance between the piston and the piezoelectric element. The areas of the piston and the piezoelectric element are designed such that maximum stress on the piezoelectric element is equal to the depolarization stress, $\sigma_d$, for maximum power output.

It is assumed that the maximum and minimum pressures attained in the chamber are equal to the high and low pressure reservoirs respectively, where $P_{LPR}$ is assumed to be zero for simplicity.

### Required operation frequency for a given power requirement

The required frequency in order to generate a certain amount of power, $W$, for the case of the chamber attached to regular diode bridge is given by:

$$f = \frac{4W}{(s_{33}^E - s_{33}^D)\sigma_d^2 A_p L_p} \tag{5.12}$$

where $s_{33}^E$ and $s_{33}^D$ are the closed circuit and open circuit compliances of the piezoelectric element respectively. Figure 5-12 compares different piezoelectric materials in terms of required frequency for a $0.5W$ power requirement at different chamber diameters and reservoir pressures. It can be seen that, $PZT-4S$ and $PZT-8$ require lower frequencies because of their very high depolarization stress, even though they have smaller coupling coefficients compared to $PZT-5H$ and $PZN-PT$. It should be noted that, the required frequency does not depend on the chamber compliance, as can be seen from equation 5.12.

It is important to note that there is a trade-off between the maximum chamber pressure($P_{HPR}$) and the operation frequency. For lower chamber pressures, higher operation frequencies are needed. In fact, for a given piston diameter the required frequency is inversely proportional to the reservoir pressure, as can be easily seen from equations 5.11 and 5.12. It can be also seen that, for larger chamber diameters, the required operation frequency is smaller since for larger chamber diameters, piezoelectric elements having larger diameter are used to satisfy equation 5.11, which results in lower frequency requirement due to the increased piezoelectric element volume.

### Required flowrate for a given power requirement

The required flowrate is given by the following equation, which was derived in Chapter 3:

$$Q = \frac{2(s_{33}^E + s_{33}^D)W}{(s_{33}^E - s_{33}^D)P_{HPR}} + C_{eff}P_{HPR}f \tag{5.13}$$

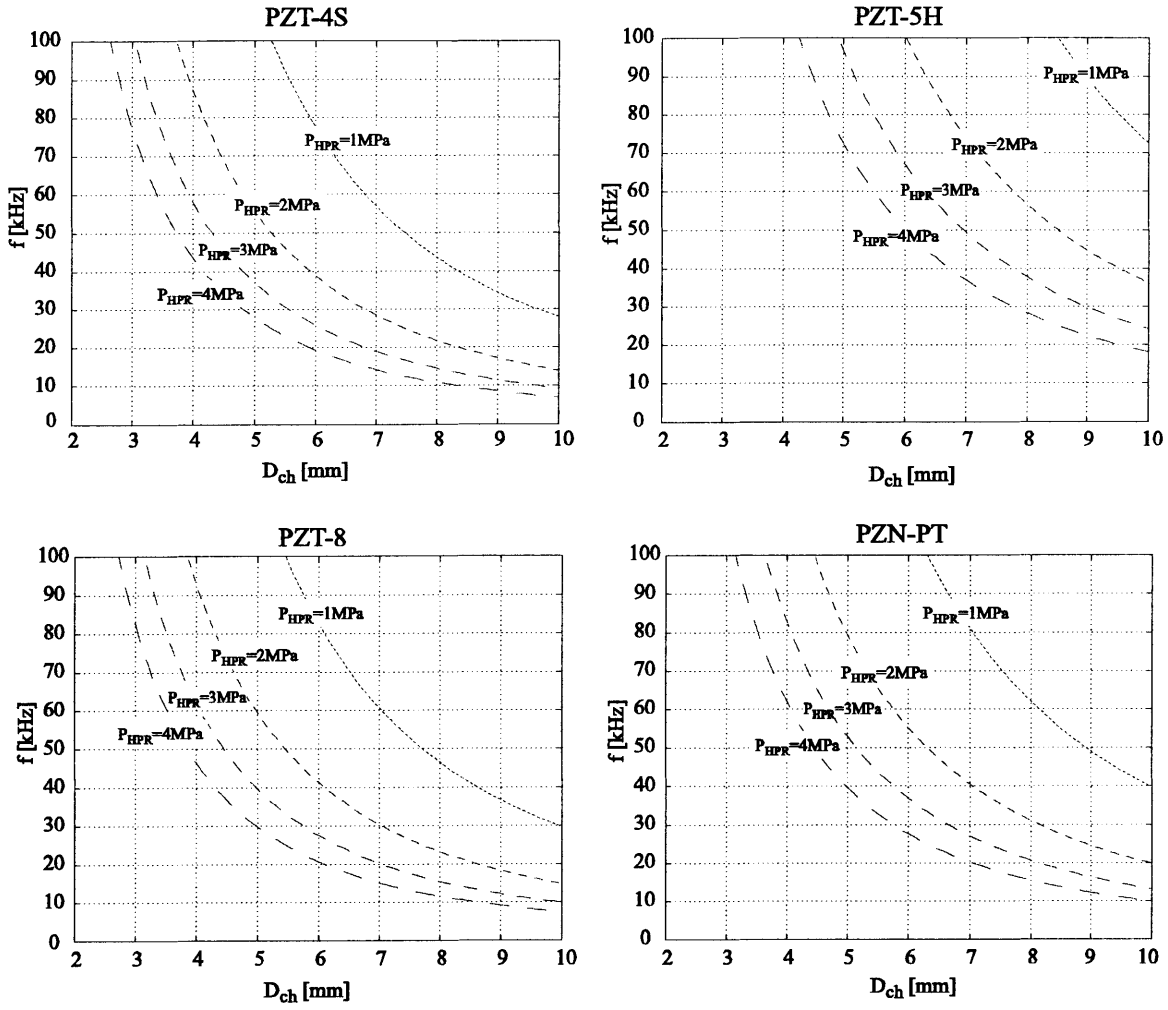


Figure 5-12: Comparison of different piezoelectric materials in terms of required operation frequency at different chamber diameters for a power requirement of 0.5W.

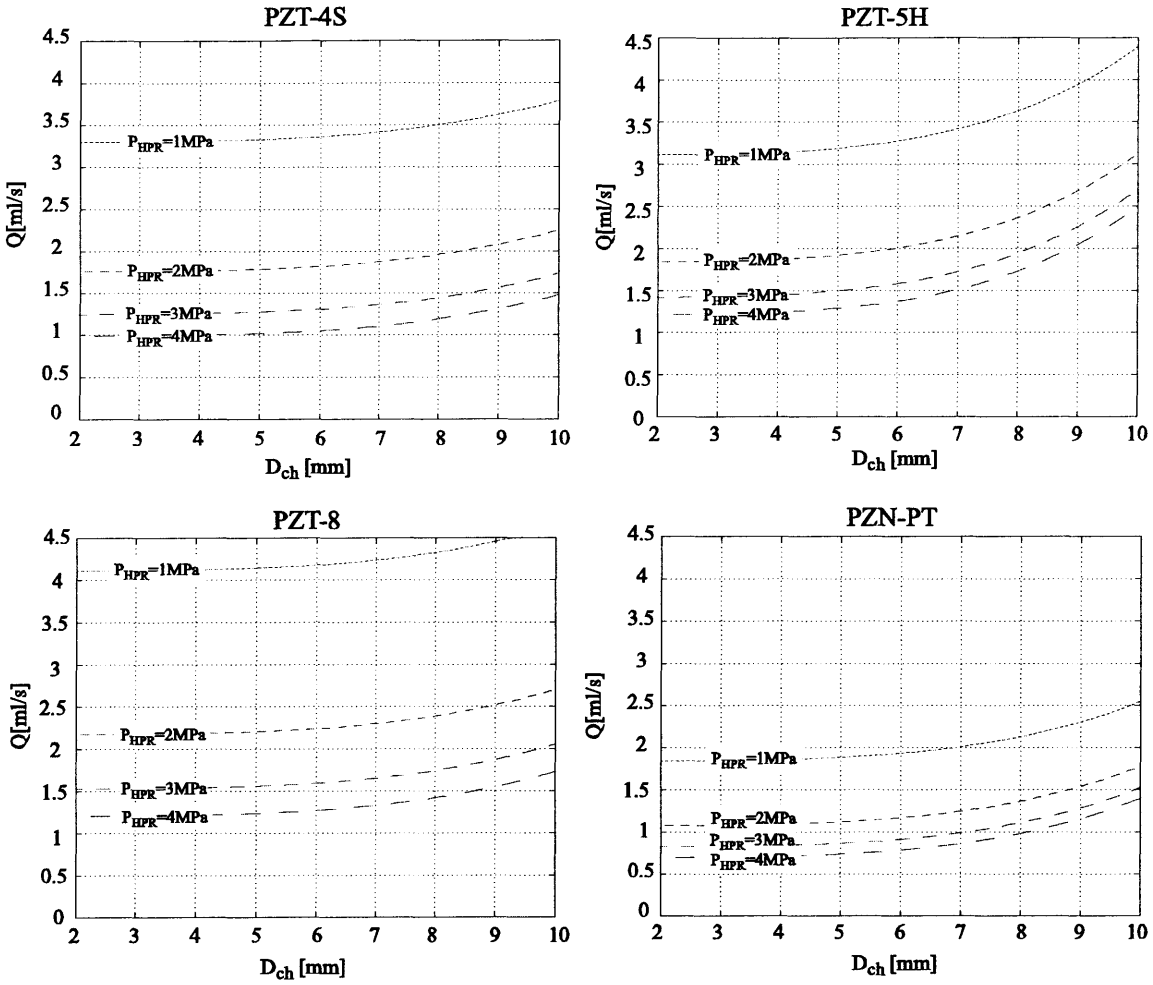


Figure 5-13: Comparison of different piezoelectric materials in terms of required flowrate at different chamber diameters for a power requirement of 0.5W.

where $f$ is the required operation frequency corresponding to the power requirement at the particular chamber diameter and reservoir pressure, as discussed in the previous subsection. Figure 5-13 shows a comparison of different piezoelectric materials in terms of required flowrate at different reservoir pressures and chamber diameters.

It can be seen that $PZN-PT$ requires the least flowrates due to its high coupling coefficient, which translates into higher system efficiencies as discussed in Chapter 3. It can be also noted that, for larger chamber diameters, higher flowrates are required. This can be explained by considering equation 5.13. There are in fact two competing effects. For larger chamber diameters, lower frequencies are needed, as shown in Figure 5-12, which suggest lower flowrates. However, larger chamber diameters result in increased chamber compliance, which is the dominating factor resulting in higher flowrates.

In this case, a trade-off exists between the required flowrate and maximum chamber pressure, namely for lower chamber pressures, higher flowrates are required.

### Efficiency

The efficiency of the system is given by:

$$\eta = \frac{W}{QP_{HPR}} \tag{5.14}$$

where the power consumption in the active valves is not considered. Figure 5-14 shows a comparison of different piezoelectric elements in terms of system efficiency for different reservoir pressures and chamber diameters. It can be seen that $PZN-PT$ provides the most efficient power generation due to its high coupling coefficient. For larger chamber diameters, the efficiency is lower due to the fact that the flowrate is higher at larger chamber diameters, as shown in Figure 5-13. It is also important to note that the efficiency decreases as the reservoir pressure increases. This can be explained considering equations 5.11, 5.12 and 5.13. Combining these equations we get:

$$Q = \frac{2(s_{33}^E + s_{33}^D)W}{(s_{33}^E - s_{33}^D)P_{HPR}} + \frac{4C_{eff}W}{(s_{33}^E - s_{33}^D)\sigma_d A_{pis} L_p} \tag{5.15}$$

which is the explicit form of equation 5.13. Using equation 5.14 we get:

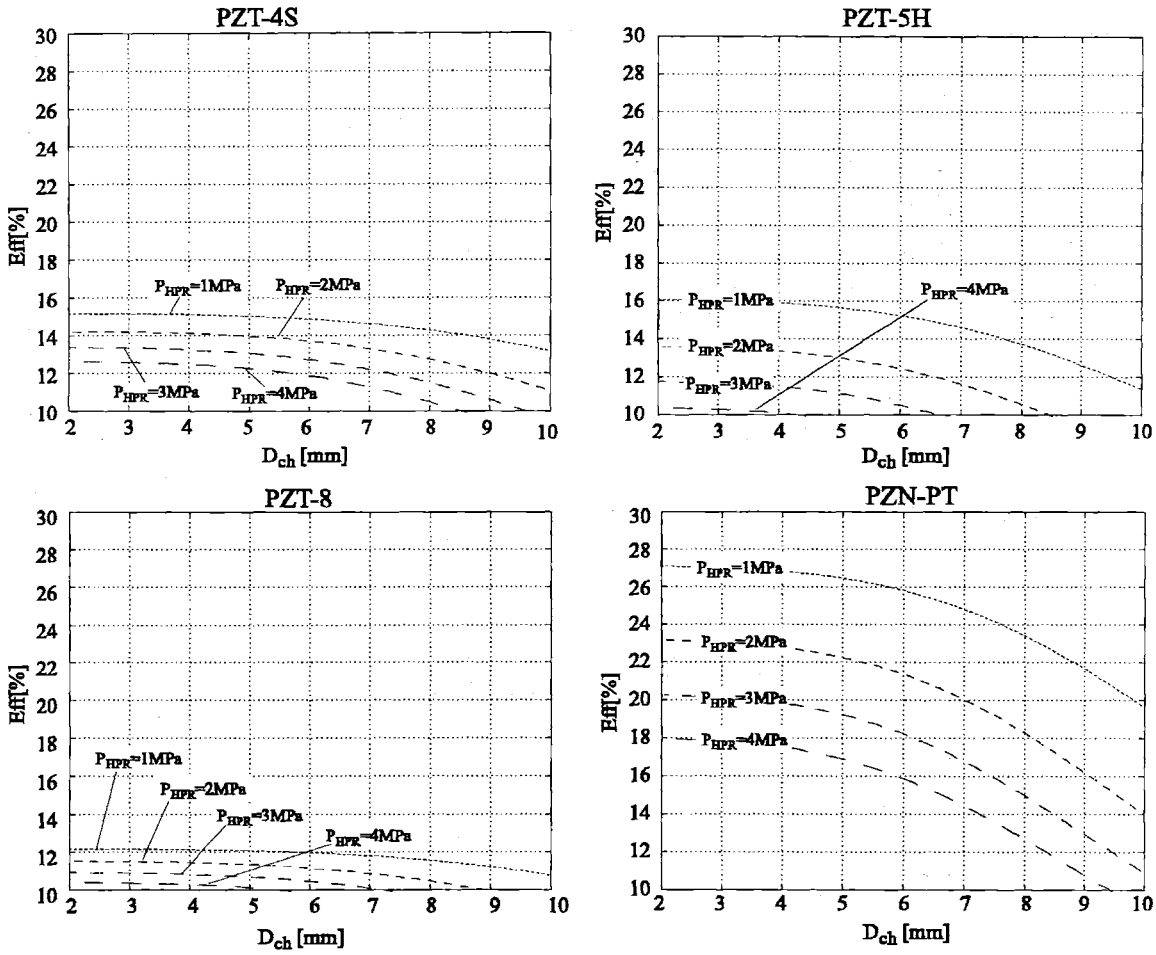


Figure 5-14: Comparison of different piezoelectric elements in terms of system efficiency for different reservoir pressures and chamber diameters.

$$\eta = \frac{W}{QP_{HPR}} = \left( \frac{2(s_{33}^E + s_{33}^D)}{(s_{33}^E - s_{33}^D)} + \frac{4C_{eff}P_{HPR}}{(s_{33}^E - s_{33}^D)\sigma_d A_{pis} L_p} \right)^{-1} \tag{5.16}$$

from which it can be easily seen that at a certain chamber diameter, the efficiency decreases with increasing reservoir pressure. It is also possible to observe that efficiency does not depend on the generated power.

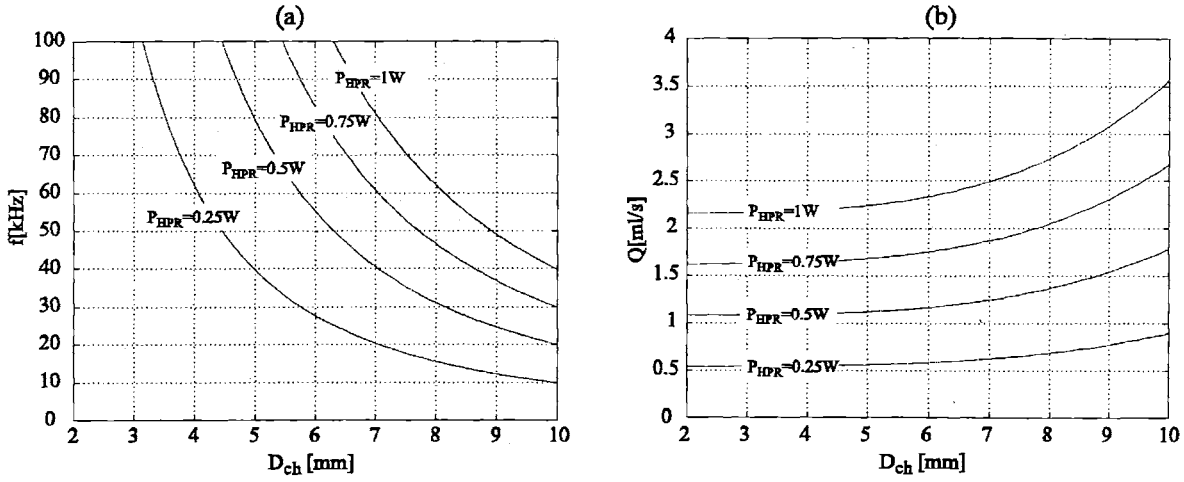


Figure 5-15: Required operation frequency and flowrate for different power requirements at different chamber diameters ($P_{HPR} = 2MPa$, piezoelectric material: $PZN - PT$ ).

#### Effect of power requirement

As can be seen from equations 5.12 and 5.16, the required operation frequency and flowrate are directly proportional to the generated power. Figure 5-15 illustrates the effect of power requirement on frequency and flowrate for the case where $P_{HPR} = 2MPa$ and piezoelectric material: $PZN - PT$.

### 5.1.5 Bias Pressure

As discussed in section 5.1.1, negative pressure in the chamber should be avoided due to cavitation. Even though the chamber is designed for positive pressure fluctuations, cavitation could occur due to unexpected fluidic resonances. Also the active valve design imposes minimum pressure requirements for the low pressure reservoir due to cavitation considerations inside the hydraulic amplification chamber. For a conservative design, the chamber pressure can be biased by a certain amount, by keeping the pressure differential $P_{HPR} - P_{LPR}$ the same, aiming for the same power as would be generated with $P_{LPR} = 0$. However, since the depolarization stress of the piezoelectric element cannot be exceeded, the effective stress band reduces, even though the pressure band remains the same. For the case where $P_{LPR} = 0$, the stress band, i.e. the difference between the maximum and minimum stress on the piezoelectric element is equal to

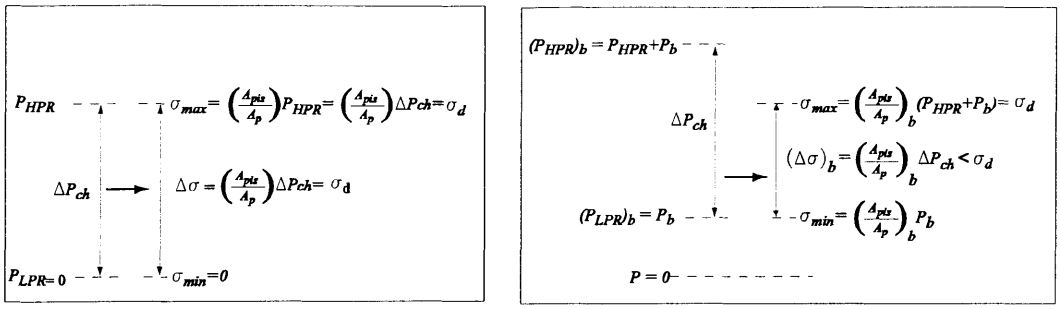


Figure 5-16: Schematic illustrating the effect of bias pressure.(a) not biased case (b) biased case

the depolarization stress, given by:

$$\Delta\sigma = \left(\frac{A_{pis}}{A_p}\right)\Delta P_{ch} = \sigma_d \tag{5.17}$$

However, for the biased case, where $P_{LPR} \neq 0$, the stress band is given by:

$$(\Delta\sigma)_b = \left(\frac{A_{pis}}{A_p}\right)_b \Delta P_{ch} < \sigma_d \tag{5.18}$$

which is smaller than the depolarization stress of the piezoelectric material. Figure 5-16 illustrates the effect of bias pressure. This means that for the same pressure differential, higher frequencies and flowrates are required, which can be seen from the following equations which are derived for the general case:

$$f_b = \frac{4W}{(s_{33}^E - s_{33}^D)(\Delta\sigma)_b^2 A_p L_p} \tag{5.19}$$

$$Q_b = \frac{2(s_{33}^E + s_{33}^D)W}{(s_{33}^E - s_{33}^D)\Delta P_{ch}} + C_{eff}\Delta P_{ch} f_b \tag{5.20}$$

or

$$Q_b = \frac{2(s_{33}^E + s_{33}^D)W}{(s_{33}^E - s_{33}^D)\Delta P_{ch}} + \frac{4C_{eff}W}{(s_{33}^E - s_{33}^D)(\Delta\sigma)_b A_{pis} L_p} \tag{5.21}$$

Figure 5-17 illustrates the effect of bias pressure on required frequency, flowrate and efficiency for the case of $0.5W$ power requirement, where $\Delta P_{ch} = P_{HPR} - P_{LPR} = 2MPa$, and

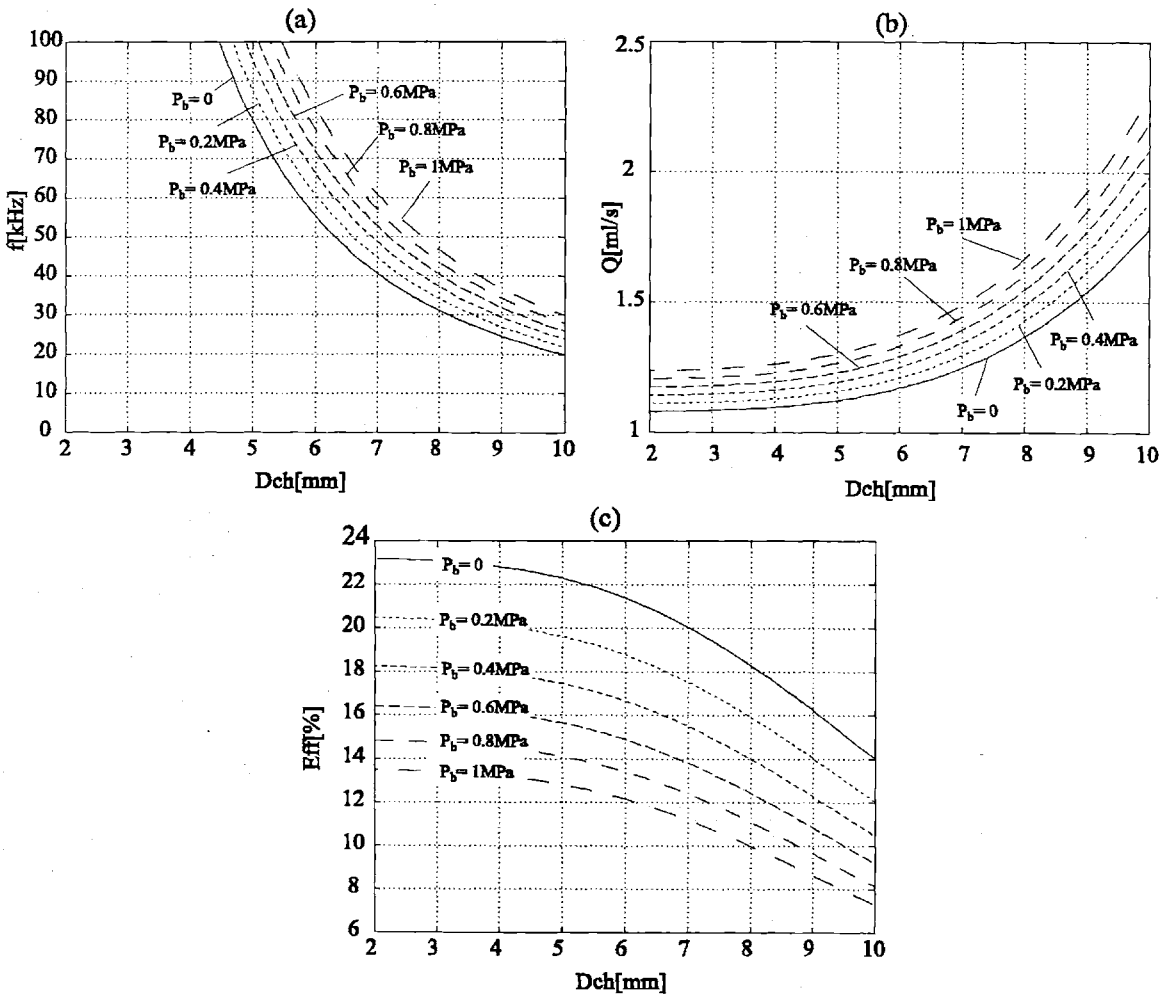


Figure 5-17: Effect of bias pressure on required frequency, flowrate and efficiency.

piezoelectric material is $PZN - PT$. It is important to note that the generated power is proportional to the square of stress band and therefore the bias pressure should be kept as small as possible. It can be easily shown that, for a given chamber diameter, the required frequency for the biased case and for the case where $P_{LPR} = 0$ are related by:

$$\frac{f}{f_b} = \left(\frac{\Delta P_{ch}}{\Delta P_{ch} + P_b}\right)^2 \tag{5.22}$$

where $P_b$ is the bias pressure. It is assumed that in both cases the pressure differential in the chamber is the same. Equation 5.22 implies that if the bias pressure is much smaller than the pressure band in the chamber, its effect is negligible. However for typical MHT devices this is not the case and the effect of bias pressure should be considered.

### 5.1.6 Scaling Issues

One of the many advantages of MEMS devices is their ability to operate at very high frequencies. In other words, they allow operation with much larger bandwidth due to their high natural frequencies. For linear systems, the scaling law for natural frequency can be obtained by considering a very simple system consisting a cantilever beam and a proof mass attached to the tip of the beam. The stiffness corresponding to the tip deflection of the beam in response to a force applied to the tip can be obtained from beam theory:

$$k = \frac{EWH^3}{4L^3} \tag{5.23}$$

where $E$ is the Youngs modulus, and $W$, $H$, and $L$ are the width, the height and the length of the beam respectively. The natural frequency of this system can be calculated by:

$$\omega_n = \sqrt{\frac{k}{m}} \tag{5.24}$$

where $m$ is the mass of the proof mass. If we define the scale factor, $\lambda$, as the ratio of the new scaled dimensions divided by the nominal, the dependence of the stiffness of the beam and the mass of the proof mass on the system scale are:

$$k \sim \lambda \qquad \text{and} \qquad m \sim \lambda^3 \tag{5.25}$$

where the scale dependence of the stiffness of the beam is obtained from equation 5.23. The natural frequency of the system is then related to its size by:

$$f_n \sim \sqrt{\frac{\lambda}{\lambda^3}} = \frac{1}{\lambda} \tag{5.26}$$

which can be generalized to any linear structure.

Similarly we can obtain the scaling laws for the power generator considering the dependence of the natural frequency, required operation frequency and compliance of the system on system scale. Consider the simple chamber structure described in Section 4.1, which consists of a fluid chamber and a compliant top support structure. Here we assume that in the energy harvesting chamber the top support structure is the only compliant structure, and the piston is rigid and perfectly sealed to piston walls without tethers. The effective compliance for this case was derived in Section 4.1 as:

$$C_{eff} = \left(\frac{V_o}{\beta_f} + C_s\right) = \left(\frac{\pi D_{ch}^2 H_{ch}}{4\beta_f} + \frac{\pi D_{ch}^6 (1-\nu^2)}{1024 E t_{top}^3}\right) \tag{5.27}$$

where $D_{ch}$ is the chamber diameter, $H_{ch}$ is the chamber height, and $t_{top}$ is the thickness of the top support structure. The dependence of the effective chamber compliance on the system scale is then

$$C_{eff} \sim \lambda^3 \tag{5.28}$$

which suggests that as the system gets smaller, the compliance gets smaller. Lets consider a case where $P_{LPR} = 0$ and the effective chamber compliance is given by equation 5.27. For a certain power requirement, the required operation frequency can be calculated as:

$$f_{req} = \frac{4W}{(s_{33}^E - s_{33}^D)\sigma^2 A_p L_p} \tag{5.29}$$

where $\sigma$ is the stress band on the piezoelectric element, which is equal to the maximum stress since $P_{LPR} = 0$. As discussed earlier, in a design procedure, the chamber diameter and the piezo diameter are chosen such that the maximum stress on the piezoelectric element is equal to the depolarization stress of the piezoelectric element. If we assume that for any design scenario

this condition will be satisfied, then the dependence of the required frequency on system scale can be obtained as:

$$f_{req} \sim \frac{1}{\lambda^3} \tag{5.30}$$

which suggests that as the system gets smaller, larger frequencies are required due to the reduced piezoelectric element volume. The required flowrate is given by:

$$Q = \frac{2(s_{33}^E + s_{33}^D)W}{(s_{33}^E - s_{33}^D)P_{HPR}} + C_{eff}P_{HPR}f_{req} \tag{5.31}$$

From equations 5.28 and 5.30 we can obtain the dependence of the required flowrate on the system scale as:

$$Q \sim \lambda^0 \tag{5.32}$$

which suggests that the required flowrate does not depend on the system scale. In smaller scale, although the system compliance reduces, the required frequency increases in the same amount which results in the same required flowrate. Since this results were derived for constant $P_{HPR}$ and required power, $W$, the system efficiency does not depend on the system scale either, which can be expressed as:

$$\eta = \frac{W}{P_{HPR}Q} \sim \lambda^0 \tag{5.33}$$

It should be noted that this analysis relies on the assumption that the active valves can operate at very high frequencies and the valves and channels can provide the required flowrates even when the system gets very small.

Consider a design case where the operation frequency is equal to the maximum bandwidth of the device. If we make the system 10 times smaller and keep the required power and $P_{HPR}$ the same, we will need 1000 times the frequency to generate the same power from the smaller device. However we can increase the operation frequency only 10 times since the natural frequency is inversely proportional to the system scale, which is expressed in equation 5.26. This implies that we can extract only one percent of the required power from the small device. However

we can fit 1000 small devices inside the original volume, which means that we can generate 10 times the original power from the same volume. This suggests that the power density is inversely proportional to the system scale, which can be expressed as:

$$PD \sim \frac{1}{\lambda} \tag{5.34}$$

This suggests that, as the system gets smaller, the power density increases. Again, it should be mentioned that, this analysis assumed that, in the smaller scale the valves and channels can provide the required flowrate regardless of the system scale. However, it is expected that viscous losses in the valves will begin to dominate beyond a certain scale and scaling further down will not be more efficient. In order to perform this study, more detailed fluid models are needed. Nevertheless, the above analysis provides a general understanding about the scaling of the system.

## 5.2 Design Procedure

This section will present a design procedure for designing the microhydraulic piezoelectric power generator. First, the design decisions made considering the issues discussed in previous sections as well as those imposed by the active valve design and fabrication process will be presented. Then, the design procedure will be described and two design examples will be presented along with simulation results.

### 5.2.1 Preliminary design decisions

As discussed in Chapter 3, the working fluid is chosen to be silicone oil due to its low viscosity and low density. It also has a comparable bulk modulus to that of water. Choice of piezoelectric element is done considering the results in sections 5.1.4, 5.1.4, and 5.1.4. From Figure 5-12 it can be seen that the piezoelectric material $PZT-5H$ has very high frequency requirements, $PZT-4S, PZT-8$ have lower and very similar frequency requirements, and $PZN-PT$ has comparable frequency requirements to those of $PZT-4S$ and $PZT-8$. If we examine Figures 5-13 and 5-14, we can see that $PZN-PT$ requires much lower flowrates and provides much efficient power generation compared to other piezoelectric materials. In Chapter 2 it was

concluded that $PZN-PT$ has the smallest energy density among the piezoelectric elements considered, which is a result of its low depolarization stress. However due to its very high coupling coefficient it provides very efficient electromechanical energy conversion and requires the lowest flowrate for a given power requirement. It should be noted that, the implication of the low energy density of $PZN-PT$ is that, larger piezoelectric material volume is needed compared to other piezoelectric materials for the same power output. However, the weight of the piezoelectric element constitutes only a small fraction of the overall system weight and the increased efficiency of $PZN-PT$ due to its much higher coupling coefficient would still overwhelm the effect of increased weight in terms of the overall system power density. The chamber height is chosen to be $200\mu m$. A preliminary study has shown that chamber heights smaller than this could cause squeeze film damping effect inside the chamber and can result in undesired losses. And, larger chamber heights would increase the chamber compliance, which would decrease the efficiency of the system. The length of the piezoelectric element is chosen to be $1mm$. This parameter is basically determined considering the actuation in the active valves, since all the piezoelectric cylinders within the system, namely the ones in the active valves and the one in the energy harvesting chamber, have the same length because of the layered structure of the device, which was explained in Chapter 1. Larger lengths would decrease the stiffness of the piezoelectric elements inside the active valves, which reduces the actuation capability, and smaller lengths could cause dielectric breakdown.

### 5.2.2 Parameters imposed by active valve design

The basic limitation of the active valves is their bandwidth. Current active valve designs predict bandwidths in the order of $10-20kHz$. Typical trade-offs in the active valve design are stroke, bandwidth and force, which are detailed in [5]. Another important limitation is the pressures that the active valves can work against, which basically imposes the maximum high reservoir pressure possible. They can typically work against pressures of $2-3MPa$. Also the active valves impose a minimum pressure requirement due to cavitation considerations in the hydraulic amplification chamber(HAC) within the active valve structure. In the design example presented, the low pressure reservoir pressure, $P_{HPR}$ is chosen as $0.5MPa$.

### 5.2.3 Parameters imposed by fabrication process

As briefly described in Chapter 1, the device consists of silicon and pyrex micromachined layers. The thickness of the layers basically dictate the thicknesses of individual components. For example, a double layer piston structure, which consist of two silicon layers bonded to each other, will have a thickness of $t_{pis} = 800\mu m$, which is the case in the design example. Since the tethers are created through deep reactive ion etching(DRIE) of a SOI wafer, the tether thickness is defined by the SOI layer. Also, the fillet radius control during the fabrication process imposes some limitations on the tether width. For example narrow tethers would be very stiff due to the relatively large fillet radius and the predictions of the linear theory used for the optimization would not valid beyond a certain tether width. The top tether thickness, $t_{tetop}$, is chosen to be $10\mu m$, whereas the bottom tether thickness is chosen to be thinner, namely, $5\mu m$, because the bottom tether does not have any functionality and therefore it should be kept as thin as possible so that it won't cause significant resistance to piston motion. The thicknesses of the top and bottom support structures are determined by the number of layers used, including the packaging layers on top and bottom portions of the device. As discussed in Chapter 3, the compliance of the system is very important in terms of system performance and they should be kept as small as possible. Therefore it is desirable to have very thick top and bottom support structures. The effective thickness would also depend on the structure of the auxiliary system in which the device is packaged. In the design examples, the top and bottom structures are assumed to have the same thicknesses, namely $t_{top} = t_{bot} = 2.5mm$, and they are assumed to comprise of all silicon layers.

### 5.2.4 Design Procedure

Figure 5-18 presents a design procedure, which will be followed after the initial design decisions are made using above considerations. The first part consists of analytical design calculations. The pressure band in the chamber is dictated by the bias pressure, $P_b$, and high pressure reservoir pressure, $P_{HPR}$. The piston diameter and piezo diameter are calculated using equations 5.11 and 5.19, and the battery voltage is calculated using equation 5.6.

These calculations are followed by the tether structure optimization, which determines the optimum tether width, $w_t$, for the given tether thicknesses and piston diameter. The designed

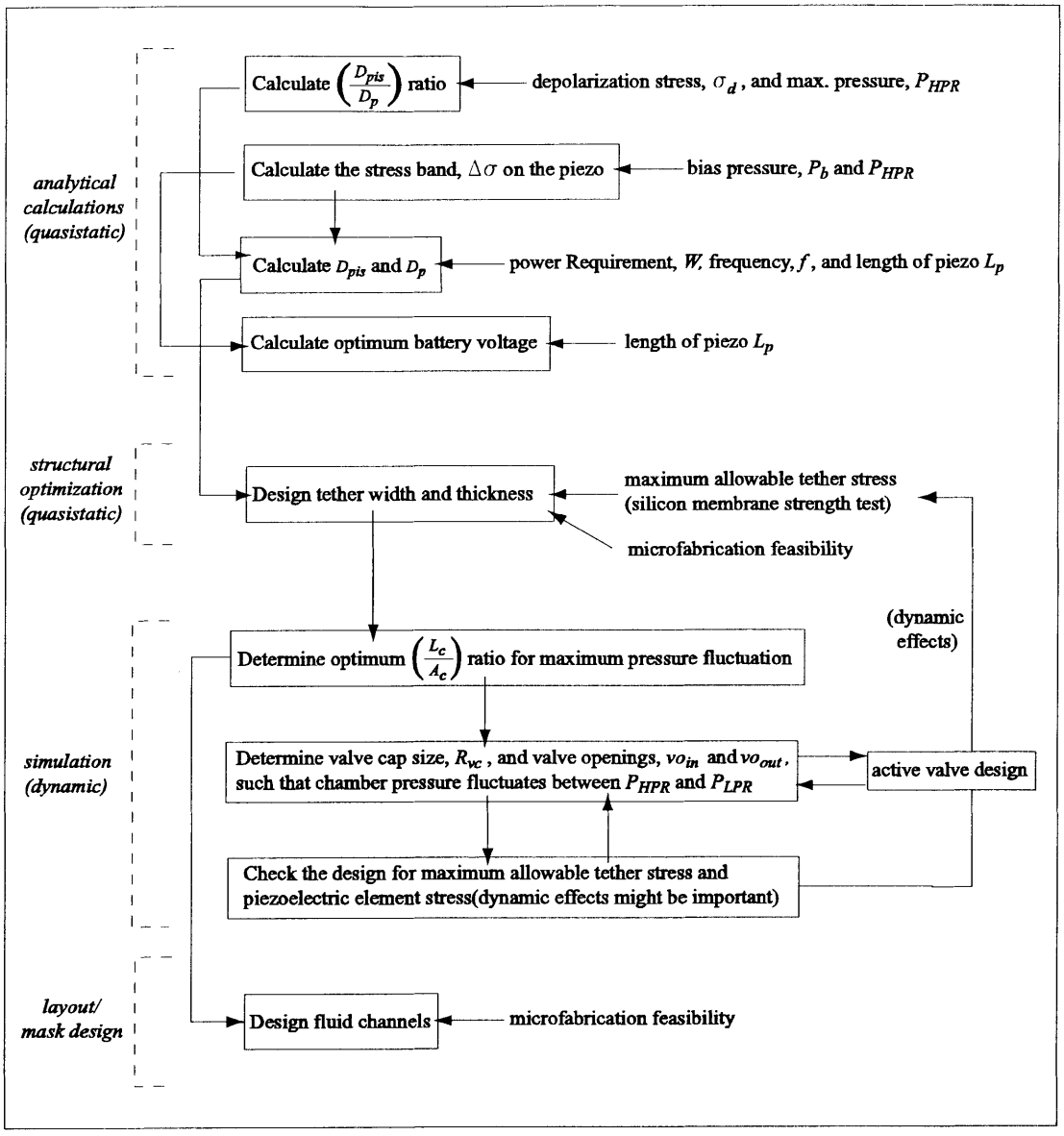


Figure 5-18: Design procedure.

tether width also determines the chamber diameter, $D_{ch}$. The geometric parameters along with the operation conditions are then fed to the system level simulation. The simulation architecture is shown 5-19 and the Simulink block diagrams are given in Appendix A.

First, simulations are performed to determine the optimum length to area ratio of the fluid channels, using arbitrary valve resistance, i.e. arbitrary valve cap size or valve openings. It is helpful to run these simulations with very small valve resistance, namely with very large valve opening or very large valve cap, since the fluidic oscillations are much more pronounced with lower valve resistances and it is easier to determine the optimum length to area ratio of the channels. Then, the valve cap size and valve opening are designed such that the chamber pressure fluctuates between reservoir pressures, namely between $P_{HPR}$ and $P_{LPR}$. At this stage, it is important to consider structural limitations, which might be imposed by the active valves. For example, a large valve cap size requires a large membrane to allow sufficient valve motion, however this may cause excessive stresses in the membrane. Or, a very large valve opening can cause the same problem. Since the same effective valve resistance can be achieved with different combinations of valve opening and valve cap size, coupled iterations may be necessary with the active valve design procedure, which is not within the scope of this thesis. Detailed information about the active valve design procedure can be found in [5].

Finally, the system is simulated, stresses in the tethers and on the piezoelectric element are checked, and design iterations are performed if necessary. Although the valves are designed to achieve the desired pressure band in the chamber, the stress band may be a little bit different than expected. This can be explained by considering equation 5.11. This equation assumes static force balance between the piezoelectric cylinder and the piston. Also, the effect of the tether is neglected since the force exerted by the tethers on the piston is generally very small compared to the force exerted by the piezo and force due to chamber pressure. As will be seen in the design examples, the dynamics of the piston does not have a significant effect on system performance and it is reasonable to assume quasi-static force balance. However, if the operation frequency is much higher, the dynamics of the piston will be important and equation 5.11 will not be valid. The design procedure presented above is followed by the layout and mask design for the fabrication.

For the piston dynamics, a damping ratio of 5% is assumed, considering the piezoelectric

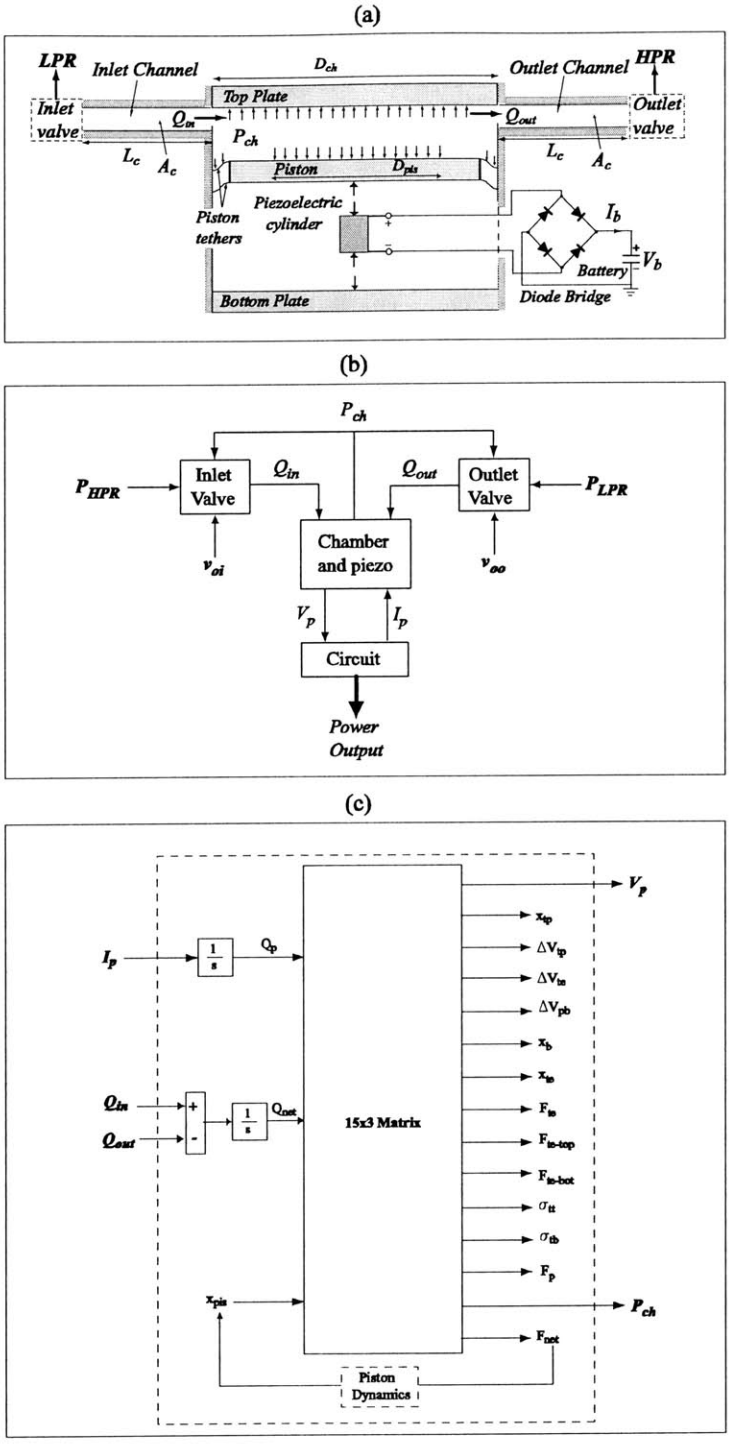


Figure 5-19: (a) System layout (b) System level simulation architecture (c) The chamber and piezo block in the overall system architecture which was developed in Chapter 4.

| **Design Decisions** | | |
|---|---|---|
| Piezoelectric material | PZN-PT | lowest flowrate requirement |
| Working fluid | silicone oil | low viscosity and density |
| Piezoelectric element length, $L_p$ | $1mm$ | active valve actuation |
| Chamber height, $H_{ch}$ | $200\mu m$ | squeeze film damping |
| **Parameters imposed by fabrication process** | | |
| Piston thickness, $t_{pis}$ | $800\mu m$ | double layer piston |
| Top and bottom support structure thickness | $2.5mm$ | packaging layers |
| Top tether thickness, $t_{tetop}$ | $10\mu m$ | fabrication feasibility |
| Bottom tether thickness, $t_{tebot}$ | $5\mu m$ | fabrication feasibility |
| **Material Limitations** | | |
| Depolarization stress of piezoelectric element, $\sigma_d$ | $10MPa$ | shouldn't be exceeded |
| Maximum allowable stress in tethers | $1GPa$ | shouldn't be exceeded |
| **Damping** | | |
| Damping ratio of piston | 5% | assumed |

Table 5.1: Summary of preliminary design decisions applied to the design examples.

element as the effective spring. Namely the damping coefficient is calculated as:

$$c = 2\zeta\sqrt{m_{pis}k_p} = 2\zeta\sqrt{m_{pis}\frac{A_p}{s_{33}^D L_p}} \tag{5.35}$$

where $\zeta$ is the damping ratio and $s_{33}^D$ is the open circuit compliance compliance of the piezoelectric element.

## 5.3 Design Examples

This section will present two design examples who have different operational requirements due to the limitations imposed by the active valves. The preliminary design decisions, parameters imposed by fabrication process and material limitations, which are valid for both examples are summarized in Table 5.1.

### 5.3.1 Design Example 1

The parameters imposed by the active valves, the design parameters obtained by applying the design procedure discussed in the previous section, and performance parameters are summarized in Table 5.2. Simulation results are shown in Figure 5-21, Figure 5-22 and Figure 5-23. The

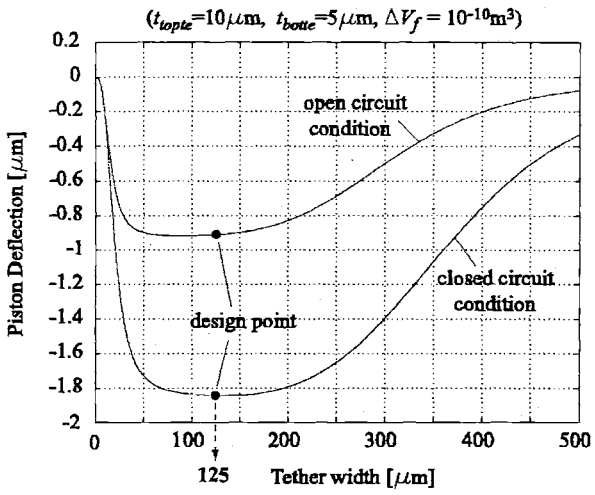


Figure 5-20: Tether structure design. Piston deflection shown for different tether widths.

tether structure optimization is shown in Figure 5-20 where the piston deflection is plotted as a function of the tether width for an added fluid volume of $\Delta V_f = 10^{-10}m^3$.

Figure 5-22 shows simulation results for the deflections and swept volumes of individual structural components. It can be seen that, as expected, the deflection of the bottom support structure is much smaller than the piston deflection, which is desirable for maximum piezoelectric element compression. Also, it can be seen that the volume swept due to tether bending, piston deformation and top support structure deformation is much smaller than the volume swept by the piston motion, which is again desirable for maximum piezoelectric element compression.

### 5.3.2 Design Example 2

The parameters imposed by the active valves, design parameters and performance parameters are summarized in Table 5.3. In this example, the performance of the active valves are very limited, which results in very small power output compared to the first example. Simulation results are shown in Figure 5-24, Figure 5-25 and Figure 5-26. The observations done for the deflections and swept volumes of the individual structural members in the first design example are also valid for this example. Namely, the deflection of the bottom support structure is

| | | |
|---|---|---|
| Power Requirement | $0.25W$ | Electrical power output |
| **Parameters imposed by active valve design** | | |
| Operation frequency, $f$ | $20kHz$ | bandwidth of active valves |
| Bias Pressure, $P_b$ | $0.5MPa$ | cavitation in HAC chamber |
| High Pressure Reservoir Pressure, $P_{HPR}$ | $3MPa$ | membrane stress limitation |
| **Important parameters resulting from operation conditions** | | |
| Pressure band in the chamber, $\Delta P_{ch}$ | $2.5MPa$ | - |
| Stress band on piezoelectric element, $\Delta\sigma$ | $8.33MPa$ | - |
| **Designed parameters** | | |
| Piston Diameter, $D_{pis}$ | $6.95mm$ | - |
| Piezoelectric cylinder diameter, $D_p$ | $3.8mm$ | - |
| Battery voltage, $V_b$ | $74.9V$ | - |
| Tether width, $w_t$ | $125\mu m$ | optimization |
| Chamber diameter, $D_{ch}$ | $7.2mm$ | - |
| Fluid channel length to area ratio, $\frac{L_c}{A_c}$ | $5000m^{-1}$ | same for inlet and outlet |
| Valve cap radius, $R_{vc}$ | $400\mu m$ | same for inlet and outlet |
| Valve opening, $vo_{in}, vo_{out}$ | $24\mu m$ | same for inlet and outlet |
| **Performance parameters** | | |
| Net flowrate, $Q_{net}$ | $0.52ml/s$ | - |
| Hydraulic power input | $1.3W$ | $(P_{HPR} - P_{LPR})Q_{net}$ |
| Efficiency, $\eta$ | 19.2% | $\frac{\text{Electrical power output}}{\text{Hydraulic power input}}$ |

Table 5.2: Summary of design and performance parameters of design example 1.

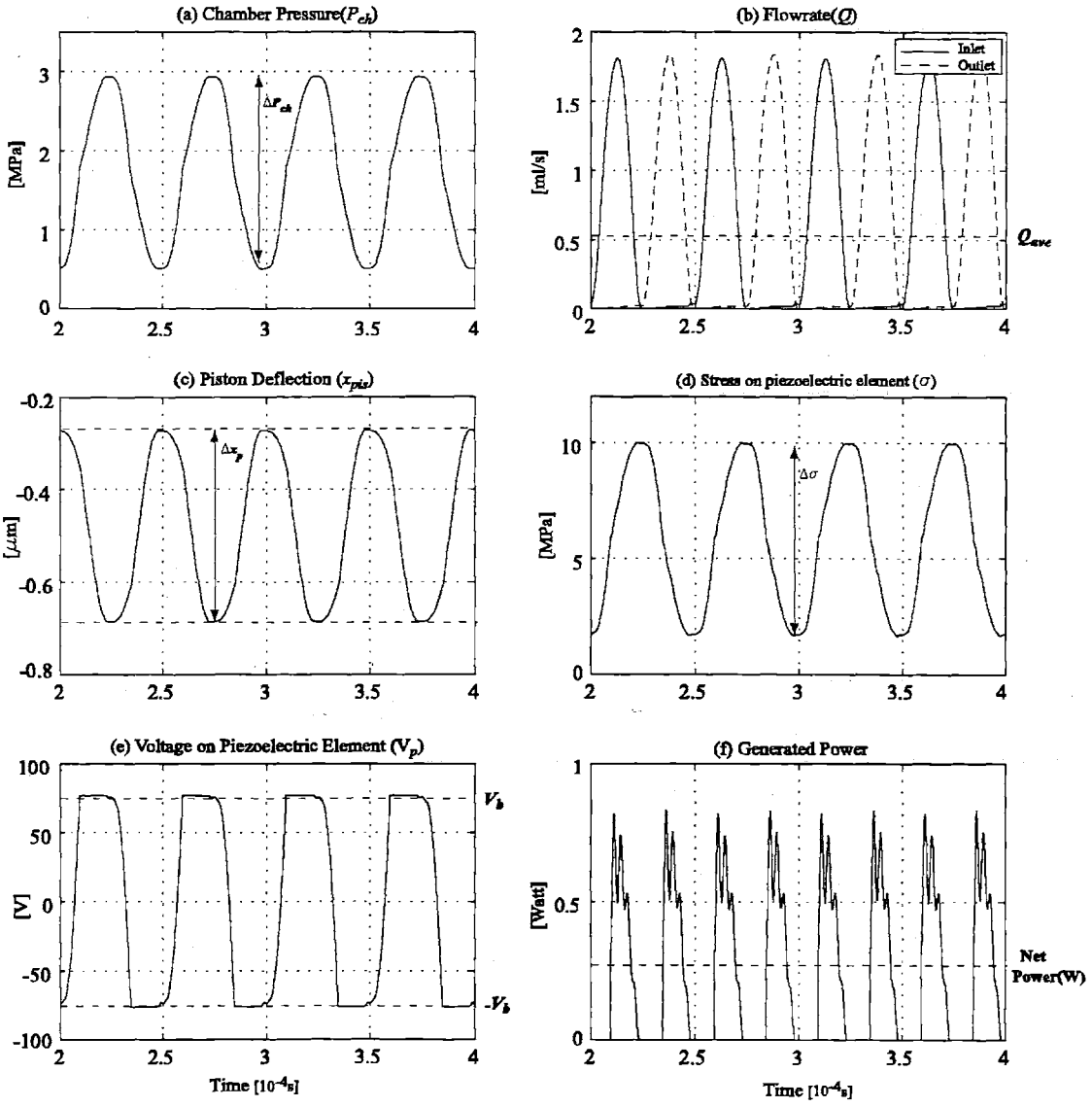


Figure 5-21: Simulation time histories of the design example 1.

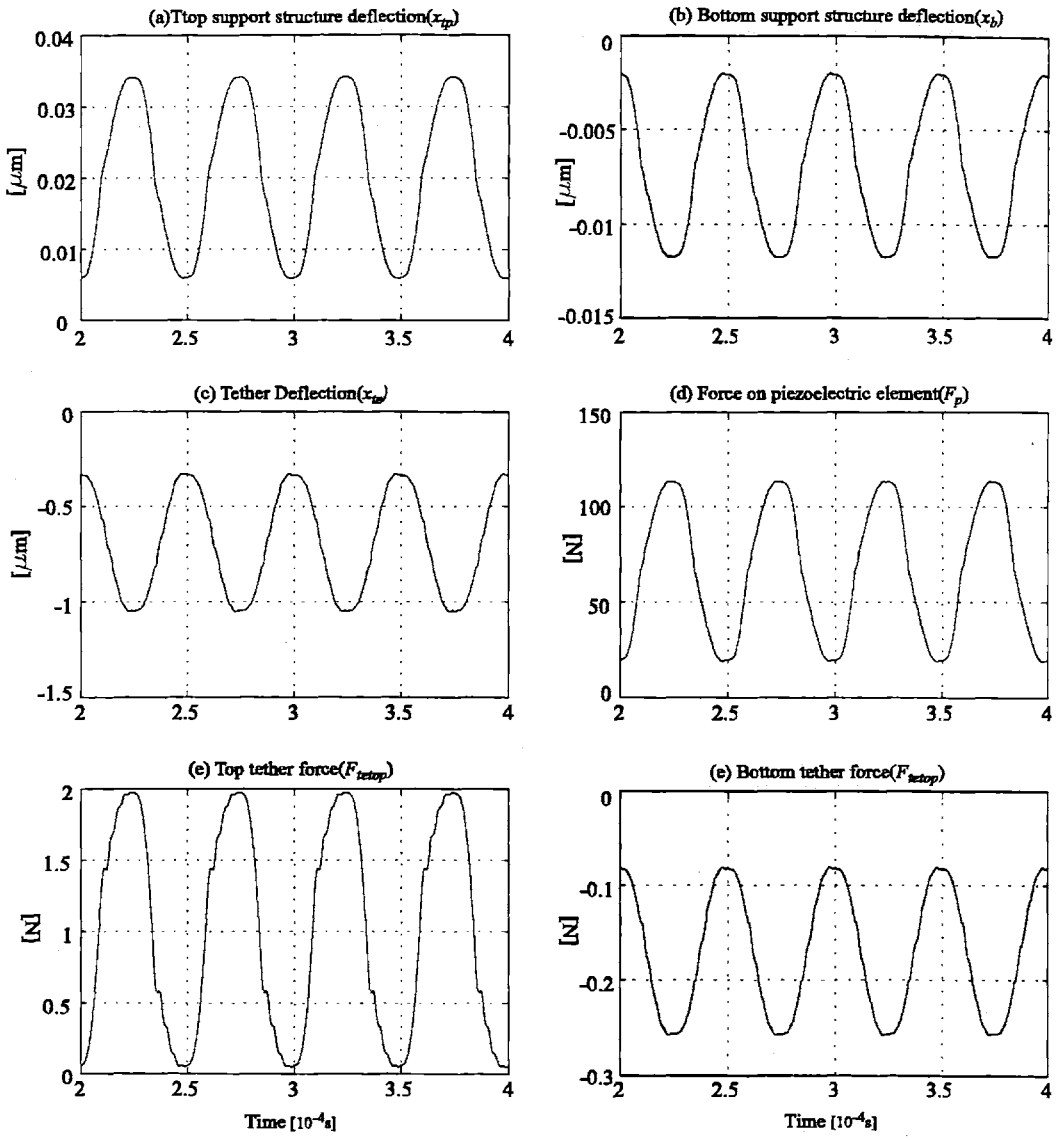


Figure 5-22: Simulation time histories of the design example 1.

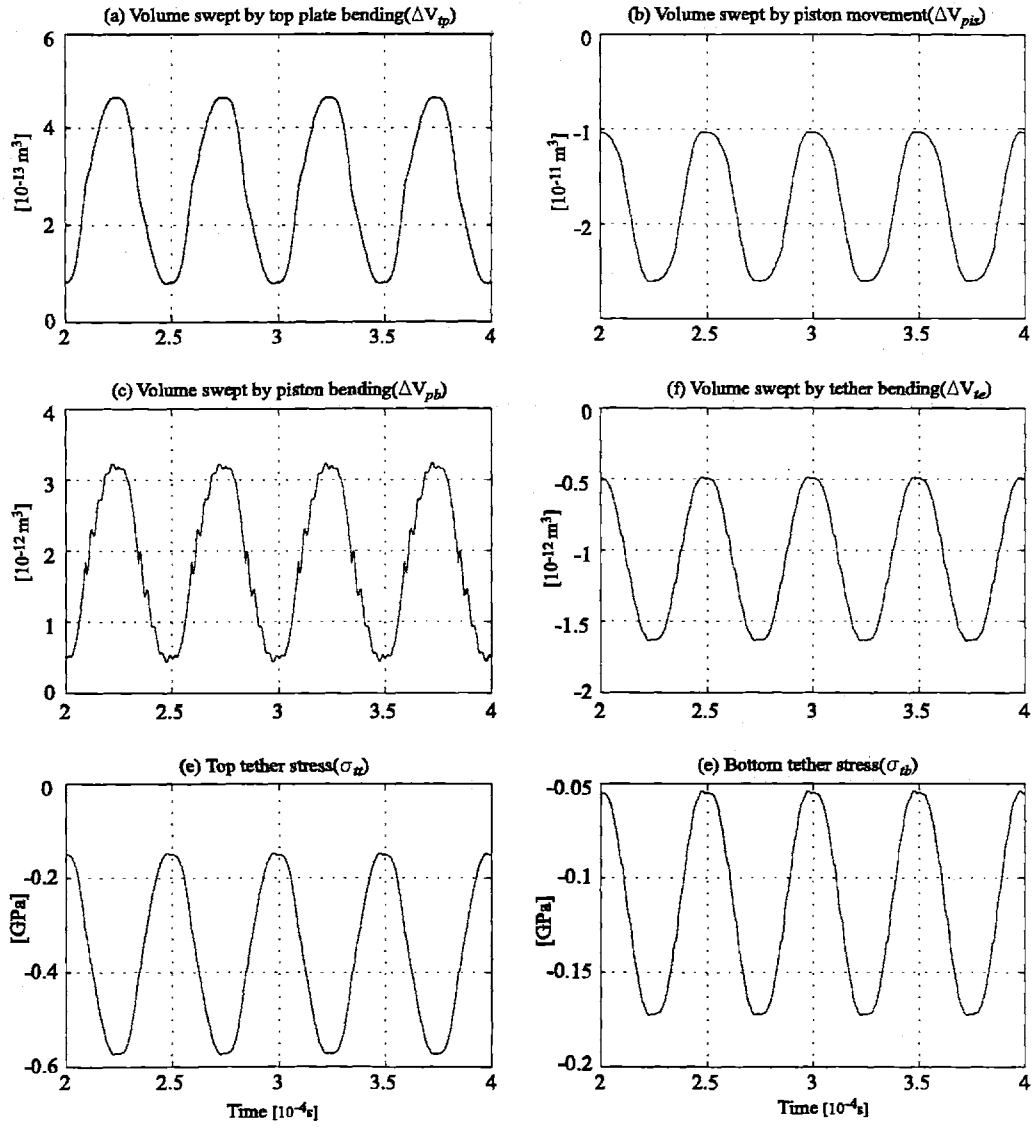


Figure 5-23: Simulation time histories of the design example 1.

| | | |
|---|---|---|
| Power Requirement | $0.01W$ | Electrical power output |
| **Parameters imposed by active valve design** | | |
| Operation frequency, $f$ | $5kHz$ | bandwidth of active valves |
| Bias Pressure, $P_b$ | $0.5MPa$ | cavitation in HAC chamber |
| High Pressure Reservoir Pressure, $P_{HPR}$ | $1.5MPa$ | membrane stress limitation |
| **Important parameters resulting from operation conditions** | | |
| Pressure band in the chamber, $\Delta P_{ch}$ | $1MPa$ | - |
| Stress band on piezoelectric element, $\Delta\sigma$ | $6.67MPa$ | - |
| **Designed parameters** | | |
| Piston Diameter, $D_{pis}$ | $4.89mm$ | - |
| Piezoelectric cylinder diameter, $D_p$ | $1.89mm$ | - |
| Battery voltage, $V_b$ | $59.9V$ | - |
| Tether width, $w_t$ | $125\mu m$ | optimization |
| Chamber diameter, $D_{ch}$ | $5.19mm$ | - |
| Fluid channel length to area ratio, $\frac{L_c}{A_c}$ | $110000m^{-1}$ | same for inlet and outlet |
| Valve cap radius, $R_{vc}$ | $150\mu m$ | same for inlet and outlet |
| Valve opening, $vo_{in}, vo_{out}$ | $9.3\mu m$ | same for inlet and outlet |
| **Performance parameters** | | |
| Net flowrate, $Q_{net}$ | $0.042ml/s$ | - |
| Hydraulic power input | $0.042W$ | $(P_{HPR} - P_{LPR})Q_{net}$ |
| Efficiency, $\eta$ | 23.8% | $\frac{\text{Electrical power output}}{\text{Hydraulic power input}}$ |

Table 5.3: Summary of design and performance parameters of design example 2.

much smaller than the piston deflection, which is desirable for maximum piezoelectric element compression and the volume swept due to tether bending, piston deformation and top support structure deformation is much smaller than the volume swept by the piston motion, which is again desirable for maximum piezoelectric element compression.

As discussed in the previous chapters, the generated power is a strong function of the stress band on the piezoelectric element and the operation frequency. As the maximum operating frequency reduces due to active valve design limitations, much larger piezoelectric elements and chamber structures are needed to generate the same amount of power. In the second design example, in order to generate the same power as in design example 1, huge chamber diameters, larger than $20mm$, is needed, which is not feasible due to the increased compliance and size constraints. As discussed earlier in Section 5.1.6, it is feasible to make smaller and multiple devices which would fit in the original volume. In section 5.1.6 it was concluded that the efficiency does not depend on system scale. As can be seen from Tables 5.2 and 5.3 the

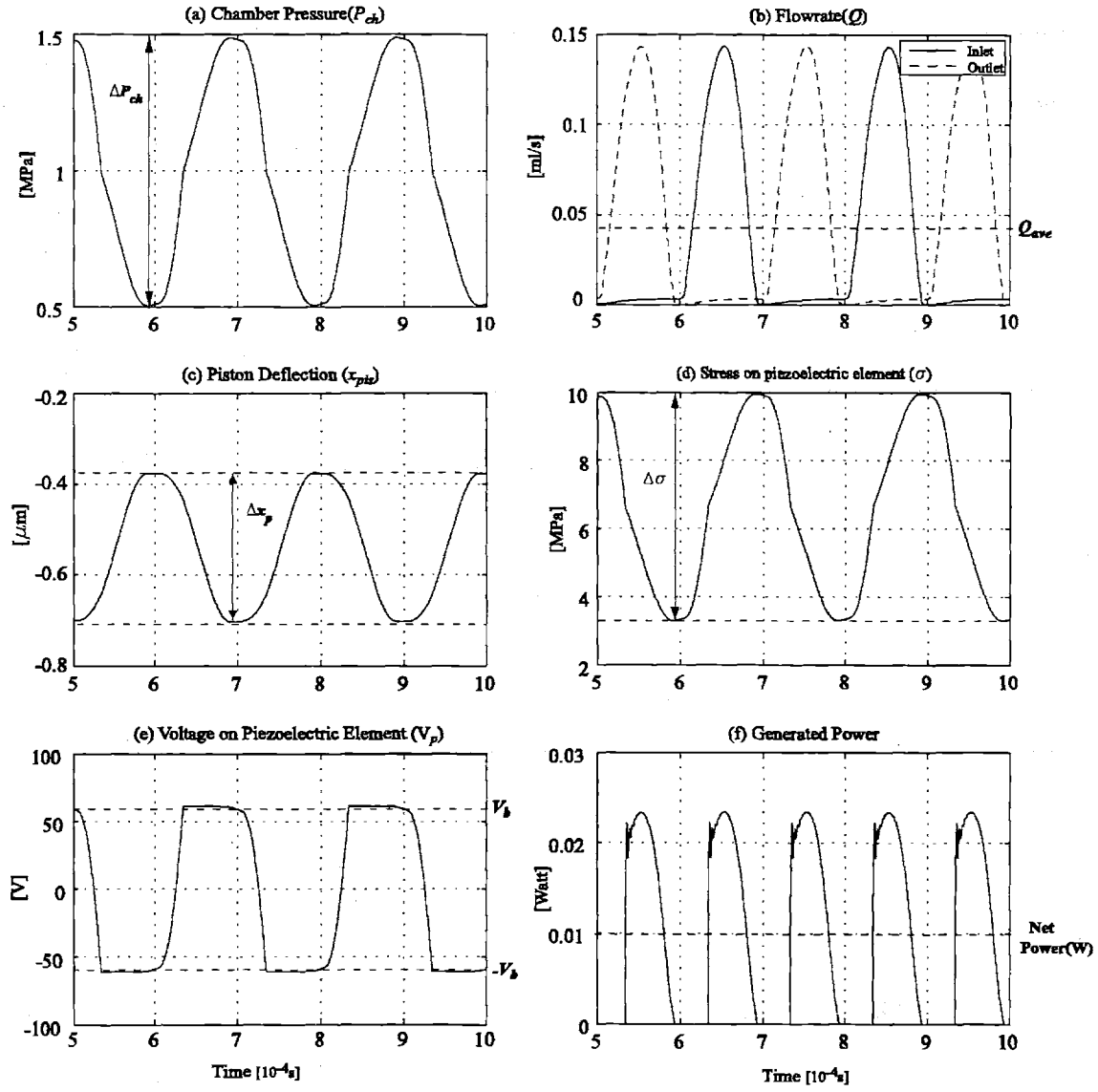


Figure 5-24: Simulation time histories of the design example 2.

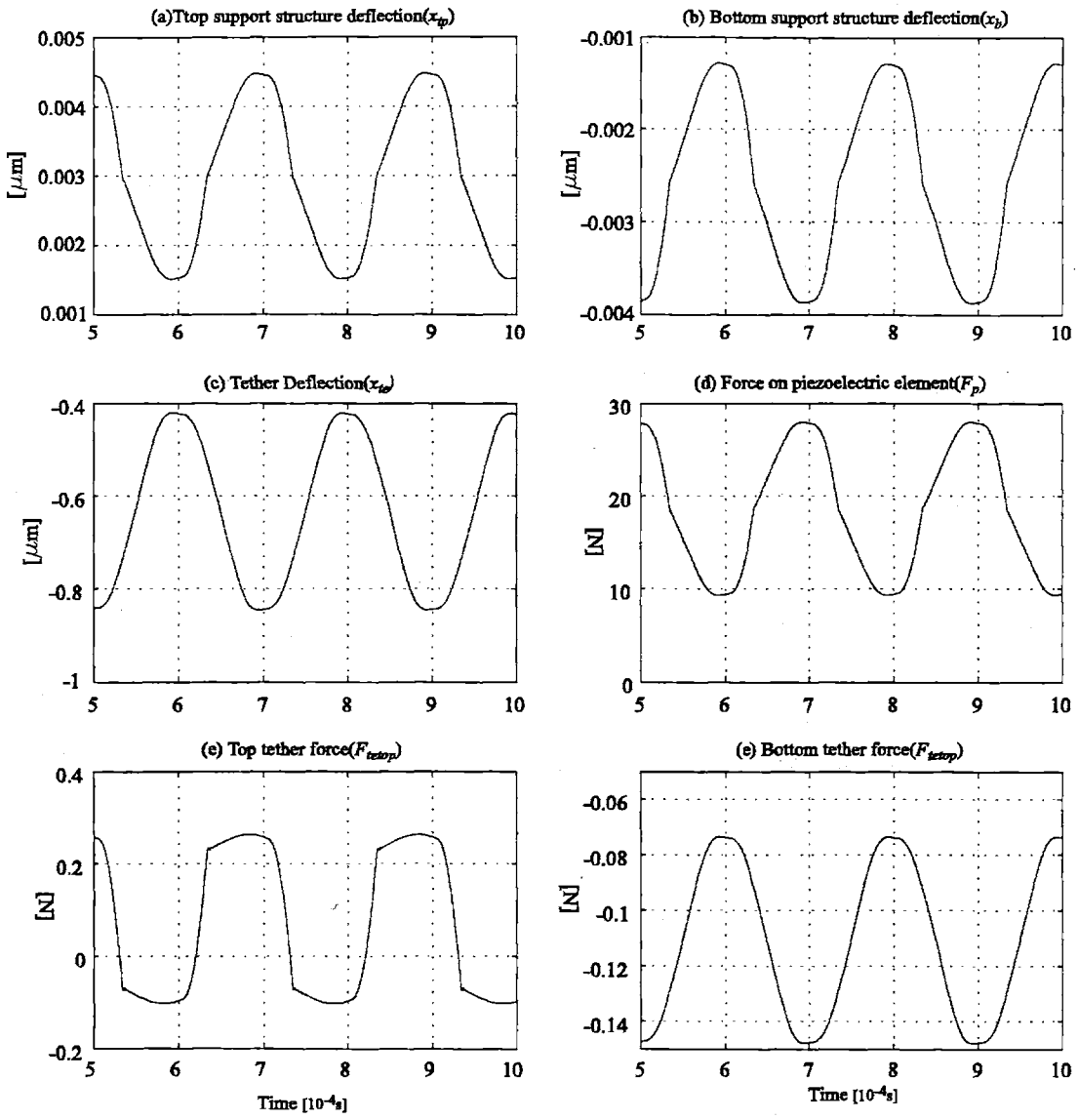


Figure 5-25: Simulation time histories of the design example 2.

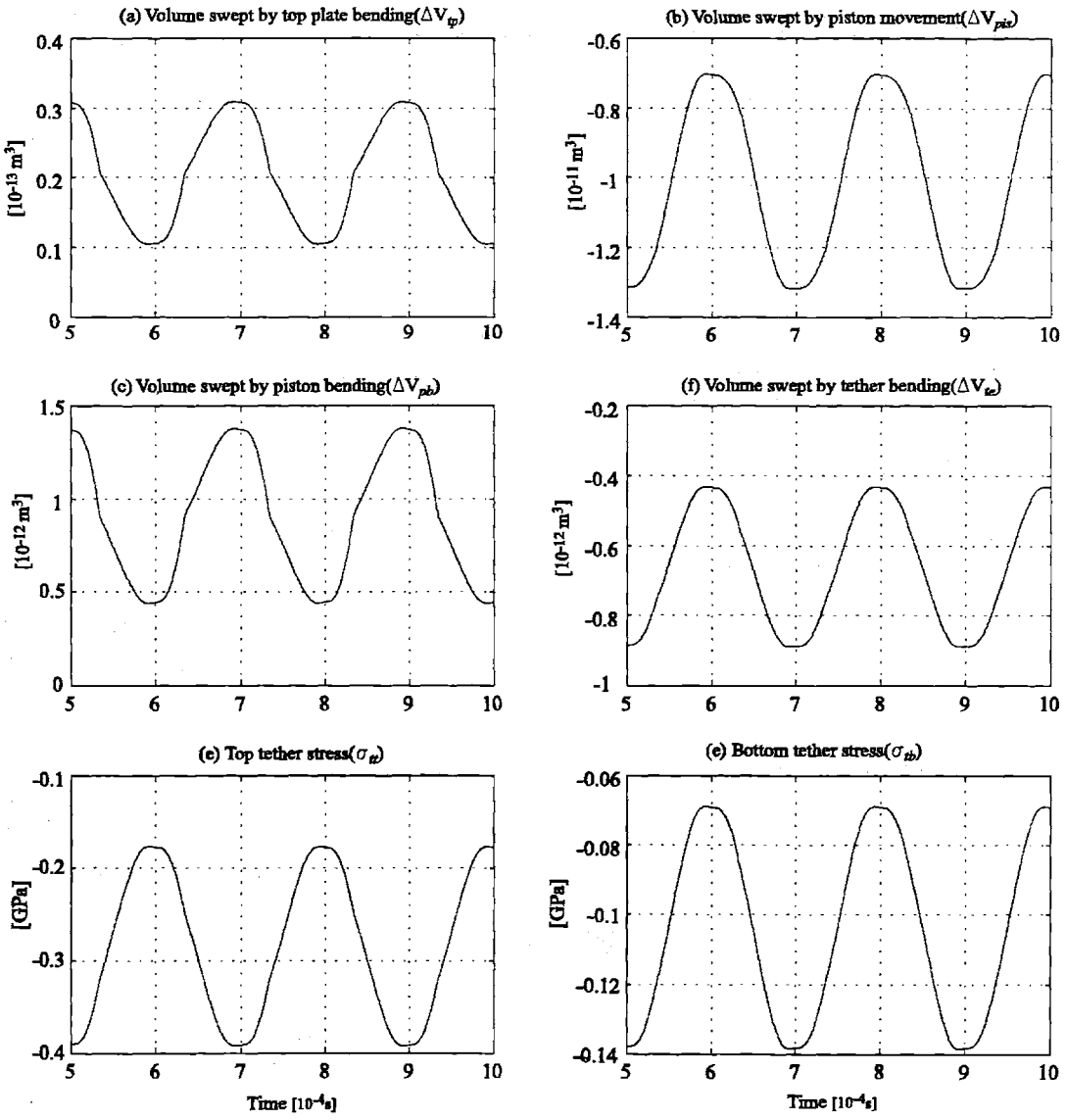


Figure 5-26: Simulation time histories of the design example 2.

second device, which is smaller than the first one, has higher efficiency. This is due to the fact that in the example, only the chamber diameter and piezo diameter are smaller. The length of the piezoelectric element, chamber height and structural thicknesses are kept constant. This resulted in a stiffer chamber compared to the case where all the dimensions were reduced. The explicit relationships and effect of geometric parameters on system scale can be seem in equation 5.27, which represents a simpler case than the actual chamber.

## 5.4 Summary

This chapter presented further design considerations and a design procedure along with two design examples. Fluidic oscillations within the system and conditions for sufficient chamber filling and evacuation is analyzed. An optimization procedure for the tether structure is presented. Trade-offs between operation conditions and their effect on the performance is discussed. Effect of system scale on the performance is discussed. Effect of the fabrication process and the active valves on the design is discussed.

# Chapter 6

# Conclusions and Recommendations for Future Work

## 6.1 Summary

The objectives of this thesis were:

- To develop a comprehensive system level model and simulation tool to analyze the main chamber and the associated fluid channels and valves of piezoelectric microhydraulic power generation devices

- To gain insight into system operation and understand the factors affecting the system performance

- Develop a design procedure, which should be complemented by the design of the active valves.

Chapter 1 presented the configuration, operation and motivation of microhydraulic-piezoelectric power generators. Primary challenges and preliminary design considerations is discussed.

Chapter 2 presented an analysis of piezoelectric power generation based on linear electromechanical energy conversion. Effect of circuitry and piezoelectric material on energy density and effective coupling factor is discussed. Models for two different circuit topologies are developed, simulations are performed and analytical expressions are derived for the generated power and effective coupling factor. Different piezoelectric materials are compared in terms of their energy densities and energy conversion efficiencies for different circuitry. It has been concluded

that, although the single crystal piezoelectric material(PZN-PT) has very high effective coupling factor, it has a very low energy density compared to PZT-8 or PZT-4S because of its small depolarization stress. Another important conclusion of this chapter is that, for a piezoelectric element, the energy density obtained with the diode bridge and voltage detector circuit is four times bigger than the energy density obtained with only the diode bridge. The effective coupling factor is a function of the coupling coefficient and the circuitry, whereas the energy density is a function of coupling coefficient, circuitry and the depolarization stress. Indeed, the effective coupling factor becomes an important criteria if the piezoelectric element is considered along with its surrounding system, for example the infrastructure which provides the force on the element, which is the energy harvesting chamber in the microhydraulic power generation device. It should be remembered that in the analysis presented in this chapter a prescribed force is imposed on the piezoelectric element. This issue is addressed in Chapter 3.

Chapter 3 presented a simple model of the energy harvesting chamber, simulations with the coupled circuitry and preliminary design considerations. The interaction of the energy harvesting chamber and the circuitry is discussed. The two circuits presented in Chapter 2 and different piezoelectric materials are compared in terms of the flowrate and frequency requirements for a given pressure differential and power requirement, and in terms of system efficiency. Analytical expressions are derived for the generated power, required flowrate, effective coupling factor and system efficiency. The most important conclusion of this chapter is that the performance of the energy harvesting chamber depends on

- Circuit topology
- Piezoelectric material($k_{33}, \sigma_d$)
- Chamber compliance($C_{eff}$).

It is also concluded that, as $k_{33}$ approaches 1 and $C_{eff}$ approaches 0, the system efficiency for the two circuits analyzed approaches 50%. This means that, even with a perfect piezoelectric material($k_{33} = 1$) and zero effective chamber compliance, which are not possible, the system efficiency cannot exceed 50%. It should be emphasized that the efficiency definition throughout the thesis corresponds only to the energy harvesting chamber. The electrical power consumption in the active valves is not considered.

Chapter 4 presented detailed modelling of the energy harvesting chamber. In Chapter 3,

an effective chamber compliance ($C_{eff}$) was assumed to be used in the simulation and in the following analysis. This chapter investigated the contribution of different structural components on the effective compliance of the chamber. Deformations of individual structural members are calculated using linear plate theory. It is assumed that the deflections due to bending are significantly larger than that due to shearing. A simulation architecture is presented to be included in overall system level simulation, which allows for inclusion of the elastic equations into dynamic simulation as well as monitoring important parameters.

Chapter 5 presented further design considerations in addition to the design issues discussed in Chapter3. These were fluidic oscillations within the system, chamber filling and evacuation, tether structure optimization, effect of operation conditions on system performance and trade-offs, and scaling issues. The system is analyzed only for the case where the chamber is attached to the regular bridge. A design procedure along with two design examples is presented. The design decisions made considering the issues discussed in previous chapters as well as those imposed by the active valve design and fabrication process is discussed. Simulation results are shown. In Chapter 2 it was concluded that $PZN-PT$ has the smallest energy density among the piezoelectric elements considered, which is a result of its low depolarization stress. However due to its very high coupling coefficient it provides very efficient electromechanical energy conversion and requires lowest flowrate for a given power requirement. It should be noted that, the implication of the low energy density of $PZN-PT$ is that, larger piezoelectric material volume is needed compared to other piezoelectric materials for the same power output. However, the weight of the piezoelectric element constitutes only a small fraction of the overall system weight and the increased efficiency of $PZN-PT$ due to its much higher coupling coefficient would still overwhelm the effect of increased weight in terms of the overall system power density.

This thesis developed a framework to analyze piezoelectric microhydraulic power generators. Insight into system operation is gained and important factors affecting system performance are analyzed.

## 6.2 Recommendations for Future Work

Recommendations for future work in terms of modeling and design can be summarized in the following subgroups:

### Piezoelectric Element

The analysis presented in this thesis is based on linear electromechanical energy conversion. More detailed analysis including nonlinear effects is required to obtain better predictions for system performance. Also, piezoelectric element coefficients only in 3-3 direction is used since the piezoelectric element is subjected to compression parallel to the polarization of the element and assuming that the element is free to expand in lateral directions, so that $T_3$ is the only nonzero stress component. However, this is not the case since the piezoelectric cylinder is bonded to the piston and bottom support structure. Finite element analysis is required to calculate the effective coefficients in 3-3 direction, namely effective $d_{33}, s_{33}^E$ and $s_{33}^D$.

### Fluid Structure Interaction

The system is analyzed for relatively low frequencies where the fluid channels were the only components whose dynamic behavior was important for system performance. At higher frequencies, the modal behavior of the piezoelectric element and the piston structure along with the fluid contained in the chamber might be important (added mass effect of the fluid). Detailed finite element models are needed to investigate the fluid structure interaction within the chamber.

### Fluid model

In this thesis, a simple fluid model based on discharge coefficients taken from published data is used. These models do not provide accurate estimation of the power consumption in the valves since it is not possible to predict the force exerted on the valve cap and valve membrane by the flow. Detailed CFD analysis can provide more insight into the fluid flow in the valve. This is very important because of the complicated geometry of the valves.

### Squeeze film damping

Squeeze film damping is a common problem in MEMS devices. Although not presented in this thesis, a preliminary analysis has shown that, for the chamber height used in the design, squeeze film effects are not important. However, for smaller devices, squeeze film damping can effect system performance significantly. Detailed analytical models and/or finite element studies are required to investigate this effect.

### Scaling Study

As the system size gets smaller, the power density increases, however, only until a certain scale. Beyond that scale, it is expected that viscous losses in the valves will begin to dominate and scaling further down will not be more efficient. In order to perform this study, more detailed fluid models are needed as mentioned earlier.

### System level analysis

This thesis concentrated on the main chamber, also called the energy harvesting chamber, of the piezoelectric microhydraulic power generators. System level simulations, including full active valve structure, should be performed to obtained better predictions about system performance and efficiency. However, it should be emphasized that, these simulations would provide realistic predictions provided that good fluid models exist, as discussed above.

# Bibliography


[1] N.W Hagood, D.C. Roberts, L. Saggere, K.S. Breuer, K.S.Chen, J.A. Carretero, H. Li, R. Mlcak, S. Pulitzer, M. A. Schmidt, S. M. Spearing, Y.H.Su. "Micro Hydraulic Transducer Technology for Actuation and Power Generation". *Proceedings of the SPIE Annual International Symposium on Smart Structures and Materials,* 7:680-688, *2000.*

[2] Seward Webb Pulitzer III, "Feasibility Assesment and Design of Micro Hydraulic Solid-State Transducers". *SM Thesis, Masssachusetts Institute of Technology, 2001.*

[3] H.Q. Li, D.C. Roberts, J.L. Steyn, K.T. Turner, J. A. Carretero, O. Yaglioglu, Y.H. SU, L. Saggere, N.W. Hagood, S.M. Spearing, M.A. Schmidt, R. Mlcak, K.S. Breuer. "A High Frequency High Flow Rate Piezoelectrically Driven MEMS Micropump". *Solid-State Sensor and Actuator Workshop, pp.* 69-72, 2000.

[4] J. A. Carretero. "Measurement and Modeling of the Flow Characteristics of Micro Disc Valves". *SM Thesis, Masssachusetts Institute of Technology,* 2001.

[5] D. C Roberts, O. Yaglioglu, J. Carretero, Y.H Su, L. Saggere, N.W. Hagood. " Modeling, Design, and Simulation of a Piezoelectrically Driven Microvalve for High Pressure, High Frequency Applications, SPIE Proceedings, 4327:366-380, 2001

[6] D. C. Roberts. "Design, Modeling, Fabrication, and Testing of a Piezoelectric Microvalve for High Pressure, High Frequency Hydraulic Applications". *PhD Thesis, Masssachusetts Institute of Technology,* 2002.

[7] K. Turner, " An Evaluation of Critical Issues for Microhydraulic Transducers: Silicon Wafer Bonding, Strength of Silicon on Insulator Membranes and Gold-Tin Solder Bonding" , *SM Thesis, Masssachusetts Institute of Technology,* 2001.

[8] D.A. Berlincourt. "Piezoelectric and Ferroelectric Energy Conversion".*IEEE Transactions on Sonics and Ultrasonics*, S-15(2):89-97,1968.

[9] M. Umeda, K.Nakamura, S. Ueha. " Analysis of the Transformation of Mechanical Impact Energy to Electric Energy Using Piezoelctric Vibrator".*Jpn. Journal of Applied Physics*, 35:3267-3273, 1996.

[10] M. Umeda, K.Nakamura, S. Ueha. "Energy Storage Characteristics of a Piezo-Generator using Impact Induced Vibration ".*Jpn. Journal of Applied Physics*, 36:3146-3151, 1997.

[11] C. N. Xu, M. Akiyama, K. Nonaka, T. Watanabe. " Electrical Power Generation Characteristics of PZT Piezoelectric Ceramics". *IEEE Transactions on Ultrasonics, Ferroelectrics, and Frequency Control*, 45(4):1065-1070, 1998.

[12] M. Goldfarb, L. D. Jones."On the Efficiency of Electric Power Generation With Piezoelectric Ceramic". *Journal of Dynamic Systems, Measurement, and Control*, Transactions of ASME, 121:566-571, 1999

[13] P. G. Jones, S. P. Beeby, E. P. James, N. M. White."The Modelling of a Piezoelectric Vibration Powered Generator for Microsystems. In *Transducers '01*, 2001

[14] D. J. Warkentin, N. W. Hagood. "Nonlinear Piezoelectric Shunting for Structural Damping". *Proceedings of SPIE,* 3041:747-757, 1997.

[15] N. W. Hagood, A. von Flotow. " Damping of Structural Vibrations with Piezolectric Materials and Passive Electrical Networks". *Journal of Sound and Vibration,* 146(2):243-268, 1991.

[16] N. W. Hagood, W. H. Chung, A. von Flotow. " Modelling of Piezoelectric Actuator Dynamics for Active Structural Control". *Journal of Intelligent Material Systems and Structures*, 1(3):327-354, 1990.

[17] W. P. Mason. "An Electromechanical Representation of a Piezoelectric Crystal Used as a Transducer". *Proceedings of the Institute of Radio Engineers*, 23(10):1252-1263, 1935.

[18] IEEE Std 176-1987 IEEE Standard on Piezoelectricicty, The Institute of Electrical and Electronics Engineers. 1987

[19] Ching-Yu Lin. "Material Characterization and Modeling for Piezoelectric Actuation and Power Generation under High Electromechanical Loading". *PhD Thesis, Massachusetts Institute of Technology*, 2002

[20] J. M. Hall, W. E. Dillon, W. C. Nunnally. "Thermo-Acoustic-Piezoelectric Power Generation". Procedings of the 26th Intersociety Energy Conversion Engineering Conference-IECEC'91, 2001.

[21] V. H. Schmidt. "Piezoelectric Energy Conversion in Windmills". Proceedings of IEEE: Ultrasonic Symposium, 2:897-904, 1992.

[22] V. H. Schmidt. "Piezoelectric Wind Generator". *United States Patent* #4,536,674.August 20, 1985.

[23] S. Nagao. "Electronic Wristwatch With Generator". *United States Patent* #5,939,707.Assignee: Seiko Epson Corporation, July 3, 1990.

[24] O. Takahashi, Y. Hashimoto, E. Nagasaka, H. Miyazaki, T. Funasaka. "Piezolectric Power Generator For a Portable Power Supply Unit and Portable Electronic Device Equipped With Same ". *United States Patent* #5,751,091.Assignee: Seiko Epson Corporation, May 12, 1998.

[25] Y. Hashimoto, O. Takahashi, H. Miyazaki, T. Funasaka, M. Furahata. "Power Generation Method and Power Generator Using a Piezoelctric Element and Electronic Device Using The Power ". *United States Patent* #5,835,996.Assignee: Seiko Epson Corporation, November 10, 1998.

[26] P. Smalser."Power Transfer of Piezoelectric Generated Energy". *United States Patent* #5,703,474. Assignee: Ocean Power Technologies Inc., December 30, 1997.

[27] G. W. Taylor, J. R. Burns. "Power Generation From Waves Near the Surface of Bodies of Water". *United States Patent* #4,404,490. September 13, 1983.

[28] J. R. Burns. "Ocean Wave Energy Conversion Using Piezoelectric Material Members". *nited States Patent* #4,685,296. August 11, 1987.

[29] M. Y. Epstein, C. B. Carroll. "Piezoelectric Electric Energy Generator". *United States Patent* #5,512,795. Assignee: Ocean Power Technologies, Inc., April 30, 1996.

[30] M. Y. Epstein. "Piezoelectric Generation of Electrical Power From Surface Waves on Bodies of Water Using Suspended Weighted Members". *United States Patent* #5,578,889. Assignee: Ocean Power Technologies, Inc., November 26, 1996.

[31] M. Y. Epstein, G. W. Taylor. "Water Craft Using Piezoelectric Materials". *United States Patent* #5,621,264. Assignee: Ocean Power Technologies, Inc., April 15, 1997.

[32] C. B. Caroll. "Frequency Multiplying Piezoelectric Generators". *United States Patent* #5,814,921. Assignee: Ocean Power Technologies, Inc., September 29, 1998.

[33] J. R. Burns. "DC Bias Scheme For Field Induced Piezoelectric Power Generators". *United States Patent* #6,201,336. Assignee: Ocean Power Technologies, Inc., March 13, 2001.

[34] E. A. Kolm, H. H. Kolm. "Piezoelectric Fluid-Electric Generator". *United States Patent* #4,387,318. Assignee: Piezo Electric Products, Inc., June 7, 1983.

[35] H. H. Kolm, E. A. Kolm. "Piezoelectric Acousto-Electric Generator". *United States Patent* #4,467,236. Assignee: Piezo Electric Products, Inc., August 21, 1984.

[36] P. A. Todd, B. R. Walker. "Piezoelectric Circuit". *United States Patent* #5,065,067. November 12, 1991.

[37] M. Kimura. "Piezo-Electricity Generation Device". *United States Patent* #5,801,475. Assignee: Seiki Company, Ltd., September 1, 1998.

[38] S. Yamashita. "Portable Piezoelctric Electric Generation Device". *United States Patent* #4,091,302. May 23, 1978.

[39] C. G. Triplett. "Vehicular Mounted Piezoelctric Generator". *United States Patent* #4,504,761. March 12, 1985.

[40] E. Dieulesaint, D. Royer, D. Mazerolle, P. Nowak. "Piezoelectric Transformers". *Electronic Letters*, 24(7):444-445, 1998.

[41] G. Ivensky, I. Zafrany, S. B. Yaakov. "Generic Operational Characteristics of Piezoeelctric Transformers". *Proceedings of IEEE: Power Electronics Specialists Conference*, 3:1657-1662, 2000.

[42] S. H. Lee, J. Hong, J.H. Yoo, G. S. Gong. " Characteristics of Piezoelectric Transformer for Power Supply". *Proceedings of IEEE: Ultrasonics Symposium,* 1:971-975, 1998.

[43] J. Navas, T. Bove, J.A. Cobos, F. Nuno, K, brebol. "Miniaturised Battery Charger Using Piezoielectric Transformers". *Proceedings of IEEE: Applied Power Electronics Conference and Exposition*, 1:492-496, 2001.

[44] A. M. Flynn, S. R. Senders. "Fundamental Limits on Energy Transfer and Circuit Considerations for Piezolectric Transformers".*Proceedings of Power Electronic Specialists Conference, IEEE Transactions*, 2:1463-1471, 1998.

[45] S. E. Park, V. Vedula, M. J. Pan, W. S. Hackenbauer, P. Pertsch, T.Shrout. "Relaxor Based Ferroelectric Single Crystals For Electromechanical Actuators". *Proceedings of the SPIE*, 3324:136-144, 1998.

[46] Q. M. Zhang, J. Zhao, K. Uchino, J. Zheng. "Change of the Weak-Field Properties of PB(ZrTi)$O_3$ Piezocermics With Compressive Uniaxial Stresses and Its Links to the Effect of Dopants on the Stability of the Polarizations in the Materials". *J. Mater. Res.*, 12(1):226-234, 1997.

[47] V. D Kugel, Q. M. Zhang, B. Xu, Q. M. Wang, S. Chandran, L.E. Cross. "Behavior of Piezoelectric Actuators under High Electric Field". *Proceedings of the Tenth IEEE International Symposium on Applications of Ferroelectrics,* 2:655-658, 1996.

[48] J. Zhao, Q. M. Zhang. "Effect of Mechanical Stress on the Electromechanical Performance of PZT and PMN-PT Ceramics". *Proceedings of the Tenth IEEE International Symposium on Applications of Ferroelectrics*, 2:971-974, 1996.

[49] G. Yang, W. Ren, S.F. Liu, A. J. Masys, B. K. Mukherjee. "Effects of Uniaxial Stress and DC Bias Field on the Piezoelectric, Dielectric, and Elastic Properties of Piezoelectric Ceramics". *Proceedings of IEEE: Ultrasonics Symposium*, 2:1005-1008 , 2000.

[50] S. Timoshenko. "Theory of Plates and Shells". McGraw-Hill, NewYork, NY, 1940.

[51] I.E. Idelchik. "Handbook of Hydraulic Resistance", FL, 1994

[52] Y.H. Su. Personal communication. *Massachusetts Institute of Technology*, 2000

[53] V. Caliskan. Personal communication. *Massachusetts Institute of Technology*, 2001

# Appendix A

# Simulink Block Diagrams

This section presents the simulink models used in this thesis. Figure A-1 shows the model of the piezoelectric element model used in Chapter 2 in order to simulate the case of applied force. Later in the thesis, namely in Chapter 4 and Chapter 5, the piezoelectric element constitutive equations are solved along with the elastic equations of the structural members of the main chamber and incorporated into the simulation architecture with a 15x3 matrix, as described in Chapter 4. Figures A-2 and A-3 present the simulink models of the regular diode bridge and the diode bridge attached to the voltage detector, respectively, used throughout the thesis. Figure A-4 presents the simulink blocks used to implement the function of the voltage detection circuit. Figure A-5 shows the simulink architecture of the full system including the main chamber, fluid models and circuitry, used in Chapter 5. Simulations in Chapter 3 are performed with a similar model. Figures A-6, A-7 and A-8 present the simulink models for the main chamber presented in Chapter 4 and the fluid models presented in Chapter 3. The circuit model used for the simulations in Chapter 5, where the system is simulated only with regular diode bridge, is the same as in Figure A-2.

**Implementation of the voltage detector circuit and silicon controlled rectifier** The operation of the voltage detection circuit was described in Chapter 2. The function of the voltage detector is implemented as follows: The voltage detector block in the Simulink model sends a signal to the switch/resistor block which is either 1 or zero depending on the detected voltage, $V_2$. The logic is as follows:

$$
\begin{aligned}
&\text{If} \quad \frac{dV_2}{dt} < 0 \quad \text{and} \quad V_2 > 0 \quad \text{signal=1 (switch on)} \\
&\text{If} \quad \frac{dV_2}{dt} > 0 \quad \text{and} \quad V_2 > 0 \quad \text{signal=0 (switch off)} \\
&\text{If} \quad \frac{dV_2}{dt} < 0 \quad \text{and} \quad V_2 < 0 \quad \text{signal=0 (switch off)} \\
&\text{If} \quad \frac{dV_2}{dt} > 0 \quad \text{and} \quad V_2 < 0 \quad \text{signal=0 (switch off)}
\end{aligned}
$$

The switch function is implemented with a resistor in the place of the SCR, whose value depends on the signal. If the signal value is 1, the value of the resistor is very small and the switch is in "on" state. If the signal value is 0, the value of the resistor is very large and the switch is in "off" state. The following parameter values are used:

Large resistance: $10^6 Ohm$, small resistance: $10^{-6} Ohm$, capacitance value: $10^{-7} F$, inductor value: $20mH$, $m = 5$, $K = 10^7$, $\omega = 5 \times 10^{12}$.

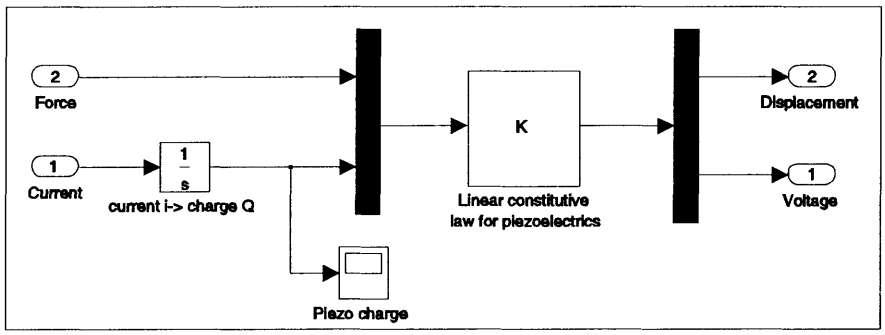


Figure A-1: Simulink model of the piezoelectric element.

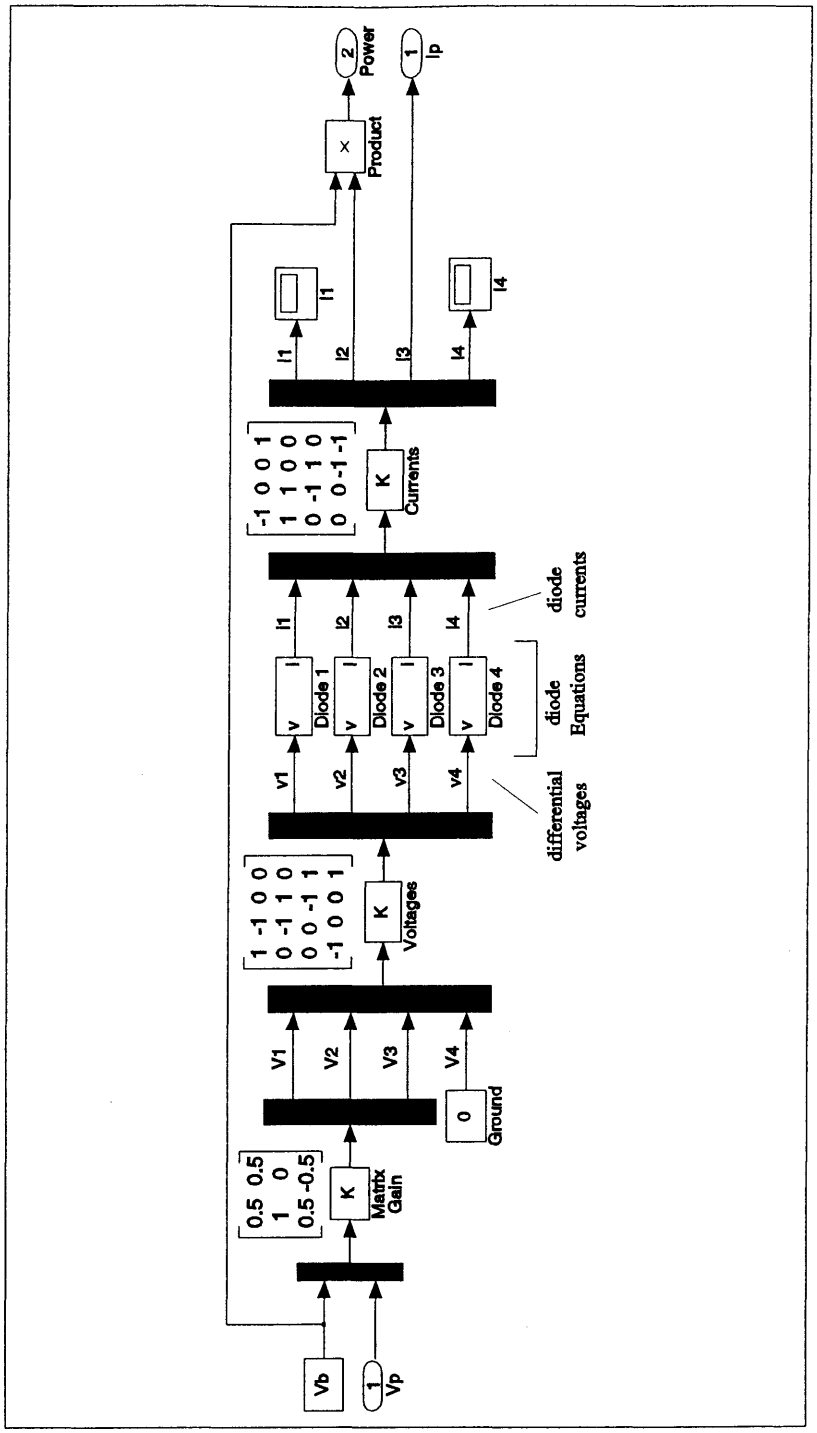


Figure A-2: Simulink model of the diode bridge.

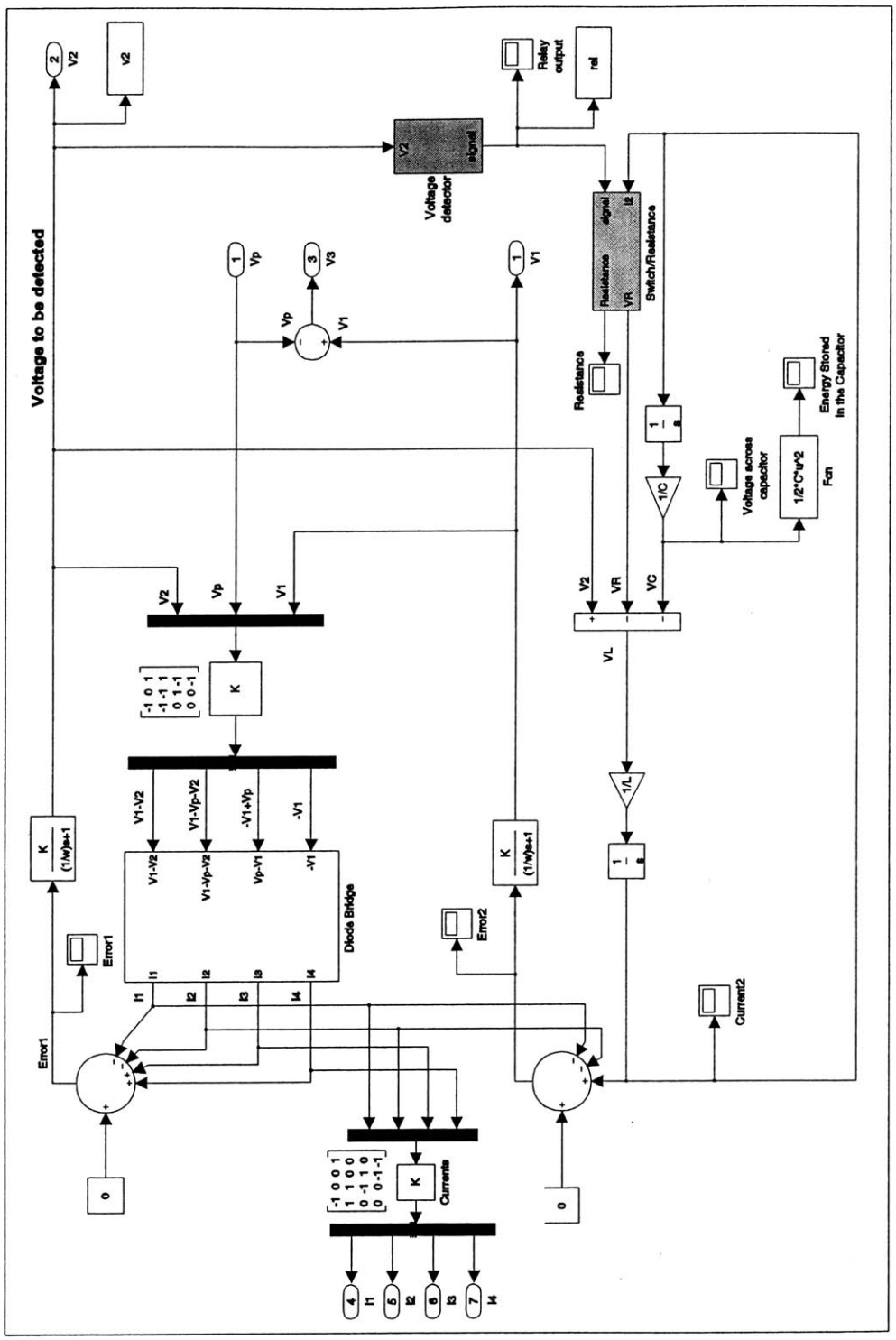


Figure A-3: Simulink model of the diode bridge attached to an inductor, voltage detector and SCR(Silicon Controlled Rectifier).

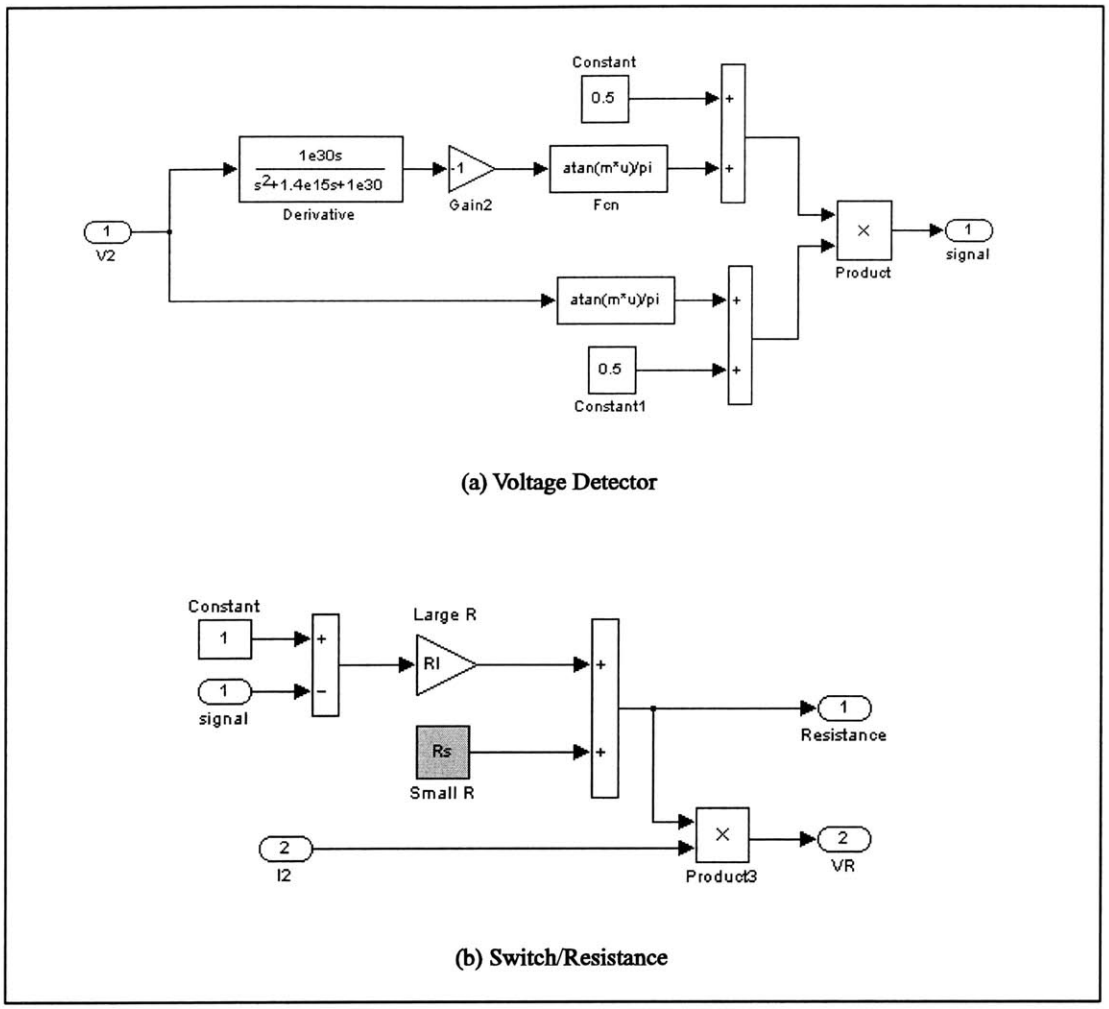


Figure A-4: Implementation of the voltage detector circuit.

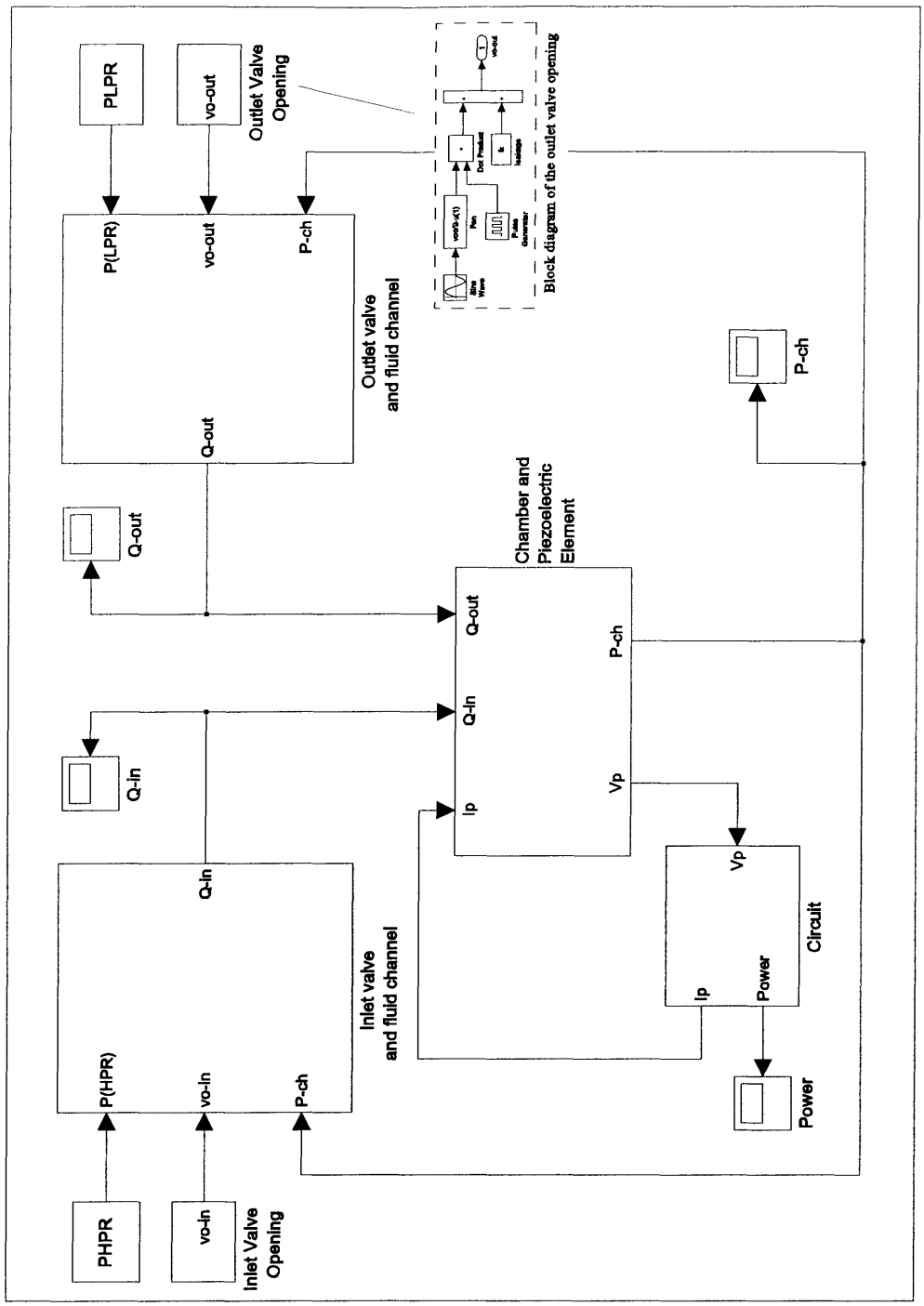


Figure A-5: Simulink model of the full system including the chamber, piezoelectric element, fluid models and circuitry.

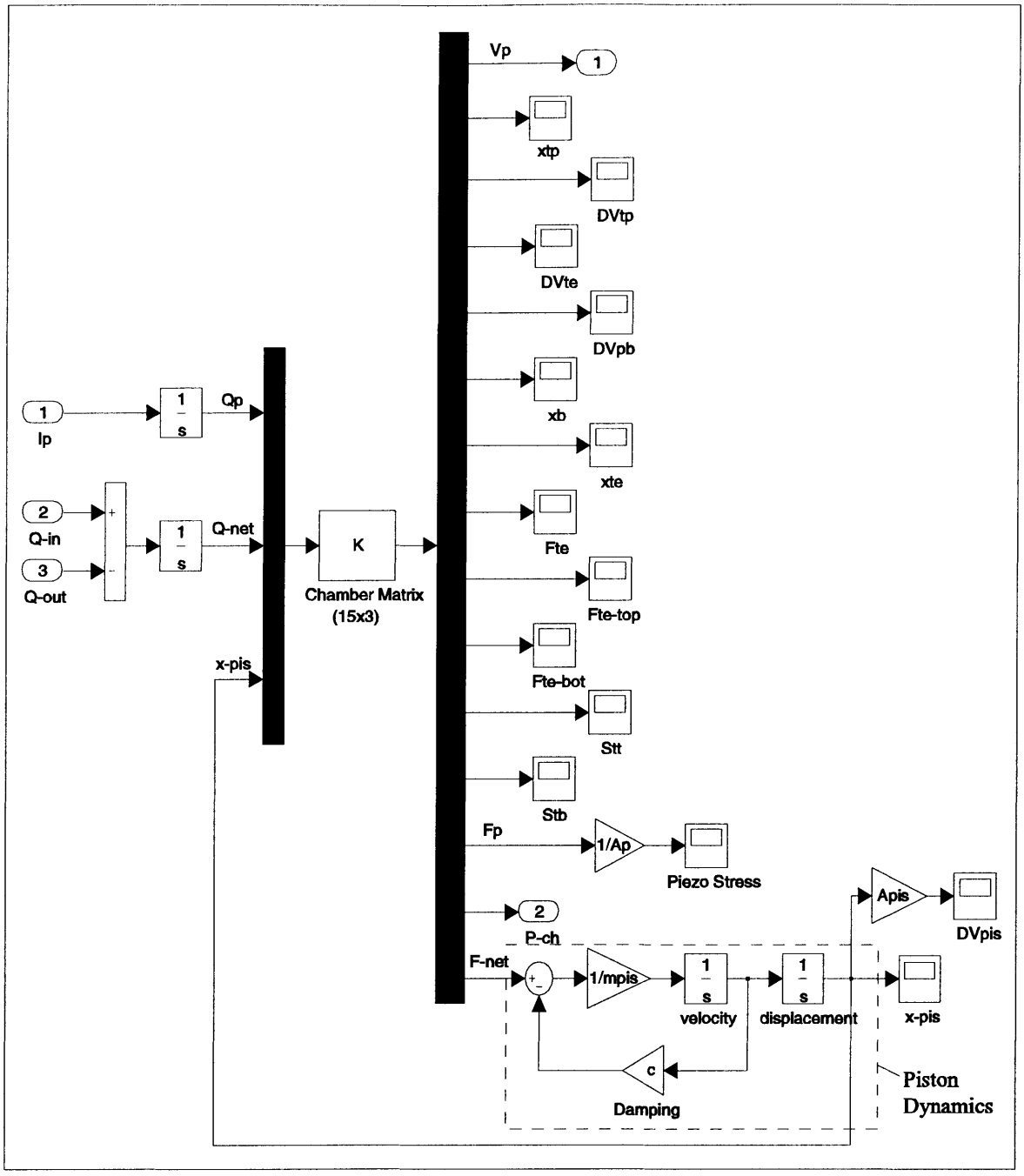


Figure A-6: Simulink model of the main chamber and the piezoelctric element.

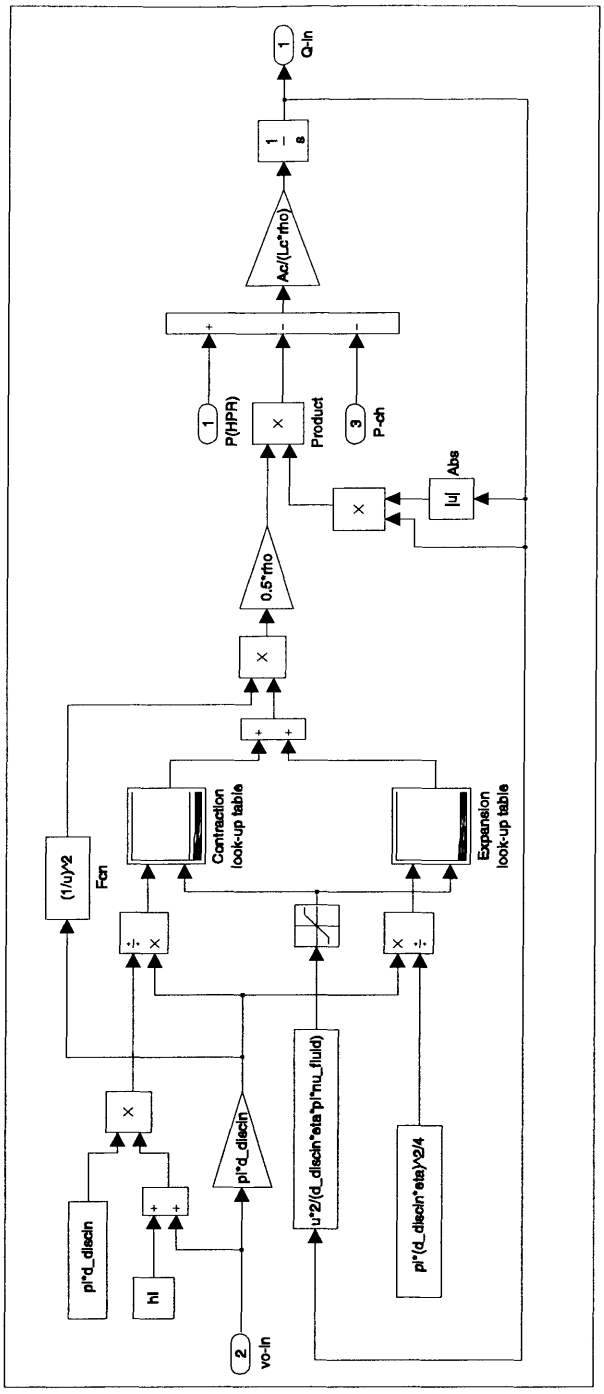


Figure A-7: Simulink model of the inlet valve and fluid channel.

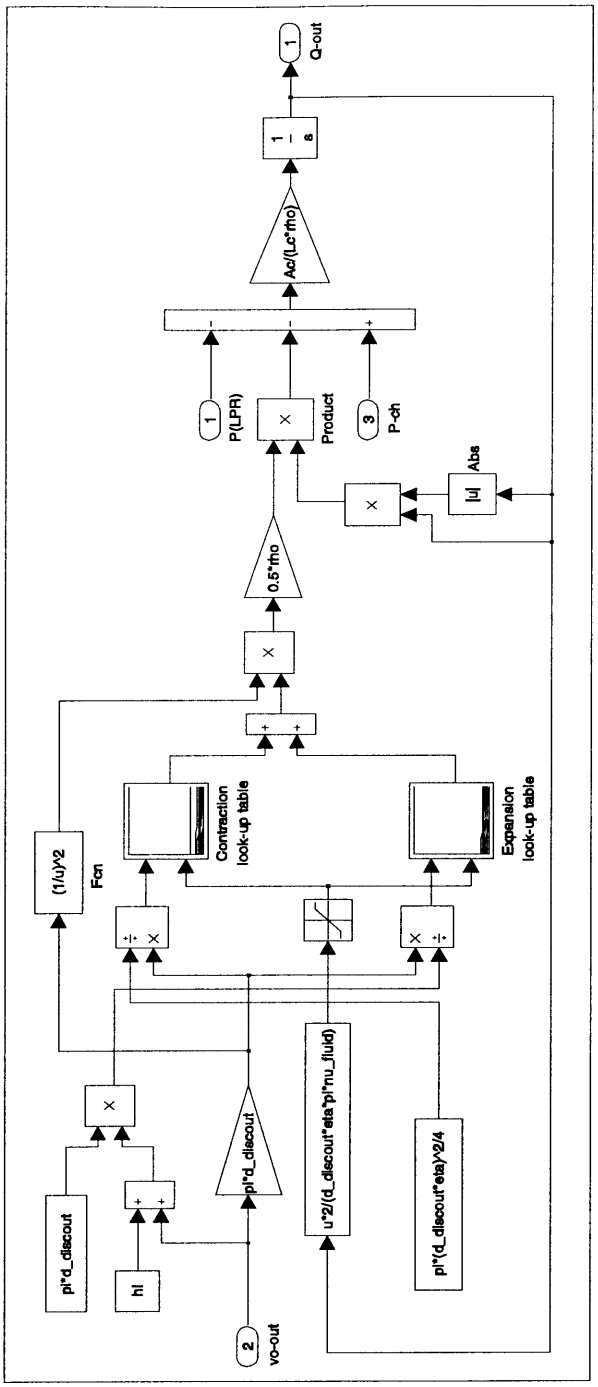


Figure A-8: Simulink model of the outlet valve and fluid channel.

# Appendix B

# Matlab Files

This section presents important Matlab codes used in the thesis.

Figure B-1presents the code used in Chapter 3 to calculate the required frequency, flowrate and efficiency for different circuitry.

Figure B-2 presents the code used to calculate the required frequency, flowrate and efficiency of the system attached to regular diode bridge for different reservoir pressures and chamber diameters in Chapter 5.

Figure B-3 presents the Matlab code used in Chapter 5 for tether optimization. The elastic equations and equations governing the chamber behavior are solved in Maple, which is presented in Appendix C.

Figure B-4 presents the Matlab code used in Chapter 5 which writes the operational and some of the geometric parameters into the Matlab workspace, which can be read by the Simulink model for the system level simulation. Also, the 15x3 matrix required by the Simulink model (Appendix A) is generated, whose coefficients are calculated by Maple, which is presented in Appendix C.

```
% This code calculates the required frequency, flowrate and efficinecy for two different circuitries.
% Effect of tethers is neglected and perfect sealing between the piston and the chamber walls is assumed.

clear all;

% Piezo properties(PZN-4.5%PT)

s33E = 81e-12  ;                        % Closed circuit compliance
s33D = 17e-12 ;                         % Open circuit compliance
Sd   = 10e6;                            % Depolarization stress
PHPR = 2e6 ;                            % High pressure reservoir
W = 0.5 ;                               % Power requirement

% Dimensions

Dpis = (4.5e-3);                        % Piston diameter(=chamber diameter since the effect of tethers is neglected)
Apis = (Dpis^2)*pi/4;                   % Piston area
Ap   = Apis*PHPR/Sd;                    % Piezo area
Dp   = sqrt(4*Ap/pi);                   % Piezo diameter
Lp   = (1e-3) ;                         % Piezo length
Vp   = Ap*Lp ;                          % Piezo volume

% Chamber stiffnes

Keff  = [1e15,2e15,3e15,4e15,5e15,6e15,7e15,8e15,9e15,1e16,2e16,3e16,4e16,5e16,...
        6e16,7e16,8e16,9e16,1e17,2e17,3e17,4e17,5e17,6e17,7e17,8e17,9e17,1e18,2e18,...
        3e18,4e18,5e18,6e18,7e18,8e18,9e18,1e19,2e19,3e19,4e19,5e19,6e19,7e19,8e19,9e19,1e20];

% RECTIFIER

% Energy stored per cycle
Er = ((s33E-s33D).*(Sd).^2.*Vp)./4;

% Required frequency[kHz]
fr = W./Er./1000;

% Required flowrate[ml/s]
Qr = (2.*(s33E+s33D).*W./((s33E-s33D).*PHPR)+(PHPR.*fr.*1000./Keff)).*1e6 ;

% Efficiency
Esysr = (W./((Qr.*1e-6).*PHPR)).*100;


% RECTIFIER+VOLTAGE DETECTOR

% Energy stored per cycle

Es = -(s33D-s33E).*Sd.^2.*Lp.*Ap.*(s33E.*Lp.*Keff.*Apis.^2+Ap).*(s33D.*Lp.*Keff.*Apis.^2+Ap)./...
     ((Ap+2.*s33E.*Lp.*Keff.*Apis.^2-s33D.*Lp.*Keff.*Apis.^2).^2);

% Required frequency[kHz]

fs = W./Es./1000 ;

% Required flowrate[ml/s]

Qs = (W.*(PHPR.^2+2.*s33E.*Lp.*Keff.*Sd.^2.*Ap-s33D.*Lp.*Keff.*Sd.^2.*Ap).*...
     (3.*s33E.*Lp.*Keff.*Sd.^2.*Ap.*PHPR.^2+s33E.*Lp.^2.*Keff.^2.*Sd.^4.*Ap.^2.*s33D+PHPR.^4-PHPR.^2.*s33D.*Lp.*Keff.*Sd.^2.*Ap)./...
     (PHPR.*(s33E.*Lp.*Keff.*Sd.^2.*Ap+PHPR.^2).*(-s33D+s33E).*Ap.*Sd.^2.*Lp.*(PHPR.^2+s33D.*Lp.*Keff.*Sd.^2.*Ap).*Keff)).*1e6;

% Efficiency

Esyss = ((s33E.*Lp.*Keff.*Sd.^2.*Ap+PHPR.^2).*(-s33D+s33E).*Ap.*Sd^2.*Lp.*(PHPR.^2+s33D.*Lp.*Keff.*Sd.^2.*Ap).*Keff./...
        ((PHPR.^2+2.*s33E.*Lp.*Keff.*Sd.^2.*Ap-s33D.*Lp.*Keff.*Sd.^2.*Ap).*...
        (3.*s33E.*Lp.*Keff.*Sd.^2.*Ap.*PHPR.^2+s33E.*Lp.^2.*Keff.^2.*Sd.^4.*Ap.^2.*s33D+PHPR.^4-PHPR.^2.*s33D.*Lp.*Keff.*Sd.^2.*Ap)))*100;


Ceff=1./Keff;                                                   % Effective compliance

figure(1)
h=semilogx(Ceff,Qr,'b--',Ceff,Qs,'r-');
set(h,'LineWidth',2)
title('Study3')
xlabel('Ceff[m^3/Pa]')
ylabel('Flowrate[ml/s]')
legend('Rectifier','Rectifier+Voltage Detector')
grid on
axis([1e-20 1e-15 0 10])

figure(2)
h=semilogx(Ceff,fr,'b--',Ceff,fs,'r-');
set(h,'LineWidth',2)
xlabel('Ceff[m^3/Pa]')
ylabel('Frequency[kHz]')
grid on

figure(3)
h=semilogx(Ceff,Esysr,'b--',Ceff,Esyss,'r-');
set(h,'LineWidth',2)
xlabel('Ceff[m^3/Pa]')
ylabel('System Efficiency[ml/s]')
legend('Rectifier','Rectifier+Voltage Detector')
grid on
```

Figure B-1: Matlab code ised in Chapter 3 to calculate the required frequency, flowrate and efficiency for different circuitry.

```
% This code calculates the required frequency, flowrate and efficiency of
% the system for different reservoir pressures and chamber diameters

clear all;

% Power requirement

W = 0.5 ;                                                    % Power requirement

% Piezo properties(PZN-PT)

s33E = 81e-12  ;                                             % Closed circuit compliance
s33D = 17e-12 ;                                              % Open circuit compliance
Sd   = 10e6;                                                 % Depolarization stress

% Silicon material properties

v    = 0.22;                                                 % Poissons ratio
E    = 165e9 ;                                               % Youngs modulus

% Silicon oil bulk modulus

Bf   = 2e9  ;                                                % Fluid bulk modulus

% Operation condition: varying PHPR

for PHPR = 1e6:1e6:4e6;

% Geometric dimensions

n = 1:0.1:10;

Dch = 1e-3*n ;                                               % Chamber diameter

Hch = 200e-6 ;                                               % Chamber height
Ach =(Dch.^2)*pi/4;                                          % Chamber area
Ap  = Ach.*PHPR./Sd;                                         % Piezo area
Lp  = 1e-3 ;                                                 % Piezo lenght
htp = 1e-3  ;                                                % Top plate thickness

% Calculation of compliances

Cs  = (16.*E.*htp.^3./(pi.*(1-v.^2).*(Dch./2).^6)).^-1;      % Top plate compliance
Cf  = (Bf./(Ach.*Hch)).^-1 ;                                 % Fluidic compliance
Ceff= Cs+Cf;                                                 % Effective compliance

% Calculation of required frequency, flowrate and efficiency

f = 4.*W./((s33E-s33D).*Sd.^2.*Lp.*Ap);                      % Required frequency

Q = 2.*(s33E+s33D).*W./((s33E-s33D).*PHPR)+Ceff.*PHPR.*f;     % Required flowrate

Eff = W./(Q.*PHPR);                                          % Efficiency

% Plotting results

figure(1)
grid
plot(Dch/1e-3,f/1e3)
title('Required frequency vs. piston diameter')
xlabel('Dpis[mm]')
ylabel('f[kHz]')
hold on

figure(2)
grid
plot(Dch/1e-3,Q/1e-6)
title('Required flowrate vs. piston diameter')
xlabel('Dpis[mm]')
ylabel('Q[ml/s]')
hold on

figure(3)
grid
plot(Dch/1e-3,Eff*100)
title('Efficiency vs. piston diameter')
xlabel('Dpis[mm]')
ylabel('Eff[%]')
hold on

end
```

Figure B-2: Matlab code used in Chapter 5 to calculate the required frequency, flowrate and efficiency of the system attached to regular diode bridge for different reservoir pressures and chamber diameters.

```
% Matlab code used in tether structure optimization.(Double layer piston)
% The expressions for kxf, kxp, kvf, kvp, xpt, P, Fpt and Ceff are obtained using Maple.

clear all;

dVf = 1e-10;                          % Input flow volume into the chamber

Dch = 7.2e-3;                         % Chamber diameter
Dp = 3.8e-3;                          % Piezo diameter
Lp = 1e-3;                            % Piezo length
Ap = Dp^2*pi/4;                       % Piezo area
Hch = 200e-6;                         % Chamber height

E = 165e9;                            % Youngs modulus
v = 0.22;                             % Poisson ratio
Bf = 2e9;                             % Bulk modulus
s33D = 81e-12;                        % Open circuit compliance

a = Dch/2;
kp = Ap/s33D/Lp;                      % Piezo stiffness
Vo = Hch*Dch^2*pi/4;                  % Initial volume of chamber

ttopte = 10e-6;
tbotte = 5e-6;

d = E*ttopte^3/(12*(1-v^2));
ds = E*tbotte^3/(12*(1-v^2));

for k= 1:1:2e3;

Dpis = (Dch)-k*0.0005e-3;

b = Dpis/2;
Apis = Dpis^2*pi/4;

% Top tether

kxf = -1/16*(b^4-2*b^2*a^2+4*b^2*a^2*log(a/b)*log(b)+a^4-4*a^2*log(a)^2*b^2+4*a^2*log(a)*b^2*log(b))/(d*pi*(b^2-a^2));
kxp = -1/64*(3*b^6-7*b^4*a^2+4*b^4*log(b)*a^2+5*b^2*a^4-4*b^4*a^2*log(a)-4*b^2*log(b)*a^4+16*b^4*log(b)*a^2*log(a/b)...
      -a^6+4*a^4*b^2*log(a)-16*a^2*log(a)^2*b^4+16*a^2*log(a)*b^4*log(b))/(d*(b^2-a^2));
kvf = 1/64*pi*(16*b^4*log(b)*a^2*log(a/b)+16*a^2*log(a)*b^4*log(b)+5*b^2*a^4-4*b^4*log(b)*a^2+4*b^4*a^2*log(a)+4*b^2*...
      log(b)*a^4-4*a^4*b^2*log(a)-16*a^2*log(a)^2*b^4-a^6-7*b^4*a^2+3*b^6-16*a^4*log(a)*b^2*log(b)-8*b^4*a^2*log(a/b)...
      +16*a^4*log(a)^2*b^2+8*a^4*b^2*log(a/b)-16*a^4*b^2*log(a/b)*log(a))/(d*pi*(b^2-a^2));
kvp = 1/192*pi*(24*a^4*b^4*log(a/b)+24*a^4*b^4-22*b^6*a^2+a^8+7*b^8-48*a^4*b^4*log(a/b)*log(a)-48*a^4*log(a)*b^4*log(b)...
      +48*a^4*log(a)^2*b^4+48*b^6*a^2*log(a/b)*log(b)+48*b^6*a^2*log(a)*log(b)-48*b^6*a^2*log(a)^2-24*b^6*a^2*log(a/b)-...
      10*a^6*b^2)/(d*(b^2-a^2));

% Bottom tether

kxfb = 1/8*b^2*log(b)/(pi*ds)-1/8*b^2/(pi*ds)+1/16*(-2*a^2*log(a)+a^2+2*b^2*log(b)-b^2)*b^2/(pi*ds*(a^2-b^2))+1/4*b^2*...
       a^2*log(a/b)*log(b)/(pi*ds*(a^2-b^2))+1/16*a^2*(a^2-2*b^2*log(b)-b^2-4*b^2*log(a)^2+2*b^2*log(a)+4*b^2*log(a)*...
       log(b))/(pi*ds*(a^2-b^2));

% Overall equations

xpis = -kxfb*(kxf*Apis-kxp)*dVf*Bf/(kxfb*Vo+kxfb*Bf*kvf*Apis-kxfb*Bf*kvp+kxf*Vo-kxf*Bf*kvp+kxf*kp*kxfb*Vo-kxf*kp*kxfb*...
       Bf*kvp+kxf*Apis^2*Bf*kxfb+kxp*Bf*kvf+kxp*Bf*kvf*kp*kxfb-kxp*Bf*kxfb*Apis);
P = Bf*dVf*(kxfb+kxf+kxf*kp*kxfb)/(kxfb*Vo+kxfb*Bf*kvf*Apis-kxfb*Bf*kvp+kxf*Vo-kxf*Bf*kvp+kxf*kp*kxfb*Vo-kxf*kp*kxfb*Bf...
    *kvp+kxf*Apis^2*Bf*kxfb+kxp*Bf*kvf+kxp*Bf*kvf*kp*kxfb-kxp*Bf*kxfb*Apis);
Ceff = Vo/Bf+(kxfb*kvf*Apis+kxp*kvf+kxp*kvf*kp*kxfb-kxfb*kvp-kxf*kvp-kxf*kp*kxfb*kvp)/(kxfb+kxf+kxf*kp*kxfb);

xp(k)    = xpis;
Pch(k)   = P;
Comp(k)  = Ceff;
Dpisn(k) = Dpis;

end

figure(2)
subplot(3,1,1)
plot((Dch-Dpisn)*1e6/2,xp/1e-6)
hold on
title('Dch fixed,Dpis varied')
ylabel('Piston Deflection[um]')
grid
subplot(3,1,2)
plot((Dch-Dpisn)*1e6/2,Pch/1e6)
hold on
ylabel('Chamber Pressure[MPa]')
grid
subplot(3,1,3)
semilogy((Dch-Dpisn)*1e6/2,Comp)
hold on
ylabel('Ceff[m^3/Pa]')
xlabel('tether width')
grid
```

Figure B-3: Matlab code used for tether optimization.

```
% This code writes the system parameters to the Matlab workspace to be read by Simulink.
% It also generates the 15x3 matrix used in Simulink, whose coefficients are calculated using Maple.

clear all;

% Fluid Properties

rho        = 760          ;                    % fluid density [kg/m^3];
nu_fluid   = 0.65e-6;                       % viscosity [m^2/sec];
mu_fluid   = rho*nu_fluid;                     % viscosity [Pa/sec];

% Valve geometry

d_discin = 2*400e-6 ;                          % inlet  valve cap diameter[m];
d_discout= d_discin ;                           % outlet valve cap diameter[m];

hI    = 100e-6;
eta   = 0.965 ;

% Valve Channel Geometry

lk    = 5e-7 ;                                 % Leakage[m]

Lc    = 5000;                                  % Channel length
Ac    = 1;                                     % Channel area

% Note: Since only L/A ratio is important in this study,
% no exact channel geometry is defined, only the ratio is determined.

% Diode Properties for the rectifier circuit

T = 300;
k = 1.38e-23;
eta = 17.25/5;
q = 1.6e-19;
Io = 1e-6;

% Operation Conditions

voi    = 24e-6 ;                               % Inlet valve opening[m]

voo    = 24e-6 ;                               % Oulet valve opening[m]

wn = 20000 ;                                   % Operation frequency[Hz]

Vb = 74.9;                                     % Battery Voltage[V]

PHPR = 3e6;                                    % High Presure Reservoire Pressure

PLPR = 0.5e6;                                  % Low Presure Reservoire Pressure


% Expansion look-up table

Re = [0, 0.05,0.1,0.2,0.3,0.4,0.5,0.6,0.9] ;

Ce = [1,10,15,20,30,40,50,100,2e2,5e2,1e3,2e3,3e3,1e15] ;

Te = [33,3.1,3.5,3.04,2.7,2.42,2.32,1.92,1.94,2.07,2.45,1.92,1.25,0.98;
      33,3.1,3.3,3.02,2.56,2.29,2.13,1.83,1.79,1.89,2.23,1.76,1.13,0.9;
      33,3.1,3.2,3,2.4,2.15,1.95,1.7,1.65,1.7,2,1.6,1,0.81;
      33,3.1,3.2,2.8,2.2,1.85,1.65,1.4,1.3,1.3,1.6,1.25,0.7,0.64;
      33,3.1,3.1,2.6,2.,1.6,1.4,1.2,1.1,1.1,1.3,0.95,0.6,0.5;
      33,3.1,3.0,2.4,1.8,1.5,1.3,1.1,1.,0.85,1.05,0.8,0.4,0.36;
      33,3.1,2.8,2.3,1.65,1.35,1.15,0.9,0.75,0.65,0.9,0.65,0.3,0.25;
      33,3.1,2.7,2.15,1.55,1.25,1.05,0.8,0.6,0.4,0.6,0.5,0.2,0.16;
      33,3.1,2.6,2,1.4,1.1,0.9,0.4,0.3,0.1,8e-2,5e-2,2e-2,1.8e-2] ;


% Contraction look-up table

Rc = [0,0.1,0.2,0.3,0.4,0.5,0.6,1]  ;

Cc = [1,10,20,30,40,50,1e2,2e2,5e2,1e3,2e3,4e3,5e3,1e4,1e15] ;

Tc = [30,5,3.3,2.5,2.16,1.98,1.4,1.13,0.94,0.77,0.6,0.97,0.92,0.6,1;
      30,5,3.2,2.4,2,1.8,1.3,1.04,0.82,0.64,0.5,0.8,0.75,0.50,0.45;
      30,5,3.1,2.3,1.84,1.62,1.2,0.95,0.7,0.5,0.4,0.6,0.6,0.4,0.4;
      30,5.,2.95,2.15,1.7,1.5,1.1,0.85,0.6,0.44,0.30,0.55,0.55,0.35,0.35;
      30,5.,2.8,2.0,1.6,1.4,1,0.78,0.5,0.35,0.25,0.45,0.5,0.3,0.3;
      30,5,2.7,1.8,1.46,1.3,0.9,0.65,0.42,0.3,0.2,0.4,0.42,0.25,0.25;
      30,5,2.6,1.7,1.35,1.2,0.8,0.56,0.35,0.24,0.15,0.35,0.35,0.20,0.20;
      30,5,2.6,1.7,1.20,0.8,0.6,0.40,0.15,0.01,0.05,0.15,0.15,0.10,0.10]  ;


% Preparation of the matrix to be fed into Simulink

ThesisSimMatrix;     % Read in matrix values from ThesisSimMatrix.m

for i=1:15
   for j=1:3
      eval(['Amatrix(i,j)=A' num2str(i)num2str(j) ';']);
   end
end
```

Figure B-4: Matlab code used for writing system parameters into the workplace to be read by the Simulink model for the system level simulation.

# Appendix C

# Maple Files

This section presents important Maple files used in the Thesis.

The first two codes are the Maple files used for tether optimization in Chapter 5. The first one solves the elastic equations of the tether structures. The second one solves the governing equation for the chamber behavior. The coefficients calculated are then fed to the Matlab code used for tether optimization presented in Appendix B.

The third code solves the elastic equations of all the structural components within the system along with the equations governing the chamber continuity and piezoelectric element behavior. The equations are solved and the coefficients for the 15x3 matrix required by the Simulink model architecture, which is described in Chapter 4, are calculated. These coefficients are written in a Matlab m.file which are then read by another Matlab code (Appendix B) to generate the 15x3 matrix. The assumptions and derivation of these equations are presented in Chapter 4.

This file solves the elastic equations corresponding to the tether structure.
Double layer piston is considered.
It is assumed that everything except the tethers are rigid.

```
> restart;
> Digits:=40:
```

## Top tether

### Define governing DE for bending of circular plate and shear force

Governing DE

```
> eqn:='diff(1/r*diff(r*diff(w(r),r),r),r)=Q(r)/d':
```

Shear force in terms of Pch(chamber pressure) and Fpt (force applied by the piston on the top tether)

```
> Q(r):=Fpt/(2*Pi*r)-(1/2)*P*(r^2-b^2)/r:
```

### Integrate the DE

```
> Q1(r):=(int(Q(r)/d,r)+C1)*r:
> Q2(r):=(int(Q1(r),r)+C2)/r:
> w(r):=int(Q2(r),r)+C3:
```

### Apply BC's

```
> BC1:=subs({r=a},w(r))=0:
> BC2:=subs({r=a},diff(w(r),r))=0:
> BC3:=subs({r=b},diff(w(r),r))=0:
> Set:=solve({BC1,BC2,BC3},{C1,C2,C3}):
> W(r):=subs(Set,w(r)):
```

### Calculation of linear coefficients for deflection and swept volume

```
> kxf:=subs({P=0,Fpt=1},subs({r=b},W(r))):
> kxp:=subs({P=1,Fpt=0},subs({r=b},W(r))):
> kvf:=subs({P=0,Fpt=1},collect(simplify(int(2*pi*r*W(r),r=b..a)),{d,P})):
> kvp:=subs({P=1,Fpt=0},collect(simplify(int(2*pi*r*W(r),r=b..a)),{d,P})):
```

## Bottom tether

### Define governing DE for bending of circular plate and shear force

Governing DE

```
> eqn:='diff(1/r*diff(r*diff(w(r),r),r),r)=Q(r)/ds':
```

Shear force in terms of Fpb (force applied by the piston on the bottom tether)

```
> Q(r):=Fpb/(2*Pi*r):
```

### Integrate the DE

```
> Q1(r):=(int(Q(r)/ds,r)+C1)*r:
> Q2(r):=(int(Q1(r),r)+C2)/r:
>
> w(r):=int(Q2(r),r)+C3:
```

### Apply BC's

```
> BC1:=subs({r=a},w(r))=0:
> BC2:=subs({r=a},diff(w(r),r))=0:
> BC3:=subs({r=b},diff(w(r),r))=0:
> Set:=solve({BC1,BC2,BC3},{C1,C2,C3}):
> W(r):=subs(Set,w(r)):
```

### Calculation of linear coefficient for deflection

```
> kxfb:=subs({P=0,Fpb=1},subs({r=b},W(r))):
```

File: Comp1.mws
This file solves the overall equations governing the chamber behavior including piston deflection, swept volume, chamber pressure, force on piezo and force on tethers.
Also the effective compliance of the system is calculated. The elastic equations governing the tether behavior are calculated using another maple file.
The results of both maple files are then fed to Matlab for tether structure optimization.

```
> restart;
> Digits:=40:
```

**Equations Governing top tether deflection**

```
> eqn1:=xpis=kxf*Fpt+kxp*P:
> eqn2:=dVt=kvf*Fpt+kvp*P:
```

**Equation Governing bottom tether deflection**

```
> eqn3:=xpis=kxfb*Fpb:
```

**Force Balance at piston-tether connection**

```
> eqn4:=Fp=Fpt+Fpb:
```

**Fluid Compliance**

```
> eqn5:=P=((dVf+dVt+xpis*Apis)/(Vo))*Bf:
```

**Piston and Piezo**

```
> eqn6:=P*Apis+Fp+kp*xpis=0:
```

**Solve equations for input dVf**

```
> sys:=solve({eqn1,eqn2,eqn3,eqn4,eqn5,eqn6},{xpis,Fp,dVt,P,Fpt,Fpb}):
> assign(sys);
> Ceff:=collect(simplify((dVf+xpis*Apis)/P),{Vo,Bf}):
```

*File: ThesisSimComp.mws*

Within the simulink model, an 15 x 3 matrix is needed, which takes as inputs ( Qp, Qnet, xpis) and solves for the outputs (Vp, xtp, DVtp, DVte, DVpb, xb, xte, Fte, Fte-top, Fte-bot, Stt, Stb, Fp, Pch, Fnet).

This code calculates the coeficients of this matrix.

```
> restart;
> Digits:=40:
```

# Governing Equations

## Top support structure

```
> EQN1 := x[tp]=k[dtp]*P[ch]:
> EQN2 := DV[tp]=k[tp]*P[ch]:
```

## Bottom Support Stucture

```
> EQN3 := x[b] = k[b]*F[p]:
```

## Piston

```
> EQN4 := x[pis]-x[te]=k[p1]*F[p]+k[p2]*P[ch]:
> EQN5 := DV[pb]=k[p3]*F[p]+k[p4]*P[ch]:
> EQN6 := F[net]=-A[pis]*P[ch]+F[p]-F[te]:
```

## Piston Tethers

```
> EQN7 := x[te]=k[tt1]*F[tetop]+k[tt2]*P[ch]:
> EQN8 := DV[te]=k[tt3]*F[tetop]+k[tt4]*P[ch]:
> EQN9 := Str[tt]=s[tt1]*F[tetop]+s[tt2]*P[ch]:
> EQN10 := x[te]=k[tb]*F[tebot]:
> EQN11 := Str[tb]=s[tb]*F[tebot]:
> EQN12 := F[te]=F[tetop]+F[tebot]:
```

## Chamber continuity

```
> EQN13 := P[ch]=B[f]/V[o]*(Q[net]+x[pis]*A[pis]+DV[pb]+DV[te]-DV[tp]):
```

## Piezoelectric Material

Linear constituive relations.

```
> EQN14 := x[b]-x[pis] = L[p]/A[p]*(sD[33]*F[p]+d[33]/eT[33]*Q[p]):
> EQN15 := V[p] = L[p]/A[p]*(d[33]/eT[33]*F[p]-1/eT[33]*Q[p]):
```

# Geometric and Material Parameters

Geometric Parameters:

```
> L[p]:=1e-3: d[p]:=3.8e-3: A[p]:=(Pi*d[p]^2)/4:
> d[pis]:=6.95e-3: w[t]:=125e-6: d[ch]:=d[pis]+2*w[t]: t[pis]:=800e-6:
  A[pis]:=(Pi*d[pis]^2)/4:
> t[tetop]:=10e-6: t[tebot]:=5e-6:
> t[bot]:=2500e-6: t[top]:=2500e-6:
> H[ch]:=200e-6: V[o]:=Pi*(d[ch]^2/4)*H[ch]:
```

Material Parameters:

```
> d[33]:=1780e-12: sD[33]:=17e-12: sE[33]:=81e-12: eT[33]:=d[33]^2/(sE[33]-sD[33]):
> E[si]:=165e9: nu[si]:=0.22: B[f]:=2e9: rho[si]:=2230: M[pis]:=rho[si]*A[pis]*t[pis]:
```

# Calculate Linear Plate Coefficients

## Top Support Structure

Circular plate clambed at its outer radius(r=a).

Positive deflection is upward.

```
> eqn:='diff(1/r*diff(r*diff(Z(r),r),r),r)=Q(r)/Ds':
> Q(r):=P[ch]*r/2:
```

```
> Q1(r):=(int(Q(r)/Ds,r)+C1)*r:
> Q2(r):=(int(Q1(r),r)+C2)/r:
> wtp(r):=subs({C2=0},int(Q2(r),r)+C3):
> BC1:=subs({r=a},wtp(r))=0:
> BC2:=subs({r=a},diff(wtp(r),r))=0:
> Set:=solve({BC1,BC2},{C1,C3}):
> Wtp:=simplify(subs(Set,wtp(r))):
> DVtp:=int(2*Pi*r*Wtp,r=0..a):
> Wtpo:=subs({r=0},Wtp):
> k[dtp]:=subs({P[ch]=1},Wtpo):
> k[dtp]:=evalf(subs({a=d[ch]/2, Ds=E[si]*t[top]^3/(12*(1-nu[si]^2))},k[dtp])):
> k[tp]:=subs({P[ch]=1},DVtp):
> k[tp]:=evalf(subs({a=d[ch]/2, Ds=E[si]*t[top]^3/(12*(1-nu[si]^2))},k[tp])):
```

## Bottom Suport Structure

Circular plate with a circular hole at the center which is clamped at its outer radius(r=a) and guided at its inner radius(r=b).
Positive deflection is upward.

```
> eqn:='diff(1/r*diff(r*diff(Z(r),r),r),r)=Q(r)/Ds':
> Q(r):=-F[p]/2/Pi/r:
> Q1(r):=(int(Q(r)/Ds,r)+C1)*r:
> Q2(r):=(int(Q1(r),r)+C2)/r:
> wb(r):=int(Q2(r),r)+C3:
> BC1:=subs({r=a},wb(r))=0:
> BC2:=subs({r=a},diff(wb(r),r))=0:
> BC3:=subs({r=b},diff(wb(r),r))=0:
> Set:=solve({BC1,BC2,BC3},{C1,C2,C3}):
> Wb:=simplify(subs(Set,wb(r))):
> k[b]:=simplify(subs({F[p]=1},subs({r=b},Wb))):
> k[b]:=evalf(subs({a=d[ch]/2, b=d[p]/2, Ds=E[si]*t[bot]^3/(12*(1-nu[si]^2))},k[b])):
```

## Piston

Circular plate with a circular hole at the center which is simply supported at its outer radius(r=a) and guided at its inner radius(r=b).
Positive deflection is upward.

```
> eqn:='diff(1/r*diff(r*diff(Z(r),r),r),r)=Q(r)/Ds':
> Q(r):=F[p]/2/Pi/r-P[ch]*r/2:
> Q1(r):=(int(Q(r)/Ds,r)+C1)*r:
> Q2(r):=(int(Q1(r),r)+C2)/r:
> wp(r):=int(Q2(r),r)+C3:
> BC1:=subs({r=a},wp(r))=0:
> BC2:=subs({r=a},diff(wp(r),r$2)+nu/r*diff(wp(r),r))=0:
> BC3:=subs({r=b},diff(wp(r),r))=0:
> Set:=solve({BC1,BC2,BC3},{C1,C2,C3}):
> Wp:=simplify(subs(Set,wp(r))):
> DVpb:=simplify(int(2*Pi*r*Wp,r=0..a)):
> k[p1]:=simplify(subs({P[ch]=0,F[p]=1},subs({r=b},Wp))):
> k[p1]:=evalf(subs({a=d[pis]/2, b=d[p]/2, Ds=E[si]*t[pis]^3/(12*(1-nu[si]^2)),
  nu=nu[si]},k[p1])):
> k[p2]:=simplify(subs({P[ch]=1,F[p]=0},subs({r=b},Wp))):
> k[p2]:=evalf(subs({a=d[pis]/2, b=d[p]/2, Ds=E[si]*t[pis]^3/(12*(1-nu[si]^2)),
  nu=nu[si]},k[p2])):
> k[p3]:=simplify(subs({P[ch]=0,F[p]=1},DVpb)):
> k[p3]:=evalf(subs({a=d[pis]/2, b=d[p]/2, Ds=E[si]*t[pis]^3/(12*(1-nu[si]^2)),
  nu=nu[si]},k[p3])):
> k[p4]:=simplify(subs({P[ch]=1,F[p]=0},DVpb)):
> k[p4]:=evalf(subs({a=d[pis]/2, b=d[p]/2, Ds=E[si]*t[pis]^3/(12*(1-nu[si]^2)),
  nu=nu[si]},k[p4])):
```

## Drive Element Tethers

**Top Tether**

Annular plate clamped at outer radius (r=a) and guided at inner radius (r=b) with pressure applied downward over tether and concentrated force applied upward at inner radius (r=b).

```
> eqn:='diff(1/r*diff(r*diff(Z(r),r),r),r)=Q(r)/Ds':
> Q(r):=F[tetop]/(2*Pi*r)-P[ch]*(r^2-b^2)/(2*r):
> Q1(r):=(int(Q(r)/Ds,r)+C1)*r:
> Q2(r):=(int(Q1(r),r)+C2)/r:
> wtt(r):=int(Q2(r),r)+C3:
> BC1:=subs({r=a},wtt(r))=0:
> BC2:=subs({r=a},diff(wtt(r),r))=0:
> BC3:=subs({r=b},diff(wtt(r),r))=0:
> Set:=solve({BC1,BC2,BC3},{C1,C2,C3}):
> Wtt:=simplify(subs(Set,wtt(r))):
> DVtt:=simplify(int(2*Pi*r*Wtt,r=b..a)):
> k[tt1]:=simplify(subs({P[ch]=0,F[tetop]=1},subs({r=b},Wtt))):
> k[tt1]:=evalf(subs({a=d[ch]/2, b=d[pis]/2,
  Ds=E[si]*t[tetop]^3/(12*(1-nu[si]^2))},k[tt1])):
> k[tt2]:=simplify(subs({P[ch]=1,F[tetop]=0},subs({r=b},Wtt))):
> k[tt2]:=evalf(subs({a=d[ch]/2, b=d[pis]/2,
  Ds=E[si]*t[tetop]^3/(12*(1-nu[si]^2))},k[tt2])):
> k[tt3]:=simplify(subs({P[ch]=0,F[tetop]=1},DVtt)):
> k[tt3]:=evalf(subs({a=d[ch]/2, b=d[pis]/2,
  Ds=E[si]*t[tetop]^3/(12*(1-nu[si]^2))},k[tt3])):
> k[tt4]:=simplify(subs({P[ch]=1,F[tetop]=0},DVtt)):
> k[tt4]:=evalf(subs({a=d[ch]/2, b=d[pis]/2,
  Ds=E[si]*t[tetop]^3/(12*(1-nu[si]^2))},k[tt4])):
> Stt:=simplify(6*(Ds*(diff(Wtt,r$2)+nu/r*diff(Wtt,r)))/(h^2)):
> s[tt1]:=simplify(subs({P[ch]=0,F[tetop]=1},subs({r=a},Stt))):
> s[tt1]:=evalf(subs({a=d[ch]/2, b=d[pis]/2, Ds=E[si]*t[tetop]^3/(12*(1-nu[si]^2)),
  nu=nu[si], h=t[tetop]},s[tt1])):
> s[tt2]:=simplify(subs({P[ch]=1,F[tetop]=0},subs({r=a},Stt))):
> s[tt2]:=evalf(subs({a=d[ch]/2, b=d[pis]/2, Ds=E[si]*t[tetop]^3/(12*(1-nu[si]^2)),
  nu=nu[si], h=t[tetop]},s[tt2])):
```

**Bottom Tether**

Annular plate clamped at outer radius (r=a) and guided at inner radius (r=b) with concentrated force applied upward at inner radius (r=b).

```
> eqn:='diff(1/r*diff(r*diff(Z(r),r),r),r)=Q(r)/Ds':
> Q(r):=F[tebot]/(2*Pi*r):
> Q1(r):=(int(Q(r)/Ds,r)+C1)*r:
> Q2(r):=(int(Q1(r),r)+C2)/r:
> wtb(r):=int(Q2(r),r)+C3:
> BC1:=subs({r=a},wtb(r))=0:
> BC2:=subs({r=a},diff(wtb(r),r))=0:
> BC3:=subs({r=b},diff(wtb(r),r))=0:
> Set:=solve({BC1,BC2,BC3},{C1,C2,C3}):
> Wtb:=simplify(subs(Set,wtb(r))):
> k[tb]:=simplify(subs({F[tebot]=1},subs({r=b},Wtb))):
> k[tb]:=evalf(subs({a=d[ch]/2, b=d[pis]/2, Ds=E[si]*t[tebot]^3/(12*(1-nu[si]^2)),
  nu=nu[si]},k[tb])):
> Stb:=simplify(6*(Ds*(diff(Wtb,r$2)+nu/r*diff(Wtb,r)))/(h^2)):
> s[tb]:=simplify(subs({F[tebot]=1},subs({r=a},Stb))):
> s[tb]:=evalf(subs({a=d[ch]/2, b=d[pis]/2, Ds=E[si]*t[tebot]^3/(12*(1-nu[si]^2)),
  nu=nu[si], h=t[tebot]},s[tb])):
```

## Solve Equations

In the Simulink model, the inputs to the matrix block are $Q_D$, Onet and xpis. It is desired to solve for each of the output variables in

terms of these inputs. The output variables are Vp,xtp,DVtp,DVte,DVpb,xb,xte,Fte,Fte-top,Fte-bot,Stt,Stb,Fp,Pch,Fnet. Once solved, each of the coefficients is assigned to the proper location in the matrix.
All the matrix coefficients are then fed to matlab matrix file, which is then called by a matlab preparation file to run the Simulink model.

```
> Solutions:=solve({EQN1,EQN2,EQN3,EQN4,EQN5,EQN6,EQN7,EQN8,EQN9,EQN10,EQN11,EQN12,EQN13
  ,EQN14,EQN15},{V[p],x[tp],DV[tp],DV[te],DV[pb],x[b],x[te],F[te],F[tetop],F[tebot],Str[
  tt],Str[tb],F[p],P[ch],F[net]}):
> A11:=evalf(subs({Q[p]=1,Q[net]=0,x[pis]=0},subs(Solutions,V[p]))):
> A12:=evalf(subs({Q[p]=0,Q[net]=1,x[pis]=0},subs(Solutions,V[p]))):
> A13:=evalf(subs({Q[p]=0,Q[net]=0,x[pis]=1},subs(Solutions,V[p]))):
> A21:=evalf(subs({Q[p]=1,Q[net]=0,x[pis]=0},subs(Solutions,x[tp]))):
> A22:=evalf(subs({Q[p]=0,Q[net]=1,x[pis]=0},subs(Solutions,x[tp]))):
> A23:=evalf(subs({Q[p]=0,Q[net]=0,x[pis]=1},subs(Solutions,x[tp]))):
> A31:=evalf(subs({Q[p]=1,Q[net]=0,x[pis]=0},subs(Solutions,DV[tp]))):
> A32:=evalf(subs({Q[p]=0,Q[net]=1,x[pis]=0},subs(Solutions,DV[tp]))):
> A33:=evalf(subs({Q[p]=0,Q[net]=0,x[pis]=1},subs(Solutions,DV[tp]))):
> A41:=evalf(subs({Q[p]=1,Q[net]=0,x[pis]=0},subs(Solutions,DV[te]))):
> A42:=evalf(subs({Q[p]=0,Q[net]=1,x[pis]=0},subs(Solutions,DV[te]))):
> A43:=evalf(subs({Q[p]=0,Q[net]=0,x[pis]=1},subs(Solutions,DV[te]))):
> A51:=evalf(subs({Q[p]=1,Q[net]=0,x[pis]=0},subs(Solutions,DV[pb]))):
> A52:=evalf(subs({Q[p]=0,Q[net]=1,x[pis]=0},subs(Solutions,DV[pb]))):
> A53:=evalf(subs({Q[p]=0,Q[net]=0,x[pis]=1},subs(Solutions,DV[pb]))):
> A61:=evalf(subs({Q[p]=1,Q[net]=0,x[pis]=0},subs(Solutions,x[b]))):
> A62:=evalf(subs({Q[p]=0,Q[net]=1,x[pis]=0},subs(Solutions,x[b]))):
> A63:=evalf(subs({Q[p]=0,Q[net]=0,x[pis]=1},subs(Solutions,x[b]))):
> A71:=evalf(subs({Q[p]=1,Q[net]=0,x[pis]=0},subs(Solutions,x[te]))):
> A72:=evalf(subs({Q[p]=0,Q[net]=1,x[pis]=0},subs(Solutions,x[te]))):
> A73:=evalf(subs({Q[p]=0,Q[net]=0,x[pis]=1},subs(Solutions,x[te]))):
> A81:=evalf(subs({Q[p]=1,Q[net]=0,x[pis]=0},subs(Solutions,F[te]))):
> A82:=evalf(subs({Q[p]=0,Q[net]=1,x[pis]=0},subs(Solutions,F[te]))):
> A83:=evalf(subs({Q[p]=0,Q[net]=0,x[pis]=1},subs(Solutions,F[te]))):
> A91:=evalf(subs({Q[p]=1,Q[net]=0,x[pis]=0},subs(Solutions,F[tetop]))):
> A92:=evalf(subs({Q[p]=0,Q[net]=1,x[pis]=0},subs(Solutions,F[tetop]))):
> A93:=evalf(subs({Q[p]=0,Q[net]=0,x[pis]=1},subs(Solutions,F[tetop]))):
> A101:=evalf(subs({Q[p]=1,Q[net]=0,x[pis]=0},subs(Solutions,F[tebot]))):
> A102:=evalf(subs({Q[p]=0,Q[net]=1,x[pis]=0},subs(Solutions,F[tebot]))):
> A103:=evalf(subs({Q[p]=0,Q[net]=0,x[pis]=1},subs(Solutions,F[tebot]))):
> A111:=evalf(subs({Q[p]=1,Q[net]=0,x[pis]=0},subs(Solutions,Str[tt]))):
> A112:=evalf(subs({Q[p]=0,Q[net]=1,x[pis]=0},subs(Solutions,Str[tt]))):
> A113:=evalf(subs({Q[p]=0,Q[net]=0,x[pis]=1},subs(Solutions,Str[tt]))):
> A121:=evalf(subs({Q[p]=1,Q[net]=0,x[pis]=0},subs(Solutions,Str[tb]))):
> A122:=evalf(subs({Q[p]=0,Q[net]=1,x[pis]=0},subs(Solutions,Str[tb]))):
> A123:=evalf(subs({Q[p]=0,Q[net]=0,x[pis]=1},subs(Solutions,Str[tb]))):
> A131:=evalf(subs({Q[p]=1,Q[net]=0,x[pis]=0},subs(Solutions,F[p]))):
> A132:=evalf(subs({Q[p]=0,Q[net]=1,x[pis]=0},subs(Solutions,F[p]))):
> A133:=evalf(subs({Q[p]=0,Q[net]=0,x[pis]=1},subs(Solutions,F[p]))):
> A141:=evalf(subs({Q[p]=1,Q[net]=0,x[pis]=0},subs(Solutions,P[ch]))):
> A142:=evalf(subs({Q[p]=0,Q[net]=1,x[pis]=0},subs(Solutions,P[ch]))):
> A143:=evalf(subs({Q[p]=0,Q[net]=0,x[pis]=1},subs(Solutions,P[ch]))):
> A151:=evalf(subs({Q[p]=1,Q[net]=0,x[pis]=0},subs(Solutions,F[net]))):
> A152:=evalf(subs({Q[p]=0,Q[net]=1,x[pis]=0},subs(Solutions,F[net]))):
> A153:=evalf(subs({Q[p]=0,Q[net]=0,x[pis]=1},subs(Solutions,F[net]))):
```

## Generation of output matrix to Matlab file

Output matrix coefficiente values to a file which Matlab/Simulink can read.

```
> interface(echo=0);
> writeto(`ThesisSimMatrix.m`);
```

Page 4

```
[ > printf(`A11 = %+2.08e;`,A11);
[ > printf(`A12 = %+2.08e;`,A12);
[ > printf(`A13 = %+2.08e;`,A13);
[ > printf(`A21 = %+2.08e;`,A21);
[ > printf(`A22 = %+2.08e;`,A22);
[ > printf(`A23 = %+2.08e;`,A23);
[ > printf(`A31 = %+2.08e;`,A31);
[ > printf(`A32 = %+2.08e;`,A32);
[ > printf(`A33 = %+2.08e;`,A33);
[ > printf(`A41 = %+2.08e;`,A41);
[ > printf(`A42 = %+2.08e;`,A42);
[ > printf(`A43 = %+2.08e;`,A43);
[ > printf(`A51 = %+2.08e;`,A51);
[ > printf(`A52 = %+2.08e;`,A52);
[ > printf(`A53 = %+2.08e;`,A53);
[ > printf(`A61 = %+2.08e;`,A61);
[ > printf(`A62 = %+2.08e;`,A62);
[ > printf(`A63 = %+2.08e;`,A63);
[ > printf(`A71 = %+2.08e;`,A71);
[ > printf(`A72 = %+2.08e;`,A72);
[ > printf(`A73 = %+2.08e;`,A73);
[ > printf(`A81 = %+2.08e;`,A81);
[ > printf(`A82 = %+2.08e;`,A82);
[ > printf(`A83 = %+2.08e;`,A83);
[ > printf(`A91 = %+2.08e;`,A91);
[ > printf(`A92 = %+2.08e;`,A92);
[ > printf(`A93 = %+2.08e;`,A93);
[ > printf(`A101 = %+2.08e;`,A101);
[ > printf(`A102 = %+2.08e;`,A102);
[ > printf(`A103 = %+2.08e;`,A103);
[ > printf(`A111 = %+2.08e;`,A111);
[ > printf(`A112 = %+2.08e;`,A112);
[ > printf(`A113 = %+2.08e;`,A113);
[ > printf(`A121 = %+2.08e;`,A121);
[ > printf(`A122 = %+2.08e;`,A122);
[ > printf(`A123 = %+2.08e;`,A123);
[ > printf(`A131 = %+2.08e;`,A131);
[ > printf(`A132 = %+2.08e;`,A132);
[ > printf(`A133 = %+2.08e;`,A133);
[ > printf(`A141 = %+2.08e;`,A141);
[ > printf(`A142 = %+2.08e;`,A142);
[ > printf(`A143 = %+2.08e;`,A143);
[ > printf(`A151 = %+2.08e;`,A151);
[ > printf(`A152 = %+2.08e;`,A152);
[ > printf(`A153 = %+2.08e;`,A153);
[ > printf(`Ap  = %+2.08e;`,evalf(A[p]));
[ > printf(`Apis= %+2.08e;`,evalf(A[pis]));
[ > printf(`Mpis= %+2.08e;`,evalf(M[pis]));
[ > writeto(terminal);
```